Experimental Study
on
the Ranque-Hilsch Vortex Tube

PROEFSCHRIFT

ter verkrijging van de graad van doctor aan de
Technische Universiteit Eindhoven, op gezag van
de Rector Magnificus, prof.dr.ir. C.J. van Duijn,
voor een commissie aangewezen door het College
voor Promoties in het openbaar te verdedigen op
dinsdag 29 november 2005 om 16.00 uur

door

Chengming Gao

geboren te HuBei, China

Dit proefschrift is goedgekeurd door de promotor:

prof.dr. A.T.A.M. de Waele

Copromotor:

dr.ir. J.C.H. Zeegers

Omslagontwerp: Paul Verspaget,
Druk: Universiteitsdrukkerij, TUE

CIP-DATA LIBRARY TECHNISCHE UNIVERSITEIT EINDHOVEN

Gao, Chengming

Experimental study on the Ranque-Hilsch vortex tube / door Chengming Gao. -
Eindhoven : Technische Universiteit Eindhoven, 2005.
Proefschrift. - ISBN 90-386-2361-5
NUR 924
Trefw.: Fysische transportverschijnselen / Gassen: Thermodynamica / Kolkstroming/ Turbulentie / Cryogene techniek.
Subject headings: Transport processes / Thermodynamics / Swirling flow / Turbulence / Cryogenics.

———*To*

My mother: Gao Cuihua; my father: Lee Kejing;
My sister: Lee Yinxia
My wife: Xu Hong; my son: Lee Jian

"In the experimental research, the appropriate experimental technology may achieve twice the result with half the effort."

Contents

Chapter 1

Introduction

1.1 Background

The Vortex Tube (VT) cooler is a device that generates cold and hot gas from compressed gas, as shown in Fig. 1.1. It contains the following parts: one or more inlet nozzles, a vortex chamber, a cold-end orifice, a hot-end control valve and a tube. When high-pressure gas (6 bar) is tangentially injected into the vortex chamber via the inlet nozzles, a swirling flow is created inside the vortex chamber. When the gas swirls to the center of the chamber, it is expanded and cooled. In the vortex chamber, part of the gas swirls to the hot end, and another part exists via the cold exhaust directly. Part of the gas in the vortex tube reverses for axial component of the velocity and move from the hot end to the cold end. At the hot exhaust, the gas escapes with a higher temperature, while at the cold exhaust, the gas has a lower temperature compared to the inlet temperature. This was first discovered by Ranque [1] in 1933, and by Hilsch [2] in 1947. In memory of their contribution the VT is also known as Ranque Vortex Tube (RVT), Hilsch Vortex Tube (HVT), and Ranque-Hilsch Vortex Tube (RHVT). In this thesis it is referred to as Ranque-Hilsch Vortex Tube (RHVT).

A RHVT has the following advantages compared to the normal commercial refrigeration device: simple, no moving parts, no electricity or chemicals, small and lightweight, low cost, maintenance free, instant cold air, durable (because of the stainless steel and clean working media), adjustable temperature [3, 4]. But, its low thermal efficiency is a main limiting factor for its application. Also the noise and availability of compressed gas may limit its application. Therefore, when compactness, reliability and lower equipment cost are the main factors and the operating efficiency becomes less important, the RHVT becomes a nice device for heating gas, cooling gas, cleaning gas, drying gas, and separating gas mixtures, DNA application, liquefying natural gas and other purposes [3, 5–7].

The underlying physical mechanism processes that determine the cooling of gas in this device have not been resolved completely in the past. The research on vortex tube generally concerns the following aspects: the compressible fluid dynamics of turbulent and unsteady flow; thermodynamics; and heat transfer. These aspects make the research complicated and challenging. The interest in this research dates back to the work by Westley [8] who states that, “Besides its possible importance as a practical device, the vortex tube presented a new and intriguing phenomenon in fluid dynamics”.

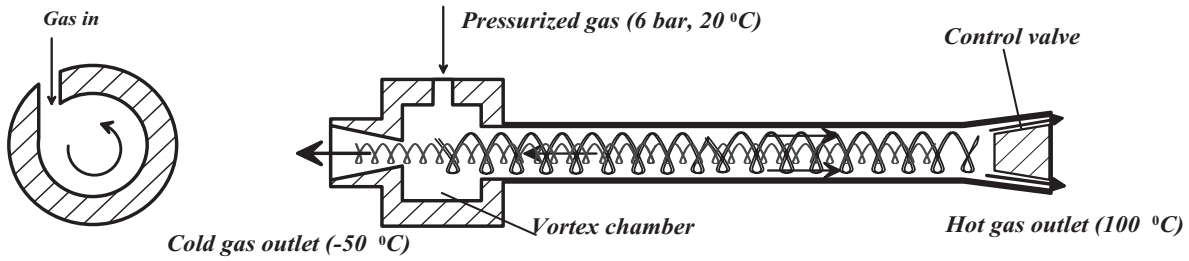

Figure 1.1: *Schematic drawing of the RHVT system.*

1.2 The state of the art

Concerning the literature we first refer to the bibliographical work [9] by Westley in 1954, in which 116 publications before 1953 have been listed and then the PhD work [10] by Soni in 1973, and the work [11] by Hellyar in 1979 with about 250 references. In this section, more recent work is divided in experimental and in theoretical researches and discussed briefly according to two different aspects.

1.2.1 Experimental development

Experimentally, three different aspects were studied in the past which include the working media, the geometry and the internal flow field:

1.2.1.1 Working medium

The first study on the separation of mixtures with the RHVT were published in 1967 by Linderstrom-Lang [12] and in 1977 by Marshall [13]. The gas mixtures (oxygen and nitrogen, carbon dioxide and helium, carbon dioxide and air, and other mixtures) were used as working medium in their work. In 2001 the RHVT system was used for carbon-dioxide separation by Kevin [14]. In 2002 the RHVT system was used to enrich the concentration of methane by Manohar [15]. In 2004, natural gas was used as working medium and with the RHVT natural gas was liquified by Poshernev [16].

In 1979 steam was used as working medium by Takahama [17]. In 1979, two-phase propane was used as the working medium by Collins [18]. It was found that when the degree of dryness[1] of the liquid and gaseous propane is higher than 0.80, a significant temperature difference maintains. With two-phase working medium, the degree of dryness is an important parameter, when the degree of dryness is larger than some critical value, energy separation occurs.

In 1988 Balmer [19] applied liquid water as the working medium. It was found that when the inlet pressure is high, for instance 20∼50 bar, the energy separation effect still exists. So it proves that the energy separation process exists in incompressible vortex flow as well.

From the above investigations it was found that the working media is very important in the operation of the RHVT system. By applying different working media, the performance

[1] the dryness ζ is defined as the ratio of the mass of gaseous part over the total mass,

$$\zeta = \frac{m_g}{m_g + m_l}$$

.

of the system can be optimized or the RHVT can be used for purposes directly related to the working medium, like gas separations, liquefying natural gas [7].

1.2.1.2 Geometry

Aspects of the geometry concerns the positioning of components like the cold exhaust, control valves and inlet nozzles. For the positioning of the cold exhaust, there are two different types of RHVT systems proposed by Ranque [20]: counterflow RHVT system (see Fig. 1.1) and uniflow RHVT system (see Fig. 1.2). When the cold exhaust is placed on the other side from the hot exhaust, it is called "counterflow". When the cold exhaust is placed at the same side of the hot exhaust, it is named "uniflow". From the experimental investigation [20–22] it was found that the performance of the uniflow system is worse than that of the counterflow system. So, most of the time, the counterflow geometry was chosen. Hilsch [2] was the first to investigate the effect of the geometry on the performance of the RHVT system.

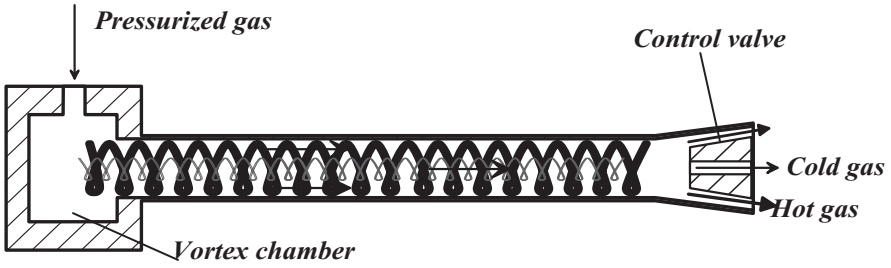

Figure 1.2: *Schematic drawing of the uniflow RHVT system.*

The effects of the placement of the control valves, and the inlet nozzles on the performance are discussed by Linderstrom-Lang in [23].

In 1955, Westley [24] experimentally optimized the geometry of the RHVT system. He found that the optimum situation can be described by a relationship between the injection area, the tube length, the vortex tube cross sectional area, the cold end orifice area and the inlet pressure. The relationship is the following:

$$\frac{A_c}{A_{vt}} \simeq 0.167, \frac{A_{in}}{A_{vt}} \simeq 0.156 + 0.176/\tau_p, \text{and } \tau_p = \frac{p_{in}}{p_c} = 7.5$$

where A_c is the flow area of the cold exhaust, A_{vt} is the flow area of the vortex tube, A_{in} is the flow area of the inlet nozzle, p_{in} is the inlet pressure and p_c is the cold exhaust pressure.

Since the 1960s, Takahama [17, 25–30] published a series of papers on the RHVT. He found that if the Mach number at the exhaust of the inlet nozzle reaches 0.5∼1, the geometry should have the following relationship in order to have larger temperature differences or larger refrigeration capacity:

$$\frac{D_{in}}{D_{vt}} = 0.2, \frac{A_{in}}{A_{vt}} = 0.08 \sim 0.17, \frac{A_c}{A_{in}} = 2.3$$

where D_{in} is the diameter of the injection tube and D_{vt} is the diameter of the vortex tube.

In 1969, Soni [10] published a study on the RHVT system considering 170 different tubes and described the optimal performance by utilizing the Evolutionary Operation Technique.

In that work, he proposed the following relationships between the design parameters

$$\frac{A_{\text{in}}}{A_{\text{vt}}} = 0.084 \sim 0.11, \frac{A_{\text{c}}}{A_{\text{vt}}} = 0.08 \sim 0.145, \frac{L_{\text{vt}}}{D_{\text{vt}}} > 45.$$

where L_{vt} is the length of the vortex tube. It can be found that all the dimensionless quantities listed above have the same order of magnitude as proposed by Westley and Takahama. In 1974, Raiskii [31] conformed the relationships experimentally.

Another type of geometry is the conical vortex tube (or divergent vortex tube), see Fig. 1.3. In 1961, Paruleker [32] designed a short conical vortex tube. By varying the conical angle of the vortex tube, he found that the parameter $L_{\text{vt}}/D_{\text{vt}}$ can be as small as 3. He found that the roughness of the inner surface of the tube has influence on its performance as well: any roughness element on the inner surface of tube will decrease the performance of the system (based on the temperature difference) up to 20%. He suggested that the designs of the vortex chamber and the inlet nozzle are very important, he mentioned that the inlet nozzle should have an Archimedean spiral shape and its cross section should be slotted. The inlet nozzle in the form of a slot was also suggested by Reynolds [33] in 1960. In 1966, Gulyaev [34] did more research on the conical vortex tube. He found that the vortex tube with a conical angle of about 2.3^o surpassed the best cylinder tube by 20%∼25% for the thermal efficiency and the refrigeration capacity. In 1968, Borisenko [35] found that the optimum conical angle for the conical vortex tube should be 3^o. The conical vortex tube was further investigated by Poshernev in 2003 and 2004 [3, 16, 36] for chemical applications.

In order to shorten the tube length, Takahama introduced the divergent vortex tube (in fact the same as the conical vortex tube but with a different name) in 1981 [30]. This divergent vortex tube can reach the same performance as the normal tube but with a smaller length. Because within the divergent tube, the cross sectional area increases to the hot end, the gradient of the gas axial velocity decreases. He suggested that the divergence angle should be in the range $1.7^o \sim 5.1^o$. With all research on divergent vortex tubes, it can be found that there exists an optimal conical angle and this angle is very small. When the flow swirls to the hot end, the cross section area increases, so the azimuthal motion is slowed down along its path.

A detwister is some kind of vortex stopper, which can be used to block the vortex motion at the exhausts. By applying the detwister, in front of the gas exhausts, the vortex motion inside dies out, so the detwister is an important improvement of the design of the vortex tube. Initially the detwister was mounted near the hot exhaust (sometimes also put close to the cold end). The detwister was proposed by Grodzovskii (cited from [37]) in 1954, Merkulov (from [37]) in 1969, and James [38] in 1972. In 1989 Dyskin [37] concluded that the hot-end detwister can improve the performance of the RHVT system and shorten the tube length; the cold-end detwister has the same positive effect on the efficiency. Further investigation shows that detwisters, placed inside the vortex tube, blocked the swirling flow to the exhausts, generated turbulence and destroyed the azimuthal motion.

In 1996, Piralishvili and Polyaev [39] introduced a new type of vortex tube: the Double-Circuit vortex tube with a conical tube to improve the performance, as shown in Fig. 1.4. At the hot end, in the center of the control valve, there is an orifice which allows feedback gas ($\dot{m}_{\text{dc}}$) to be injected into the vortex tube. The feedback gas has the same temperature as the inlet gas but with low pressure. With this design, the cooling power of the system is increased and the performance of the vortex tube is improved.

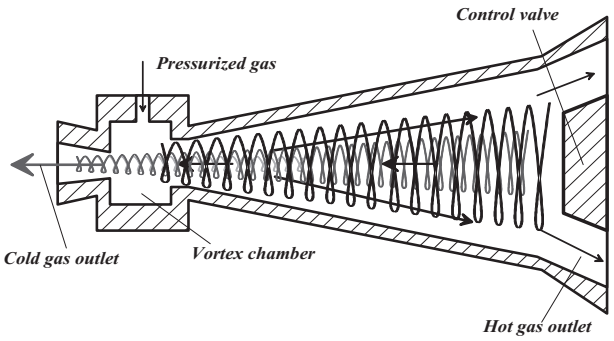

Figure 1.3: *Schematic drawing of the conical vortex tube.*

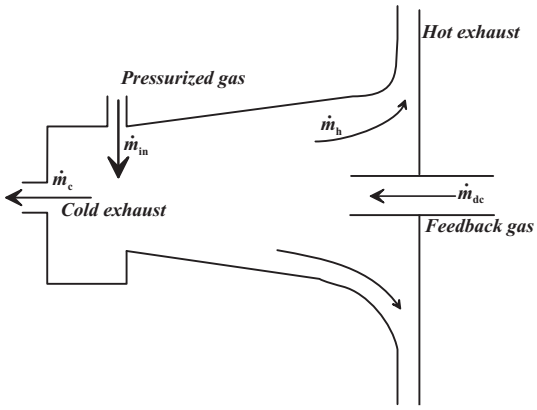

Figure 1.4: *Schematic drawing of the Double-Circuit Vortex Tube.*

In practice, multiple stage vortex tube systems have been introduced for improving the performance. A two-stage vortex tube system was built up in 2001 by Guillaume and Jolly [40]. They found that the temperature difference at each stage is larger than that generated by the single stage vortex tube under the same operation conditions.

The strong noise level, created by the system, indicates the existence of sound inside the RHVT. In order to reduce the sound level and convert the acoustic energy into heat, in 1982, Kurosaka [41], Chu [42] and Kuroda in 1983 [43] introduced an acoustic muffler. They found that with the muffler the performance of the system was better than without.

Now commercial vortex tubes are manufactured by ITW Vortex, Exair, etc [4, 44–49]. They apply the ideas of the detwister, conical tube, and acoustic muffler.

1.2.1.3 The internal flow field

The investigation of the flow field inside the VT began with flow-visualization techniques such as liquid injection and smoke. In 1950 Roy [50] injected colored liquid into the RHVT system to investigate the flow pattern. In 1959, Lay [51] injected water inside the RHVT system, but nothing could be seen. In 1962, Sibulkin [52] used a mixture of powdered carbon and oil. In 1996, Piralishvili [39] used kerosene with the mass ratio of 1:30. In 1962, Smith [53, 54] used smoke. With the injection of liquid, all investigations concentrated on tracking the flow trail on the end wall and using a lucite tube as the vortex tube for tracking the liquid elements visually. From the flow trail on the end wall, the gas velocity distribution shows solid body rotation in the center which is similar to the Rankine vortex motion. Visualization by means of smoke shows the flow path inside the tube along the axis. The velocity distribution also shows the similarity with the Rankine vortex motion. From the flow pattern inside the tube, the two different parts of the swirling flow can be distinguished: with an axial motion towards the hot end is the peripheral region and with axial motion towards the cold end is the central region. With these visualization techniques, the advantage is that it is very easy to qualitatively determine the flow field inside the tube. The disadvantage is that it is not possible to obtain quantitative information of the flow and to find the temperature field inside the tube.

The visualization techniques can only give us a qualitative description of the flow field inside the vortex tube. For more detailed flow information, like the pressure, temperature, and

velocity fields inside the system, probes are required. Sheller in 1957 [55], Lay in 1959 [51,56], Holman in 1961 [57], Smith [53,54] and Sibulkin [52,58,59] in 1962, Reynolds in 1962 [33,60], Takahama [25–28,30], Ahlborn in 1997 [61], Gao in 2005 [62] all used a Pitot tube for pressure measurement and thermocouple to measure the temperature. The probes used by Sheller, Lay, Holman, Smith, Reynolds and Takahama have large size compared to the system geometry. The error introduced by the probes cannot be neglected and the velocity in the center cannot be measured [61]. The probe used by Ahlborn is small, but in his work the probe is not calibrated, and the error can be up to 25% [61]. The probe used by Reynolds was not calibrated either, so the results can only be used for qualitative analysis [60]. More detailed descriptions about these techniques will be given in later sections.

In summary, the purposes of all these experimental investigations are: first of all, to find empirical expressions which can be used for optimizing the RHVT system; secondly, to apply the RHVT for wide application purposes, like cooling and heating, cleaning, purifying and separation, etc.; finally, to investigate the internal process and to understand the mechanism of the energy separation. In the past, a lot of experimental studies have been published. The improvements of the RHVT performance due to the geometric adjustments could not be explained completely. Furthermore the experimental techniques have some limitations and need to be improved. In this thesis, we employ a specially designed Pitot tube, thermocouple and a hot-wire anemometry for fluctuation measurements, turbulence and spectra analysis.

1.2.2 Theoretical development

Theoretical studies have been carried out in parallel with experiments. Most theories are based on results obtained from the related experimental work, some are based on numerical simulations. In 1997 Gutsol [63] and in 2002 Leont'ev [64] have published detailed reviews about the RHVT theories. So, the summary on the theories given here will be brief.

1.2.2.1 Adiabatic compression and adiabatic expansion model

The first explanation was given by Ranque [1,20]. He explained that the energy separation is due to adiabatic expansion in the central region and adiabatic compression in the peripheral region. In 1947 Hilsch [2] used similar ideas to explain the phenomenon in the RHVT, but introduced the internal friction between the peripheral and internal gas layers. He used this model to explain his experimental results rather well. Because the process in the RHVT is not truly adiabatic [63,65], this model was later rejected (see Fulton [66]).

1.2.2.2 Heat transfer theory

In 1951, Scheper [67] proposed a heat transfer theory for the RHVT system based on his experimental work. This model is based on empirical assumptions for the heat transfer and is incomplete.

1.2.2.3 Effect of friction and turbulence

In 1950, Fulton [66] explained that the energy separation is due to the free and forced vortex flow generated inside the system. He stated that:"Fresh gas before it has traveled far in the tube, succeeds in forming an almost free vortex in which the angular velocity or rpm is low

at the periphery and very high toward the center. But friction between the layers of gas undertakes to reduce all the gas to the same angular velocity, as in a solid body." During the internal friction process between the peripheral and central layers, the outer gas in turn gains more kinetic energy than it loses internal energy and this leads to a higher gas temperature in the periphery; the inner gas loses kinetic energy and so the gas temperature is lower. Fulton found that the maximum temperature difference $\Delta T_{\mathrm{c,max}}(= T_{\mathrm{in}} - T_{\mathrm{c}})$ has a relationship with the Prandtl number

$$\frac{\Delta T_{\mathrm{c,max}}}{\Delta T_{\mathrm{is}}} = 1 - \frac{1}{2P_{\mathrm{r}}} \text{ (see Equation 25 in [66])} ,$$

where ΔT_{is} is calculated based on an assumption of an isentropic expansion process:

$$\Delta T_{\mathrm{is}} = T_{\mathrm{in}} \left(1 - (\frac{p_{\mathrm{c}}}{p_{\mathrm{in}}})^{(\gamma-1)/\gamma} \right) .$$

Lay [51] used the potential and forced vortex motion for the RHVT analysis and proposed via an elegant mathematical formalization that the internal friction effect and turbulence are the main reason for the energy separation. Kreith [68], Alimov [69] also attributed the friction effect as reason for the energy separation. Reynolds [70,71], Deissler [72] also pointed out that the energy separation is due to friction and turbulence.

Van Deemter [73] in 1951 performed numerical simulation work based on the extended Bernoulli equation. He had similar ideas as Fulton and calculated the temperature profile as scaled by the turbulent Prandtl number. There is a remarkable agreement between his model and Hilsch's measurements.

Deissler [72], Reynolds [70, 71], Sibulkin [52, 58, 59] and Lewellen [74] all presented mathematical analysis based on the turbulent N-S equation. Based on their analysis, they come to the common conclusion that heat transfer between flow layers by temperature gradients and by pressure gradients due to turbulent mixing, turbulent shear work done on elements are the main reasons for the energy separation.

At the author's former university, Xi'an Jiaotong University, this theory was further investigated with numerical simulation method and experimental studies [75–77]. The work concluded that the energy separation is mainly due to internal friction and turbulence characterized by the turbulent viscosity number.

Gutsol [63] summarized many existent Russian theories in the past in a critical review. He proposed a turbulence model with exchange of the micro-volumes motion effect to explain the energy separation. Gutsol explained that due to the turbulent motion at the exhaust of the inlet nozzle, turbulent vortex motion exists inside the vortex tube at different layers. Via this turbulent mass transfer an exchange of kinetic energy and heat takes place between fluid layers. This theory is similar to the inner friction theory proposed by Fulton but more mathematical.

The internal friction, mentioned in the friction and turbulence models, is the viscous friction between different gas layers. This is different from the roughness and friction mentioned by Paruleker [32]. The friction referred to in Paruleker is the friction between the wall surface and flow.

The friction and turbulence models are incomplete. The relationships proposed by different authors include a lot of turbulent parameters, which are difficult to determine and rely on assumptions. Another disadvantage is that the models do not consider geometrical effects. All these difficulties limit the applications of these models.

1.2.2.4 Acoustic streaming model

Kurosaka, Chu and Kuroda [41–43] from the University of Tennessee explained the VT with the phenomenon of acoustic streaming. They focused their research on the fundamental functions of ordered/disordered turbulence and found a relationship between the acoustic resonance frequencies and the forced vortex motion frequency. They proposed that the energy separation inside the RHVT is due to the damping of the acoustic streaming along the axis of the tube towards the hot exhaust. In Chapter 6 the frequencies found from the spectral analysis on the samples taken by the hot-wire anemometry also have these relationships and indicate the existence of the acoustic phenomena.

1.2.2.5 Secondary circulation model

Ahlborn [61, 78] proposed a so-called secondary circulation model based on his experimental results. He found that the cumulative mass flow over the cross section of the vortex tube in the cold end direction is larger than the cold exhaust flow, which implies the existence of a secondary circulation flow in the VT. With this secondary circulation model, the RHVT can be considered as a classical refrigeration device and the secondary circulation flow can be thought as a classical cycle [78].

The secondary flow pattern has also been noted experimentally by Linderstrom-Lang [23, 79], Fulton [66], Scheper [67], Ahlborn [61] and Gao [62], and numerically explained by Cockerill [22], Frohlingsdorf [80], Gutsol [81] and Aljuwayhel [82]. The main difference among all these secondary flow patterns is whether the secondary flow is a closed cycle or not. Linderstrom-Lang, Fulton, Scheper and Cockerill suggested it as an open cycle, while Ahlborn, Gao, Gutsol, Frohlingsdorf and Aljuwayhel suggested a closed cycle. More detailed analysis on the secondary circulation model is discussed in later Chapters. We have chosen to modify this secondary circulation model in this thesis, see Chapter 2.

In summary, as pointed out by van Deemter [73] and Gutsol [63] most of these theories can only either explain their own works and could not match with the others, or be used for qualitative analysis only. This indicates also that the above theories are incomplete. The above mentioned theories point out two directions of theoretical research, which gives hints for further investigations. One is focussing on thermodynamics (compression and expansion), turbulent flow, viscous friction, internal heat transfer, and acoustics. The other one is concerning the flow pattern, like secondary circulation. The further analysis of these two aspects form the main body of this thesis.

1.3 Preview of this thesis

In the Low Temperature group at the TU Eindhoven, research is focused on new cooling technologies and their applications. The pulse-tube cryocooler is the main research theme of the group. Another research subject is thermoacoustics. A common property of pulse-tube cooler, thermoacoustic cooler and Ranque-Hilsch vortex tube is that these have (almost) no moving parts. Furthermore the incomplete understanding of the physical mechanisms occurring in the tube are also a challenge to start working on this subject. This thesis starts research in the RHVT direction for the Low Temperature group.

As discussed in Section 1.2, in the past 70 years, the history follows the pattern of initial enthusiasm, then apathy, and later renewed interest. After Hilsch presented his work, the investigations of RHVT were starting to become prosperous and interested many researchers due to the magical phenomena, sometimes referred to as Maxwell's demons, occurring in the vortex tube. But due to the inefficient operation, interest in the VT died down during the 1970s. In the 1980s, researchers in the former USSR showed renewed interest and introduced it to China as well. Now in some universities, the RHVT system is a teaching example in thermodynamics lectures. In this thesis we perform fundamental investigations on the RHVT system (to measure the turbulence and the acoustics inside the system). This includes the design of the RHVT system, design and calibration of the measurement techniques and the analysis of the experimental results.

First of all, in Chapter 2, the theoretical analysis of the RHVT system based on the thermodynamic laws is introduced. The secondary circulation model from Ahlborn [78] is introduced. The comments on this model is given in order to further modify it. The modified relationships include vortex chamber geometrical effects. After that, the thermal efficiencies of the RHVT system are defined.

In Chapter 3 the measurement techniques and the calibrations are explained in detail. Here a special designed Cylinder type Pitot tube is used for the pressure measurements, a thermocouple is used for the temperature measurements and a single probe Hot-wire anemometry (SPHWA) is used for the turbulence and the velocity measurements. Then in Chapter 4 the design and investigation of a small RHVT system are described to get the first impression of these techniques. It shows that the designed measurement techniques operate very well and the accuracies of these techniques are acceptable. Comparison of the results from this small RHVT system and the work of others is presented. The thermal efficiencies of the small system are calculated, which shows that the efficiencies are lower than 5%. With the calculated cumulative mass flow over the cross sections, a secondary circulation flow is found experimentally.

In Chapter 5 the design of the inlet nozzle is introduced based on gas dynamical analysis. The influences of the operation parameters (inlet pressure, inlet mass flow) and the geometrical parameters (length of nozzle, inlet and exhaust diameters of the nozzle) on the exhaust Mach number, the exhaust momentum and the exhaust pressure are investigated. In Chapter 6, the design of a larger system and the influence of the different components on the performance are discussed, and an optimized system is chosen for further analysis. All the experimental results, based on different techniques, are sampled individually. At the end the velocity, pressure and temperature mappings are shown based on the results from three techniques. In Chapter 7, the thesis is summarized and conclusions are formulated.

References

[1] M.G. Ranque. Experiences sur la detente avec production simultanees dun echappement dair chaud et dun echappement dair froid. *J. de Physique et de Radium*, 7(4):112–115, 1933.

[2] R. Hilsch. The use of the expansion of gases in a centrifugal field as cooling process. *Rev. Sci. Instrum.*, 18(2):108–113, 1947.

[3] L. Khodorkov, N.V. Poshernev, and M.A. Zhidkov. The vortex tube—a universal device for heating, cooling, cleaning, and drying gases and separating gas mixtures. *Chemical and Petroleum Engineering*, 39(7-8):409–415, July 2003.

[4] Exair.com. `http://www.exair.com/vortextube/vt_page.htm`.

[5] R. Ebmeier, S. Whitney, S. Alugupally, M. Nelson, N. Padhye, G. Gogos, and H.J. Viljoen. Ranque-Hilsch Vortex Tube thermocycler for DNA amplification. *Instrumentation Science and Technology*, 32(5):567 – 570, 2004.

[6] R.F. Boucher and J.R. Tippetts. Vortex-tube-driven thermo-electricity. In *Sixth triennal international symposium on Fluid Control, Measurement and Visualization*, 6th, Sherbrooke, Canada, Paper 50, August 2000.

[7] Method of natural gas liquefaction. Russia patent No. 2202078 C2, April 2003.

[8] R. Westley. Vortex tube performance data sheets. Cranfield College Note 67, College of Aeronautics, 1957.

[9] R. Westley. A bibliography and survey of the vortex tube. Cranfield College Note 9, College of Aeronautics, 1954.

[10] Y. Soni. *A parameteric study of the Ranque-Hilsch tube*. PhD dissertation, University of Idaho Graduate School, U.S.A., Oct. 1973.

[11] K.G. Hellyar. Gas liquefaction using a Ranque-Hilsch vortex tube: Design criteria and bibliography. Report for the degree of Chemical Engineer, September 1979.

[12] C.U. Linderstrom-Lang. On gas separation in Ranque-Hilsch vortex tubes. *Z. Naturforschg.*, 22(a):835–837, April 1967.

[13] J. Marshall. Effect of operating conditons, physical size and fluid characteristics on the gas separation performance of a Linderstrom-Lang vortex tube. *Int. J. Heat Mass Transfer*, 20:227–231, 1977.

[14] K.T. Raterman, M. Mckellar, A. Podgomey, D. Stacey, and T. Turner. A vortex contactor for carbon dioxide separations. In *First National Conference on Carbon Sequestration*. National Energy Technology Laboratory, U.S.A., `http://www.netl.doe.gov/publications/proceedings/01/carbon_seq/7b3.pdf`, May 2001.

[15] M.R. Kulkarni and C.R. Sardesai. Enrichment of Methane concentration via separation of gases using vortex tubes. *J. Energy Engrg*, 128(1):1–12, April 2002.

[16] N.V. Poshernev and I.L. Khodorkov. Natural-gas tests on a conical vortex tube (CVT) with external cooling. *Chemical and Petroleum Engineering*, 40(3-4):212–217, March 2004.

[17] H. Takahama, H. Kawamura, S. Kato, and H. Yokosawa. Performance characteristics of energy separation in a steam-operated vortex tube. *Int. J. Engng Sci.*, 17:735–744, 1979.

[18] R.L. Collins and R.B. Lovelace. Experimental study of two-phase propane expanded through the Ranque-Hilsch tube. *Trans. ASME, J. Heat Transfer*, 101:300–305, May 1979.

[19] R.T. Balmer. Pressure-driven Ranque-Hilsch temperature separation in liquids. *Trans. ASME, J. Fluids Engineering*, 110:161–164, June 1988.

[20] M.G. Ranque. Method and apparatus for obtaining from a fluid under pressure two currents of fluid at different temperatures. US Patent No. 1952281, March 1934.

[21] C.D. Fulton. Comments on the vortex tube. *J. ASRE Refrigerating Engng*, 58:984, 1950.

[22] T. Cockerill. Ranque-Hilsch vortex tube. Master thesis, University of Cambridge, 1995.

[23] C.U. Linderstrom-Lang. *Studies on transport of mass and energy in the vortex tube—The significance of the secondary flow and its interaction with the tangential velocity distribution.* Riso report, Denmark, September 1971.

[24] R. Westley. Optimum design of a Vortex Tube fpr achieving larger temperature drop ratios. Cranfield College Note 30, College of Aeronautics, 1955.

[25] H. Takahama and K. Kawashima. *An experimental study of vortex tubes.* Research, 1960.

[26] H. Takahama. Studies on vortex tubes (1) experiments on efficiency of energy separation (2) on profiles of velocity and temperature. *Bulletin of JSME*, 8(31):433–440, 1965.

[27] H. Takahama and N. Soga. Studies on vortex tubes (2nd report): Reynolds number. the effects of the cold air rate and the partial admission of nozzle on the energy separation. *Bulletin of JSME*, 9(33):121–130, 1966.

[28] H. Takahama and etc. Studies on vortex tubes (3rd report): Variations of velocity, temperature and energy with axial distance, the mechanism of energy separation. *Bulletin of JSME*, 235:503–510, 1966.

[29] H. Takahama and H. Yokosawa. *An experimental study of vortex tubes(where the vortex chamber includes a divergent tube).* Research, 1981.

[30] H. Takahama and H. Yokosawa. Energy separation in vortex tubes with a divergent chamber. *Trans. ASME, J. Heat Transfer*, 103:196–203, May 1981.

[31] Y.D. Raiskii and L.E. Tunkel. Influence of vortex-tube configuration and length on the process of energetic gas separation. *Journal of Engineering Physics and Thermophysics*, 27(6):1578 – 1581, December 1974.

[32] B.B. Parulekar. The short vortex tube. *The Journal of Refrigeration*, 4:74–80, July and August 1961.

[33] A.J. Reynolds. *Studies of Rotating fluids a) Plane Axisymmetric Flow, b) Forced Oscillations in a Rotating fluid, c) The Ranque-Hilsch Vortex Tube.* PhD dissertation, University of London, September 1960.

[34] A.I. Gulyaev. Investigation of conical vortex tubes. *Journal of Engineering Physics*, 10(3):193–195, 1966.

[35] V.A. Safonov A.I. Borisenko and A.I. Yakovlev. The effect of geometric parameters on the characteristics of a conical vortex cooling unit. *Journal of Engineering Physics and Thermophysics*, 15(6):1158–1162, 1968.

[36] N.V. Poshernev and I.L. Khodorkov. Experience from the operation of a conical vortex tube with natural gas. *Chemical and Petroleum Engineering*, 39(9-10):602–607, September 2003.

[37] L.M. Dyskin. Characteristics of a vortex tube with detwisting of cold flow. *Journal of Engineering Physics and Thermophysics*, 57(1):756–758, July 1989.

[38] R.W. James and S.A.Mashall. Vortex tube refirgeration. *Refrigeration and air conditioning*, pages 69–88, June 1972. Part 2.

[39] S.A. Piralishvili and V.M. Polyaev. Flow and thermodynamic characteristics of energy separation in a Double-Circuit vortex tube—an experimental investigation. *Experimental Thermal and Fluid Science*, 12:399–410, 1996.

[40] D.W. Guillaume and J.L. Jolly. Demonstrating the achievement of lower temperatures with two-stage vortex tubes. *Review of Scientific Instruments*, 72(8):3446–3448, August 2001.

[41] M. Kurosaka. Acoustic streaming in swirling flow and the Ranque-Hilsch (vortex-tube) effect. *J. Fluid Mech.*, 124:139–172, 1982.

[42] J.G. Chu. *Acoustic streaming as a mechanism of the Ranque-Hilsch effect*. PhD dissertation, University of Tennessee, Knoxville, Dec. 1982.

[43] H. Kuroda. *An experimental study of temperature separation in swirling flow*. PhD dissertation, University of Tennessee, Knoxville, Dec. 1983.

[44] Arizona Vortex Tube Manufacturing Company. `http://www.arizonavortex.com/vortextubes.htm`.

[45] AirTX The Air Research Technology Company. `http://www.airtxinternational.com/catalog/vortex_tubes.php`.

[46] ITW Air management. `http://www.itw-air.com/index.php`.

[47] ITW Vortec. `http://www.vortec-nl.com/`.

[48] Newman Tools Inc. `http://www.newmantools.com/vortex.htm`.

[49] Vortexair.biz. `http://www.vortexair.biz/Cooling/SPOTCOOLPROD/spotcoolprod.htm`.

[50] R. MacGee Jr. Fluid action in the vortex tube. *J. ASRE Refrigerating Engng*, 58:974–975, 1950.

[51] J.E. Lay. An experimental and analytical study of vortex-flow temperature separation by superposition of spiral and axial flow, part II. *Trans. ASME J. Heat Transfer*, 81:213–222, Aug. 1959.

[52] M. Sibulkin. Unsteady, viscous, circular flow part 3. application to the Ranque-Hilsch vortex tube. *J. Fluid Mech.*, 12:269–293, 1961.

[53] J.L. Smith Jr. An experimental study of the vortex in the cyclone separator. *Trans. ASME, J. B. Engng*, 84:602–608, Dec. 1962.

[54] J.L. Smith Jr. An analysis of the vortex flow in the cyclone separator. *Trans. ASME, J. B. Engng*, 84:609–618, Dec. 1962.

[55] W. A. Scheller and G. Martin Brown. The Ranque-Hilsch vortex tube. *Fluid Mechanics in Chemical Engineering*, 49(6):1013–1016, 1957.

[56] J.E. Lay. An experimental and analytical study of vortex-flow temperature separation by superposition of spiral and axial flow, part I. *Trans. ASME J. Heat Transfer*, 81:202–212, Aug. 1959.

[57] J.P. Holman and G.D. Moore. An experimental study of vortex chamber flow. *Trans. ASME, J. B. Engng*, 83:632–636, Dec. 1961.

[58] M. Sibulkin. Unsteady, viscous, circular flow part 1. the line impulse of angular momentum. *J. Fluid Mech.*, 11:291–308, 1961.

[59] M. Sibulkin. Unsteady, viscous, circular flow part 2. the cylinder of finite radius. *J. Fluid Mech.*, 12:148–158, 1961.

[60] A.J. Reynolds. A note on vortex-tube flow. *J. Fluid Mech.*, 14:18–20, 1962.

[61] B. Ahlborn and S. Groves. Secondary flow in a vortex tube. *Fluid Dynamics Research*, 21:73–86, 1997.

[62] C.M. GAO, K.J. Bosschaart, J.C.H. Zeegers, and A.T.A.M. de Waele. Experimental study on a simple Ranque-Hilsch vortex tube. *Cryogenics*, 45(3):173, 2005.

[63] A. Gutsol. The Ranque effect. *Physics-Uspekhi*, 40(6):639–658, 1997.

[64] A.I. Leont'ev. Gas-dynamic methods of temperature stratification (a Review). *Fuild Dynamics*, 37(4):512–529, 2002.

[65] B. Ahlborn, J.Camire, and J.U. Keller. Low-pressure vortex tubes. *J. Phys. D: Appl. Phys.*, 29:1469–1472, 1996.

[66] C.D. Fulton. Ranque's tube. *J. ASRE Refrigerating Engng*, 58:473–479, 1950.

[67] G.W. Scheper. The vortex tube–internal flow data and a heat transfer theory. *J. ASRE Refrigerating Engng*, 59:985–989, 1951.

[68] F. Kreith and D. Margolis. Heat transfer and friction in turbulent vortex flow. *Flow, Turbulence and Combustion*, 8(1):457 – 473, January 1959.

[69] R.Z. Alimov. Flow friction and heat and mass transfer in a swirled flow. *Journal of Engineering Physics and thermophysics*, 10(4):251 – 257, April 1966.

[70] A.J. Reynolds. On the dynamics of turbulent vortical flow. *Z. angew. Math. Phys.*, 12:149–158, 1961.

[71] A.J. Reynolds. Energy flow in a vortex tube. *Z. Angew. Math. Phys.*, 12:343–356, 1961.

[72] R.G. Deissler and M. Perlmutter. Analysis of the flow and energy separation in a turbulent vortex. *Int. J. Heat Mass Transfer*, 1:173–191, 1960.

[73] J.J. van Deemter. On the theory of the Ranque-Hilsch cooling effect. *Appl. Sci. Res.*, 3:174–196, 1951.

[74] W.S. Lewellen. A solution for three-dimentional vortex flows with strong circulation. *J. Fluid Mech.*, 14:420–432, 1962.

[75] Q.H. Wu. The internal process analysis and the experimental investigation on the Ranque-Hilsch vortex tube. Master thesis, Xi'an Jiaotong University, Xi'an, China, 1991.

[76] J.B. Yang. Mathematical model of vortex tube and experimental study of optimizing performance parameters in vortex tube. Master thesis, Xi'an Jiaotong University, Xi'an, China, 1991.

[77] Y.B. Zhang. The theoretical and experimental study on vortex tube. Master thesis, Xi'an Jiaotong University, Xi'an, China, 1993.

[78] B. Ahlborn and J.M. Gordon. The vortex tube as a classic thermodynamic refrigeration cycle. *J. Appl. Phys.*, 88(6):3645–3653, 2000.

[79] C.U. Linderstrom-Lang. *Gas separation in the Ranque-Hilsch vortex tube model calculations based on flow data.* Riso report, Denmark, June 1966.

[80] W. Frohlingsdorf. *Unterschungen zur kompressiblen Strömung und Energietrennung im Wirbelrohr nach Ranque und Hilsch.* PhD dissertation, Ruhr-Universitat-Bochum, 1997. In German.

[81] A. Gutsol and J.A. Bakken. A new vortex method of plasma insulation and explanation of the Ranque effect. *J. Phys. D: Appl. Phys.*, 39:704–711, 1998.

[82] G.F. Nellis N.F. Aljuwayhel and S.A. Klein. Parametric and internal study of the vortex tube using a cfd model. *International Journal of Refrigeration*, 28(2):442–450, 2005.

Chapter 2

Theoretical analysis of the RHVT

Since the 1930s, the mechanism of the energy separation inside the RHVT system has puzzled researchers. Even now, there is no clear theory that can explain the phenomenon completely. In this chapter, the thermodynamical laws are applied to the RHVT system itself. With these laws, the relationships between the entrance and exhaust gas properties and the maximum pressure ratio in the system have been found. The secondary circulation model proposed by Ahlborn [1, 2], is named here the "original secondary circulation model" (OSCM). In this model, Ahlborn applied some assumptions and some ideas which are pointed out in this Chapter. Here, the secondary circulation model is modified. We will call it the "modification of Ahlborn's model" (MAM). The chamber influence is considered and the compressible flow analysis (gas dynamics) is applied in the analysis of the inlet nozzle. The comparison between the two models shows that MAM agrees better with the measurement than OSCM. At the end, the thermal efficiencies are defined, analyzed, and derived as functions of the inlet and exhaust gas properties.

2.1 Thermodynamical analysis of the RHVT system

The following symbols for the geometric parameters are defined: D_{vc} is the inner diameter of the vortex chamber, D_{vt} is the inner diameter of the vortex tube, D_{ce} the diameter of the cold exhaust orifice, D_{cr} is the critical diameter. Inside the vortex chamber, D_{cr} denotes the position where the azimuthal velocity changes from the solid body rotation motion to the potential vortex motion, while inside the vortex tube, D_{cr} denotes the position where the axial velocity is zero. In practice, inside the chamber D_{cr} is the same as D_{vt}, and inside the tube, D_{cr} varies with cross sections.

2.1.1 Introduction

Fig.2.1 shows the control volume considered in the thermodynamical analysis. This control volume is taken as a black box. For the analysis, only the gas properties at the walls, at the inlet and exhaust are of interest, i.e. for the analysis details of the internal process do not need to be considered.

In this system, there are three open boundaries namely A_{in}, A_{h} and A_{c}. The gas properties on these open boundaries are listed as follows. On A_{i}: p_{i}, T_{i}, ρ_{i}, V_{i}, $\overset{*}{H}_{\mathrm{i}}$, with subscript i,

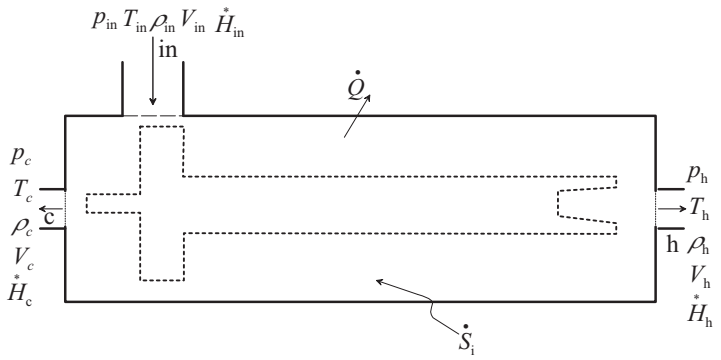

Figure 2.1: *Control volume as a black box for the thermodynamical analysis.*

the indexes "in", "h" and "c" for inlet, hot and cold, respectively. p is the pressure, T the temperature, ρ the density, V the velocity and $\overset{*}{H}$ the enthalpy flux.

In the steady flow, mass conservation between inlet flow ($\dot{m}_{\mathrm{in}}$), cold ($\dot{m}_{\mathrm{c}}$) and hot ($\dot{m}_{\mathrm{h}}$) outlet flows reads

$$\dot{m}_{\mathrm{in}} = \dot{m}_{\mathrm{h}} + \dot{m}_{\mathrm{c}} \tag{2.1}$$

With $\dot{m}_{\mathrm{c}}$ the cold exhaust mass flow, expressed as $\varepsilon\dot{m}_{\mathrm{in}}$, and $\dot{m}_{\mathrm{h}}$ the hot exhaust mass flow, expressed as $(1-\varepsilon)\dot{m}_{\mathrm{in}}$, obtained

$$\dot{m}_{\mathrm{in}} = (1-\varepsilon)\dot{m}_{\mathrm{in}} + \varepsilon\dot{m}_{\mathrm{in}} \tag{2.2}$$

where ε is the cold fraction. Its conventional definition is

$$\varepsilon = \frac{\dot{m}_{\mathrm{c}}}{\dot{m}_{\mathrm{in}}} \quad . \tag{2.3}$$

2.1.2 The first law of thermodynamics

Neglecting the velocity contribution and the potential energy, the first law of thermodynamics reads [3]

$$\dot{U} = \sum_k \dot{Q}_k + \sum_k \overset{*}{H}_k - \sum_k p_k \dot{\mathrm{V}}_k + P \tag{2.4}$$

where U is the internal energy of the system, and $\dot{U}$ is the rate of change of the internal energy. The internal energy is only state dependent. In the analysis, the system is considered as steady, and $\dot{U} = 0$. $\dot{Q}_k$ are heat flows at the various regions of the boundary. If heat flows from outside into the system, it is counted as positive. The RHVT system is assumed to be insulated, so $\dot{Q}_k = 0$. $\overset{*}{H}$ is the enthalpy flow into the system defined as $\overset{*}{H} = \overset{*}{n}h_{\mathrm{m}} = \dot{m}h$. Because the openings are large, the velocities at these openings are much lower than the sound speed, so the velocity term in these enthalpy flows can be neglected. In that case, for a calorically perfect gas the specific enthalpy depends linearly on the temperature

$$h = c_{\mathrm{p}}T,$$

here c_{p} is the specific heat at constant pressure, is constant. In Eq. 2.4 $\dot{V}_k$ is the rate of change of the volume of the system at various moving boundaries. For the control volume,

this term is zero. P takes into account all other forms of work done on the system by the environment.

Applying the first law on the system shown in Fig. 2.1, it follows that

$$\begin{array}{ll} & 0 = \dot{m}_{\rm in}\left[c_{\rm p}T_{\rm in} - (1-\varepsilon)c_{\rm p}T_{\rm h} - \varepsilon c_{\rm p}T_{\rm c}\right], \\ \text{or} & T_{\rm in} - (1-\varepsilon)T_{\rm h} - \varepsilon T_{\rm c} = 0 \quad . \end{array} \tag{2.5}$$

Taking

$$\Delta T_{\rm h} = T_{\rm h} - T_{\rm in},$$
$$\Delta T_{\rm c} = T_c - T_{\rm in}$$

and

$$\Delta T_{\rm hc} = T_{\rm h} - T_{\rm c},$$

the following relationships can be derived,

$$\begin{array}{l} T_{\rm in} = (1-\varepsilon)T_{\rm h} + \varepsilon T_{\rm c} \\ \varepsilon\Delta T_{\rm c} = (\varepsilon - 1)\Delta T_{\rm h} \\ \Delta T_{\rm h} = \varepsilon\Delta T_{\rm hc} \\ \Delta T_{\rm c} = -(1-\varepsilon)\Delta T_{\rm hc} \quad . \end{array} \tag{2.6}$$

These relationships express the inlet and exhaust temperatures as functions of the cold fraction ε.

2.1.3 The second law of thermodynamics

The second law of thermodynamics reads [3]

$$\dot{S} = \sum_k \frac{\dot{Q}_k}{T_k} + \sum_k \overset{*}{S}_k + \sum_k \dot{S}_{ik} \quad \text{with} \quad \dot{S}_{ik} \geq 0 \tag{2.7}$$

where $\dot{S}$ is the rate of increase of the entropy of the system. For the RHVT system in the steady state $\dot{S} = 0$. T_k represents the temperatures at which the heat flow $\dot{Q}_k$ enters the system from the outside. $\overset{*}{S}_k$ represents the entropy flow into the system due to matter flowing into the system, given as $\overset{*}{S}_k = \dot{m}_k s_k$, where s_k is the specific entropy of the matter flowing into the system. $\dot{S}_{\rm i}$ are the entropy production rates due to irreversible processes. Each of the entropy production rates is always positive. The most important irreversible processes in the RHVT system are:

- heat flow over a temperature difference;
- mass flow over a pressure difference;
- viscous dissipation.

Applying the second law of thermodynamics to the RHVT with $\dot{Q} = 0$, gives

$$\begin{array}{rl} 0 = & \overset{*}{S}_{\rm in} - \overset{*}{S}_{\rm h} - \overset{*}{S}_{\rm c} + \dot{S}_{\rm i} \\ \dot{S}_{\rm i} = & \overset{*}{S}_{\rm h} + \overset{*}{S}_{\rm c} - \overset{*}{S}_{\rm in} \\ = & \dot{m}_{\rm in}\left[(1-\varepsilon)(s_{\rm h} - s_{\rm in}) + \varepsilon(s_{\rm c} - s_{\rm in})\right] \quad . \end{array} \tag{2.8}$$

With R_m the specific gas constant. With the ideal gas assumption, the relation for the specific entropy becomes [3]

$$\mathrm{d}s = c_p \frac{\mathrm{d}T}{T} - R_\mathrm{m} \frac{\mathrm{d}p}{p} \quad . \tag{2.9}$$

Integrating the above equation from state 1 to state 2, gives

$$s_2 - s_1 = c_p \ln \frac{T_2}{T_1} - R_\mathrm{m} \ln \frac{p_2}{p_1} \tag{2.10}$$

Substituting Eq. 2.10 into Eq. 2.8 and assuming $p_\mathrm{c} = p_\mathrm{h} = p_\mathrm{a}$ (p_a is the ambient pressure), we have

$$\begin{aligned} \dot{S}_\mathrm{i} = &\ \dot{m}_\mathrm{in} \left[(1-\varepsilon)(s_\mathrm{h} - s_\mathrm{in}) + \varepsilon(s_\mathrm{c} - s_\mathrm{in})\right] \\ = &\ \dot{m}_\mathrm{in} \left[(1-\varepsilon)(c_p \ln \tfrac{T_\mathrm{h}}{T_\mathrm{in}} - R_\mathrm{m} \ln \tfrac{p_\mathrm{h}}{p_\mathrm{in}}) + \varepsilon(c_p \ln \tfrac{T_\mathrm{c}}{T_\mathrm{in}} - R_\mathrm{m} \ln \tfrac{p_\mathrm{c}}{p_\mathrm{in}})\right] \\ = &\ \dot{m}_\mathrm{in} R_\mathrm{m} (\tfrac{1}{\Gamma} \ln \tfrac{T_\mathrm{h}^{1-\varepsilon} T_\mathrm{c}^{\varepsilon}}{T_\mathrm{in}} - \ln \tfrac{p_\mathrm{h}^{1-\varepsilon} p_\mathrm{c}^{\varepsilon}}{p_\mathrm{in}}) \\ = &\ \dot{m}_\mathrm{in} R_\mathrm{m} (\tfrac{1}{\Gamma} \ln \tfrac{T_\mathrm{h}^{1-\varepsilon} T_\mathrm{c}^{\varepsilon}}{T_\mathrm{in}} - \ln \tfrac{p_\mathrm{a}}{p_\mathrm{in}}) \geq 0 \end{aligned} \tag{2.11}$$

where $\gamma = c_p / c_v$ and

$$\Gamma = \frac{\gamma - 1}{\gamma} = \frac{R_\mathrm{m}}{c_p}.$$

From Eq. 2.11, we have

$$\begin{aligned} &\tfrac{1}{\Gamma} \ln \tfrac{T_\mathrm{h}^{1-\varepsilon} T_\mathrm{c}^{\varepsilon}}{T_\mathrm{in}} - \ln \tfrac{p_\mathrm{a}}{p_\mathrm{in}} \geq 0 \\ &T_\mathrm{h}^{1-\varepsilon} T_\mathrm{c}^{\varepsilon} = T_\mathrm{sm}^{*} \geq T_\mathrm{in} (\tfrac{p_\mathrm{a}}{p_\mathrm{in}})^{\Gamma} \end{aligned} \tag{2.12}$$

here T_sm^{*} is the temperature assumed to be $T_\mathrm{h}^{1-\varepsilon} T_\mathrm{c}^{\varepsilon}$. When it equals to $T_\mathrm{in} (\frac{p_\mathrm{a}}{p_\mathrm{in}})^{\Gamma}$, which is the temperature after the isentropic expansion process from T_in and p_in to the pressure p_a.

If the process in the system is reversible, then Eq. 2.12 becomes

$$T_\mathrm{h}^{1-\varepsilon} T_\mathrm{c}^{\varepsilon} = T_\mathrm{sm}^{*} = T_\mathrm{in} (\frac{p_\mathrm{m}}{p_\mathrm{in}})^{\Gamma}. \tag{2.13}$$

In case of an irreversible process, Eq. 2.11 quantifies the entropy production rate

$$\dot{S}_i = \dot{m}_\mathrm{in} R_\mathrm{m} \left[\frac{1}{\Gamma} \ln \frac{T_\mathrm{h}^{1-\epsilon} T_\mathrm{c}^{\varepsilon}}{T_\mathrm{in}} - \ln \frac{p_\mathrm{a}}{p_\mathrm{in}}\right] = \dot{m}_\mathrm{in} R_\mathrm{m} \left[\frac{1}{\Gamma} \ln \frac{T_\mathrm{sm}^{*}}{T_\mathrm{in}} + \ln \frac{p_\mathrm{in}}{p_\mathrm{a}}\right]. \tag{2.14}$$

We introduce

$$\frac{1}{\Gamma} \ln \frac{T_\mathrm{sm}^{*}}{T_\mathrm{in}} + \ln \frac{p_\mathrm{in}}{p_\mathrm{a}} = \frac{\dot{S}_i}{\dot{m}_\mathrm{in} R_\mathrm{m}} = \Theta_\mathrm{ir} > 0. \tag{2.15}$$

The factor Θ_ir represents the dimensionless entropy generation from the irreversible processes. Finally, Eq. 2.15 can be written as

$$T_\mathrm{sm}^{*} = \mathrm{e}^{\Gamma \Theta_\mathrm{ir}} T_\mathrm{in} (\frac{p_\mathrm{a}}{p_\mathrm{in}})^{\Gamma}. \tag{2.16}$$

Eq. 2.16 can be combined with Eq. 2.6 from the first law via the factor Θ_ir. In this way, T_h and T_c can be written as functions of the other parameters. We assume that $T_\mathrm{in} = 300$

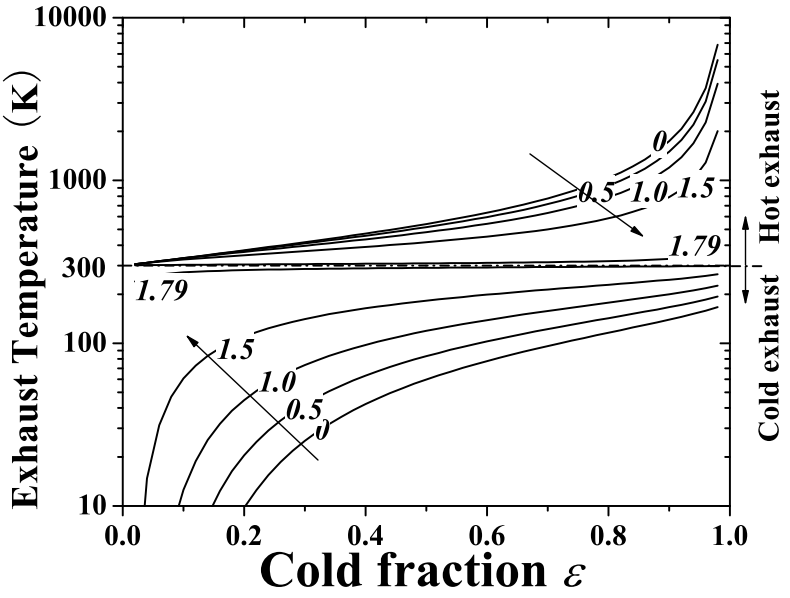

Figure 2.2: *Hot and cold exhaust temperatures as functions of cold fraction ε based on thermodynamic analysis with the irreversible processes factor Θ_{ir} at $p_{in} = 6$ bar, $T_{in} = 300$ K, and $p_a = 1$ bar. The numbers on the curve are the values of the factor Θ_{ir}.*

K, $p_{\rm in} = 6$ bar, $p_{\rm h} = p_{\rm c} = 1$ bar. For different cold fractions ε, we obtain the two exhaust temperatures, as shown in Fig. 2.2.

When $\Theta_{\rm ir} = 0$, the process inside the RHVT system is reversible. When the cold fraction is close to zero, in this extreme case, almost all the inlet gas exhausts from the hot side and the temperature at the cold side is absolute zero. The hot exhaust temperature is very close to the inlet temperature. Practically, it is not possible to generate this extremely low temperature.

When the cold fraction is close to one, almost all the gas will escape from the cold side. According to the adiabatic process assumed, the cold exhaust temperature will depend on the pressure drop over the RHVT system, about 170 K. Again because of the first law, the hot exhaust temperature becomes infinite. In practice, the hot exhaust temperature will never be infinite, since the process inside the RHVT system will never be reversible.

For all cases with nonzero $\Theta_{\rm ir}$, for the cold fraction increasing the hot and cold exhaust temperatures increase. For a given cold fraction, if $\Theta_{\rm ir}$ increases between zero and $\ln(p_{\rm in}/p_{\rm a})$, the hot exhaust temperature decreases, while the cold exhaust temperature increases.

If $\Theta_{\rm ir} < \ln(p_{\rm in}/p_{\rm a})$, i.e. in the example of Fig. 2.2 for $\Theta_{\rm ir} < 1.79$, then $\ln T^*_{\rm sm}/T_{\rm in} < 0$ and $T^*_{\rm sm} < T_{\rm in}$, the process inside the RHVT can be thought as an expansion, reversible or irreversible. Otherwise, $\Theta_{\rm ir} \geq \ln(p_{\rm in}/p_{\rm a})$, i.e. in the example of Fig. 2.2 $\Theta_{\rm ir} \geq 1.792$, then $\ln T^*_{\rm sm}/T_{\rm in} \geq 0$ and $T^*_{\rm sm} \geq T_{\rm in}$, so the process could not be thought as an expansion any more, and the calculated results have no physical meaning.

2.2 Secondary circulation model by Ahlborn

Since the 1930s, the flow pattern inside the RHVT system has been an important research topic [4–20]. All these works noted the existence of a secondary flow inside the RHVT system. In 1990s, Ahlborn [1,2,21] further explained the existence of the secondary circulation, proved it experimentally, and proposed an Original Secondary Circulation Model (abbreviated as OSCM) to explain the energy separation.

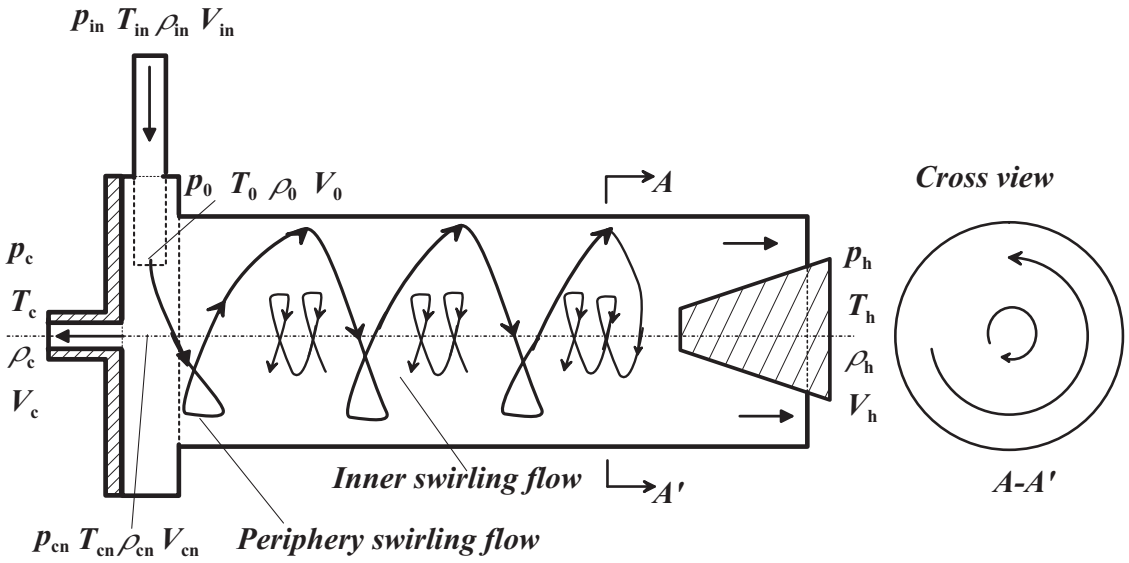

(a) The periphery and inner swirling flows.

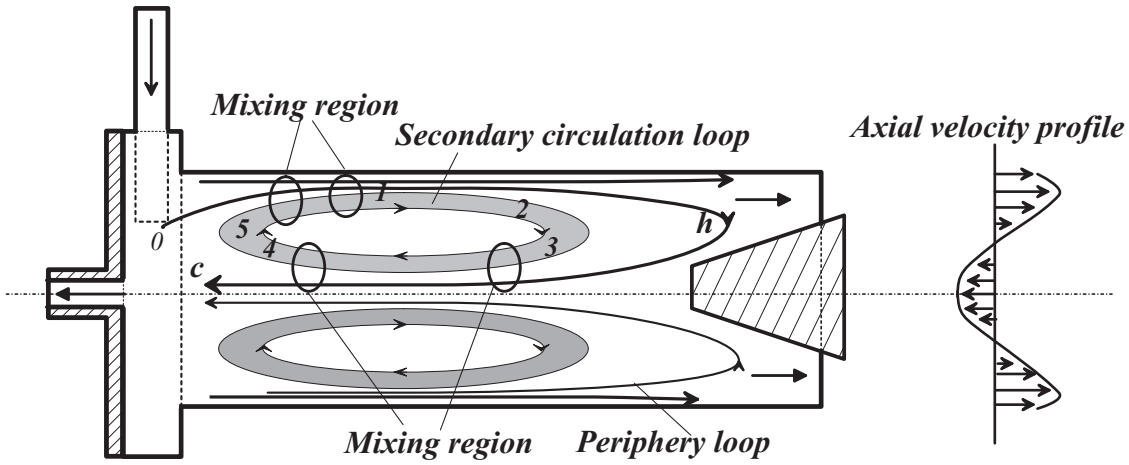

(b) The secondary circulation and periphery loops.

Figure 2.3: *The secondary circulation model. The numbers "0"∼"5" show the imagined positions where the assumed processes start and end.*

2.2.1 OSCM by Ahlborn et al., heat exchange model

Fig. 2.3 shows the general principle of the OSCM proposed by Ahlborn. (a) shows that inside the system there exist two swirling flows. One flow swirls to the hot end in the peripherical region, named the peripherical swirling flow. The other flow anti-swirls to the cold exit in the center region, named the internal swirling flow. Both swirling flows generate a high rotating speed vortex motion inside the vortex tube. They also generate two loops (see (b)). One is the gray region shown in the figure, named the secondary circulation (SC) loop, which acts as the refrigerant or working fluid in a normal refrigeration cycle. The other is named the periphery loop, which is an open loop. The gas that exits this loop is renewed by the injected gas. Some gas elements in this loop first pass the peripherical region from the entrance to the hot end, and escape from the hot end. Other gas elements stay in the loop and return axial direction to the cold end in the center, and exit via the cold exhaust. This loop acts as the high and low temperature environments like in a normal refrigeration cycle. Based on this general idea, it is assumed that work is transferred between the inner regions of low pressure and the peripherical regions of high pressure, and that internal energy is transfered between the inner and peripherical regions via the two loops. All these energy transfer processes together are supposed to lead to the energy separation. The OSCM is built on this consideration.

In order to analyze the processes inside the system, we follow the treatment by Ahlborn. Consider Fig. 2.3, in which numbers "0"∼"5" show positions for the processes inside the SC loop (see Ahlborn [2]). The following parts are distinguished:

a) Heat rejection (0→1, 5→1): Near the inlet nozzles, the temperature T_0 of the entering gas element in the periphery loop (0) is lower than the temperature T_5 of the gas element in the SC-loop (5). The incoming gas element and the gas element in the SC-loop mix together. The temperature after mixing is T_1. Denoting the mass flow by $\dot{m}_0$ for the incoming stream, $\dot{m}_{\rm sc}$ for the SC-loop, Ahlborn et al. assume the following enthalpy balance to hold, neglecting the kinetic energies,

$$\dot{m}_0(T_1 - T_0) = \dot{m}_{\rm sc}(T_{\rm c} - T_1) \quad , \tag{2.17}$$

in which temperature T_5 has been replaced by the cold gas temperature $T_{\rm c}$.

b) Adiabatic deceleration: When following the peripheral circulation towards the hot end, the rotating gas elements at (1) with Mach number $M_{\rm a,0}$ decelerate due to friction. Ahlborn et al. assume an adiabatic deceleration process in which

$$T_{\rm h} = T_1(1 + \frac{\gamma - 1}{2} M_{\rm a,0}^2) = T_1(1 + \Gamma X) \quad , \tag{2.18}$$

(here the notation $X = \gamma/2M_{\rm a,0}^2$ has been adopted, following Ahlborn et al.).

c) Heat absorption (h→4, 3→4): The hot gas in the peripherical loop h partly returns to the cold end near the center of the tube with a mass flow $\dot{m}_{\rm c}$. There, the hot gas mixes with the SC-loop, for which the temperature T_3 is assumed equal to T_1. After mixing, the temperature becomes $T_{\rm c}$. The heat balance is:

$$\dot{m}_{\rm sc}(T_{\rm c} - T_1) = \dot{m}_{\rm c}(T_{\rm h} - T_{\rm c}) \quad . \tag{2.19}$$

It implies that the hot gas is cooled by mixing with the gas in the SC-loop.

Combing Eqs. 2.17 and 2.19 yields, with $\varepsilon = \dot{m}_{\rm c}/\dot{m}_0$:

$$T_1 = T_0 + \varepsilon(T_{\rm h} - T_{\rm c}) \quad . \tag{2.20}$$

2.2.2 The normalized pressure ratio X

Ahlborn et al. assume that the vortical motion of the gas in the vortex chamber can be approximated as a solid body rotation with $V = \Omega_{\rm v} r$, V varying from 0 at the axis to $V_0 = \Omega_v R_{\rm vc}$ at the outer radius $R_{\rm vc}$. The pressure distribution then follows the momentum balance,

$$\frac{\partial p}{\partial r} = \rho \Omega_{\rm v}^2 r \quad . \tag{2.21}$$

Ahlborn et al. neglect the radial variation of the density, resulting into the following difference between the pressure $p_{\rm c}$ at the center and the pressure p_0 at the outer radius

$$p_0 - p_{\rm c} = \frac{1}{2}\rho_0 \Omega_{\rm v}^2 R_{\rm vc}^2 = \frac{1}{2}\rho_0 v_0^2 = \frac{1}{2}\rho_0 c_0^2 M_{\rm a,0}^2 = \frac{\gamma}{2} p_0 M_{\rm a,0}^2. \tag{2.22}$$

Then, defining a normalized pressure ratio X,

$$X \equiv \frac{p_0 - p_{\rm c}}{p_0}, \tag{2.23}$$

the relation between X and $M_{\rm a,o}^2$ follows from Eq. 2.22,

$$X = \frac{\gamma}{2} M_{\rm a,0}^2, \tag{2.24}$$

Usually, p_0 is not known a priori, but will depend on Mach number $M_{\rm a,0}$ and inlet pressure $p_{\rm in}$. For this relation, Ahlborn et al. incorrectly applied a momentum balance in incompressible flow approximation to find,

$$\gamma M_{\rm a,0} \simeq \frac{p_{\rm in} - p_0}{p_0} \tag{2.25}$$

Combination of Eqs. 2.23, 2.24 and 2.25 leads to their expression for the pressure ratio $p_{\rm in}/p_{\rm c}$

$$\tau_{\rm p} = \frac{p_{\rm in}}{p_{\rm c}} = \frac{2X+1}{1-X} \quad . \tag{2.26}$$

It can be found that the maximum value of $\tau_{\rm p}$ is 8 when $M_{\rm a,0} = 1$ and $\gamma = 1.4$.

2.2.3 The OSCM model

Instead of solving Eqs. 2.18 and 2.20, Ahlborn et al. present an approximation based on a simplifying assumptions regarding the values of T_0 and T_1. It is assumed that T_0 and T_1 are close to $T_{\rm c}$. It is difficult to prove the mathematical correctness of their derivation. Here we

note their final expressions [1, 2, 21, 22]

$$\frac{T_\mathrm{h}}{T_\mathrm{c}} = 1 + \frac{(\gamma-1)}{\gamma} X(\varepsilon+1) = 1 + \Gamma X(\varepsilon+1) \tag{2.27a}$$

$$\frac{T_\mathrm{h}}{T_\mathrm{in}} = 1 + \frac{6\Gamma X\varepsilon}{4+3\Gamma X} \tag{2.27b}$$

$$\frac{T_\mathrm{c}}{T_\mathrm{in}} = \frac{1+\frac{6\Gamma X\varepsilon}{4+3\Gamma X}}{1+\Gamma X(\varepsilon+1)} \tag{2.27c}$$

$$\frac{\Delta T_\mathrm{h}}{T_\mathrm{in}} = \frac{T_\mathrm{h}-T_\mathrm{in}}{T_\mathrm{in}} = \frac{6\Gamma X\varepsilon}{4+3\Gamma X} \tag{2.27d}$$

$$\frac{\Delta T_\mathrm{c}}{T_\mathrm{in}} = \frac{T_\mathrm{c}-T_\mathrm{in}}{T_\mathrm{in}} = \frac{\frac{6\Gamma X\varepsilon}{4+3\Gamma X} - \Gamma X(1+\varepsilon)}{1+\Gamma X(1+\varepsilon)} \tag{2.27e}$$

$$X = \frac{\gamma}{2} M_{\mathrm{a},0}^2 \ . \tag{2.27f}$$

2.2.4 Comments on the model of Ahlborn et al.

Ahlborn et al. have formulated a "physical" model of the RHVT (named "Original Secondary Circulation Model") by employing its similarity with a heat pump [1, 2]. According to the OSCM, the following remarks should be made:

1. The compressibility of the working fluid is sometimes disregarded, sometimes taken as an essential component. For example, the entrance flow in the nozzle is described in their publication [22] as incompressible, while important phenomena as "choking" in a throat can only be explained with a correct formulation based on compressibility. Furthermore, it is not possible to find the exit Mach number for a nozzle from an integral momentum balance.

2. The kinetic energy of the peripheral fluid and of the fluid in the SC-loop is sometimes taken into account, sometimes not. The arguments are not given. It is correct that the lowest temperature in the vortex tube can be found near the entrance. But this low temperature is a direct consequence of the high kinetic energy. Still, it is assumed that in the mixing region near the entrance ($0 \rightarrow 1$ for the peripheral flow and $5 \rightarrow 1$ for the flow in the SC-loop) the enthalpy flow remains constant while the kinetic energy is disregarded. But in an overall adiabatic setting this only holds for the stagnation enthalpies, including the kinetic energies of the mixing fluid. If this would be implemented in the theory we would find $T_\mathrm{c} = T_\mathrm{h} = T_\mathrm{in}$, in other words, the model would fail.

3. Ahlborn et al. assumed the velocity distribution inside the vortex chamber to be a Rankine vortex motion, which is experimentally correct and acceptable. But in their description, they only considered the solid body rotation in the center region of the Rankine vortex motion, and not the potential vortex motion in the peripheral region. If the peripheral region is considered as well, then the parameter X should contain information on the geometry.

4. Let us assume that T_0 is adiabatically related to T_in, according to

$$T_\mathrm{in} = T_0\left(1 + \frac{\gamma-1}{2} M_{\mathrm{a},0}^2\right) = T_0(1+\Gamma X) \ . \tag{2.28}$$

If we substitute T_0 from Eq. 2.28 in Eqs. 2.18 and 2.20, and combine this with the general energy balance (see Eq. 2.6), we would find $T_\mathrm{h} = T_\mathrm{c} = T_\mathrm{in}$, which is a disappointing result.

5. It should be concluded that the OSCM from Ahlborn et al. cannot be considered as a satisfactory theoretical model of the flow inside the RHVT, but that its merit is based on its success as an empirical description of the RHVT performance.

2.2.5 Modification of Ahlborn et al.'s model

Based on the above mentioned remarks, the OSCM is modified in the following aspects:

(a) The Mach number $M_{\mathrm{a},0}$ is calculated based on compressible flow through a throat

$$\frac{p_\mathrm{in}}{p_0} = (1 + \Gamma_2 M_{\mathrm{a},0}^2)^{1/\Gamma} \quad . \tag{2.29}$$

(b) Because in the vortex chamber, the geometry is axi-symmetric and the axial velocity v_z and radial velocity v_r are much smaller than v_θ and can be neglected, the momentum equation is simplified to [22]

$$\frac{\partial p}{\partial r} \simeq \frac{\rho v_\theta^2}{r} \quad . \tag{2.30}$$

So, the pressure distribution inside the vortex chamber merely depends on the tangential velocity v_θ profile. The Rankine velocity profile (see Fig. 2.4) reads [23]

$$v_\theta = \begin{cases} \Omega_\mathrm{v} r & 0 \le r \le R_\mathrm{cr} \\ \frac{\Gamma_\mathrm{c}}{r} & R_\mathrm{cr} \le r \le R_\mathrm{vc}. \end{cases} \tag{2.31}$$

Here Γ_c is the vortex circulation, Ω_v is the vortex vorticity. In the vortex chamber, there are a few radii: one is the chamber radius R_vc; the critical radius R_cr; the vortex tube radius R_vt; the last one is the radius R_cn near the center which can be thought as the same of the cold exhaust orifice radius. Experimentally, R_cr equals R_vt (see Chapter 6). When $r = R_\mathrm{vc}$, the velocity should be the nozzle exit velocity V_0. The continuity of velocity at $r = R_\mathrm{cr} = R_\mathrm{vt}$ requires $\Gamma_\mathrm{c}/R_\mathrm{cr} = \Omega_\mathrm{v} R_\mathrm{cr}$. For the vortex circulation and the vorticity in Eq. 2.31 we find

$$\begin{aligned} \Gamma_\mathrm{c} &= V_0 R_\mathrm{vc}, \text{ and} \\ \Omega_\mathrm{v} &= \tfrac{V_0 R_\mathrm{vc}}{R_\mathrm{cr}^2}. \end{aligned}$$

The velocity distribution of Eq. 2.31 can be substituted in the momentum equation 2.30 and integrated. Ahlborn et al. assumed a constant density in the vortex chamber. With the same approximation, the following pressure distribution is obtained

$$p(r) = \begin{cases} c_1 + \frac{1}{2}\rho\Omega_\mathrm{v}^2 r^2 & (0 \le r \le R_\mathrm{cr}) \\ c_2 - \frac{\rho\Gamma_\mathrm{c}^2}{2r^2} & (R_\mathrm{cr} \le r \le R_\mathrm{vc}) \end{cases} \tag{2.32}$$

where c_1 and c_2 are to be determined from the boundary conditions

$$p = p_0 \text{ at } r = R_\mathrm{vc}$$

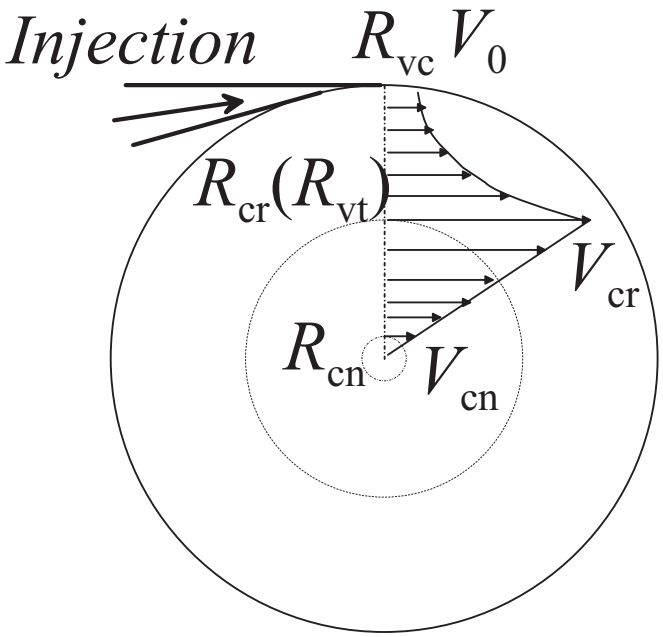

Figure 2.4: *Rankine velocity distribution in the vortex chamber:* R_{vc} *is the radius of the vortex chamber; normally the maximum velocity inside the vortex chamber occurs when the radius reaches the vortex tube radius, so* R_{cr} *is equal to the vortex tube radius* R_{vt} *(see Chapter 6).* R_{cn} *is close to the center of the vortex chamber.*

and continuity of pressure at $r = R_{cr}$.

Finally we obtain

$$p_0 - p_c = p_0 \frac{\gamma}{2} M_{a,0}^2 \frac{2R_{vc}^2 - R_{cr}^2}{R_{cr}^2} \quad . \tag{2.33}$$

So the normalized pressure ratio X reads

$$\begin{aligned} X &= \tfrac{\gamma}{2} M_{a,0}^2 \tfrac{2R_{vc}^2 - R_{cr}^2}{R_{cr}^2} \quad , \\ M_{a,0}^2 &= \tfrac{2}{\gamma} X' \quad , \end{aligned} \tag{2.34}$$

so X' varies from 0 to 0.7 for nitrogen. At the same time, we introduce a parameter

$$\tau_R = \frac{R_{cr}}{R_{vc}} = \frac{R_{vt}}{R_{vc}}. \tag{2.35}$$

τ_R is dependent on the geometry of the vortex chamber and varies from 0 to 1. X' and X have the following relationship

$$X' = \frac{\tau_R^2}{2 - \tau_R^2} X, \tag{2.36}$$

so X is the normalized pressure ratio, is dependent on these pressures, in other words, it is dependent on X' and τ_R.

(c) The pressure ratio $\tau_{\rm p}$ over the vortex tube is computed with Eqs. 2.29 and 2.33 (or 2.34). It reads

$$\begin{aligned}\tau_p &= \frac{p_{\rm in}}{p_{\rm c}} = \frac{(1+\Gamma_2 M_{\rm a,0}^2)^{1/\Gamma}}{1-\frac{\gamma}{2}M_{\rm a,0}^2\frac{2R_{\rm vc}^2-R_{\rm cr}^2}{R_{\rm cr}^2}} \\ &= \frac{(1+\Gamma_2 M_{\rm a,0}^2)^{1/\Gamma}}{1-\frac{\gamma}{2}M_{\rm a,0}^2(\frac{2}{\tau_{\rm R}^2}-1)} \\ &= \frac{(1+0.2M_{\rm a,0}^2)^{7/2}}{1-0.7M_{\rm a,0}^2(\frac{2}{\tau_{\rm R}^2}-1)} \quad ,\end{aligned} \tag{2.37}$$

when $M_{\rm a,0}=0$, $\tau_{\rm p}=1$. It can be found that when $\tau_{\rm R}=1$ (the case used by Ahlborn et al.) in order to achieve "choking" condition at the exhaust of the nozzle, the pressure ratio $\tau_{\rm p}$ should be around 6.3 which is much less than what is found from Ahlborn et al.'s model. The reason for this difference is that Ahlborn et al. applied an incorrect incompressible momentum balance to the nozzle flow.

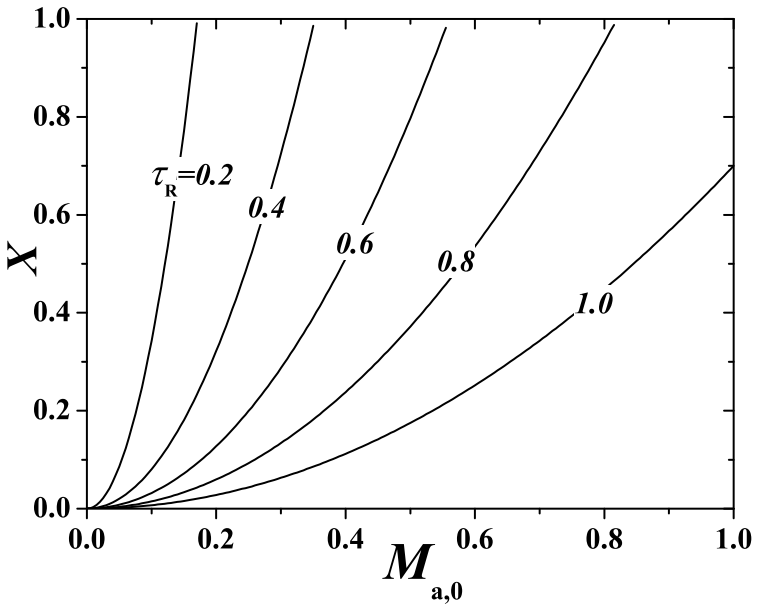

Figure 2.5: *Normalized pressure ratio* $X\ (=(p_0-p_{\rm c})/p_0)$ *vs.* $M_{a,0}$ *for different* $\tau_{\rm R}\ (=R_{\rm vt}/R_{\rm vc})$.

Fig. 2.5 shows the relation between the normalized pressure ratio X and the Mach number $M_{\rm a,0}$ for different ratios $\tau_{\rm R}$. When $\tau_{\rm R}=1$, the maximum normalized pressure ratio X is 0.7 which is the same as obtained by Ahlborn. It should be noted that the model only gives reasonable results when the density difference in the vortex chamber is sufficiently small, i. e. $X<0.5$.

(d) We shall adopt a similar enthalpy balance as derived by Ahlborn et al., i.e. (Eqs. 2.17, 2.19 and 2.20)

$$\dot{m}_0(T_{\rm c}-T_1)=\dot{m}_{\rm c}(T_{\rm h}-T_{\rm c}),$$

or

$$T_1 = T_0+\varepsilon(T_{\rm h}-T_{\rm c}) \ . \tag{2.38}$$

We will not make use of of Eq. 2.18. The temperature T_0 is adiabatically connected to the inlet temperature T_{in}, assuming the stagnation enthalpy to be a conserved quantity

$$T_{\mathrm{in}} = T_0(1 + \Gamma_2 M_{\mathrm{a},0}^2) = T_0(1 + \Gamma X') \ . \tag{2.39}$$

Combination of Eq. 2.38 and 2.39 yields,

$$\frac{T_{\mathrm{h}}}{T_{\mathrm{c}}} = 1 + \frac{1}{\varepsilon}\frac{T_1}{T_{\mathrm{c}}} - \frac{1}{\varepsilon(1 + \Gamma X')}\frac{T_{\mathrm{in}}}{T_{\mathrm{c}}}. \tag{2.40}$$

Further, we shall adopt the assumption of Ahlborn et al. that T_1 is approximately equal to T_{c}. We then find,

$$\frac{T_{\mathrm{h}}}{T_{\mathrm{c}}} \simeq 1 + \frac{1}{\varepsilon} - \frac{1}{\varepsilon(1 + \Gamma X')}\frac{T_{\mathrm{in}}}{T_{\mathrm{c}}}. \tag{2.41}$$

Solving Eq. 2.6 from energy conservation and Eq. 2.41, the relationships for the modified Ahlborn et al.'s model are obtained

$$\frac{T_{\mathrm{h}}}{T_{\mathrm{c}}} = 1 + \frac{\Gamma X^{'}}{1 + \varepsilon\Gamma X'} \tag{2.42a}$$

$$\frac{T_{\mathrm{c}}}{T_{\mathrm{in}}} = \frac{1 + \varepsilon\Gamma X^{'}}{1 + \Gamma X'} \tag{2.42b}$$

$$\frac{T_{\mathrm{h}}}{T_{\mathrm{in}}} = 1 + \frac{\varepsilon\Gamma X^{'}}{1 + \Gamma X'} \tag{2.42c}$$

$$\frac{\Delta T_{\mathrm{h}}}{T_{\mathrm{in}}} = \frac{\varepsilon\Gamma X^{'}}{1 + \Gamma X'} \tag{2.42d}$$

$$\frac{\Delta T_{\mathrm{c}}}{T_{\mathrm{in}}} = \frac{(\varepsilon - 1)\Gamma X^{'}}{1 + \Gamma X'} \tag{2.42e}$$

$$X = \frac{\gamma}{2} M_{\mathrm{a},0}^2 (\frac{2}{\tau_{\mathrm{R}}^2} - 1), \text{ and } X^{'} = \frac{\tau_{\mathrm{R}}^2}{2 - \tau_{\mathrm{R}}^2} X \ . \tag{2.42f}$$

It should be noted that also the modified Ahlborn et al.'s model (MAM) has to be considered as an empirical model, based on rather crude approximations and on questionable assumptions.

2.2.6 Comparison of the computations with OSCM and MAM

Fig. 2.6 shows the results calculated with Eq. 2.27 from the analysis of Ahlborn et al.. Fig. 2.7 shows the results calculated with Eq. 2.42 from this work. As shown in these figures, when the cold fraction ε and X or $X^{'}$ increases, the temperature ratio $T_{\mathrm{h}}/T_{\mathrm{in}}$ increases as well. For both cases, $T_{\mathrm{h}}/T_{\mathrm{in}}$ can be about 1.25 in the OSCM, and only about 1.15 with MAM. When $X < 0.1$, the temperature ratio $T_{\mathrm{c}}/T_{\mathrm{in}}$ varies very rapidly from 0.98 to 0.8 with OSCM. When $X > 0.1$, if X increases and ε decreases, $T_{\mathrm{c}}/T_{\mathrm{in}}$ decreases from 0.98 to 0.84. Its minimum value for OSCM is about 0.8. With MAM, derived in this work, if X increases and ε decreases, $T_{\mathrm{c}}/T_{\mathrm{in}}$ decreases from about 1.0 at $X^{'}$ about 0 and ε about 1 to 0.84 at $X^{'}$ about 0.7 and ε about 0. So it shows that the ranges of the temperature ratios predicted with OSCM are always wider than those with MAM. It also shows that when $X = 0$, which means that $p_0 = p_{\mathrm{c}}$, there is no flow inside the system, the temperature ratios $T_{\mathrm{c}}/T_{\mathrm{in}}$ and $T_{\mathrm{h}}/T_{\mathrm{in}}$ must be unity. In the OSCM, the temperature ratio $T_{\mathrm{c}}/T_{\mathrm{in}}$ can be 0.72 (when $X < 0.05$), which is unrealistic and indicates the inconsistency of the OSCM.

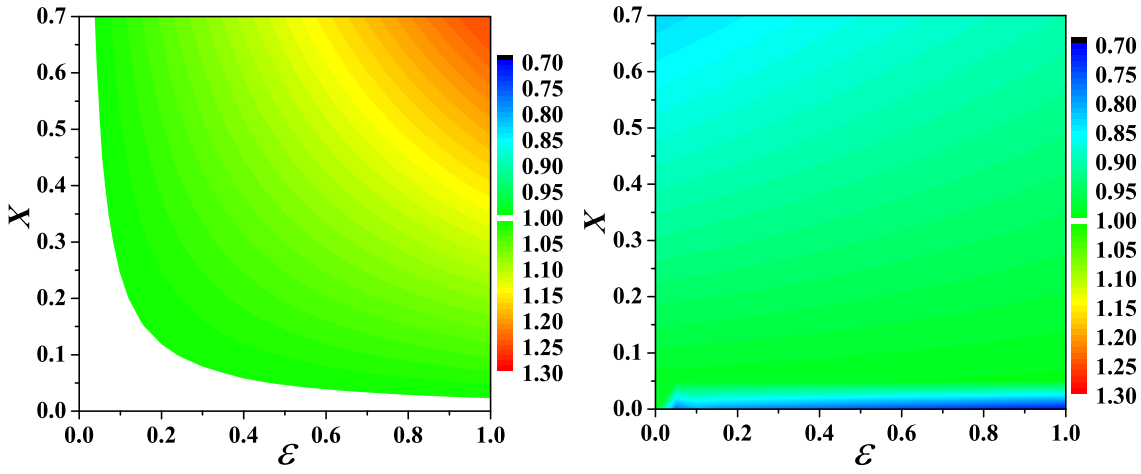

(a) Contour plot for T_h/T_{in} *(b) Contour plot for T_c/T_{in}*

Figure 2.6: *Contour plots of the temperature ratios (T_h/T_{in}, T_c/T_{in}) based on Eqs. 2.27b and 2.27c.*

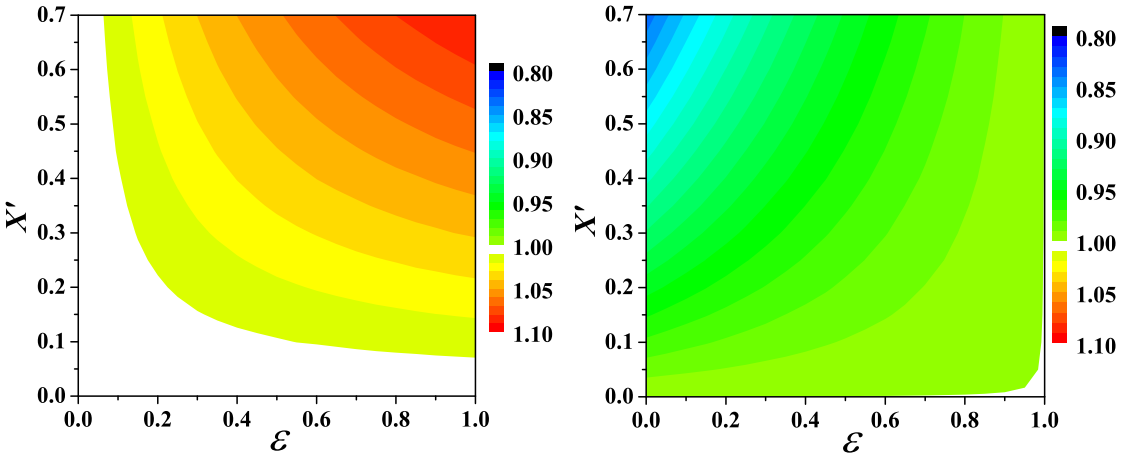

(a) Contour plot for T_h/T_{in} *(b) Contour plot for T_c/T_{in}*

Figure 2.7: *Temperature ratios based on Eq. 2.42.*

2.3 Efficiencies of the RHVT system

The definition of the efficiency of the RHVT cooler has always puzzled researchers in this field [5]. Only Fulton [5] proposed his definition of the efficiency of the RHVT as a cooler. This is not sufficient. In this section the definitions of the efficiencies of the RHVT system are defined and listed.

2.3.1 Thermal efficiencies for the RHVT system

The RHVT can be used not only as a cooler, but also as a heater. So the definition of the efficiency should consider both effects. For different applications, different efficiencies are used.

The coefficient of performance (COP) of a *cooler* is normally defined as the cooling power

$\dot{Q}_c$ gained by the system divided by the work power P input [3]. So the COP of the cooler, denoted by COP_{cr} is expressed as

$$COP_{cr} = \frac{\dot{Q}_c}{P}. \tag{2.43}$$

Here the cooling power can be calculated according to the cooling capacity of the cold exhaust gas (e.g. the heat necessary to heat up the cold exhaust gas from the cold exhaust temperature to the applied temperature. Here T_{in} is chosen.)

$$\dot{Q}_c = \dot{m}_c c_p (T_{in} - T_c).$$

In a conventional refrigeration system, there is a compressor, so the work power is the input power of the compressor. But in the RHVT system, usually a compressed gas source is used, so it is not easy to define the work power. By analogy the work used to compress the gas from the exhaust pressure up to the input pressure with a reversible isothermal compression process,

$$P = \dot{m}_{in} R_m T_{in} \ln (p_{in}/p_c),$$

as used in [5], can be expressed as

$$COP_{cr} = \frac{1}{\Gamma} \frac{\varepsilon (T_{in} - T_c)}{T_{in} \ln \frac{p_{in}}{p_c}}. \tag{2.44}$$

For the *heat pump*, the coefficient of performance is presented as the heating power divided by the work power used. For the RHVT system, the heating power can be expressed as the heating capacity of the hot exhaust gas

$$\dot{Q}_h = \dot{m}_h c_p (T_h - T_{in}).$$

The work power used by the system is taken the same as used above for the cooler. So the coefficient of performance of the RHVT as a heat pump, denoted as COP_{hp} is

$$\begin{aligned} COP_{hp} &= \frac{\dot{Q}_h}{P} \\ &= \frac{1}{\Gamma} \frac{(1-\varepsilon)(T_h - T_{in})}{T_{in} \ln(\frac{p_{in}}{p_c})} \\ &= COP_{cr}. \end{aligned} \tag{2.45}$$

2.3.2 Efficiency for a perfect isentropic expansion

In section 2.1, we analyzed the RHVT process as an isentropic expansion. In this case

$$\eta_{is} = \frac{T_{in} - T_c}{T_{in} - T_s}. \tag{2.46}$$

For an isentropic expansion, the exhaust temperature is

$$T_s = T_{in} (\frac{p_c}{p_{in}})^{\Gamma} = T_{in} (\frac{1}{\tau_p})^{\Gamma} \tag{2.47}$$

2.3.3 Carnot Efficiency

2.3.3.1 Definition of efficiencies

The Carnot COP is the maximum efficiency for all heat engines [3]. So, it is also the maximum for the RHVT system. The COPs for Carnot cycles are [3]

$$COP_{\mathrm{cn,cr}} = \frac{T_{\mathrm{c}}}{T_{\mathrm{in}} - T_{\mathrm{c}}} \tag{2.48a}$$

$$COP_{\mathrm{cn,hp}} = \frac{T_{\mathrm{h}}}{T_{\mathrm{h}} - T_{\mathrm{in}}} \tag{2.48b}$$

here Eq. 2.48a is $COP_{\mathrm{cn,cr}}$ for Carnot refrigeration cycle and Eq. 2.48b is the coefficient for Carnot heat pump cycle.

2.3.3.2 The Criterion on Carnot cycle basis

In order to judge the quality of the RHVT system as a thermal engine, Carnot cycle efficiency can be used as a reference. The ratios of the efficiencies as defined in section 2.3.1 and Carnot COPs are defined as

$$\eta_{\mathrm{cn,cr}} = \frac{COP_{\mathrm{cr}}}{COP_{\mathrm{cn,cr}}}, \tag{2.49}$$

and,

$$\eta_{\mathrm{cn,hp}} = \frac{COP_{\mathrm{hp}}}{COP_{\mathrm{cn,hp}}}. \tag{2.50}$$

The two expressions are

$$\begin{cases} \eta_{\mathrm{cn,cr}} & = \frac{\varepsilon(T_{\mathrm{in}}-T_{\mathrm{c}})^2}{\Gamma T_{\mathrm{in}} T_{\mathrm{c}} \ln(\frac{p_{\mathrm{in}}}{p_{\mathrm{c}}})} \\ \eta_{\mathrm{cn,hp}} & = \frac{(1-\varepsilon)(T_{\mathrm{h}}-T_{\mathrm{in}})^2}{\Gamma T_{\mathrm{in}} T_{\mathrm{h}} \ln(\frac{p_{\mathrm{in}}}{p_{\mathrm{c}}})} \end{cases}$$

2.4 Summary

In this chapter, a thermodynamic analysis, the Ahlborn et al. secondary circulation model and its modification, and the efficiencies of the RHVT have been discussed. The thermodynamic analysis suggests that the RHVT process is considered as an isentropic compression and expansion. With the introduced irreversibility factor Θ_{ir}, it was found that the Ranque-Hilsch effect exists only when the irreversibility factor is lower than the critical value. The critical value of Θ_{ir} only depends on the pressure ratio p_{in}/p_0. In order to improve the performance, it is better to decrease the irreversibility factor Θ_{ir} or increase the pressure ratio.

The OSCM, proposed by Ahlborn and co-workers, has been described and analyzed. We found that it should be considered as an empirical description of the Ranque-Hilsch vortex tube performance. We have formulated a modified Ahlborn et al.'s model (MAM) that should be interpreted as an empirical model as well. In MAM, it is found that the normalized pressure ratio X depends also on the geometric parameter of the RHVT chamber—the critical radius ratio τ_R. The Mach number $M_{\mathrm{a},0}$ and the critical radius ratio τ_R are related to each other. By increasing the critical radius ratio τ_R and increasing the pressure ratio τ_p, it is possible to reach a larger $M_{\mathrm{a},0}$. Finally the relations between the three temperatures (T_{in}, T_{h}, T_{c}),

the cold fraction ε, the normalized pressure ratio X, and the critical radius ratio τ_R have been deduced. A comparison of the two models OSCM and MAM shows that the range of the temperature ratios predicted by the MAM in this work is smaller than that from the OSCM under the same operating conditions. The thermal efficiencies, efficiency as a isentropic expansion process and Carnot Engine efficiencies are listed.

References

[1] B. Ahlborn, J.U. Keller, and E. Rebhan. The heat pump in a vortex tube. *J. Non-Equilibrium Thermodynamics*, 23(2):159–165, 1998.

[2] B. Ahlborn and J.M. Gordon. The vortex tube as a classic thermodynamic refrigeration cycle. *J. Appl. Phys.*, 88(6):3645–3653, 2000.

[3] A.T.A.M. de Waele, P.P. Steijaert, and J. Gijzen. Thermodynamical aspects of pulse tubes. *Cryogenics*, 37:313–324, 1997.

[4] M.G. Ranque. Experiences sur la detente avec production simultanees dun echappement dair chaud et dun echappement dair froid. *J. de Physique et de Radium*, 7(4):112–115, 1933.

[5] C.D. Fulton. Ranque's tube. *J. ASRE Refrigerating Engng*, 58:473–479, 1950.

[6] C.D. Fulton. Comments on the vortex tube. *J. ASRE Refrigerating Engng*, 58:984, 1950.

[7] R. MacGee Jr. Fluid action in the vortex tube. *J. ASRE Refrigerating Engng*, 58:974–975, 1950.

[8] G.W. Scheper. The vortex tube–internal flow data and a heat transfer theory. *J. ASRE Refrigerating Engng*, 59:985–989, 1951.

[9] W. A. Scheller and G. Martin Brown. The Ranque-Hilsch vortex tube. *Fluid Mechanics in Chemical Engineering*, 49(6):1013–1016, 1957.

[10] J.E. Lay. An experimental and analytical study of vortex-flow temperature separation by superposition of spiral and axial flow, part I. *Trans. ASME J. Heat Transfer*, 81:202–212, Aug. 1959.

[11] J.E. Lay. An experimental and analytical study of vortex-flow temperature separation by superposition of spiral and axial flow, part II. *Trans. ASME J. Heat Transfer*, 81:213–222, Aug. 1959.

[12] W.S. Lewellen. A solution for three-dimentional vortex flows with strong circulation. *J. Fluid Mech.*, 14:420–432, 1962.

[13] C.U. Linderstrom-Lang. *Gas separation in the Ranque-Hilsch vortex tube model calculations based on flow data.* Riso report, Denmark, June 1966.

[14] C.U. Linderstrom-Lang. Gas separation in the Ranque-Hilsch vortex tube. *Int. J. Heat Mass Transfer*, 7:1195–1206, 1964.

[15] C.U. Linderstrom-Lang. On gas separation in Ranque-Hilsch vortex tubes. *Z. Naturforschg.*, 22(a):835–837, April 1967.

[16] C.U. Linderstrom-Lang. *Studies on transport of mass and energy in the vortex tube—The significance of the secondary flow and its interaction with the tangential velocity distribution.* Riso report, Denmark, September 1971.

[17] T. Cockerill. Ranque-Hilsch vortex tube. Master thesis, University of Cambridge, 1995.

[18] W. Frohlingsdorf. *Unterschungen zur kompressiblen Strömung und Energietrennung im Wirbelrohr nach Ranque und Hilsch.* PhD dissertation, Ruhr-Universitat-Bochum, 1997. In German.

[19] W. Frohlingsdorf and H. Unger. Numerical investigations of the compressible flow and the energy separation in the Ranque-Hilsch vortex tube. *Int.J. Heat Mass Transfer*, 42:415–422, 1999.

[20] J.M. Gordon and C.N. Kim. *Cool Thermodynamics—The engineering and physics of predictive, diagnostic and optimization methods for cooling system.* Cambridge International Science Publishing, 2000.

[21] B. Ahlborn and S. Groves. Secondary flow in a vortex tube. *Fluid Dynamics Research*, 21:73–86, 1997.

[22] B. Ahlborn, J.U. Keller, R. Staudt, G. Treitz, and E. Rebhan. Limits of temperature separation in a vortex tube. *J. Phys. D: Appl. Phys.*, 27:480–448, 1994.

[23] A. Ogawa. *Vortex flow.* CRC Press, 1992.

Chapter 3

Calibration of the measuring probes

3.1 Introduction

In this chapter, we discuss the calibration of the Cylinder type Pitot Tube (CPT) [1–4] and the single probe hot-wire anemometry (SPHWA) [5–8]. At the end, we also analyze the performance of the thermocouple (THC) probes numerically. With the calibrations and the numerical model, the accuracies of these measurement techniques have been analyzed. The typical error of the Mach number, measured with the CPT, is less than 15%; the typical error of the SPHWA is less than 5%, and the error of the thermocouple is less than 1%.

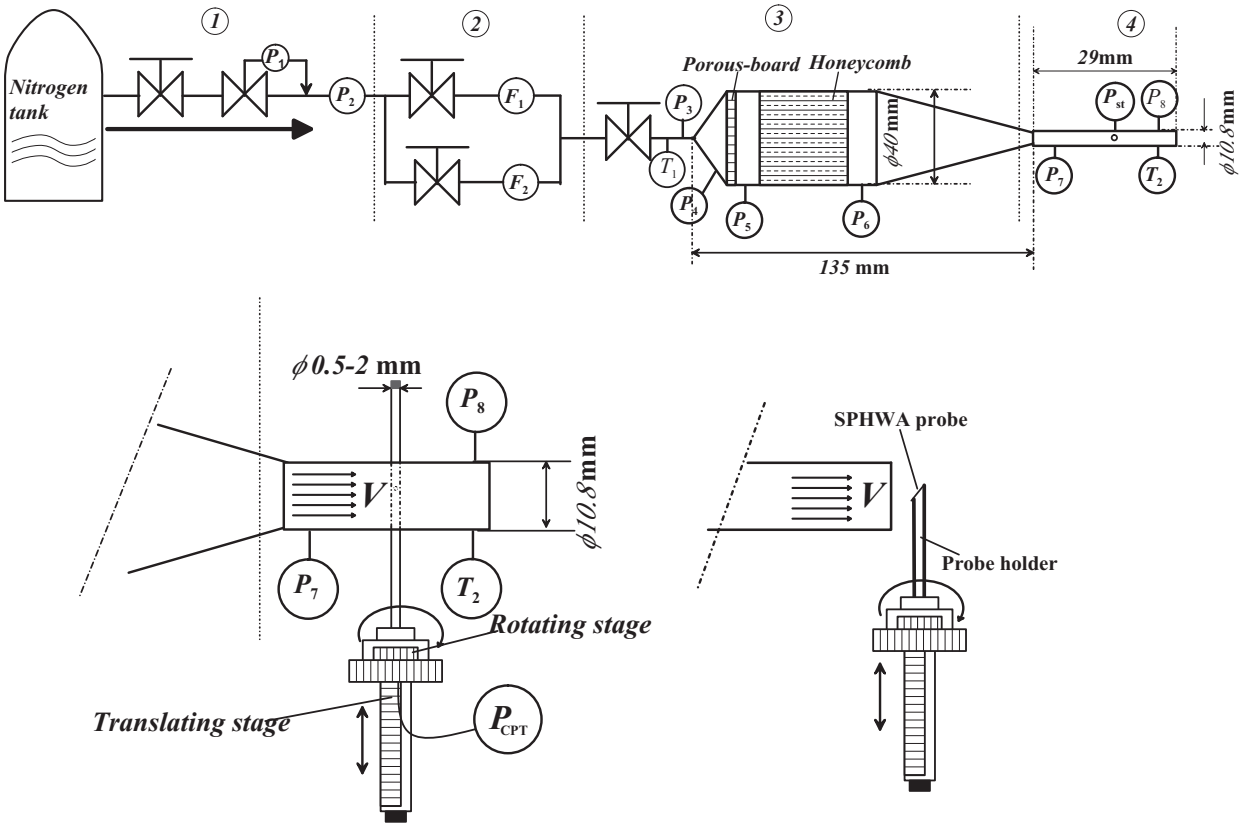

Figure 3.1: *Schematic drawing of the calibration set-up.*

3.2 Calibration set-up

3.2.1 Introduction of the set-up and test samples

A calibration set-up was designed and installed, as shown in Fig. 3.1, in order to realize similar flow conditions as in the vortex tube, and to reach high Mach numbers during the calibration. It consists of the following four parts: 1) the regulator section which is used to keep the input gas pressure constant; 2) two shunted flow meters (flow meter 1 is within 7.0 g/s (20 Nm^3/h) and flow meter 2 is within 70 g/s (200 Nm^3/h) and valves; 3) the wind tunnel used to decrease the disturbances inside the flow and stratify the flow; 4) the measurement section. The nitrogen gas, coming from the liquid nitrogen supply tank (not shown in Fig. 3.1), first flows through the regulator valve, passes the flow metering section, enters the windtunnel, and finally arrives at the measurement section. There are translation and rotation stages mounted on the calibration set-up. With the rotation stage as shown Fig. 3.1, the 360^0 CPT angle-dependent pressure and SPHWA angle-dependent signal profiles at one measurement point can be found.

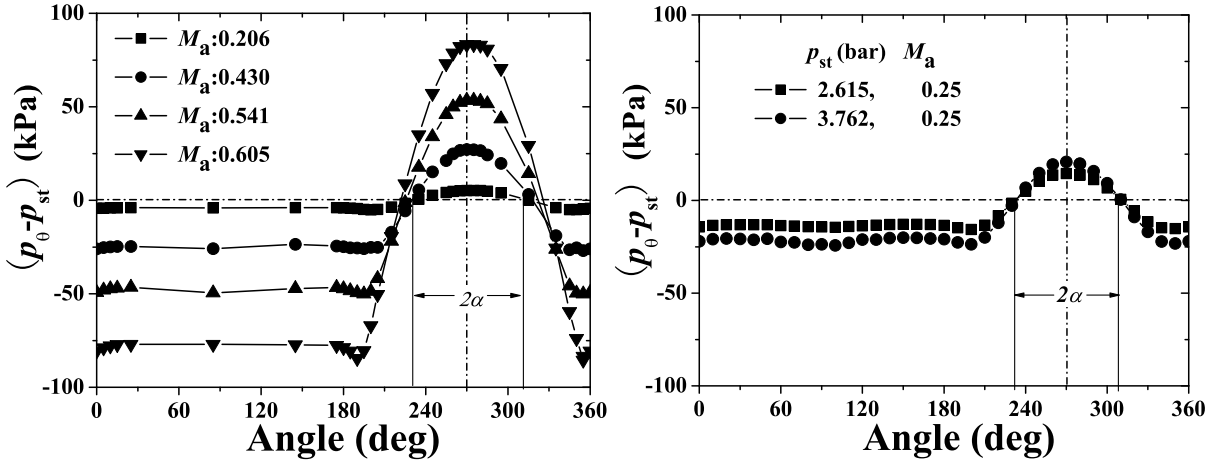

(a)At normal static pressure (about 1 bar) *(b)Higher static pressure (larger than 1 bar)*

Figure 3.2: *Example of the angle-dependent surface pressure distributions (a) at different Mach numbers and (b)at different static pressures and also different Mach number measured in the calibration set-up by the CPT. At the angle of* 270^0*, the gas flow faces to the CPT measurement hole and the measured pressure reaches the maximum.*

Fig. 3.2 (a) and (b) show the typical angle-dependent pressure profile measured by the CPT technique for different Mach numbers and different static pressures. When the flow faces the measurement hole on the CPT, the measured pressure is maximum, so this angle can be used to determine the flow direction in the flow field. Fig. 3.3 shows the typical voltage profile measured by the SPHWA technique at the different inclinations. If the signal is maximum, the velocity is perpendicular to the wire, and at the minimum, the velocity is parallel to the probe, see Section 3.4.3. So the maximum and minimum values have about 90 degrees phase shift. The angle at which the maximum value occurs can be used to determine the flow direction. With the translation stage the velocity profile across the calibration tube can be determined.

3.2.2 Flow properties along the measurement section

In order to determine the gas speed from the mass flowmeter, the velocity profile is measured by a 1 mm medical needle Standard Stagnation Pitot Tube (SSPT). The procedure is as follows:

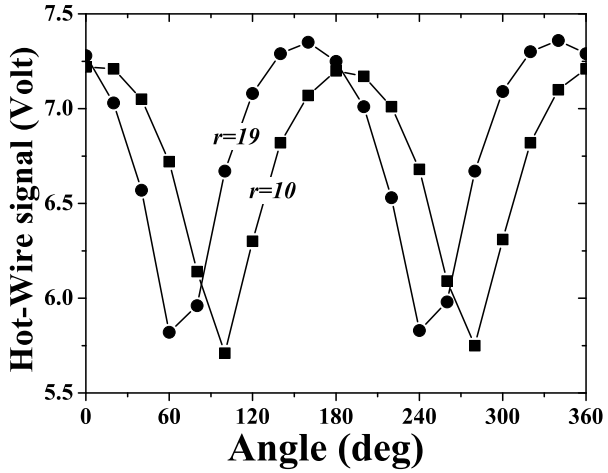

Figure 3.3: *Sample of how the SPHWA signal varies with angle measured in RHVT system. The numbers refer to the position along the radius from the center in mm.*

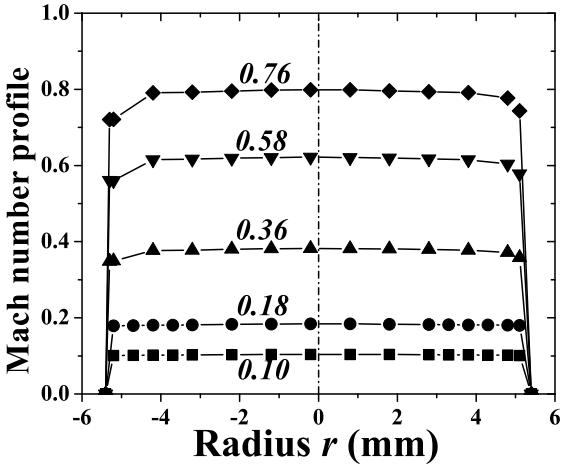

Figure 3.4: *Mach number profile determined by the SSPT. The numbers are the average Mach number based on mass flowmeter reading.*

Fig. 3.4 shows the velocity profiles along the measurement section for different Mach numbers as based on the SSPT. The velocity profile in the center region as measured with the SSPT technique is flat and symmetrical, so, during the calibration, the center of the measurement section was taken as the calibration point.

The cumulative mass flow over the cross section of the windtunnel based on the velocity profile measured with the SSPT technique as given by

$$\dot{m}_{\rm pt} = \int_0^R \rho 2\pi r v(r) {\rm d}r$$

can be divided by the mass flow $\dot{m}_{\rm fm}$ from the flowmeter.

$$\tau_{\dot{\rm m}} = \frac{\dot{m}_{\rm pt}}{\dot{m}_{\rm fm}} \simeq 1. \tag{3.1}$$

In ideal circumstances, this ratio $\tau_{\dot{m}}$ should be equal to 1. The ratio is plotted in Fig. 3.5 (a). The volume speed calculated based on the velocity profile agrees with that from the flowmeter very well, and the typical error is 3% within the accuracy of the flowmeter.

The center of the measurement cross section was chosen as the reference point, so the ratio $\tau_{\rm v}$ of the velocity at the center $V_{\rm c}$ as measured by the SSPT technique to the cross section average velocity $\overline{V}_{\rm fm}$ determined from the flow meters is very important

$$\tau_{\rm v} = \frac{V_{\rm c}}{\overline{V}_{\rm fm}}. \tag{3.2}$$

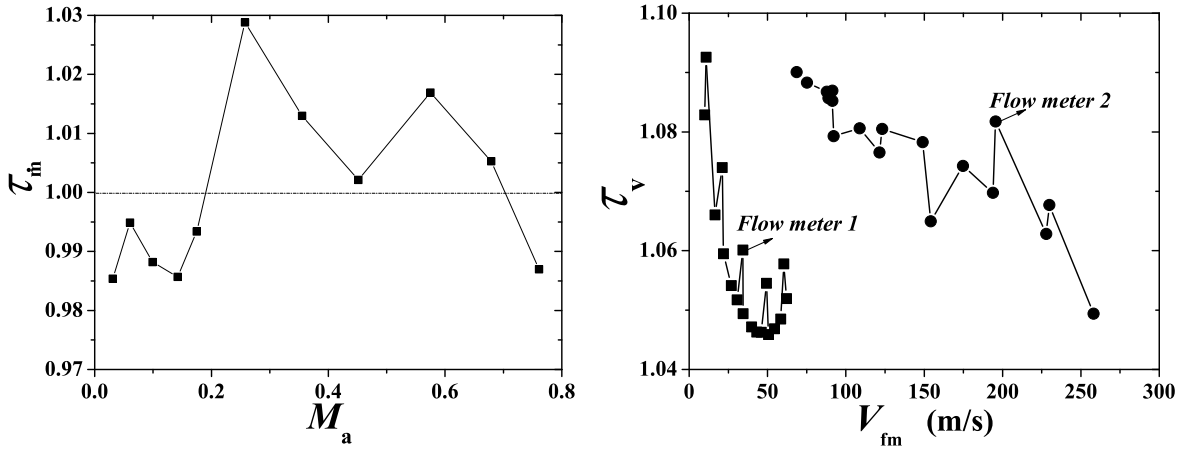

(a) $\tau_{\dot{m}}$. *(b)* τ_{v}.

Figure 3.5: *Flow properties of the measurement section*

Fig. 3.5 (b) shows τ_{v} as function of the velocity. The velocity at the center of the cross section is always larger than the average velocity as based on the FM, so $\tau_{\mathrm{v}} > 1$. If the input flow is lower than 7.0 g/s related to V_{fm}, flowmeter 1 is used. Otherwise, flowmeter 2 is used. The ratio τ_{v} of the velocity is calculated based on the readings of the two flow meters. When the input flow is around 7.0 g/s, with the flowmeter 1, the ratio of the velocity is about 1.06; while for the flowmeter 2, it is about 1.09. The difference is about 3% which is within the range of the accepted calibration error.

3.3 The cylinder type Pitot tube technique (CPT)

3.3.1 The principle of the Pitot tube technique

Bernoulli's theorem [1, 2] states that along a stream-line, the relation between velocity and pressure is given by

$$\frac{1}{2}V^2 + \int \frac{\mathrm{d}p}{\rho} + g\Delta h = Const. = C \ . \tag{3.3}$$

The $g\Delta h$ term is negligibly small, and when the velocity is zero, then C is the stagnation pressure p_{sg}. Considering the compressibility and the changes of the density and temperature, the sound speed and the Mach number, etc. [1, 2], Eq. 3.3 can be written as

$$p_{\mathrm{sg}} = p_{\mathrm{st}} \left[1 + \Gamma_2 M_a^2\right]^{\frac{1}{\Gamma}} \tag{3.4}$$

where Γ and Γ_2 are defined in Chapter 2.

With the series expansion, Eq. 3.4 yields for $\Gamma_2 < 1$ (for nitrogen $\Gamma_2 = 0.2$)

$$\begin{aligned} p_{\mathrm{sg}} &= p_{\mathrm{st}} \left[1 + \tfrac{\gamma}{2} M_{\mathrm{a}}^2 + \tfrac{\gamma}{8} M_{\mathrm{a}}^4 + \tfrac{\gamma(2-\gamma)}{48} M_{\mathrm{a}}^6 + ...\right] \\ &= p_{\mathrm{st}} + \tfrac{\gamma}{2} M_{\mathrm{a}}^2 p_{\mathrm{st}} \left[1 + \tfrac{1}{4} M_{\mathrm{a}}^2 + \tfrac{2-\gamma}{24} M_{\mathrm{a}}^4 + ...\right] \end{aligned} \tag{3.5}$$

i.e.

$$p_{\mathrm{sg}} = p_{\mathrm{st}} + \frac{1}{2}\rho V^2 [1 + \frac{1}{4} M_{\mathrm{a}}^2 + \frac{2-\gamma}{24} M_{\mathrm{a}}^4 + ...] \ .$$

Eq. 3.4 is the principal equation for the PT technique, which shows that the PT technique determines the square of the velocity. When $M_a \leq 0.2$, Eq. 3.4 can be simplified to

$$p_{sg} \simeq p_{st} + \frac{1}{2}\rho V^2 \tag{3.6}$$

with an error less than 0.5% for the measured V. Considering that the typical Mach number in the vortex tube for most cases (see [9–11]) is larger than 0.2, Eq. 3.4 is used.

3.3.2 The Pitot tube technique

The stagnation and static pressures occurring in Eq. 3.4 can be measured with a PT technique. The velocity and the flow direction can be determined with the PT technique as well [2].

A typical commercial Standard Pitot tube consists of a few measurement tubes. Normally, there is a central tube which acts as the stagnation pressure tube and the static pressure is measured through circumferential holes at right angles to the flow direction via a set of other tubes, as shown in Fig. 3.6 (a) [1, 2].

The normal commercial PT has a diameter of about 3 mm [10, 12] or larger [1, 2]. When it is inserted in the vortex flow field, the influence will be very strong because of blockage and flow disturbance. Sometimes, the measured results even can be distorted [3].

When a PT is used in the vortex tube, it should be as small as possible, in this case, the commercial PT is not convenient. For our application, a special PT, Cylinder type Pitot tube (CPT) [3, 4, 11] was designed, as shown in Fig. 3.6 (b). The CPT consists of a capillary with 1 mm diameter, which is closed at one side and at the other side is connected to a pressure sensor. In the cylinder wall only one hole is drilled. The CPT can be rotated around its axis and translated along its axis via rotation and translation stages. During the rotation, the stagnation and static pressure can be found from the angle-dependent surface pressure distribution and by using a calibration.

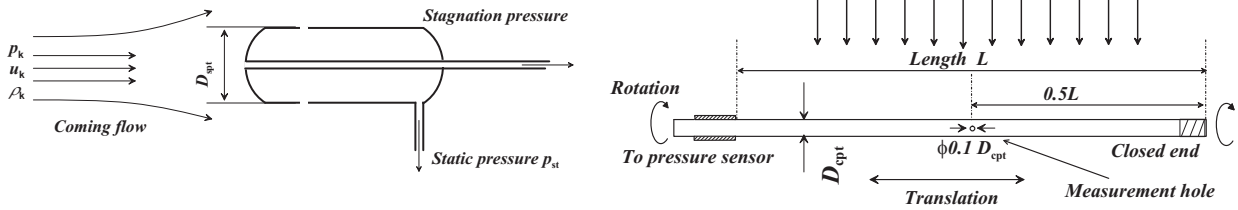

(a) Commercial Standard PT. D_{spt} is outer diameter.

(b) Special designed CPT. D_{cpt} is outer diameter.

Figure 3.6: *Schematic drawing of Pitot Tubes.*

3.3.3 Mechanism of the CPT technique

3.3.3.1 Typical measured pressure profile

When fluid flows across a cylinder, the angle-dependent pressure distribution on the cylinder surface can be determined. Although this pressure distribution is Reynolds and Mach number dependent. All these distributions are very similar, even for the higher static pressure flow fields, as shown in Fig. 3.2.

From Fig. 3.2, it can be found that the angle dependent CPT pressure profiles have the following features:

1. *When the hole on the CPT faces the flow direction, the pressure measured from the hole is maximal. The maximum pressure represents the stagnation pressure similar to the normal PT technique.*

2. *During the rotation of the CPT, the measured surface pressure is angle-dependent*

$$p = p(\alpha),$$

so it is possible to determine the pressure which equals the static pressure in the flow field. In Fig. 3.2, the static pressure appears at the angular positions where the pressure difference is zero.

3. *The inclination angle α where the measured pressure equals the static pressure can be found as function of Mach number, Reynolds number or size of the CPT, etc.*

In order to combine the measured pressure profiles with the PT principles and interpret these pressure profiles, a calibration procedure is necessary.

3.3.3.2 The calibration parameters for the CPT technique

Considering these measurement features, there are two parameters which should be calibrated: one is the inclination angle at which the pressure on the surface equals the static pressure, and the other one is a calibration factor for the Mach number. For the inclination angle, it can be determined directly from the calibrated differential pressure profiles. The calibration factor f_c is a factor that corrects the measured Mach number. This factor can be calculated with the equation

$$f_c = \frac{M_{a,cpt}}{M_{a,ref}}. \tag{3.7}$$

The Mach number calculated with the measured pressure is

$$M_{a,cpt} = \sqrt{\frac{1}{\Gamma_2}\left(\left(\frac{p_{sg}}{p_{\alpha:st}}\right)^{\Gamma} - 1\right)}.$$

where p_{sg} is the maximum pressure in the angle-dependent surface pressure distribution and $p_{\alpha:st}$ is the pressure at the angle which is equal to the calibration angle of the static pressure. The reference Mach number $M_{a,ref}$ can be obtained from the flow profile in the cross section and the average Mach number derived from the flowmeter.

3.3.4 Calibration of the CPT and analysis

In order to analyze the CPT tube size effect, three different sizes CPT tubes were used in the calibration: one CPT tube with 2 mm diameter and a 0.2 mm hole; one with 1 mm diameter and a 0.1 mm hole and one with 0.5 mm diameter and a 0.05 mm hole. For the CPT with diameter of 0.5 mm, the typical response time is around 5∼10 minutes. For practical reasons, the CPT in our experiments had an outer diameter of 1 mm with a 0.1 mm hole.

3.3.4.1 Non-dimensional parameters

In the calibration the Reynolds and Mach numbers are used as the variable parameters. The Reynolds number is defined as

$$R_{\mathrm{e}} = \frac{\rho V D_{\mathrm{cpt}}}{\mu} \tag{3.8}$$

where D_{cpt} is the diameter of the CPT tube, ρ is the gas density, V is the measured velocity, and μ is the dynamic viscosity.

The reference Mach number is chosen as the Mach number at the center of the cross section, so it is calculated as

$$M_{\mathrm{a,ref}} = M_{\mathrm{a,c}} = \tau_{\mathrm{v}} M_{\mathrm{a,fm}} \tag{3.9}$$

where τ_{v} is defined in Eq. 3.2, and $M_{\mathrm{a,fm}}$ is the average Mach number based on the flowmeter.

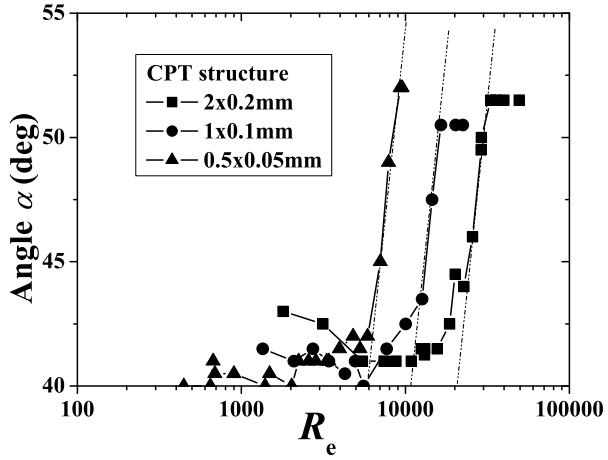

Figure 3.7: *Inclination angle α as function of Reynolds number.*

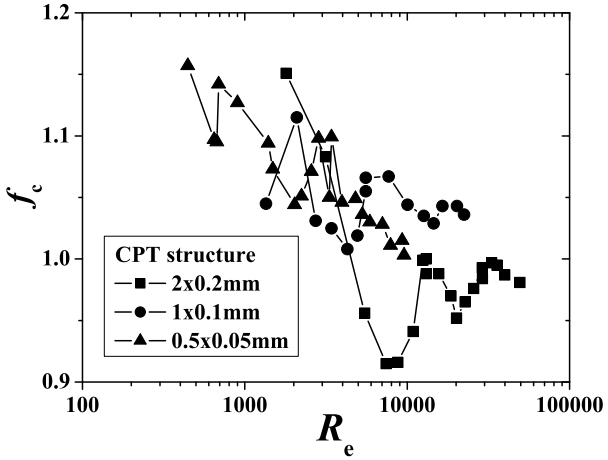

Figure 3.8: *Calibration factor f as function of Reynolds number.*

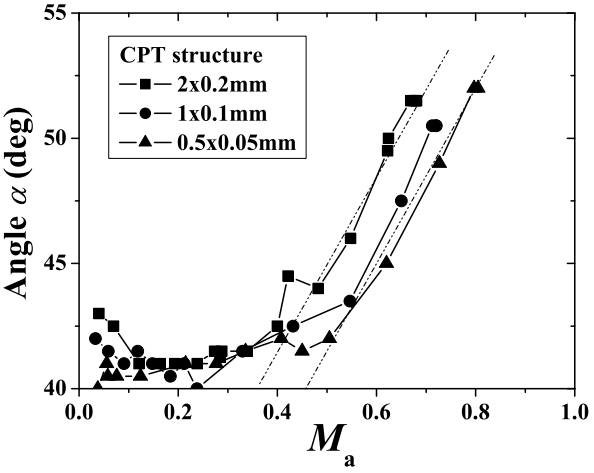

Figure 3.9: *Inclination angle as function of Mach number.*

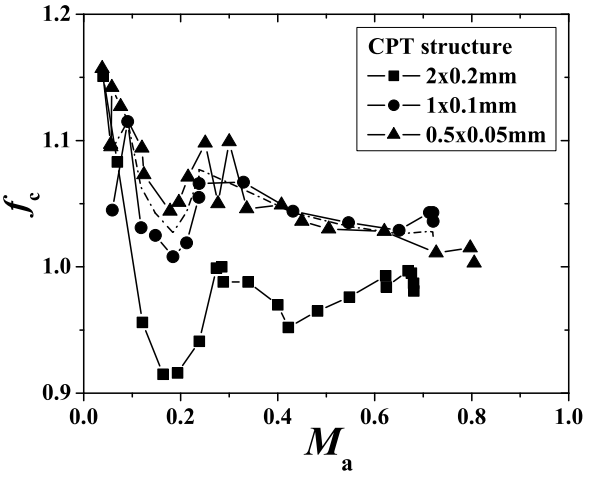

Figure 3.10: *Calibration factor as function of Mach number.*

The Reynolds number of the measurements ranges from 500 to 50000. The Mach number is from $0.02 < M_{\mathrm{a}} < 0.8$. One expects an influence of both Reynolds number as well as

Mach number on the calibration. In Fig. 3.7 the angle is plotted at which the static pressure equals the measured pressure. This angle increases from 41^0 approximately. Remarkable is that these curves depend on the tube diameter. The calibration factor f_c is shown in Fig. 3.8 versus the Reynolds number. Corrections amount up to $\pm 5\%$. The 0.5 mm and 1 mm CPT cases are quite similar, whereas the 2 mm CPT measurement is significantly different. Careful studying of the graphs showed again that here the Reynolds number is not the most relevant parameter, which is also observed in the measurements in [2].

In Figs. 3.9 and 3.10, the inclination angle and calibration factor are now plotted as function of the Mach number. These graphs are much more similar and make clear that M_a is the dominant parameter. The plot of the 2 mm CPT clearly is shifted significantly from the other 2 cases. We attribute this to windtunnel blockage which amounts to about 20% in case of the 2 mm tube. At these larger blockage factors the flow field changes considerably [2, 13].

Summarizing we state that:

1. *The calibration is influenced by Reynolds as well as Mach numbers. There might be a functional dependency $f(M_a, R_e)$ in the Mach and Reynolds numbers parameter space, but the Mach number dependency dominates the Reynolds number dependency.*

2. *Blockage effects occur in case of the 2 mm CPT which must be rejected for the calibration.*

3. *For the practical interpretation of the calibration, the Mach number is taken as the calibration variable.*

3.3.4.2 Calibration Results

During the experiments, the CPT with diameter 1 mm and a pressure hole of 0.1 mm is applied. So the specified calibration angle α and the factor f_c are functions of the Mach number. The results are shown in Fig. 3.11.

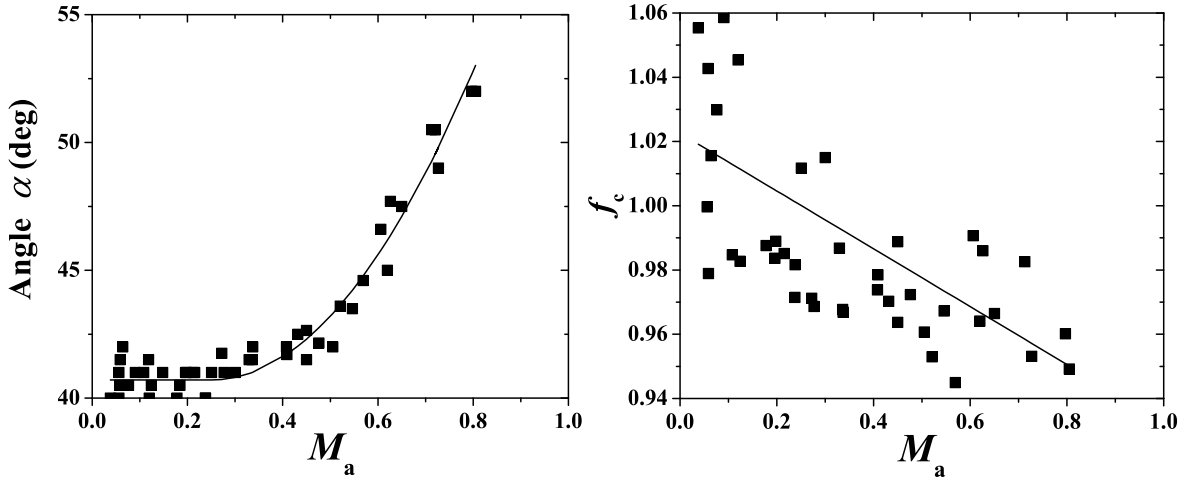

(a)Calibration angle α *(b) Calibration factor f_c*

Figure 3.11: *Calibration parameters vs. Mach number.*

Fig. 3.11 (a) shows the angle as a function of Mach number, which is expressed by the

following equation

$$\begin{cases} \alpha = 40.7 & 0.03 \leq M_\mathrm{a} \leq 0.25 \\ \alpha = 40.0M_\mathrm{a}^2 - 20.0M_\mathrm{a} + 43.2 & 0.25 \leq M_\mathrm{a} \leq 0.7. \end{cases} \tag{3.10}$$

When the Mach number is lower than 0.25, the inclination angle is constant as 40.7^0, which corresponds to the value given in [2] (the angle is taken as constant 40^0 or 44^0). But when the Mach number is larger than 0.25, a polynomial calibration is used, while in [2], still a constant is used.

Fig. 3.11 (b) shows the calibration factor as expression of the Mach number

$$f_\mathrm{c} = -0.09M_\mathrm{a} + 1.03 \tag{3.11}$$

when $M_\mathrm{a} = 0.25$, f_c is 1. The typical errors for the angle α and factor f_c are 3% and 4%, respectively. Using the functions of the angle α and the factor f_c, based on the measured angle-dependent surface pressure, the Mach number can be determined iteratively.

3.3.5 The application of the CPT

With the CPT, the pressure and velocity field can be determined, as illustrated in Fig. 3.12. With the rotation and translation stages, the angle-dependent surface pressure distribution at the measurement point can be determined, as well as the pressure profiles at any position along the radius. As discussed in section 3.3.3, when the measurement hole faces the flow, the pressure is maximum. So the flow direction inside the RHVT is determined. Assuming the radial velocity component to be negligibly small, using the inclination angle, the measured velocity can be separated into the azimuthal and axial components. The radial speed, however, cannot be determined.

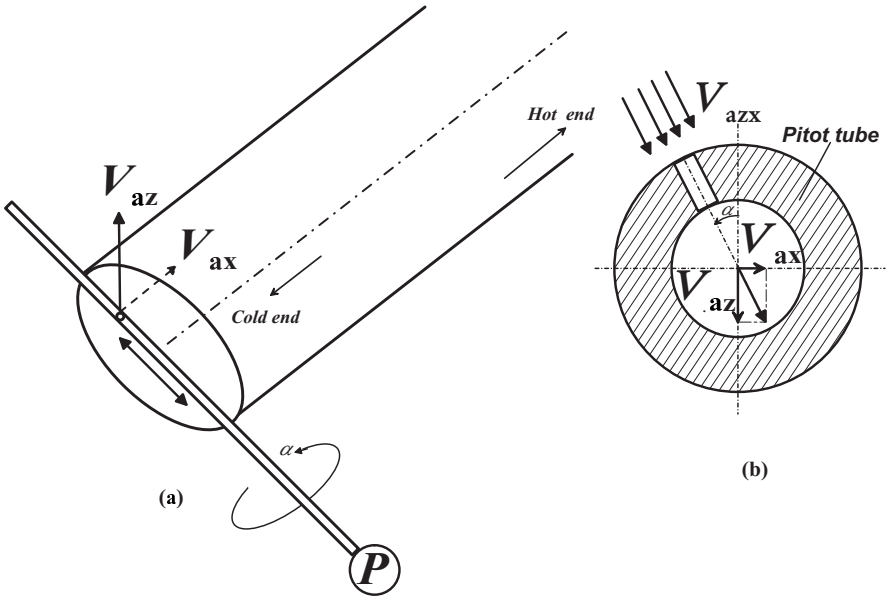

Figure 3.12: *Application of the CPT technique in the RHVT system with the rotation and translation stages.*

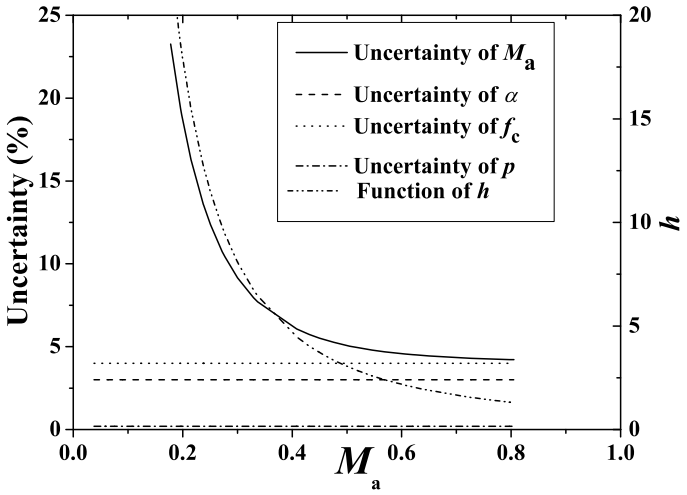

Figure 3.13: *Mach number error analysis.*

3.3.5.1 Interpreting the measurements

According to Eqs. 3.10 and 3.11 and the angle-dependent surface pressure distribution, the Mach number can more accurately be calculated iteratively,

$$\begin{cases} \Gamma_2(f_c M_a)^2 &= \left(\frac{p_{sg}}{p_{\alpha:st}}\right)^{\Gamma} - 1 \\ \alpha &= \alpha(M_a) \\ f_c &= f(M_a) \\ p &= p(\alpha) \end{cases} \tag{3.12}$$

Here f_c and α are Mach number dependent, p is a function of α and M_a is f_c, p and α dependent. By starting with an initial f_c of 1, α of 40.7 and repeating the calculation for successive determined M_a, f_c and α values, this iteration leads to a good approximation of M_a.

3.3.5.2 Standard deviation uncertainty analysis

Based on Eq. 3.12, the typical uncertainty for the Mach number depends on the errors in the stagnation pressure, static pressure and the factor f_c. The Standard Deviation Uncertainty (SDU) [14] for the Mach number is

$$(\frac{\delta M_a}{M_a})^2 = \left(h(M_a, f_c)\frac{\delta p_0}{p_0}\right)^2 + \left(h(M_a, f_c)\frac{\delta p_{\alpha:st}}{p_{\alpha:st}}\right)^2 + \left(\frac{\delta f_c}{f_c}\right)^2. \tag{3.13}$$

and

$$h = \frac{\Gamma}{2} + \frac{1}{\gamma M_a^2 f_c^2} \ .$$

So the relative error in M_a can be calculated based on the relative errors in total pressure and static pressure and calibration factor

$$\varepsilon_{M_a} = \sqrt{(h\varepsilon_{p_0})^2 + (h\varepsilon_{p_{\alpha:st}})^2 + (\varepsilon_{f_c})^2} \tag{3.14}$$

where, ε_{p_0} is the relative error in the stagnation pressure, which depends on the accuracy of the pressure meter, here chosen as 0.2%; $\varepsilon_{p_{\alpha:\mathrm{st}}}$ is the relative error in the static pressure, which depends on the accuracy of the pressure meter and error in the inclination angle at a given Mach number and ε_{f_c} is the calibration error in the factor f_c. These related errors are shown on Fig. 3.13. When the Mach number is 0.25, the SDU measurement error is about 12%. So, the relative error in the Mach number is estimated as 15%.

3.3.5.3 Miscellaneous effects

In review papers [2, 13, 15], interference, yaw and displacement effects are discussed. The interference effects become significant only when $D_{\mathrm{pt}}/\delta > 0.22$ (δ is the boundary-layer thickness) [13]. In our experiments, the diameter of the CPT cylinder is only 1 mm, so the interference effects can be neglected. Looking to displacement and wall effects they find that, for the cantilever CPT, the errors in the pressure of up to $\pm 8\%$ are possible as the probe is moved across the tube. This is because of the onset of interference between the probe tip and the wall. For the the probe spanning the tube, the error is found to give about half the error of the cantilever type. This was ascribed to the occurrence of cross flow in the wake of cylinder. We did not study these effects but the CPT we used is similar to the probe spanning the tube mentioned in [2]. By using the results from others we estimate that wall effects become important only when the measurement hole is close to the wall. The yaw effect for the CPT is about $\pm 5^0$ which will result in error in pressure less than 1% [2, 13], so it is not important for our Pitot tube. The variations of the probe reading with the pitch effect are usually much the same as the variations with the yaw effect [2], so the pitch effect is not important in our research as well. Blockage was mentioned in section 3.4. Its influence in RHVT system is unclear. Blockage is also occurring in RHVT system due to rotational flow blockage, which can be 10% as followed from comparing hot-wire anemometry measurements with CPT results in the RHVT.

3.3.5.4 Advantage and disadvantage of CPT

With the CPT, the pressure and velocity fields inside the RHVT can be measured. The CPT has the following advantages:

1) Easy to design and manufacture.

2) Very simple to install in the RHVT for the experiments.

3) Easy to understand the physical meaning of the results, as it can be used for the pressure and the velocity measurements. It is very reliable for the pressure measurements.

4) Low cost.

The disadvantages of the CPT technique are:

1) The CPT technique can only be used for the mean pressure and mean velocity measurements. It is impossible to measure the turbulence parameters with the CPT because of the relatively long response time.

2) According to the above error analysis, the CPT has a sufficient accuracy for the estimation of the pressure information inside the RHVT system, especially for the stagnation

pressure p_{sg}. But for the Mach number, especially for Mach number lower than 0.25, the error can be about 15%. More accurate velocity measurements should be done with the hot-wire anemometry discussed in the next section.

3) The radial velocity component cannot be determined.

3.4 Single probe hot-wire anemometry (SPHWA)

3.4.1 Introduction

HWA is a device used for the measurements of the velocity and the temperature of flowing fluids. The principle of the device is based on the balance of the convection heat transfer from a heated wire or film element placed in a flowing fluid. The main principles that will be discussed here include heat transfer, the sensitivity coefficients of the hot-wire signal, the frequency response. At the end, the effect of the density is also considered.

3.4.1.1 Principle of operation

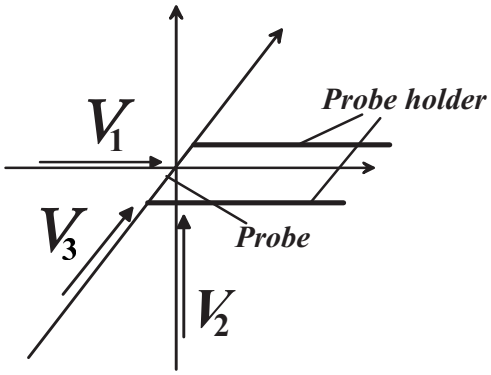

Figure 3.14: *The wire-fixed coordinate system and the corresponding velocity components.*

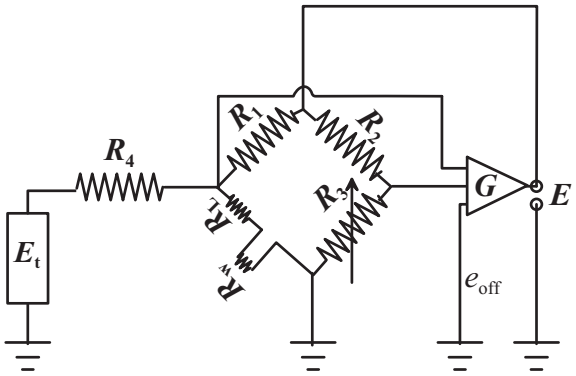

Figure 3.15: *The Wheatstone bridge applied for the SPHWA anemometry (Fig. 2.12 in [7]).*

Fig. 3.14 shows the velocity components in the hot-wire probe fixed coordinate system. When a heated wire is placed in a fluid flow, in the steady state and ignoring the conductive end heat losses, the heating power $\dot{Q}_w$ generated by the wire should be the same as the convective heat losses $\dot{Q}_f$,

$$\dot{Q}_w = \dot{Q}_f. \tag{3.15}$$

Normally, the hot-wire resistance is linearly dependent on the temperature. In practice, the reference temperature is often selected as room temperature (20 ^{0}C), so the relationship between the resistance and temperature is

$$R_w = R_{20}\,(1 + \alpha_{20}(T_w - T_{20})) \tag{3.16}$$

with R_{20} the wire resistance at temperature as 20 ^{0}C, α_w the temperature coefficient of resistivity (in our work, $\alpha_w = 0.0036$ /K), T_w is the wire temperature. The heating power,

generated by the wire, is

$$\dot{Q}_{\mathrm{w}} = I^2 R_{\mathrm{w}}. \tag{3.17}$$

with I the electrical current.

The convective heat losses can be calculated based on the convection heat transfer coefficient. So it depends on the speed of the flow (velocity vector V), the temperature difference between the gas and the wire, gas properties: density ρ, viscosity μ, thermal conductivity κ, specific heat c_p, temperature T_{f} and pressure p. Using non-dimensional parameters, such as Nusselt N_{u}, Reynolds R_{e}, and Prandtl P_{r}

$$N_{\mathrm{u}} = \frac{hD_{\mathrm{w}}}{\kappa},\ P_{\mathrm{r}} = \frac{c_p \mu}{\kappa} \tag{3.18}$$

where h is the heat transfer coefficient in $\mathrm{J/m^2sK}$, D_{w} is the hydraulic diameter of the probe. The heating power, taken away by the flow, is

$$\dot{Q}_{\mathrm{f}} = h\pi D_{\mathrm{w}} l_{\mathrm{w}} (T_{\mathrm{w}} - T_{\mathrm{f}}) = h\pi D_{\mathrm{w}} l_{\mathrm{w}} \frac{R_{\mathrm{w}} - R_{\mathrm{f}}}{\alpha_{20} R_{20}} \tag{3.19}$$

with l_{w} the length of the probe, T_{w} the wire temperature, R_{w} the hot-wire resistance at the wire temperature and R_{f} the hot-wire resistance at the flow temperature. The heat transfer coefficient h can be calculated using the Nusselt number N_{u}, which can be expressed in terms of the Prandtl number P_{r} and the Reynolds number R_{e}, using Kramers' expression [16]

$$N_{\mathrm{u}} = 0.42 {P_{\mathrm{r}}}^{0.2} + 0.57 {P_{\mathrm{r}}}^{0.33} {R_{\mathrm{e}}}^{0.5}. \tag{3.20}$$

So, combining the above equations, a relatively simple heat transfer relationship can be derived for a hot-wire probe, (see Bruun [6, 7]),

$$I^2 R_{\mathrm{w}} = \frac{\pi l \kappa}{\alpha_{20}} \frac{R_{\mathrm{w}} - R_{\mathrm{f}}}{R_{20}} (0.42 P_{\mathrm{r}}^{0.2} + 0.57 P_{\mathrm{r}}^{0.33} R_{\mathrm{e}}^{0.50}) \tag{3.21}$$

In the RHVT, the gas density assumed to compute R_{e} varies from position to position, while the parameters l_{w}, κ, α_{20}, R_{20} and P_{r} are constant. Introducing the wire voltage $E_{\mathrm{w}} = IR_{\mathrm{w}}$, Eq. 3.21 may be written in the form

$$\frac{E_{\mathrm{w}}^2}{R_{\mathrm{w}}} = (A_1 + B_1 (R_{\mathrm{e}})^{0.5})(R_{\mathrm{w}} - R_{\mathrm{f}}) = (\hat{A}_1 + \hat{B}_1 (R_{\mathrm{e}})^{0.5})(T_{\mathrm{w}} - T_{\mathrm{f}}) \tag{3.22}$$

here, $\alpha_{20} R_{20}$ has been included in the factors A_1 and B_1 introduced above.

The response equation is often expressed in terms of the anemometry output E. For a balanced anemometry bridge—Wheatstone bridge, see Fig. 3.15, the relationship between E and E_{w} is

$$E = \frac{R_1 + R_{\mathrm{L}} + R_{\mathrm{w}}}{R_{\mathrm{w}}} E_{\mathrm{w}} \tag{3.23}$$

where R_1 is the resistance in the Wheatstone bridge, R_{L} is the resistance of the connecting cable and the SPHWA holders, R_{w} is the hot-wire probe resistance, as shown in Fig. 3.15. In practice, for the CT model (constant temperature), R_1 and R_{L} are constant values, R_{w} stays virtually constant if the gas temperature stays constant as well, so, in principle, Eq. 3.22 can be simplified to

$$E^2 = A_2 + B_2 (R_{\mathrm{e}})^n = A_2 + \hat{B}_2 (\rho V \frac{D}{\mu})^n. \tag{3.24}$$

Assuming that the gas viscosity is constant, Eq. 3.24 is simplified to the power law

$$E^2 = A + B(\rho V)_e^n \tag{3.25}$$

where A, B and n are calibration parameters independent of the velocity and temperature [7], $(\rho V)_e$ is an effective (ρV) term, which is related to the velocity vector V and density ρ. In practice, only the effective velocity vector is taken into account, and the real, mean density ρ is used for converting the ρV term into V.

3.4.1.2 Effective velocity vector

As discussed in [6, 7] by Bruun, a hot-wire anemometry has different responses to the three velocity components, V_1, V_2, V_3, shown in Fig. 3.14. In particular, the sensitivity to the velocity component V_3 which is parallel to the hot-wire probe is very small. The effective velocity is defined as based on the so-called Jorgensen equation which takes these factors into account

$$V_e^2 = V_1^2 + h^2 V_2^2 + k^2 V_3^2 \tag{3.26}$$

where h and k are sensitivity coefficients. Their typical value for a standard plated hot-wire probe are 1.05 and 0.2, respectively [7].

3.4.2 The calibration of the SPHWA

In this work, single probe hot-wire anemometry (SPHWA) was used. In order to apply the SPHWA, calibration is necessary to find the calibration parameters A, B and n in Eq. 3.25.

During the calibration and the experiments, some assumptions were made: 1) It is assumed that all the measurements can be repeated under the same operating conditions. With this assumption when the pressures at the entrance and exhaust are the same, the inlet flow and cold fraction are the same and the RHVT system is the same, the velocity field, pressure field and temperature field inside the system should be the same; 2) The pressure and temperature profiles in the RHVT system are the mean profiles. Fluctuations are neglected; 3) The gas density inside the RHVT is only dependent on the mean static pressure and static temperature, and density fluctuations can be neglected.

Eq. 3.25 can now be written as

$$E^2 = A + B(\overline{\rho} V_e)^n. \tag{3.27}$$

Fig. 3.16 shows the procedure of the effective velocity calculation during the calibration. Because of the experimental limitations we can only calibrate its components, V_2 and V_3. The effective velocity

$$\overline{\rho} V_e = \sqrt{1.05^2 (\overline{\rho} V_2)^2 + 0.2^2 (\overline{\rho} V_3)^2}. \tag{3.28}$$

Fig. 3.16 also shows that the two velocity components V_2 and V_3 have the following relationship with the velocity V at the calibration point and the inclination angle θ

$$\begin{cases} V_2 &= V \sin\theta \\ V_3 &= V \cos\theta \end{cases} \tag{3.29}$$

where θ is the angle between the probe and the flow direction at the measurement point; V is the reference velocity V_{ref} at the measured position (center of the measurement section), and is determined by the flow meter(see Eqs. 3.2 and 3.9)

$$V_{\text{ref}} = \tau_{\text{v}} V_{\text{fm}} \quad .$$

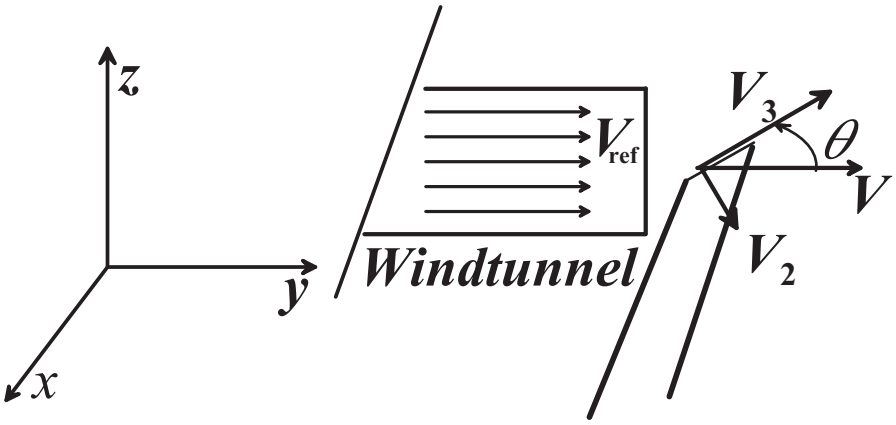

Figure 3.16: *The effective velocity analysis for the calibration. The exhaust of the windtunnel is parallel to the y axis, and perpendicular to the probe holder. By rotating the axis of the hot wire the measured signal varies with the inclination angle θ. So if $\theta = 0^0$, the measured velocity V is V_3, and if $\theta = 90^0$, the measured velocity V is V_2. If θ is in between 0^0 and 90^0, the measured velocity V can be divided into V_2 and V_3 with Eq. 3.29. V_1 cannot be measured.*

By substituting the above equation into Eq. 3.28, the relationship between the effective velocity, the mass flow rate, and the inclination angle is found

$$\rho V_e = \tau_{\mathrm{v}} \frac{\dot{m}_{\mathrm{fm}}}{A} \sqrt{1.1025 \sin\theta^2 + 0.04 \cos\theta^2}. \tag{3.30}$$

3.4.2.1 Calibration result

According to Eq. 3.27, a least-squares curve fitting method, based on the sum of errors squared (SES) is applied to optimize the calibration constants. Using the power-law relationship,

$$SES = \sum_{i=1}^{N} (E_{\mathrm{r}}^2 - E_{\mathrm{c}}^2)^2 \tag{3.31}$$

where E_{r} is the measured calibration voltage and E_{c} is the voltage calculated from Eq. 3.27, the minimum in SES has to be computed by varying A, B and n.

There are two ways to deal with the factor A in Eq. 3.27. Theoretically, A should be equal to E_0^2. E_0 is the signal read from the SPHWA probe when the velocity in the system is zero. Practically, A can also be calibrated simultaneously with B and n by the SES method. Fig. 3.17 shows the calibration results based on the effective ρV term to determine E_0.

To compare the above two calibration methods, the quality of the fit can be described by the (related) normalized standard deviation,$\varepsilon_{\rho V}$

$$\varepsilon_{\rho V} = (\frac{1}{N} \sum_{i=1}^{N} (1 - \frac{(\rho V)_{\mathrm{r}}}{(\rho V)_{\mathrm{c}}})^2)^{(1/2)} \tag{3.32}$$

where $(\rho V)_{\mathrm{r}}$ is the measured results based on the flowmeter; $(\rho V)_{\mathrm{c}}$ is the calculated as based on the Eq. 3.25 by using the measured voltage value at the relevant $(\rho V)_{\mathrm{r}}$ and these calibration factors A, B and n.

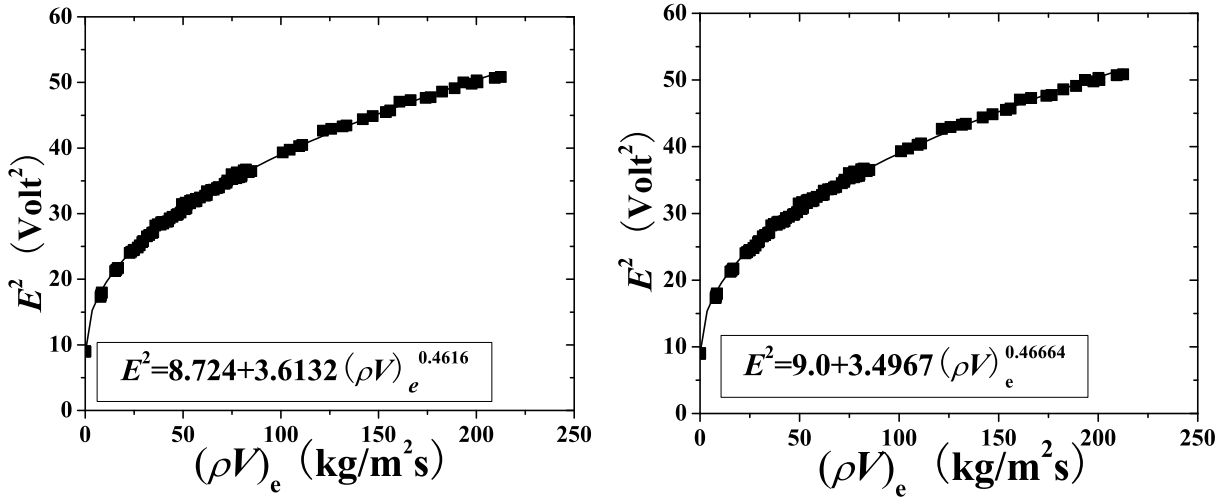

(a) $A \neq E_0^2$ *(b)* $A = E_0^2$

Figure 3.17: *The calibration results of the SPHWA probe.*

3.4.2.2 Accuracy analysis

The factors A, B and n as well as the normalized standard deviation $\varepsilon_{\rho V}$ in the above two methods of the calibration are shown in Table 3.1.

Type	Factor A	Factor B	Factor n	$\varepsilon_{\rho V}$
set I	8.724	3.6132	0.4616	3.7%
set II	9.0	3.4967	0.46664	9.3%

Table 3.1: *Comparison of the accuracies for the two sets of the calibration factors.*

The normalized standard relative deviation $\varepsilon_{\rho V}$ from Eq. 3.32 is smaller than 10 %. During the experiments in the RHVT system, set I of the calibration is used. The accuracy of the experiments for the total ρV_e term is estimated as 4%.

During the calibration, it is not possible to measure and calibrate the velocity component V_1 due to the placement of the set-up. In [6, 7], the sensitivity factor for V_1 is 1. When applying the SPHWA in the RHVT system, the uncertainty for the V_1 component (radial velocity) is estimated to be about 10%.

3.4.3 The application of the SPHWA technique in RHVT system

The SPHWA signal can be described by the sum of an average and a fluctuating term,

$$E(t, \theta, r) = \overline{E(r, \theta)} + e(t, \theta, r) \tag{3.33}$$

where, t means time, θ is the inclination angle and r is the position. For a fixed position r, Eq. 3.33 is simplified as

$$E(t, \theta) = \overline{E(\theta)} + e(t, \theta) \tag{3.34}$$

where, the term $\overline{E(\theta)}$ expresses the relationship between the mean signal and the inclination angle θ, as shown in Fig. (3.18), $e(t, \theta)$ is the fluctuation which is dependent on the time and the inclination angle.

3.4.3.1 The mean velocity analysis

When inserting the SPHWA probe inside the RHVT, the component $\overline{\rho V_1}$ in Fig. (3.14) is always the mean radial velocity $\overline{\rho V_{\rm r}}$. The difference between the maximum and the minimum signals in Fig. (3.3) occurs because of the other two components $\overline{\rho V_2}$ (mean azimuthal component $\overline{\rho V_{\rm az}}$) and $\overline{\rho V_3}$(mean axial component $\overline{\rho V_{\rm ax}}$). Using the effective velocity analysis, it can be shown that when the combined velocity component $\overline{\rho V_{2,3}}$ is parallel to the SPHWA probe, the signal is minimum, named $\overline{E_\theta}_{\rm min}$, and when $\overline{\rho V_{2,3}}$ is perpendicular to the probe, the signal is maximum $\overline{E_\theta}_{\rm max}$, as shown in Fig. 3.18. The inclination angle between the maximum and minimum signals is about 90^0 degrees. Here, the inclination angle θ for the maximum signal shows the flow direction of the velocity component $\overline{\rho V_{2,3}}$ and it should be equal to the inclination angle measured by CPT techniques.

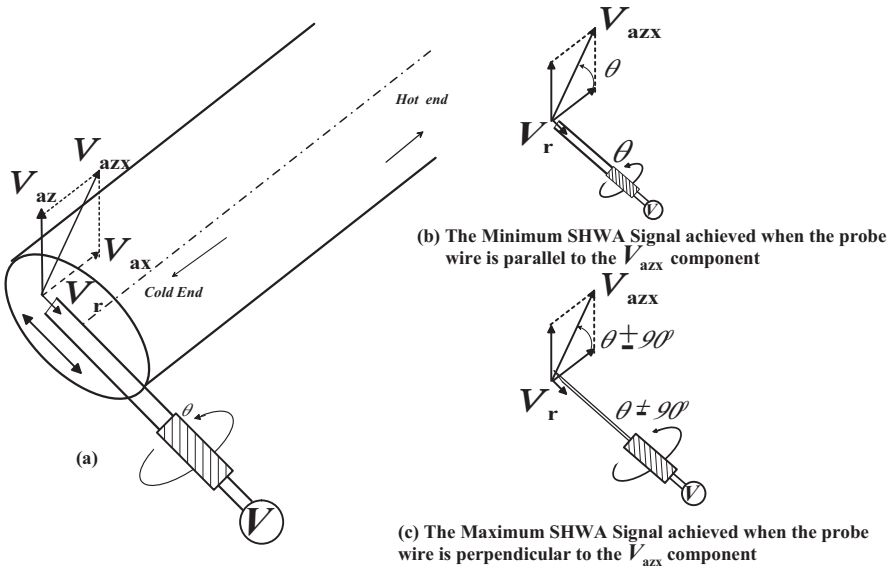

Figure 3.18: *The application of the SPHWA technique inside the RHVT. When V_{azx} (the composition of $V_{\rm az}$ and $V_{\rm ax}$) is parallel to the probe, the signal is minimum, and when it is perpendicular to the probe, then the signal is maximum.*

With the signals $\overline{E_\theta}_{\rm min}$ and $\overline{E_\theta}_{\rm max}$, the 3D velocity components inside the RHVT system can be determined. For the maximum signal, the following holds

$$(\overline{\rho V_e}_{\rm max})^2 = (\overline{\rho V_1})^2 + (1.05\overline{\rho V_{2,3}})^2. \tag{3.35}$$

For the minimum signal, the $\overline{\rho V}$ term is

$$(\overline{\rho V_e}_{\rm min})^2 = (\overline{\rho V_1})^2 + (0.2\overline{\rho V_{2,3}})^2. \tag{3.36}$$

In this way, the mean mass flow density components $\overline{\rho V_1}$ and $\overline{\rho V_{2,3}}$ are determined. To calculate the individual components $\overline{\rho V_2}$ and $\overline{\rho V_3}$, we only need to use the angle θ at which the maximum signal was measured. For instance, the three components $\overline{\rho V}$ inside the RHVT can be derived as:

$$\begin{aligned} \overline{\rho V}_{\rm r} &= \overline{\rho V}_1 \\ \overline{\rho V}_{\rm ax} &= \overline{\rho V}_{2,3} \sin\theta \\ \overline{\rho V}_{\rm az} &= \overline{\rho V}_{2,3} \cos\theta \end{aligned} \tag{3.37}$$

3.4.3.2 Analysis of the fluctuations

The voltage of the SPHWA sample is expressed as a function of the time, the inclination angle θ and position x by Eq. 3.35. So the relevant density×velocity can be expressed as,

$$(\rho V) = \overline{(\rho V)} + (\rho V)' \tag{3.38}$$

where, (ρV) is the real time, angle and position dependent term; $\overline{(\rho V)}$ is the mean value, dependent on the angle and position; $(\rho V)'$ is the fluctuation term. According to the constant density assumption, the fluctuation can be written as $(\rho v')$ as well.

For a fixed angle θ and position x, the Eqs. 3.35 and 3.38 can then be simplified as

$$\begin{aligned} E(t) &= \overline{E} + e(t) \\ (\rho V)(t) &= \overline{(\rho V)} + (\rho V)'(t) \simeq \overline{(\rho V)} + (\rho v')(t). \end{aligned} \tag{3.39}$$

At a fixed angle θ and position x, the $(\rho V)(t)$ term can be calculated based on the mean signal $E(t)$ with Eq. 3.27, as

$$E(t)^2 = A + B(\rho V)_e^n. \tag{3.40}$$

So, for the mean term, it follows that [7],

$$\overline{E}^2 = A + B(\overline{\rho V_e})^n. \tag{3.41}$$

The fluctuation term can be formed by differentiating with respect to time Eq. 3.40,

$$2EE' = nB(\rho V_e)^{n-1}(\rho V_e)' = nB(\rho V_e)^{n-1}(\rho v_e'). \tag{3.42}$$

So the time derivation of the density×velocity term becomes

$$\begin{aligned} (\rho v_e') &= \tfrac{2EE'}{nB(\rho V_e)^{n-1}} \\ &= \tfrac{2Ee}{nB(\rho V_e)^{n-1}} \end{aligned} \tag{3.43}$$

For E and (ρV_e) it is a good approximation to take the mean values $\overline{E}$ and $\overline{\rho V_e}$ [7]. So during the experiments, the fluctuation term is calculated using

$$(\rho v_e') = \frac{2\overline{E}e}{nB\overline{(\rho V_e)}^{n-1}}. \tag{3.44}$$

In order to understand the turbulence information, the statistics tools [17] (such as the probability density function (PDF), the root-mean-square fluctuation (RMSF), the skewness and the flatness, the spectrum analysis with the fast fourier transform (FFT)) are used.

@ Definition of the PDF

The Probability Density Function (PDF) is the continuous probability function, $f(x)$, which satisfies the following properties:

a) the probability that x is between two values a and b is

$$p[a \leq x \leq b] = \int_a^b f(x)\mathrm{d}x, \tag{3.45}$$

b) it is positive for all real x,

c) the integral of the probability function over all values is equal to one, that is

$$\int_{-\infty}^{\infty} f(x)\mathrm{d}x = 1. \tag{3.46}$$

The PDF is used to analyze the signal sample measured by the SPHWA technique. Fig. 3.19 shows a typical example.

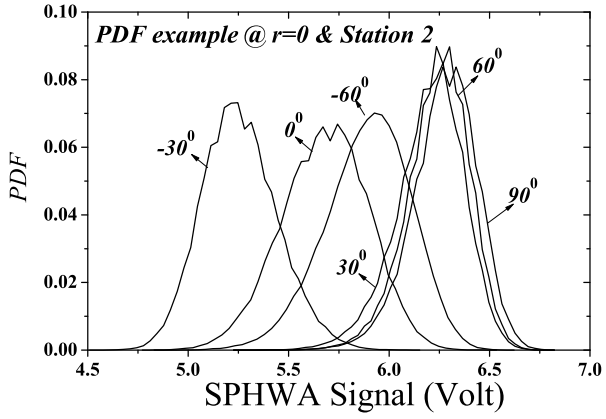

Figure 3.19: *Typical example of the PDF of the SPHWA sample (under cold fraction $\epsilon \simeq 0.39$ with $200Nm^3/h$ inlet flow).*

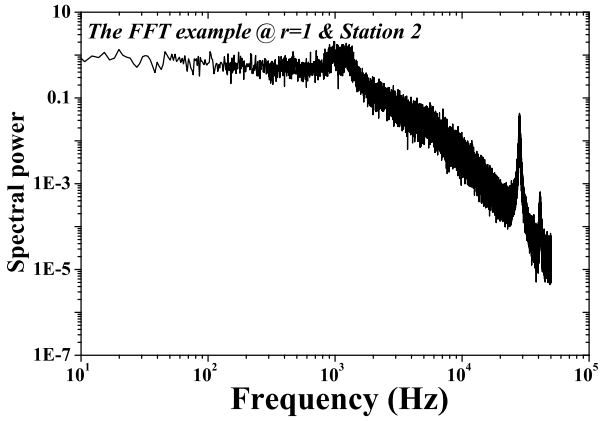

Figure 3.20: *Typical example of the FFT spectrum of the SPHWA sample (under the same conditions as Fig. 3.19).*

ⓑ Definition of the root-mean-squared fluctuation

The root-mean-squared fluctuation (RMSF) (δ_{rs}) is calculated using the time-dependent fluctuations in the SPHWA signal at the same angle θ. The function is defined as

$$(\delta_{\mathrm{rs}}(\theta))^2 = \frac{1}{T}\int_0^T (\rho v'(t,\theta))^2 \mathrm{d}t \simeq \frac{1}{N}\sum_{i=1}^{N} (\rho v'_{(i)}(\theta))^2. \tag{3.47}$$

In the measurements, the signals obtained are discrete time series, so here N is the number of data points in the series and depends on the sample frequency and time, ρV_i is the value in the series.

So in the RHVT system δ_{rs} for the measurement position is angle-dependent. In the final experiments, it was treated as root-mean-squared parameter again based on the angle of δ_{rs}, details are described in Chapter 6.

ⓒ Definition of the skewness

Skewness is a measure of symmetry, or, more precisely, the lack of symmetry. A distribution, or data set, is symmetric if it looks the same to the left and right of the center point. The skewness is calculated as

$$S_{\mathrm{sk}} = \frac{\frac{1}{T}\int_0^T (\rho V'(t))^3 \mathrm{d}t}{\delta^3} \simeq \frac{\frac{1}{N}\sum_{i=1}^{N} (\rho v'_{(i)})^3}{\delta^3}. \tag{3.48}$$

where δ is the root-mean-squared fluctuation discussed above.

The skewness for a normal distribution is zero. Any symmetric data set $\rho V'_{(i)}$ should have a skewness zero. Negative values for the skewness indicate a data set that is skewed left and positive values indicate that the data set is skewed right.

ⓓ Definition of the flatness

The flatness is also named Kurtosis in some textbooks. It is a measure of whether the data are peaked or flat relative to a normal distribution. Data sets with high flatness tend to have a flat peak near the mean value, decline rather rapidly, and have long tails. Data sets with low flatness tend to have a sharp top near the mean rather than a sharp peak. The equation for the flatness is

$$F_{\rm fl} = \frac{\frac{1}{T}\int_0^T (\rho v'(t))^4 {\rm d}t}{\delta^4} \simeq \frac{\frac{1}{N}\sum\limits_{i=1}^{N} (\rho v'_{(i)})^4}{\delta^4}. \tag{3.49}$$

The flatness for a standard normal distribution is 3.0. When the flatness is larger than 3.0, that means the data has a "peaked" distribution; otherwise, the data has a "flat" distribution.

ⓔ Spectrum analysis with fast fourier transform (FFT)

As discussed above, the measured signal is time-dependent. Based on Fourier analysis, the signal can be decomposed into a discrete series of sinusoidal components. The SPHWA signal sample is a noisy signal in the time domain. In order to determine the relevant signal frequencies, the FFT method is used. Assume the SPHWA sample signal $E(t)$, the sample frequency $F_{\rm sf}$, then the FFT method for the sample is calculated as

$$\left\{ \begin{array}{c} N = 2^{round(\log_2(F_{\rm sf}))} \\ E_{\rm fft} = fft(E(t), N) \\ PE_{\rm fft} = E_{\rm fft}. * conj(E_{\rm fft})/N \\ f_{\rm fft} = F_{\rm sf} * (0:N)/N \end{array} \right. \tag{3.50}$$

where, $round(x)$ is a MatLab function [18] to round the element x to the nearest integer, for example, $round(2.1)$ gives 2, and $round(1.9)$ gives 2; $fft(X, N)$ is also a MatLab function [18] to compute the discrete Fourier transform of vector X by computing with the fast Fourier transform (FFT) algorithm; and $conj(X)$ is a MatLab function [18] to compute the complex conjugate of element X. All these functions are standardized in MatLab software (detailed derivations and applications on these functions can be found in [18]). With the computation, $PE_{\rm fft}$ is an array of the spectrum power at various frequencies $f_{\rm fft}$. Fig. 3.20 shows a typical example of the FFT spectrum analysis for the final experimental SPHWA sample. The figure is very noisy, so it is necessary to smooth the spectrum.

ⓕ Smoothing of the spectrum

In order to filter the useful information from the noisy spectrum, the spectrum is smoothed based on the frequencies

$$\begin{cases} N_{\rm sm}(i) = 1 & \text{, if } f_{\rm fft}(i) \le 1 \\ N_{\rm sm}(i) = N_0^{round(\log_{10}(f_{\rm fft}(i)))} & \text{, if } f_{\rm fft}(i) \ge 1 \\ \overline{PE_{\rm fft}}(i) = \frac{\sum_{j=i-N_{\rm sm}}^{i+N_{\rm sm}} PE_{\rm fft}j}{2N_{\rm sm}} \end{cases} \tag{3.51}$$

where, i is varying from 1 to $N_{\rm tot}$, which is used to rebuild the spectrum power in the spectrum array; $N_{\rm sm}$ is the smoothing step which is dependent on the related spectrum frequency; N_0 is the fundamental number for the smoothing step. If $N_0 = 1$, there is no smoothing, if $N_0 = 2$, the plot of the spectrum is improved a little bit, if N_0 is too big, then the results are constant. During the experiments, N_0 is chosen 3.

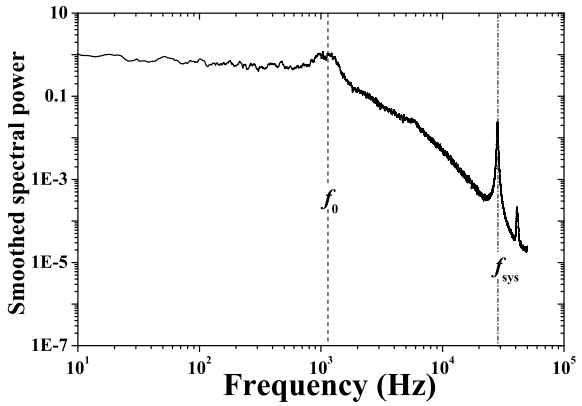

Figure 3.21: *The smoothed spectrum of Fig. 3.20*

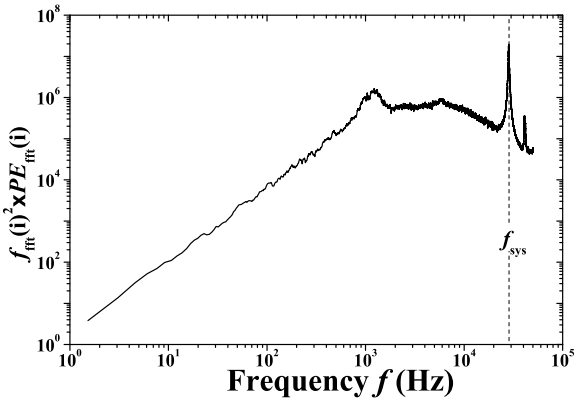

Figure 3.22: *The $f_{\rm fft}(i)^2 * PE_{\rm fft}(i)$ results of Fig. 3.21*

Fig. 3.21 shows the smoothed spectrum from Fig. 3.20. It shows that a peak at the frequency f_0. It is remarkable that there is another frequency $f_{\rm sys}$ at about 30000 Hz. This peak exists in all the SPHWA samples. For determining wether a frequency has a physical meaning, we computed the $f_{\rm fft}(i)^2 * PE_{\rm fft}(i)$ term. When the plot of the $f_{\rm fft}(i)^2 * PE_{\rm fft}(i)$ term appears the second peak, this frequency and even larger frequencies have no physical meaning [19]. Fig. 3.22 shows the $f_{\rm fft}(i)^2 * PE_{\rm fft}(i)$ term result vs frequency based on Fig. 3.21. So we can find that when the frequency is larger than 20000 Hz, the frequency has no physical meaning. So we can determine that the measured SPHWA signal only has one relevant frequency with peak spectrum power, which is around 1000 Hz.

ⓖ Acoustic phenomena

Sometimes peak frequencies, found by the FFT analysis with one SPHWA sample data set, form a series (like series (1, 1.5, 2.5) or (1, 2, 3, 4) as shown in Fig. 3.23) with a basic frequency. In [20–22], Kurosaka et al. gave the relationships between the basic frequency and higher harmonics. They defined that in that case these are acoustic frequencies. A series of

frequencies can prove the existence of acoustic phenomena inside the RHVT. If only one peak frequency exists for SPHWA sample, as shown in Fig. 3.21, it is more likely related to the rotation frequency of the vortex core.

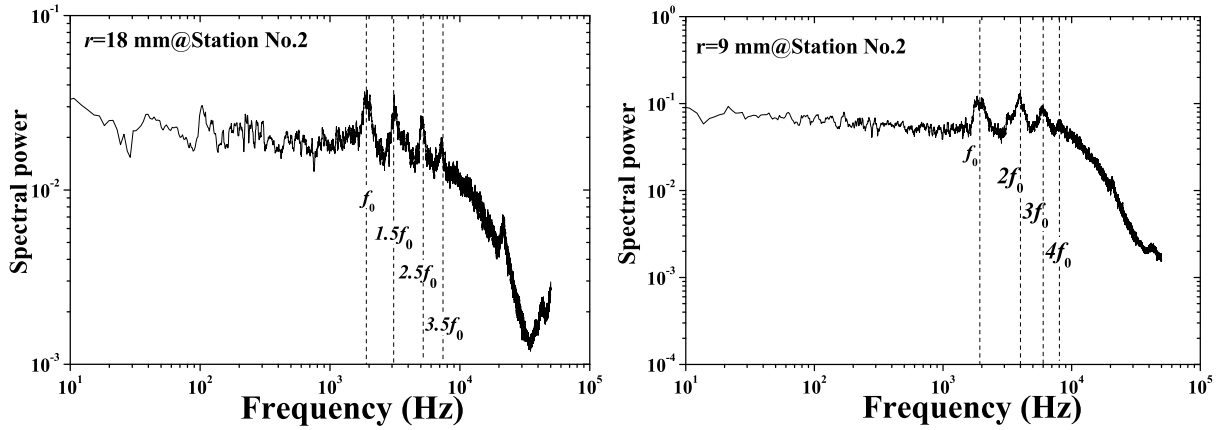

(a) *(b)*

Figure 3.23: *Acoustic frequency examples measured by SPHWA with cold fraction* $\epsilon \simeq 0.28$ *and inlet flow around 200* Nm^3/h. *(a) with the series as (1, 1.5, 2.5, 3.5) and (b) with the series as (1, 2, 3, 4).*

3.5 Comparison of the Pitot tube and hot-wire techniques

Based on the descriptions in Section 3.3 and 3.4, the Pitot tube and the hot-wire techniques both can be used for the velocity measurement. The main differences are that, the CPT technique can only be used for the mean velocity measurement, and it can only predict two components of the velocity. The SPHWA technique can be used for the mean ρV term measurement as well as to determine the fluctuations. The disadvantage of the SPHWA technique is that the measured result contains the gas density, which should be determined independently by the CPT and the thermocouple.

3.6 Temperature measurements

The temperature can be measured via different sensors, like thermocouple, thermal resistors, etc.

The principle of the thermal resistor is to measure the resistance of platinum. The most common types (PT100&PT1000) have resistances which are a linear function of the temperature. At 0 ^{0}C, PT100 has a resistance of 100 ohm and PT1000 has 1000 ohm. Their linear functions are

$$\begin{cases} T = 2.575R + 15.924 & ,223\ \mathrm{K} \leq T \leq 373\ \mathrm{K}, \quad PT100 \\ T = 0.258R + 15.924 & ,223\ \mathrm{K} \leq T \leq 373\ \mathrm{K}, \quad PT1000 \end{cases} \tag{3.52}$$

where R is the resistance, in ohm, T is the indicated temperature in K. In Chapter 4, PT100 is used to measure the inlet and two exhaust temperatures. In Chapter 6, PT1000 is used.

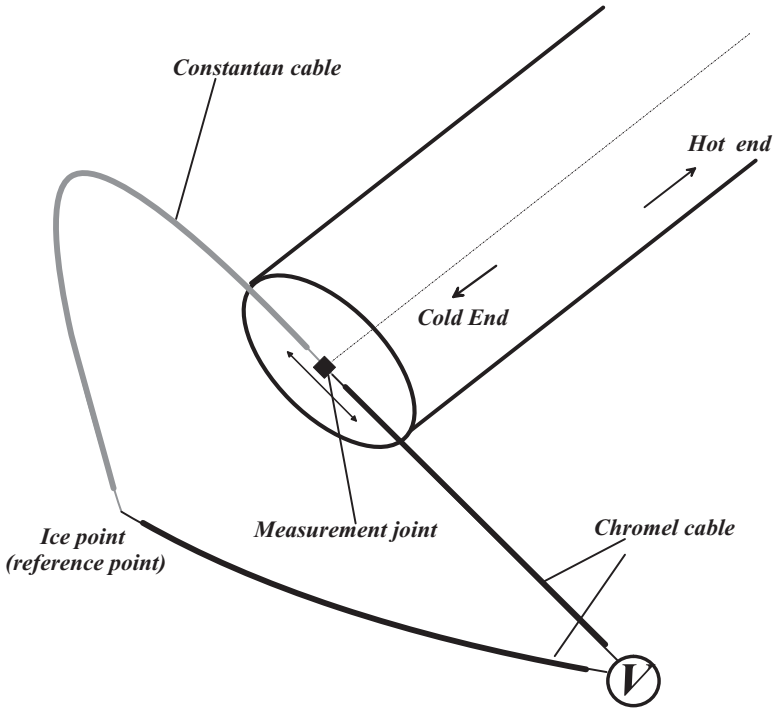

Figure 3.24: *The schematic drawing of the thermocouple applied in the RHVT system.*

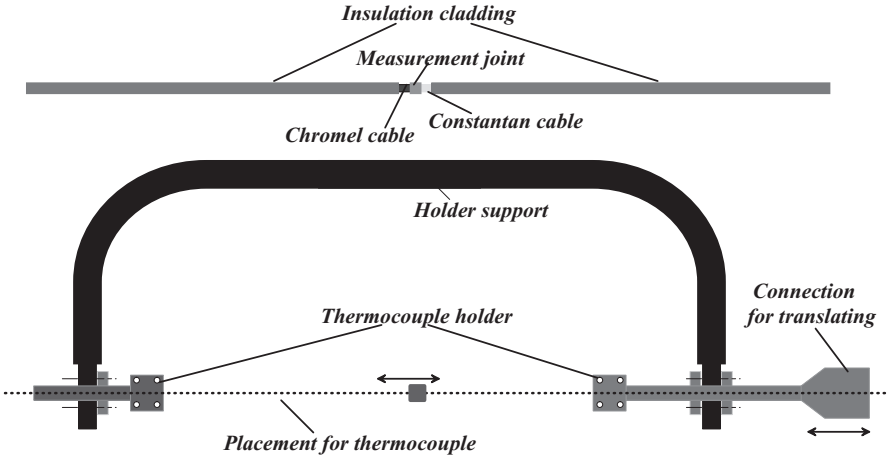

Figure 3.25: *Design of the thermocouple and the holder. With this holder, the thermocouple can be translated along the vortex tube radius precisely.*

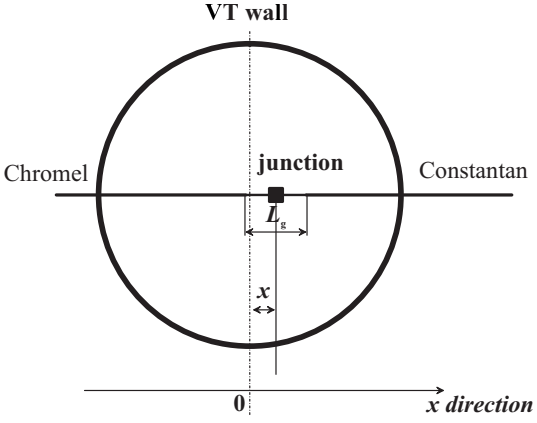

Figure 3.26: *Cross section of the RHVT with a thermocouple. The Chromel and Constantan wires are insulated, except in the measurement gap with length L_g.*

All these measured temperatures are the recovery temperatures. To indicate the stagnation temperature the recovery coefficient and the local velocity are needed. In [23, 24], the recovery coefficient for the thermocouple inside the flow was given as a plot of the Mach number and the Knudsen number

$$K_{\mathrm{n}} = (\pi\gamma/2)^{1/2} M_{\mathrm{a}}/R_{\mathrm{e}}.$$

When the Mach number is less than 1, and the Knudsen number is less than 0.7, the recovery coefficient varies between 0.95 and 1.05. So, taking the recovery temperature as the stagnation temperature is acceptable. In [25], the recovery factor was suggested as 0.85 for laminar flow and about 0.88 for turbulent flow. In this thesis, the recovery factor is taken as 1, i.e. the measured temperature is taken as the stagnation temperature. In this section, the error of the measured temperature is simulated numerically.

3.6.1 Type E thermocouple (THC)

A type E thermocouple is designed and built, which contains a chromel wire and a constantan wire. It is mounted on a saw-like frame which can be mounted on the translation stage, as shown in Fig. 3.24 and 3.25. The chromel and constantan wires are jointed inside a copper-nickel tube with outer diameter of about 0.8 mm and length of about 1 mm, as shown in Fig. 3.25. With this design, the thermocouple can be translated along the radius of the station. Compared with the commercial type E thermocouple, this design is novel and different.

With our novel design, a numerical analysis is used for the accuracy analysis.

3.6.2 Analysis on the THC technique

Fig. 3.26 shows the model for the THC technique analysis; the thermocouple wires are insulated with teflon, which is removed over a length L_{g} (the "gap length", about 5 mm) around the measurement junction, and the measurement joint is made of nickel with the length of about 1 mm. So, during the analysis, the thermocouple is considered based on the heat balance of a wire inside a flow.

As discussed before, the joint temperature, which is the recovery temperature, should be the same as the temperature to be measured. In principle this is the stagnation temperature. So during the measurement, any heat flux through the wires can cause a significant error on the temperature measurement. A brief analysis is made here to estimate the typical uncertainty due to heat transfer.

3.6.2.1 Energy equations for unsteady situation

The unsteady energy equation for a wire with diameter D_{w} and heat conduction coefficient κ_{w}, inserted into a flow, reads (taking the wire as one dimensional)

$$\rho_{\mathrm{w}} c_{\mathrm{w}} \frac{\partial T_{\mathrm{w}}}{\partial t} = \kappa_{\mathrm{w}} \frac{\partial^2 T_{\mathrm{w}}(x)}{\partial x^2} + \frac{4h(x)}{D_{\mathrm{w}}} \left[T_{\mathrm{f}}(x) - T_{\mathrm{w}}(x)\right], \tag{3.53}$$

where ρ_{w} is the wire density, c_{w} is the wire heat capacity, T_{f} is the static temperature of the flow, T_{w} is the wire temperature, h is the heat transfer coefficient and is calculated using the Nusselt number N_{u} (see Eq. 3.20), κ_{w} is the wire heat conductivity coefficient. In Eq. 3.53, the left hand term is the increase of the internal energy and the first and second terms of the right hand give the heat transfer via conduction and convection respectively.

3.6.2.2 Dimensionless groups

To find the dimensionless groups for the analysis of thermocouple, Eq. 3.53 can be considered three times, each time omitting one term. In the following, the material properties ρ_w, κ_w, c_w and D_w as well as the heat transfer coefficient $h(x)$ are taken constant, implying a constant flow velocity V_f and flow temperature T_f.

ⓐ Steady equation

For a steady situation, Eq. 3.53 simplifies to

$$\underbrace{\frac{4h}{D_w}\left[T_f - T_w(x)\right]}_{\text{heat transfer between flow and wire}} + \underbrace{\kappa_w \frac{d^2 T_w(x)}{dx^2}}_{\text{heat conduction in the wire}} = 0. \tag{3.54}$$

The general solution of Eq. 3.54 can be written as

$$T_w(x) = T_f + C_1 e^{ax} + C_2 e^{-ax} \tag{3.55}$$

where

$$a = 2\sqrt{h/\left(D_w \kappa_w\right)},$$

C_1 and C_2 are coefficients that depend on the boundary conditions. In order to simplify the problem, for a wire with length L_w, we assume that the temperatures at $x = 0$ and L_w are the same and equal to the room temperature $T_w(0) = T_w(L_w) = T_r$, and at the middle of the wire $x = L_w/2$, the wire temperature distribution is symmetrical $dT_w/dx|_{x=L_w/2} = 0$, so C_1 and C_2 can be rewritten as

$$C_1 = \frac{T_r - T_f}{1+\exp(aL_w)}$$

$$C_2 = \frac{T_r - T_f}{1+\exp(-aL_w)}.$$

Eq. (3.55) and coefficients C_1 and C_2 suggest that a good dimensionless group to characterize the problem is aL, with L a typical length scale of the configuration.

For the thermocouple wire with insulation, stripped around the measurement junction, an appropriate length scale is the gap length $L_g = L_w$. For good measurement conditions, aL_g should be large; this will cause the measurement junction temperature T_w to approach the flow temperature T_f

$$aL_g = 2\sqrt{\frac{h}{D_w \kappa_w}} L_g \gg 1. \tag{3.56}$$

ⓑ No heat conduction

The assumption is that the Fourier number $F_o \ll 1$

$$\frac{\kappa_w}{\rho_w c_w}\frac{t_c}{L^2} \ll 1,$$

the heat conduction term in Eq. 3.53 can be neglected. Then Eq. 3.53 becomes

$$\rho_w c_w \frac{\partial T_w}{\partial t} - \frac{4h}{D_w}\left[T_f(x) - T_w(x)\right] = 0. \tag{3.57}$$

Assuming a periodic flow temperature $T_\mathrm{f} = T_0 \exp(\mathrm{i}\omega t)$ with frequency ω and a corresponding solution $T_\mathrm{w} = T_1(x) \exp(\mathrm{i}\omega t)$, the following expression is found for the frequency response of the amplitude

$$\mathrm{Re}(\frac{T_1}{T_0}) = \frac{1}{1+(\omega\tau)^2} \tag{3.58}$$

where the characteristic time

$$\tau = \frac{D_\mathrm{w}\rho_\mathrm{w}c_\mathrm{w}}{4h}$$

is introduced. The phase shift of T_w with respect to T_f is given by the imaginary part of T_1/T_0, which is following

$$\mathrm{Im}(\frac{T_1}{T_0}) = \frac{\omega\tau}{1+(\omega\tau)^2}\,. \tag{3.59}$$

A dimensionless group, arising from Eqs. 3.58 and 3.59, is $\omega\tau$. If the wire temperature T_w follows the flow temperature T_f, it is required that the phase shift between these two temperature should be small, which means that $\omega\tau$ should be small

$$\omega\tau = \frac{\omega D_\mathrm{w}\rho_\mathrm{w}c_\mathrm{w}}{4h} \ll 1. \tag{3.60}$$

ⓒ No heat transfer with the surroundings

In case of an insulated cylinder, Eq. 3.53 can be rewritten as

$$\rho_\mathrm{w}c_\mathrm{w}\frac{\partial T_\mathrm{w}}{\partial t} = \kappa_\mathrm{w}\frac{\partial^2 T_\mathrm{w}(x)}{\partial x^2}. \tag{3.61}$$

In [26], a periodic solution of Eq. 3.61 is

$$T_w(x,t) = A(x)\sin(\omega t + \phi(x,t))\,. \tag{3.62}$$

Again, the phase shift ϕ is not of interest here. The amplitude A is given in [26] as

$$A^2 = \frac{\cosh 2kx - \cos 2kx}{\cosh 2kL_\mathrm{w} - \cos 2kL_\mathrm{w}}, \tag{3.63}$$

where L_w is the length of the wire and $k = (\rho_\mathrm{w}c_\mathrm{w}\omega/(2\kappa_\mathrm{w}))^{1/2}$ is introduced. Eq. (3.63) corresponds to the problem of a perfectly insulated wire, kept at $T = 0$ at $x = 0$ and forced to a periodic temperature $T = \sin(\omega t)$ at $x = L_\mathrm{w}$. The length k^{-1} can be regarded as the typical propagation length of the imposed wave $\sin(\omega t)$ due to conduction in the wire. This leads to the third dimensionless group in the unsteady heat conduction/transfer problem:

$$kL_\mathrm{w} = \sqrt{\frac{\rho_\mathrm{w}c_\mathrm{w}\omega}{2\kappa_\mathrm{w}}}\cdot L_\mathrm{w} = \sqrt{\frac{1}{2F_\mathrm{o}}}. \tag{3.64}$$

Summarizing, the three dimensionless groups defined previously can be related to the following physical quantities:

1. aL_g: heat transfer / heat conduction. A large aL_g means that heat conduction through the wire can be neglected: the wire temperature equals the flow temperature.

2. $\omega\tau$: oscillation / heat transfer. A small $\omega\tau$ implies that the heat transfer is effective: oscillations in the flow temperature are "picked up" by the wire.

3. kL_w: oscillation / conduction. If kL_w is small, conduction causes an oscillation at one end to "propagate" through the wire.

Note that the following holds for the dimensionless groups aL_g (3.56), $\omega\tau$ (3.60) and kL_w (3.64):

$$\left(\frac{kL_\mathrm{w}}{aL_\mathrm{g}}\right)^2 = \frac{1}{2}\omega\tau, \tag{3.65}$$

which implies that only two numbers can be chosen, the third follows from eq. (3.65). More detailed analysis on the parameters and their influence on the temperature errors can be found in report [27].

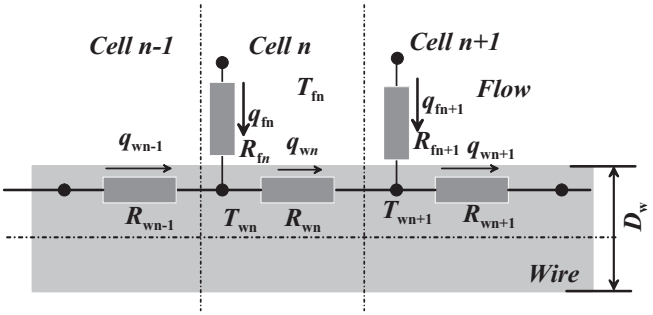

Figure 3.27: *Network model for the heat transfer from a flow to a wire with the grids. The gray part is the wire. The heat is transferred from gas to the wire via these grids and conducted axially through the wire.*

3.6.2.3 Numerical solution for steady case

A numerical method has been developed for the analysis of the steady case for which the wire is divided into N cells. For each cell, Eq. 3.54 must hold, which can be expressed by a network system shown in Fig. 3.27 for one cell. This simple system will first be tested to check if the result of the numerical method corresponds to the analytical result Eq. 3.55. For cell n, the following set of equations can be written

$$T_{\mathrm{f}n} - T_{\mathrm{w}n} = q_{\mathrm{f}n} R_{\mathrm{f}n} \tag{3.66a}$$
$$T_{\mathrm{w}n-1} - T_{\mathrm{w}n} = q_{\mathrm{w}n-1} R_{\mathrm{w}n-1} \tag{3.66b}$$
$$T_{\mathrm{w}n} - T_{\mathrm{w}n+1} = q_{\mathrm{w}n} R_{\mathrm{w}n} \tag{3.66c}$$
$$q_{\mathrm{w}n} = q_{\mathrm{f}n} + q_{\mathrm{w}n-1} \tag{3.66d}$$

where q denotes the heat flux (in W). The resistances R (K/W) are defined by

$$\begin{aligned} R_{\mathrm{f}n} &= \tfrac{1}{hA_{\mathrm{f}n}} = \tfrac{N}{L}\tfrac{1}{\pi h D_\mathrm{w}} \\ R_{\mathrm{w}n} &= \tfrac{l_n}{\kappa_{\mathrm{w}n} A_{\mathrm{w}n}} = \tfrac{L}{N}\tfrac{4}{\pi\kappa D_\mathrm{w}^2} \end{aligned} \tag{3.67}$$

where $A_{\mathrm{f}n}$ is the contacting surface area between the fluid and the wire in cell n, $A_{\mathrm{w}n}$ is the cross section area of the wire in cell n, L is the wire length, $R_{\mathrm{f}n}$ is the heat transfer resistance from the flow to the wire via their contacting surface in cell n and $R_{\mathrm{w}n}$ is the heat conduction resistance from the cell n to $n+1$.

Using energy conservation within each cell n, a set of N linear equations is deduced of the following form

$$\overrightarrow{\overrightarrow{A}}\overrightarrow{T_{\mathrm{w}}} = \overrightarrow{T_{\mathrm{f}}}, \tag{3.68}$$

where $\overrightarrow{T_{\mathrm{w}}}$ and $\overrightarrow{T_{\mathrm{f}}}$ are N-dimensional vectors representing the wire temperature and the flow temperature, respectively, and $\overrightarrow{\overrightarrow{A}}$ is an $N \times N$ band matrix. When the flow temperature $\overrightarrow{T_{\mathrm{f}}}$ and the boundary conditions are given, the wire temperature $\overrightarrow{T_{\mathrm{w}}}$ can be determined by solving the above matrix equation.

3.6.2.4 Comparison the analytic and numerical solutions

The result of a numerical calculation is shown in Fig. 3.28, where the analytical solution, using the same parameters, is included. The data for the calculations are shown in table 3.2.

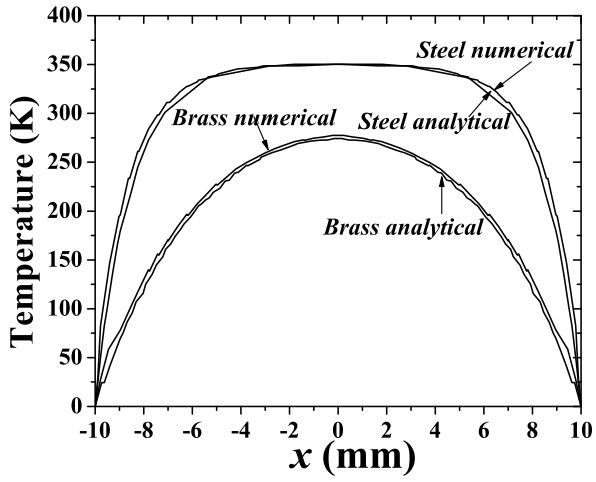

Figure 3.28: *Comparison of analytical and numerical solution to the simple case of the heat transfer problem with steel and brass wires.*

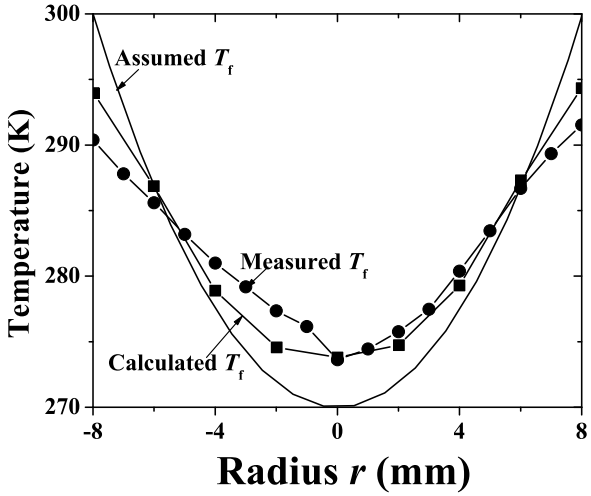

Figure 3.29: *Result of the numerical method applied to a typical situation in the vortex tube.*

input		flow numbers	
V	200 m/s	R_{e}	12484
T_{f}	400 K	P_{r}	0.715
T_{ref}	300 K	N_{u}	57.4
μ	$18.6 \cdot 10^{-6}$ Pa s	h	1504 $\mathrm{W\,m^{-2}\,K^{-1}}$
c_{g}	1007 $\mathrm{J\,kg^{-1}\,K^{-1}}$		
κ_{g}	$26.2 \cdot 10^{-3}$ $\mathrm{W\,m^{-1}\,K^{-1}}$	thermal conductivity	
ρ_{g}	1.161 $\mathrm{kg\,m^{-3}}$	steel κ_{w}	13 W/Km
L_{w}	0.02 m	brass κ_{w}	125 W/Km
D_{w}	0.001 m		

Table 3.2: Parameters for the calculation of the simple system.

The agreement between the analytical and numerical solution is good; the slightly higher result by the numerical approach can be traced back to the implementation of the boundary condition: due to the finite length of a grid cell, the boundary conditions are located half a cell length outside the real boundary.

3.6.2.5 Application on the estimation of the thermocouple measurement

To obtain an indication of the error that can be expected in a thermocouple measurement, the above numerical model is used with parabolic profiles for both the flow velocity $V_\mathrm{f}(x)$ and flow temperature $T_\mathrm{f}(x)$, roughly corresponding to the profiles measured with the Pitot tube and the thermocouple (in Chapter 4). As a boundary condition for the wire, 300 K is chosen well outside the vortex tube (10 mm), to account for the region outside the vortex tube where almost no heat transfer takes place. The position of the thermocouple junction is varied from one vortex tube wall $x = -8$ mm to the opposite wall $x = 8$ mm. The result of the calculations is shown in Fig. 3.29, consisting of 9 calculated values for the expected temperature readings.

Because the heat conduction coefficients for Chromel and Constantan are very close to each other, the calculated temperature profile is practically symmetric.

The maximum difference between the assumed flow temperature T_f and the temperature that would be indicated by the thermocouple is ~ 5 K, and the relative error on the absolute temperature is less than 2%. Compared with the literature, the maximum error of the thermocouple is taken as 2% and considered acceptable for our purpose.

More detailed information about the analysis on this numerical simulation model and the simulation for the thermocouple can be found from the report [27].

3.7 Summary

In this chapter, the calibrations on the CPT and the SPHWA techniques are explained in detail. It has been found that the measured Mach number with the CPT has a maximum error of about 15%. Inserting of the CPT may affect the flow field inside the RHVT and introduce errors. With the SPHWA technique, the variable ρV_e has an error of about 5%. The turbulence parameters can also be obtained with the SPHWA. The disadvantage of the SPHWA technique is that the results depend on the local density ρ which could not be measured by SPHWA directly. The density ρ is calculated based on the static pressure from the CPT and the static temperature from the THC. A numerical model for indicating the accuracy of the thermocouple is introduced. With the numerical model, it is found that the maximum temperature error for the specified measurement is taken as 5%. In the literature, a recovery factor of 95% or 88% is recommended, which means the error is about 5% or even more. So it is acceptable to take the measured temperature as the stagnation temperature.

References

[1] E. Ower and R.C. Pankhurst. *The measurement of air flow.* Pergamon Press, the 4th edition, 1966.

[2] D.W. Bryer and R.C. Pankhurst. *Pressure-probe methods for determining wind speed and flow direction.* Her Majesty's Stationery Office, London, 1971.

[3] B. Ahlborn and S. Groves. Secondary flow in a vortex tube. *Fluid Dynamics Research*, 21:73–86, 1997.

[4] C.M. GAO, J.C.H. Zeegers, K.J. Bosschaart, and A.T.A.M. de Waele. The calibration for a cylinder type pitot tube technique. In *ICEC Int. Crygenic Engineering Conference: Proceedings 20th*, Beijing China, May 2004.

[5] R.D. Cooper and M.P. Tulin. *Turbulence measurements with the Hot-wire anemometry.* North Atlantic Treaty Organization Advisory Group for Aeronautical Research and Development, Paris, August 1955.

[6] P. Bradshaw. *An introduction to trubulence and its measurement.* Pergamon Press, 2nd edition, 1985.

[7] H.H. Bruun. *Hot-Wire Anemomtery: Principles and Signal Analysis.* Oxford University Press, University of Bradford, 1995.

[8] R. Johnston and S. Fleeter. Compressible flow Hot-Wire calibration. *Experiments in Fluids*, 22:444–446, 1997.

[9] A.J. Reynolds. A note on vortex-tube flow. *J. Fluid Mech.*, 14:18–20, 1962.

[10] H. Takahama. Studies on vortex tubes (1) experiments on efficiency of energy separation (2) on profiles of velocity and temperature. *Bulletin of JSME*, 8(31):433–440, 1965.

[11] C.M. GAO, K.J. Bosschaart, J.C.H. Zeegers, and A.T.A.M. de Waele. Experimental study on a simple Ranque-Hilsch vortex tube. *Cryogenics*, 45(3):173, 2005.

[12] J.E. Lay. An experimental and analytical study of vortex-flow temperature separation by superposition of spiral and axial flow, part I. *Trans. ASME J. Heat Transfer*, 81:202–212, Aug. 1959.

[13] S.H. Chue. Pressure probes for fluid measurement. *Prog. Aerospace Sci.*, 16:147–223, 1975.

[14] T.G. Beckwith, R.D. Marangoni, and J.H. Lienhard V. *Mechanical measurements.* Addison-Wesley Publishing Company, 5th edition, 1993.

[15] C.W. Hubbard and W. Mass. Investigation of errors of pitot tubes. *Trans. ASME*, 61:477–506, 1939.

[16] H. Kramers. Heat transfer from spheres to flowing media. *Physica*, 12:61, 1946.

[17] C. Croarkin and P. Tobias, editors. *e-Handbook of Statistical Methods.* Statistical Engineering Division, NIST, http://www.nist.gov/stat.handbook/.

[18] *MATLAB User Guide: Function Reference*, volume 1. The MathWorks, Inc., 1984.

[19] C.Gao, J.C.H. Zeegers, and W. van de Water. Private communication, Sept. 2004.

[20] M. Kurosaka. Acoustic streaming in swirling flow and the Ranque-Hilsch (vortex-tube) effect. *J. Fluid Mech.*, 124:139–172, 1982.

[21] J.G. Chu. *Acoustic streaming as a mechanism of the Ranque-Hilsch effect.* PhD dissertation, University of Tennessee, Knoxville, Dec. 1982.

[22] H. Kuroda. *An experimental study of temperature separation in swirling flow.* PhD dissertation, University of Tennessee, Knoxville, Dec. 1983.

[23] A. Hirschberg. Totale temperatuur en snelheidsmetingen aan een aangepaste sonische vrije straal. Master thesis, Delft University of Technology, Delft, the Netherlands, October 1975.

[24] A. Hirschberg and J.C. van Muiswinkel. A correlation of recovery temperature data for cylinders in a compressible flow at high Reynolds numbers. *International Journal of heat and mass transfer*, 20(6):669–674, 1977.

[25] H. Schlichting. *Boundary layer theory, Chapter XV.* Mc Graw Hill series in mechanical engineering. Mc Graw Hill Book Co. Inc., 4th edition, 1958.

[26] H.S. Carslaw and J.C. Jaeger. *Conduction of Heat in Solids.* Clarenton Press, Oxford, UK, 1st edition, 1959.

[27] K.J. Bosschaart. Thermocouple wire analysis. Internal report, Eindhoven University of Technology, Eindhoven, the Netherlands, March 2003.

Chapter 4

Investigation on a small RHVT and comparison with other work

4.1 Introduction

To understand the cooling mechanism of this device, it is necessary to know the pressure, temperature, and velocity distributions inside the tube. In order to get a first impression of the RHVT system, a small RHVT system was built and investigated based on the two measurement techniques CPT and THC discussed in Chapter 3. The present results was compared with the work of others. At the end, the efficiencies of the present set-up were investigated, which showed that the thermal processes for the energy separation inside the RHVT is highly irreversible.

4.2 Investigation on a small RHVT system

In this section, the experimental setup and the results obtained with it are introduced.

4.2.1 Experimental setup—small RHVT system

Fig. 4.1 shows the RHVT schematically. It consists of the following components: *(a)* an input nozzle, *(b)* a vortex chamber (30 mm inner diameter, 11 mm length), *(c)* a tube (inner diameter 16 mm, length 205 mm), *(d)* a control valve at the hot-end, and *(e)* a cold-end plate with a hole of diameter 4 mm in the center. The details of the present set-up and those of other researches are given in Table 4.1. All components are made of brass except the cold-end plate that is made of phenol fabric for reducing the heat conduction. There is one measurement port in the vortex chamber and there are 8 along the tube. The influence of the tube entrance condition on the performance has never been investigated before. In order to study this influence, the entrance was smoothed with $R_{\mathrm{sm}} = 0.0$ mm, $R_{\mathrm{sm}} = 1.5$ mm and $R_{\mathrm{sm}} = 3.0$ mm respectively, shown in Fig.4.2. The results from different entrance conditions will be compared.

Fig. 4.3 shows the overall view of the experimental setup. A regulator is used to control the input pressure of the nitrogen. The fractions of the separated flow are controlled by the valve V. The total flow and the cold flow are both measured with flow meters. A heat

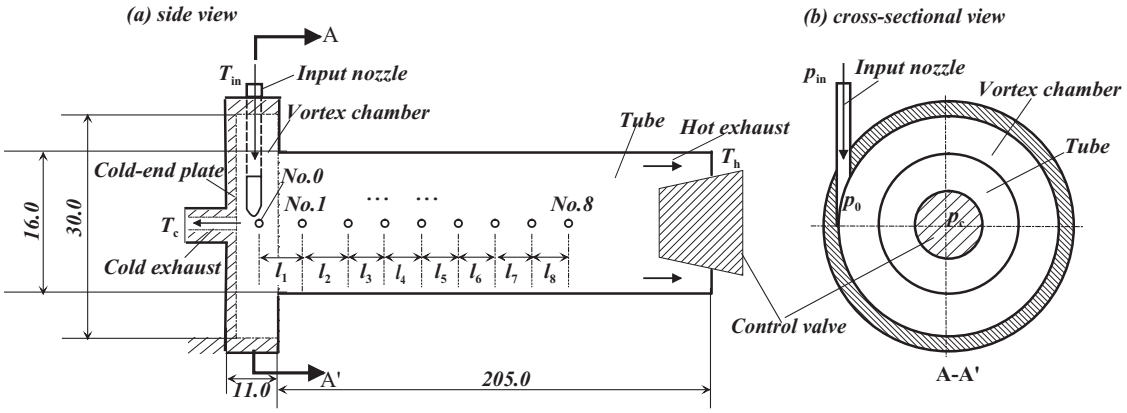

Figure 4.1: *Schematic drawing of RHVT. Compressed gas is tangentially injected in the vortex chamber, hot and cold gas exhaust at the right and left sides respectively.* p_{in} *is the inlet static pressure of the gas,* p_0 *is the static pressure at the exhaust of the inlet nozzle,* p_{c} *is the static pressure at the center* $r = 0$ *of the vortex chamber.* $No.0$ *hole is placed in the middle of the vortex chamber.* $l_1 = 23.5$, $l_2 = 24.0$, $l_3 = l_4 = ... = l_8 = 20.0$, *Unit: mm.*

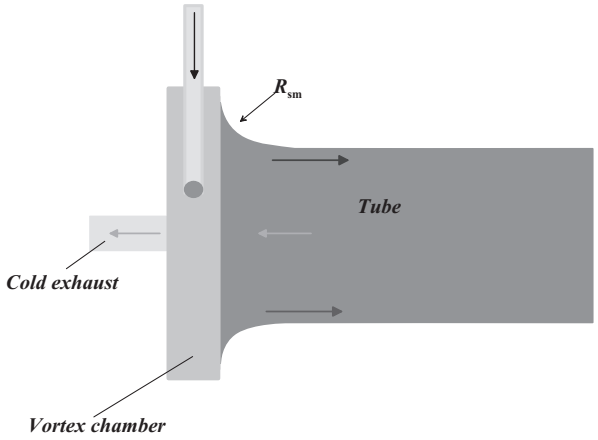

Figure 4.2: *Schematic drawing of the tube's entrance inside the vortex chamber. Different values for* R_{sm} *are taken:* 0.0, 1.5 *or* 3.0 *mm, and expressed as* $R_{\mathrm{sm}}/R_{\mathrm{vt}}$*:* $0.0, 0.188, 0.375$.

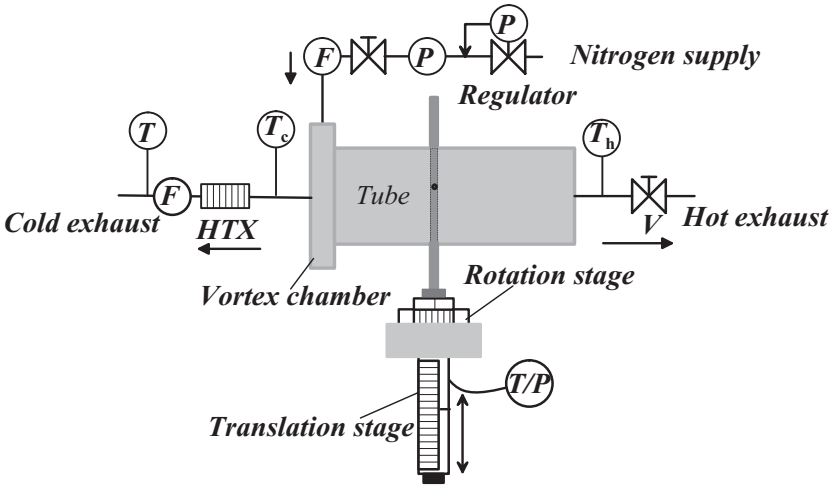

Figure 4.3: *Overview of the experimental setup and the translation and rotation stage. With the translation and rotation stages, CPT measurement hole can be translated along the capillary's axis within a range of 150 mm and rotated within a range of* 360 *deg at a certain position. The arrows show the flow directions.*

exchanger HTX is installed at the cold end to warm up the cold flow before it enters the flow meter. The hot and cold exhaust temperatures are measured with PT100 sensors.

The Cylinder Type Pitot Tube (CPT) developed for the measurements of the pressure and velocity in the RHVT is mounted on a translation and rotation stage (see Fig. 4.3, described in Section 3.2.1).

4.2.2 Pressure measured by CPT and velocity distributions inside the small RHVT

During the experiments, the input pressure p_{in} of the nitrogen is kept constant at 6.5 bar. The valve V at the hot end is kept at a fixed setting. This results in constant operating conditions and comparable results for the three inlet entrance configurations presented in Fig. 4.2. The measured pressures and temperatures will be described and analyzed in the subsequent subsections.

4.2.2.1 Pressure measured by CPT

Typical angle-dependent pressure distributions measured by CPT are shown in Fig. 4.4, which are the results at Station 1 for the case where the entrance to the vortex tube was sharp, i.e. $R_{\text{sm}} = 0$ mm. The angle here is defined by the position of the hole in the wall of CPT (Fig. 3.6 (b)). During the investigation, the set-up is mounted as shown in Fig. 4.3, cold exhaust at the left-hand side and hot exhaust at right-hand side, and set-up is horizontal, when the hole is vertical up, the angle is defined as zero. There is a maximum pressure which is the stagnation pressure, two similar minimum pressures, and a base pressure in every curve. The two minimum pressures are located symmetrically mirrored to the location of the maximum. The angle difference between the minimum and maximum is about 90^0. When the CPT translates along its axis, the pressure distribution at the different positions have a similar shape, but the peak value and the angle at which the maximum pressure occurs are different. The angle at which the pressure is maximal always faces the flow direction. So the shift of the angle shows us the change in direction of the local gas flow. This is important as it is a measure for the flow in the axial direction. The shifts are relatively small, as shown in Fig. 4.4 by the dash-dot line. When the angle for the maximum pressure is 0^0 or 180^0, the gas has only a azimuthal velocity component. The pressure distributions measured at the other stations and cases are very similar to those in Fig. 4.4.

The calibration of CPT has been discussed in Section 3.3. The static pressure is determined by a so-called static pressure angle α via the measured angle-dependent pressure profile. The velocity inside the VT is three-dimensional, however, in most studies [1, 2] the radial component is noted as only about 1% of the total velocity and is not an essential part [1]. The CPT can only determine two-dimensional flow as mentioned in Chapter 3. The velocity normal to the axis of CPT, consisting of the azimuthal and axial components, can be measured with CPT. The velocity and its components can be written as

$$\begin{cases} M_{\text{a}} = \sqrt{\frac{1}{\Gamma_2}[(\frac{p_{\text{sg}}}{p_{\text{st}}})^{\Gamma} - 1]}/f_{\text{c}} \\ M_{\text{a,az}} = M_{\text{a}} \cos\alpha \\ M_{\text{a,ax}} = M_{\text{a}} \sin\alpha \end{cases} \tag{4.1}$$

[1] In Chapter 6, the radial velocity component inside the RHVT is measured and analyzed. It shows that the radial velocity component occurs in the center region, in the peripheral region the radial component is zero.

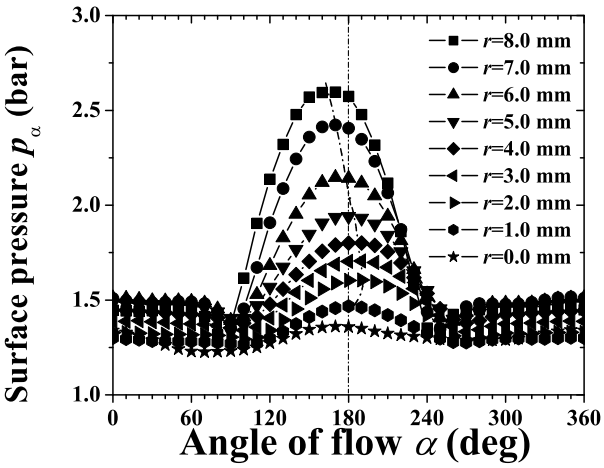

Figure 4.4: *Typical angle-dependent pressure distributions by the CPT. The results at Station 1 inside the vortex tube near the entrance for case* $R_{\rm sm} = 0.0$ *mm at cold fraction* $\varepsilon = 0.27$. *The numbers from 0 to 8 are the measurement positions in mm, which take one-half of the diameter. The dash-dot line shows the maximum pressures which is defined as stagnation pressure and shows the flow direction as well. In the center of the tube, the maximum measured pressure is not as distinct as that in other positions, so the flow direction is not easy to determine. The measurement angle error is less than* 5^0.

where $M_{\rm a}$ is the Mach number; p is pressure; $f_{\rm c}$ is a calibration parameter (defined by Eq. 3.7); α is the angle at the stagnation pressure as shown in Fig. 3.12 in the Chapter 3, γ is the ratio of specific heat capacities, which for nitrogen is 1.40, and Γ is defined in Chapter 2. The subscripts "sg" means stagnation, "st" means static; "az" means azimuthal component and "ax" means axial component. According to the calibration, the velocity calculated using Eq. 4.1 has an error less than 15% (see Section 3.3.5).

4.2.2.2 Flow direction inside the RHVT system

From the measured pressure distributions, the flow directions inside the vortex tube are determined. The results are shown in Fig. 4.5. If the angle is zero, the axial gas velocity is zero. At stations 1 and 2, the gas flow consists of two regions. *1)* At the periphery, in an annular region from the wall to some critical radius $r_{\rm c}$, the gas flows to the hot end, flow angle positive. *2)* In the central region, the gas flows towards the cold end, flow angle negative.

At Station 1 its angle seems to lead to zero again. We believe that this may be an indication of a secondary reverse flow in the core. For the sharp entrance case i.e. $R_{\rm sm} = 0$ mm, there is one point at $r = 0$ where the angle is positive (about 10^0), which can be due to measurement errors. The small reverse flow region in the sharp entrance case i.e. $R_{\rm sm} = 0$ mm is more clear than for the other two cases. The critical radius at which the axial flow reverses is similar for all three cases, decreases when the station moves to the hot end. At Station 1 it is 5 mm, at Station 2 is 4.5 mm. The maximum measurement error of the angle is 5^0.

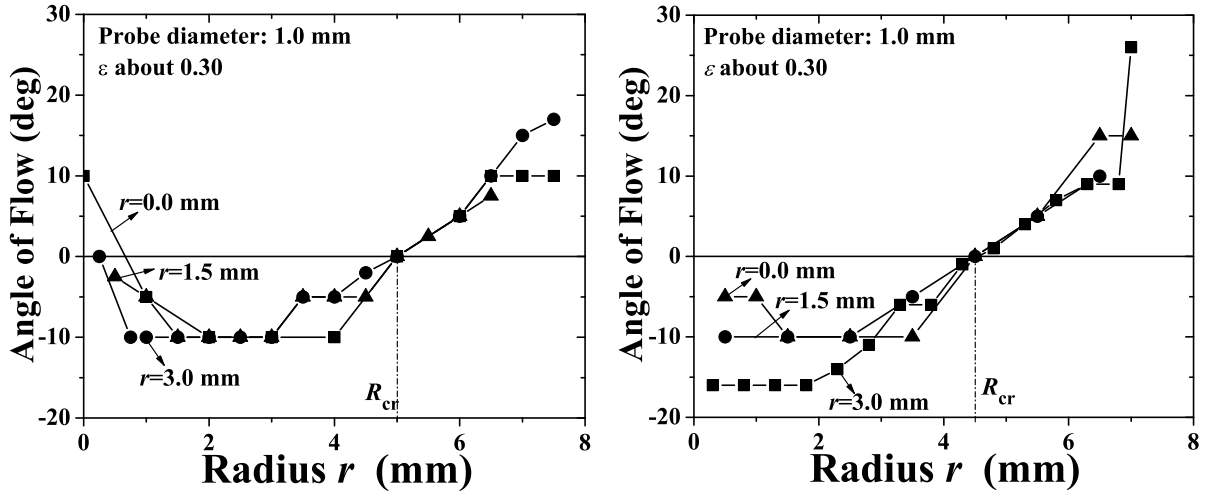

(a) Station 1 *(b) Station 2*

Figure 4.5: *Comparison of the flow directions. The positive angle means gas flows to the hot end, the negative angle means gas flows to the cold end. The wall is at* $r = 8$ *mm.*

4.2.2.3 Velocity distributions

Using Eq. 4.1, the azimuthal and axial flow Mach numbers ($M_{\mathrm{a,az}}$ and $M_{\mathrm{a,ax}}$) are calculated, and shown in Fig. 4.6. At Station 1, the axial Mach number $M_{\mathrm{a,ax}}$ varies between -0.1 and $+0.2$. For the three cases, $M_{\mathrm{a,ax}}$ are similar. Near the center, the part of the gas that flows towards the hot side has an axial Mach number of about 0.05. $M_{\mathrm{a,az}}$ for case $R_{\mathrm{sm}} = 0$ mm varies from about 0.2 to 0.5, but for cases $R_{\mathrm{sm}} = 1.5$ mm and $R_{\mathrm{sm}} = 3.0$ mm it increases from about 0.2 at the center to 0.85 near the wall.

At Station 2 Fig. 4.6 (b), $M_{\mathrm{a,ax}}$ varies between -0.15 and $+0.15$, and in the peripheral region the axial Mach number profiles are very similar for the three cases, however, in the central region, $M_{\mathrm{a,ax}}$ for case $R_{\mathrm{sm}} = 3.0$ mm is larger than that for case $R_{\mathrm{sm}} = 0$ mm and $R_{\mathrm{sm}} = 1.5$ mm, as well as the azimuthal speed. $M_{\mathrm{a,az}}$ distributions at Station 2 for cases $R_{\mathrm{sm}} = 1.5$ mm and $R_{\mathrm{sm}} = 3.0$ mm vary from 0.3 near the center to 0.55 near the wall; for case $R_{\mathrm{sm}} = 0$ mm, it varies from 0.25 near the center to 0.45 near the wall.

Surprisingly, a non-zero azimuthal velocity component is found at the center for all measurements. This might be caused by the asymmetrical inlet nozzle and the wobbling of the vortex core. It is found that rounding off the entrance can increase the axial and azimuthal speeds inside the RHVT system.

4.2.3 Temperature measurements inside the small RHVT

A Chromel-Constantan thermocouple (THC) with a 0.8 mm diameter wire was used to measure the recovery temperature T_{r} at different radius along the cross section. Normally, the recovery coefficient is about 0.95 [3–5] when the Mach number is less than 1 and the Knudsen K_{n} is less than 0.2. So the measured recovery temperature can be taken as the stagnation temperature T_{sg}. The design of the thermocouple has been explained in Section 3.6. The hot and cold end exhaust temperatures are measured by the installed thermal resistors PT100.

The static temperature T_{st} can be calculated from the stagnation temperature and Mach

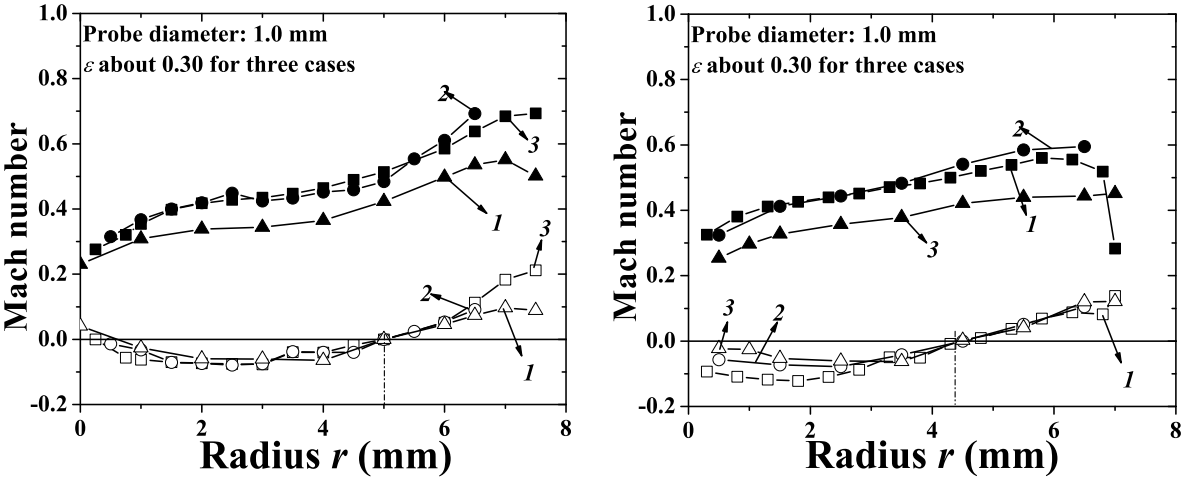

(a) Station 1 *(b) Station 2*

Figure 4.6: *Comparison of the Mach number components. The solid symbols show the azimuthal Mach number, and the open symbols show the axial Mach number. "1" is for the sharp entrance case i.e.* $R_{\rm sm} = 0$ *mm, "2" for the case smoothed with* $R_{\rm sm} = 1.5$ *mm and "3" for the case smoothed with* $R_{\rm sm} = 3.0$ *mm.*

number at the same location, using the following equation [1, 2]

$$T_{\rm st} = \frac{T_{\rm sg}}{1 + \Gamma_2 M_{\rm a}^2}. \tag{4.2}$$

4.2.3.1 The recovery temperature distributions in the sharp entrance Case $R_{\rm sm} = 0$ mm

Fig. 4.7 (a) shows the measured recovery temperature distributions at stations 1, 2, 5 and 8. The temperature difference between the center and the region near the wall at station 1 is about 23 K, about 16 K at station 2, 13 K at station 5 and 10.5 K at the last station near the hot exhaust. There is a strong radius dependence. Fig. 4.7 (a) also shows that the temperature at the center of station 1 measured is about 2.5 K lower than the measured cold exhaust temperature. The temperature near the wall at the last station near the hot exhaust measured by THC is about 3.5 K higher than the hot exhaust temperature measured by thermal resistance PT100. The recovery temperature distributions for all four stations are symmetric except the one at station 5. The asymmetric distribution along station 5 is not expected and the reason may be due to the shift of the reference position. If the center position shifts to the left side about 1.5 mm, the plot is symmetric as well, see the dashed curve in Fig. 4.7 (a). Because of the mixing and averaging effect, the exhaust temperature is only an average temperature, so the temperature near the wall at the hot side is higher than the hot exhaust temperature and the temperature at the center at the cold side is lower than the cold exhaust temperature.

4.2.3.2 The calculated static temperature distributions in Case $R = 0$ mm

The static temperature profiles shown in Fig. 4.7 (b) are calculated with Eq. 4.2. At Stations 1 and 2, they are calculated based on the measured Mach numbers. The static temperature

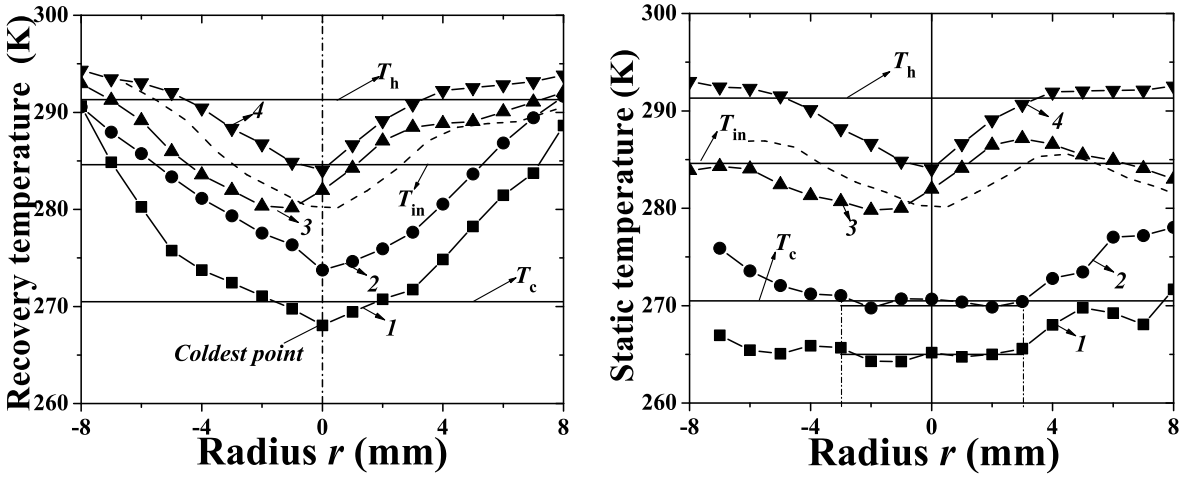

(a) Recovery temperature distributions *(b) Static temperature distributions*

Figure 4.7: *Radius dependent temperature distribution inside the RHVT. "1": station 1 close to the chamber; "2": station 2; "3": station 5 and "4" station 8 close to the hot exhaust.*

distributions in the central region for Stations 1 and 2 are constant. The static temperature increases at radii larger than 3 mm. The static temperature near the wall for both Stations is about 5 K higher than that at the center. The stagnation temperature in the central region of Station 1 is 2.5 K lower than the cold exhaust temperature. After passing the inlet nozzle, the gas experiences a partly reversible expansion and reaches the lowest temperature inside the vortex tube, after which the gas temperature increases because of the heat exchange and turbulent mixing between different gas layers; see also Ahlborn [6, 7], Gutsol [8] and Bejan [9]. Unfortunately, the velocity profiles at Stations 5 and 8 were not measured. Therefore, the static temperature profiles for these two stations are calculated based on the assumption of solid-body rotation: the maximum Mach number near the wall 0.5 and 0.15, respectively. The values of these maximum Mach numbers are based on the maximum Mach number at Station 1 and 2 with linear distribution assumption over the tube in the peripheral region. The static temperature for Station 5 is non-symmetric, while shifting the center position, the dashed curve shows the symmetric results. Both calculated static temperature profiles at Stations 5 and 8 show that in the peripheral region ($4 < r < 8$), the static temperature is very flat.

4.3 Comparison of present results with results of others

In this section, we compare our results with the results by Takahama [1], Reynolds [10, 11] and Ahlborn [12] who have used similar measuring techniques. Their system parameters are shown in table. 4.1, where D_{vt} is the inner diameter of the tube, L_{vt} the inner length of the tube; D_{n} and N are the inner diameter and the number of the tangential nozzles, respectively, D_{n} for Reynolds' work is the equivalent diameter because he used tangential slots instead of circular nozzles; D_{pt} and D_{mh} are the out diameter of the Pitot tube and the diameter of the measurement hole respectively; Z/D_{vt} is the distance from the measured station to the inlet nozzle divided by the tube diameter. It is not possible to make a unique comparison as all Z/D_{vt} differ.

Author	D_{vt}	L_{vt}	Nozzle		D_c	Pitot tube		ε	Z/D_{vt}	p_{in}
			D_n	N		D_{pt}	D_{mh}	$(\dot{m}_c/\dot{m}_{in})$		(bar)
Takahama [1]	52.8	7920	10.91	4	–	3	–	0.5	0.5; 5.5	–
Reynolds [10, 11]	76.2	1219.2	2.84	8	31.75	1.6	0.25	–	1.5; 6.0	2.35
Ahlborn [12]	25.4	608	–	–	8.2	1.6	0.3	0;1	0.18	2.38
This work	16	205	3	1	4	1	0.1	0.27; 0.32; 0.33	1.47; 2.97	6.5

Table 4.1: *Dimensional work conditions used by different researchers.(length unit: mm; and "–" means that the parameter is not known.)*

4.3.1 Dimensionless properties

Considering Takahama's [1] work, only the dimensionless results can be found, in order to be comparable, dimensionless properties are also used in this work and the definition of these properties are based on [1].

The dimensionless azimuthal and axial velocity are defined as [1]

$$\begin{aligned} \hat{V}_{az} &= \frac{V_{az}}{\max(V_{az})} \\ \hat{V}_{ax} &= \frac{V_{ax}}{\max(V_{az})} \end{aligned} \tag{4.3}$$

where V_{az} is the azimuthal velocity, V_{ax} is the axial velocity, and $\max(V_{az})$ is the maximum azimuthal velocity at the same station.

The dimensionless recovery and static temperatures are defined as [1]

$$\begin{aligned} \hat{T}_{r,sg} &= \frac{T_r - T_w}{V_{max}^2/(2c_p)} \\ \hat{T}_{r,st} &= \frac{T_{r,st} - T_{st}}{V_{max}^2/(2c_p)} \end{aligned} \tag{4.4}$$

where the subscript r is the radius and w means near the wall, V_{max} is the maximum absolute value of the total velocity measured at the same station. The dimensionless radius is taken as

$$\hat{r} = \frac{2r}{D_{vt}}. \tag{4.5}$$

4.3.2 Comparison of Results

4.3.2.1 The comparison of the geometrical parameters

As mentioned in [1, 2, 12, 13], the important geometrical parameters are: the ratio: L_{vt}/D_{vt}, the ratio of the total inlet nozzle area A_{in} over the vortex tube cross sectional area A_{vt}: $\tau_A = A_{in}/A_{vt}$, the ratio of the cold exhaust diameter over the vortex tube diameter D_c/D_{vt} and the number of nozzles N and the blockage effects (the blockage effect is calculated based on the ratio of the CPT cross section over the flow cross sectional area $(4D_{pt}/(\pi D_{vt}))$). The main reasons for the difference in results obtained by the various authors may be due to the differences between these parameters, which are listed in Table 4.2.

4.3.2.2 Dimensionless velocity

Fig. 4.8 (a, b) show the dimensionless azimuthal velocity distributions close to the inlet nozzle. There are remarkable differences between the profiles. Generally the profile peaks near the

Author	L_{vt}/D_{vt}	τ_A (%)	N	D_c/D_{vt} (%)	Blockage effect (%)
Takahama [1]	150	17	4	–	26.3
Reynolds [10,11]	16	1.1	8	42	2.7
Ahlborn [12]	24	–	–	32.3	8.0
This work	12.8	3.5	1	25	7.9

Table 4.2: *The comparison of the important geometrical parameters.*

outer radius. The result of Reynolds is exceptional with high speeds at the center of the vortex tube, which perhaps is due to the oscillation of the vortex column.

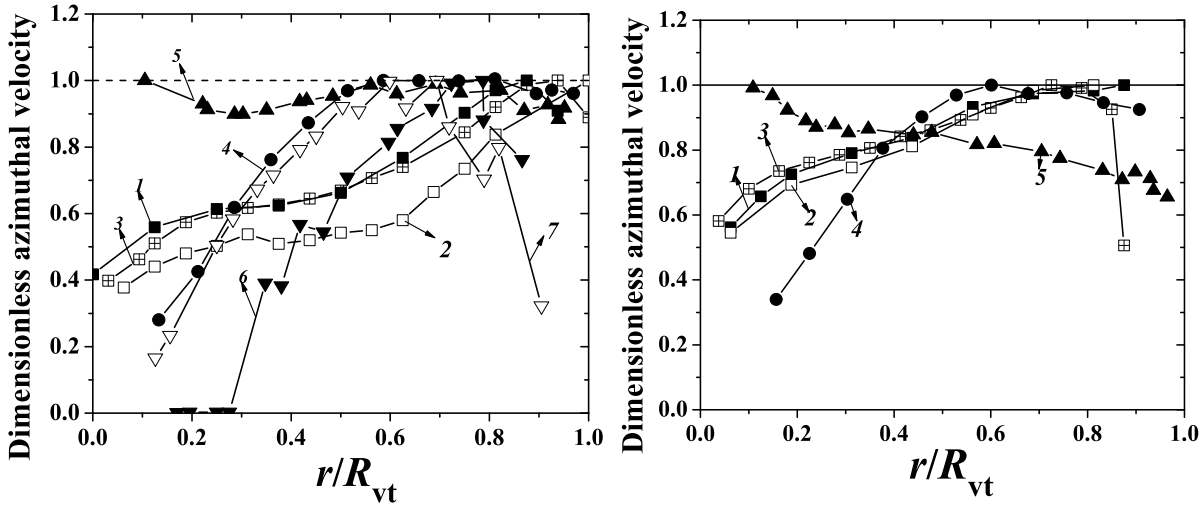

(a) Near inlet. *(b) Further downstream.*

Figure 4.8: *Comparison of the dimensionless azimuthal velocities. "1", "2" and "3" are for the present work cases* $R_{sm} = 0$ *mm,* 1.5 *mm and* 3.0 *mm. "4" is for the work by Takahama, "5" by Reynolds, "6" and "7" by Ahlborn. The operating conditions for these curves are shown in the table below. Here* τ_Z *means* Z/D_{vt}.

Subfigure	"1"		"2"		"3"		"4"		"5"		"6"		"7"	
	τ_Z	ε	τ_Z	ε	τ_Z	ε	τ_Z	ε	τ_Z	ε	τ_Z	ε	τ_Z	ε
(a)	1.47	0.27	1.47	0.32	1.47	0.33	0.5	0.5	1.50	–	0.18	0	0.18	1
(b)	2.97	0.27	2.97	0.32	2.97	0.33	5.5	0.5	6.0	–				

In (a) Ahlborn's results show that, if the cold fraction is zero, the circular region in the center with radius about $0.3R$ the azimuthal velocity is about zero. If the cold fraction is 1, the azimuthal velocity near the wall drops very fast. In (b), the maximum azimuthal velocity measured by Reynolds appears in the center, and the azimuthal velocity drops near the wall. It seems that the gas flow inside the vortex tube has a very thin boundary layer near the wall. Takahama's 3 mm Pitot tube didn't allow him to measure the velocities at smaller radii because of the influence on the flow field from inserting the probe. Also in our case, it was very difficult to measure in the center where a zero azimuthal velocity is expected. Fig. 4.9 shows the dimensionless axial velocity distributions. Normally, the maximum axial velocity is less than half of the maximum azimuthal velocity at the same station. When the

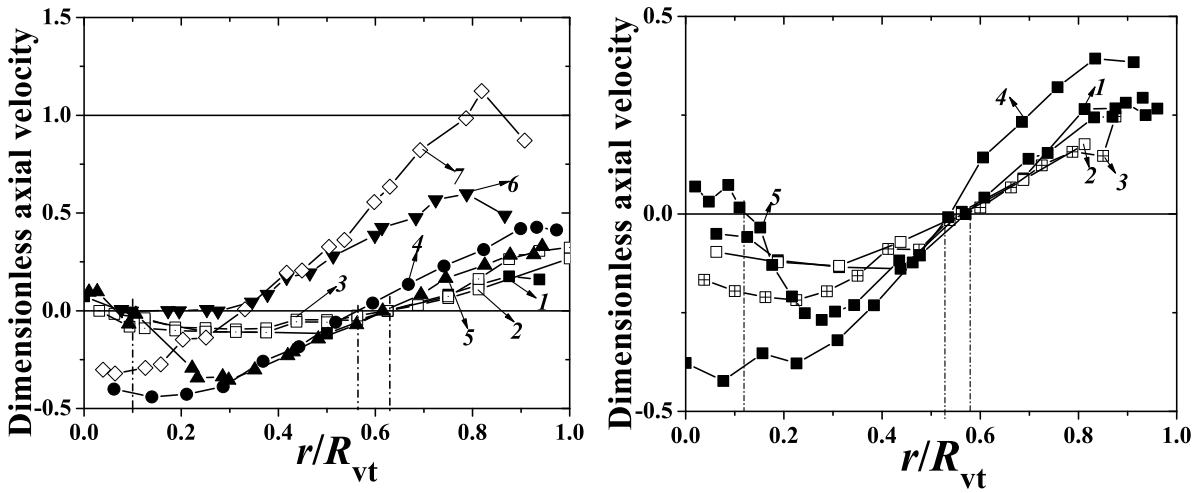

(a) Near inlet *(b) Further downstream*

Figure 4.9: *Comparison of the dimensionless axial velocities. The operating conditions for curves "1"∼"7" are the same as that listed in Fig. 4.8.*

cold fraction is 1 and the measuring station is very near to the inlet of the vortex chamber, Ahlborn shows that his axial velocity is even higher than the maximum azimuthal velocity near the wall. Note that the plotted dimensionless axial speed is made dimensionless by using the maximum azimuthal speed in Eq. 4.3. In Fig. 4.9 (a), at the station near the inlet nozzle, the axial velocities divide into two regions, which include the core in the center region with radius about $0.5R$, and the annular peripheral region. Even at a station τ_Z $(= Z/D_{\mathrm{vt}}) = 5.9$, Reynolds found these regions (Fig. 4.9 (b)). The gas in the core region swirls to the cold end and the gas in the peripheral annulus rotates to the hot end. In Fig. 4.9 (b), the radius at which the axial velocity is zero is similar about 0.55, except the radius found by Ahlborn which is about 0.35.

4.3.2.3 Dimensionless temperature

Ahlborn did not show temperature distributions in [12]. So here only the results from Takahama and Reynolds are used. Fig. 4.10 (a) shows the comparison of the dimensionless recovery temperature distributions. The dimensionless recovery temperatures differ from Reynolds work, as the maximum dimensionless velocities near the center in Reynolds' work are factor 2 larger. The stagnation temperature near the outer radius is larger and at the center is the minimum. Fig. 4.10 (b) shows the comparison of the dimensionless static temperature distributions. The dimensionless static temperatures are similar, except of that one at case $R_{\mathrm{sm}} = 0$ mm at Station $\tau_Z = 1.47$. The dimensionless static temperature reaches a maximum near the wall, and has a minimum at the dimensionless radius of about 0.3.

4.4 Analyzing the results on the small RHVT system

4.4.1 Analyzing based on the model mentioned in Chapter 2

In Chapter 2, the secondary circulation model from Ahlborn has been explained. As a basis, the extended secondary circulation model also has been found in Chapter 2. Here, the

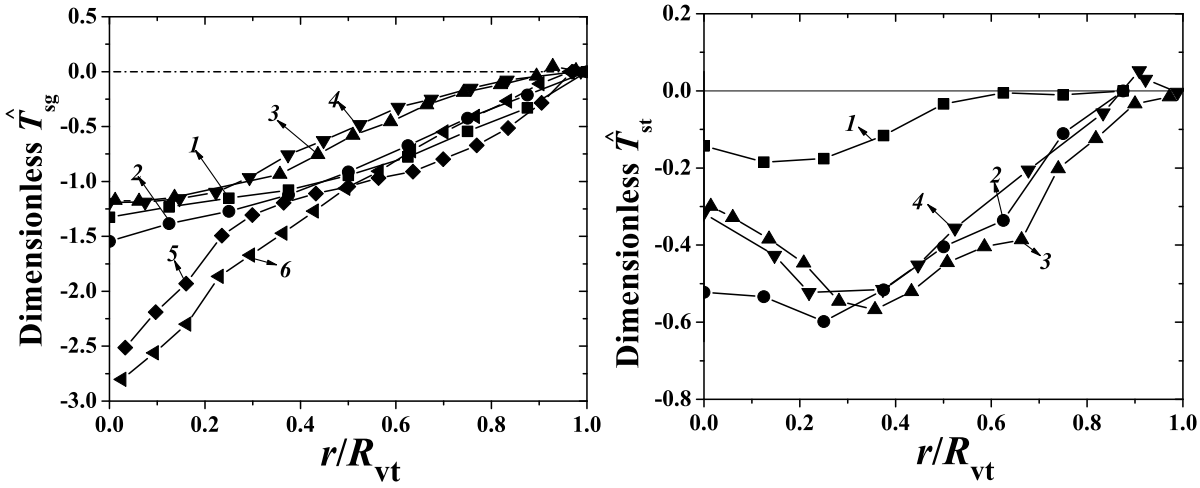

(a) Stagnation temperature distributions. *(b) Static temperature distributions.*

Figure 4.10: *Comparison of the dimensionless temperature. "1" and "2" are for the present work with case $R_{sm} = 0$ mm at Stations 1 and 2, "3" and "4" are for the work by Takahama with the cold fraction 0.5 at Stations τ_Z about 1.5 and 5.5, "5" and "6" are for the work by Reynolds at Stations τ_Z about 1.5 and 15 and the cold fraction is unknown.*

experimental results are analyzed using these two models.

4.4.1.1 General measurement results and operating conditions

The inlet pressure is kept constant at 6.3 bar. The cold and hot exhaust pressures are the room pressure, about 1 bar. The cold fractions ε are 0.27 for case $R_{sm} = 0$ mm, 0.32 for case $R_{sm} = 1.5$ mm and 0.33 for case $R_{sm} = 3.0$ mm. The maximum pressure measured by CPT on Station 1 is about 2.8 bar and the maximal static pressure is about 2.3 bar; the minimal pressure near the center measured by CPT is 1.4 bar and the minimal static pressure is about 1.3 bar. The room pressure p_r is about 1 bar, so p_c is taken as the mean value 1.15 bar. Considering that the vortex chamber has a diameter of about 28 mm, and the vortex tube diameter is about 16 mm, the critical radius ratio τ_R is taken as 0.571. By combining Eq. 2.29 and Eq. 2.33, the pressure at the nozzle exhaust p_0 can be calculated, which is about 5.42 bar, and the parameter X (defined in Chapter 2) is about 0.788. And the parameter X' (defined in Chapter 2) is about 0.153. The Mach number at the exhaust of the inlet nozzle is about 0.47. The maximum azimuthal Mach number in the vortex chamber, based on the Rankine velocity distribution in Chapter 2, is calculated as 0.82. The maximum azimuthal Mach number measured in Station 1 in Fig. 4.6 is about 0.55 for case $R_{sm} = 0$ mm, 0.8 for case $R_{sm} = 1.5$ mm, and 0.7 for case $R_{sm} = 3.0$ mm. So the results from case $R_{sm} = 0$ mm show the larger velocity drop near the entrance of the vortex tube; while rounding off the entrance, the velocity drops get less, which can be found from from the results from case $R_{sm} = 1.5$ mm and case $R_{sm} = 3.0$ mm. Also the lower velocity drops give us confidence on applying the secondary circulation model.

4.4.1.2 Comparison the theoretical and experimental results

According to the analysis in Chapter 2, applying the above defined operating conditions, the calculated temperature results based on the modification of Ahlborn et al.'s model (MAM) and

the original Secondary Circulation Model (OSCM) from Ahlborn are shown in the following tables. As mentioned above in section 4.4.1.1, the parameters for all three cases are taken the same except for the cold fraction; X is taken as 0.788; τ_R is taken as 0.57; and X' is taken as 0.153. The cold fraction ε for case $R = 0$ mm is 0.274, for case $R = 1.5$ mm is 0.324 and for case $R = 3.0$ mm is 0.331.

Terms	**Case $R_{\mathrm{sm}} = 0$ mm**	**Case $R_{\mathrm{sm}} = 1.5$ mm**	**Case $R_{\mathrm{sm}} = 3.0$ mm**
$\dot{m}_{\mathrm{in}}$ (g/s)	8.2	8.4	8.34
$\dot{m}_{\mathrm{h}}$ (g/s)	5.98	5.64	5.58
$\dot{m}_{\mathrm{c}}$ (g/s)	2.26	2.71	2.76
Cold fraction ε	0.27	0.32	0.33
T_{in} (K)	285.6	293.7	296.2
$T_{\mathrm{h,m}}$ (K)	291.3	303.8	305.25
$T_{\mathrm{c,m}}$ (K)	270.5	275.1	278.4
p_{in} (bar)	6.3	6.3	6.3
p_{c} (bar)	1.15	1.15	1.15
p_{r} (atm)	1.0	1.0	1.0

Table 4.3: *Summary of experimental results and of operating conditions.*

Terms	Experiment			MAM in this work			Ahlborn's OSCM		
Case R	0 mm	1.5 mm	3.0 mm	0 mm	1.5 mm	3.0 mm	0 mm	1.5 mm	3.0 mm
$T_{\mathrm{c}}/T_{\mathrm{in}}$	0.947	0.937	0.940	0.969	0.971	0.972	0.839	0.843	0.843
$T_{\mathrm{h}}/T_{\mathrm{in}}$	1.020	1.034	1.031	1.012	1.014	1.014	1.287	1.298	1.300
$\Delta T_{\mathrm{c}}/T_{\mathrm{in}}$	−0.053	−0.063	−0.060	−0.031	−0.029	−0.028	−0.161	−0.158	−0.157
$\Delta T_{\mathrm{h}}/T_{\mathrm{in}}$	0.020	0.034	0.031	0.012	0.014	0.014	0.287	0.298	0.300

Table 4.4: *Temperature ratios based on the measurement results*

Table 4.4 shows all the temperature ratios based on the measurement results in table 4.3 and based on the two secondary circulation models. It shows that MAM in this work agrees better with the measurements than Ahlborn's OSCM model.

4.4.2 The efficiencies of the small RHVT system

In Chapter 2, the efficiencies of the RHVT system based on different applications have been analyzed. With the definitions of these efficiencies, the relevant efficiencies of the small RHVT system will be calculated in this section.

4.4.2.1 The irreversible parameter Θ_{ir}

According to Eq. 2.15 in Chapter 2, the following equation will hold,

$$\frac{1}{\Gamma}(\ln \frac{T_{\mathrm{h}}^{1-\varepsilon} T_{\mathrm{c}}^{\varepsilon}}{T_{\mathrm{in}}}) - \ln \frac{p_{\mathrm{h}}^{1-\varepsilon} p_{\mathrm{c}}^{\varepsilon}}{p_{\mathrm{in}}} = \frac{\dot{S}_{\mathrm{i}}}{\dot{m}_{\mathrm{in}} R_{\mathrm{m}}} = \Theta_{\mathrm{ir}}.$$

The irreversibility parameters Θ_{ir} in this investigation are 1.70 for case $R = 0$ mm, 1.71 for $R = 1.5$ mm and 1.70 for $R = 3.0$ mm.

All parameters Θ_{ir} are high, even close to the critical value (under the operating conditions like the inlet pressure 6 bar, the exhaust pressure 1 bar and the inlet temperature 300 K, the critical value for Θ_{ir} is about 1.79, see Chapter 2.). This indicates that the process inside the RHVT system is highly irreversible.

4.4.2.2 Thermal coefficient of performances

The thermal coefficient of performance (COP) for the RHVT system has two different definitions based on the different applications. They are for the cooler COP_{cr} (see Eq. 2.44) and for the heat pump COP_{hp} (see Eq. 2.45). They have the following relationship

$$COP_{\mathrm{cr}} = COP_{\mathrm{hp}}. \tag{4.6}$$

Detailed information about these COP's can be found in Chapter 2. With the working conditions in table 4.3, the COP's have been calculated and listed in table 4.5. It shows that the COP's are very small. As a cooler or a heat pump, the small RHVT system has a coefficient of performance lower than 5%. The calculated COP's basically agree with the theoretical relationship Eq. 4.6. The thermal COP_{hp} for cases $R = 1.5$ mm and $R = 3.0$ mm are a little bit higher than these COP_{cr}, which perhaps is due to the measurement error.

COP**s**	**Case** $R_{\mathrm{sm}} = 0$ **mm**	**Case** $R_{\mathrm{sm}} = 1.5$ **mm**	**Case** $R_{\mathrm{sm}} = 3.0$ **mm**
COP_{cr} %	3.0	4.2	4.1
COP_{hp}%	3.0	4.8	4.2

Table 4.5: *The thermal coefficient of performances of the small RHVT system*

4.4.2.3 The efficiency by analogy with a perfectly isentropic expansion

As mentioned in Chapter 2, the RHVT process can be thought off as a perfect isentropic expansion process by analogy. And the efficiency by analogy as a perfect isentropic expansion process is defined by Eq. 2.46, which is repeated below

$$\eta_{\mathrm{is}} = \frac{T_{\mathrm{in}} - T_{\mathrm{c}}}{T_{\mathrm{in}} - T_{\mathrm{is}}}.$$

4.4.2.4 Carnot coefficient of performances

Carnot COP's of the RHVT system are defined by Eq. 2.48 based on the Carnot cooling and heating cycles. And by using the Carnot cycle as criterion basis, the proportions of the thermal efficiencies to the Carnot efficiencies are given by Eqs. 2.48, 2.49 and 2.50 are listed as

$$COP_{\mathrm{cn,cr}} = \frac{T_{\mathrm{c}}}{T_{\mathrm{in}} - T_{\mathrm{c}}}$$

$$COP_{\mathrm{cn,hp}} = \frac{T_{\mathrm{h}}}{T_{\mathrm{h}} - T_{\mathrm{in}}}$$

$$\eta_{\mathrm{cn,cr}} = \frac{COP_{\mathrm{cr}}}{COP_{\mathrm{cn,cr}}}$$

$$\eta_{\mathrm{cn,hp}} = \frac{COP_{\mathrm{hp}}}{COP_{\mathrm{cn,hp}}}.$$

Efficiencies	**Case $R_{\mathrm{sm}} = 0$ mm**	**Case $R_{\mathrm{sm}} = 1.5$ mm**	**Case $R_{\mathrm{sm}} = 3.0$ mm**
η_{is} %	14	17	16
$COP_{\mathrm{cn,cr}}$	18	15	16
$COP_{\mathrm{cn,hp}}$	51	30	34
$\eta_{\mathrm{cn,cr}}$ %	0.17	0.29	0.26
$\eta_{\mathrm{cn,hp}}$ %	0.06	0.16	0.13

Table 4.6: *The results of the efficiencies by analogy with a perfectly isentropic expansion and the Carnot cycle basis*

Table 4.6 shows the calculated results of the efficiency by analogy with a perfect isentropic expansion, the Carnot efficiencies, and The criterion on Carnot cycle basis. The first row in table 4.6 shows that all the cold exhaust temperatures are about 1.5 times larger than the temperature in a perfect isentropic expansion process under the same inlet and exhaust pressures and the inlet temperature. The second row shows the COP_{cn} as a Carnot cooling cycle basis. It shows that within the temperature region between the inlet and cold temperatures, all these $COP_{\mathrm{cn,cr}}$s are about 15. As a Carnot heat pump cycle basis, $COP_{\mathrm{cn,hp}}$s are higher than 30, especially for case $R_{\mathrm{sm}} = 0$ mm which is about 51. The last two rows show the proportions of the experimental thermal efficiencies on these Carnot cycles basis COP_{cn}s, it shows that the cooling and heating processes inside the RHVT system are far away from the ideal Carnot cycles.

4.4.3 Secondary circulation calculation

As mentioned above, the gas flow in the vortex tube has two regions, the central part towards the cold end direction and the periphery towards the hot end direction. With the measured axial velocity profiles, the cumulative mass flows over the circle region from $0 \sim r$ can be calculated by the integration on this area, as shown in Fig. 4.11,

$$\dot{m}_r = \int_0^{A_r} \rho V_{\mathrm{ax}} \mathrm{d}A = \int_0^r 2\pi\rho V_{\mathrm{ax,r}} r \mathrm{d}r \tag{4.7}$$

here the density ρ was calculated based on the ideal-gas law by the local gas properties static pressure p_{st} and static temperature T_{st}, the axial velocity $V_{\mathrm{ax,r}}$ can be calculated based on the local axial Mach number $M_{\mathrm{a,ax}}(r)$ and the local static temperature T_{st}.

The temperature used in Eq.(4.7) is the static temperature, which has about 5 K variation along the radius at the same station, as shown in Fig. 4.7(b). So here, the static temperature at the same station is taken as a constant with less than 1% error. We approximated the pressure $p(r)$ as a second-order polynomial with less than 2% error and $M_{\mathrm{a,ax}}(r)$ as a third-order polynomial with less than 1.5% error. By simple adding these errors together,, the typical error in the mass flows is less than 5%.

The mass flows were determined at Station 2 for the three cases. Fig. 4.12 shows the mass flows as function of r/R_{vt}. The mass flows from case(a) and (b) are very close to the measured hot exhaust mass flows as measured by the mass flow meter giving confidence in all measurements. The minimum mass flows in the case $R_{\mathrm{sm}} = 0$ mm and case $R_{\mathrm{sm}} = 1.5$ mm are about 2 g/s, which are less than the measured cold exhaust mass flows (2.26 and 2.71 g/s). This proves that a small fraction of the cold exhaust gas directly comes from the vortex chamber, as shown in Fig. 4.13 (b). This was also noted by Fulton [14] and Gutsol [15]. The

minimum mass flow for case $R_{\mathrm{sm}} = 3.0$ mm is about 3 g/s and is again larger than the cold exhaust mass flow (2.7 g/s). The reason for this is the recirculation flow in the vortex tube, as mentioned by Ahlborn [12].

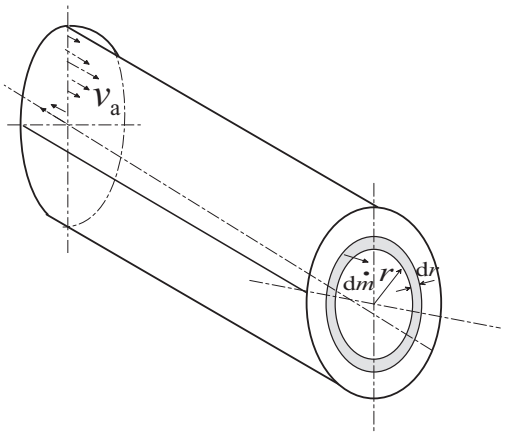

Figure 4.11: *The integration of the cumulative mass flow.*

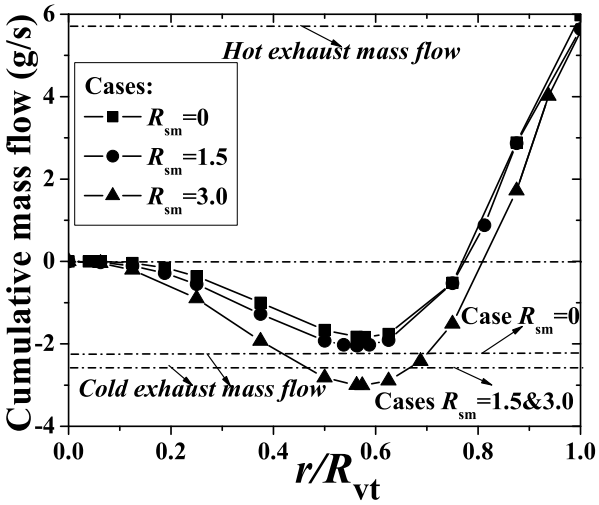

Figure 4.12: *The mass flows as functions of r/R at the No.2 station for three cases.*

Combining Fig. 4.6(a) and (b) a vector plot of the flow field can be drawn. From this the axial flow pattern inside the vortex tube can be made, as shown in Fig. 4.13(a). The axial velocity separates into two parts. In the peripheral region hot gas flows to the hot end, in the central region, the cold gas flows to the cold region. The radius at which the axial velocity reverses decreases from the cold end to the hot end along the axis. Based on the axial flow pattern, and combining with Fig. 4.12, a secondary circulation flow pattern is found, as shown in Fig. 4.13 (b). After leaving the nozzle, the gas is divided into two different parts in the vortex chamber; a large part (I) swirls to the hot end via the peripheral region, and the left part (II) directly escapes from the cold exhaust via the wall boundary layer. When part (I) flows toward the hot end, it separates gradually into two parts (III and IV): one part (III) exhausts through the hot end valve and the other part (IV) spins back to the cold end. When part (IV) reaches the cold end, some (VI) exhausts through the cold end, and some (V) enters the secondary circulation [7, 16]. This is proved by the mass flow calculation. So we can conclude that a secondary circulation really exists, and rounding off the entrance can enhance and extend the secondary circulation. In case $R_{\mathrm{sm}} = 3.0$ mm it is stronger than these in cases (a) and (b), and extends to the No.2 station at about $0.2L$.

4.5 Summary

We like to conclude that:

1. The pressure, temperature, and velocity fields inside a simple RHVT have been found.

2. The pressure, temperature, and velocity fields inside the RHVT from the present work have been compared with the works from Takahama, Reynolds, and Ahlborn. There are remarkable differences between these velocity profiles, especially with the results of

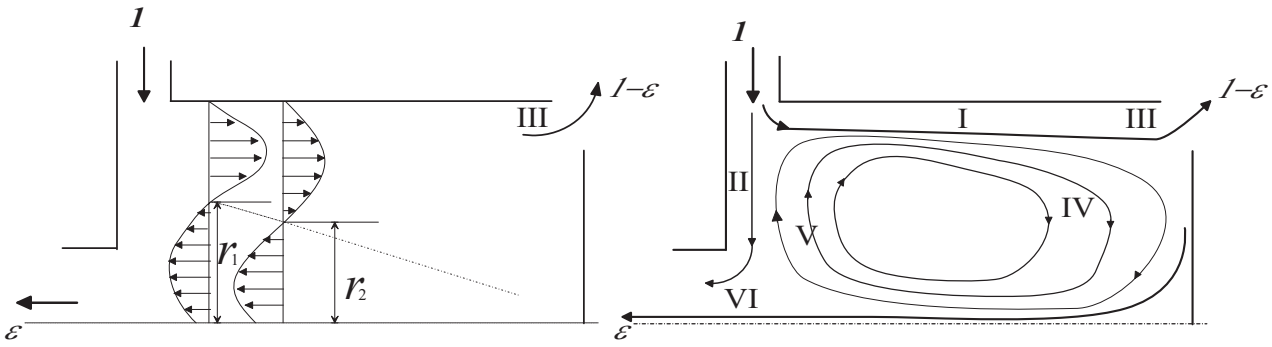

(a) The axial flow pattern *(b) The secondary circulation flow pattern*

Figure 4.13: *The flow pattern inside the RHVT. r_1 and r_2 are the reverse radius at the stations. During this measurement, it is about 5 mm at station 1 and 4.5 mm at station 2.*

Reynolds. We expect the different sizes of the vortex tube, different numbers of inlet nozzle and different sizes of the probes are the main reasons in this difference.

3. Remarkable are the apparent nonzero azimuthal speeds at the center of the tube, which exist in most works. This might be due to instabilities with respect to the vortex core motion itself. This is of interest for a new forthcoming experimental study.

4. The general results in this work have been analyzed based on the theoretical equations from MAM and OSCM models in Chapter 2. It shows that MAM from the present work agrees better with the measurement than OSCM model. The efficiencies of the small RHVT system have also been analyzed. The thermal efficiencies show that for a cooler or a heat pump the COP of the RHVT is lower than 5% and does not reach 0.3% of the COP of the respective Carnot cycle. The irreversible parameter Θ_{ir} is very close to the critical value. All these efficiencies show that inside the RHVT system, strongly irreversible processes occur.

5. The flow pattern in the RHVT has been found, showing secondary circulation inside the vortex tube. With the model from Ahlborn the temperature difference generated by the RHVT is calculated. It depends on the type of the working fluid, the normalized pressure ratio, and the cold fraction. Rounding off the entrance increases the cold fraction in the system under the same operating conditions, and enhances the secondary circulation inside the vortex tube itself and extends the circulation closer to the vortex chamber in the vortex tube, at last improves the performance of the RHVT.

6. The comparison and the theoretical analysis of the experimental results gave us confidence on our work. In the later chapters, more detailed experimental work will be shown, the theoretical analysis will not be discussed.

References

[1] H. Takahama. Studies on vortex tubes (1) experiments on efficiency of energy separation (2) on profiles of velocity and temperature. *Bulletin of JSME*, 8(31):433–440, 1965.

[2] H. Takahama and N. Soga. Studies on vortex tubes (2nd report): Reynolds number. the effects of the cold air rate and the partial admission of nozzle on the energy separation. *Bulletin of JSME*, 9(33):121–130, 1966.

[3] A. Hirschberg. Totale temperatuur en snelheidsmetingen aan een aangepaste sonische vrije straal. Master thesis, Delft University of Technology, Delft, the Netherlands, October 1975.

[4] A. Hirschberg and J.C. van Muiswinkel. A correlation of recovery temperature data for cylinders in a compressible flow at high Reynolds numbers. *International Journal of heat and mass transfer*, 20(6):669–674, 1977.

[5] K.J. Bosschaart. Thermocouple wire analysis. Internal report, Eindhoven University of Technology, Eindhoven, the Netherlands, March 2003.

[6] B. Ahlborn, J.U. Keller, R. Staudt, G. Treitz, and E. Rebhan. Limits of temperature separation in a vortex tube. *J. Phys. D: Appl. Phys.*, 27:480–448, 1994.

[7] B. Ahlborn and J.M. Gordon. The vortex tube as a classic thermodynamic refrigeration cycle. *J. Appl. Phys.*, 88(6):3645–3653, 2000.

[8] A. Gutsol. The Ranque effect. *Physics-Uspekhi*, 40(6):639–658, 1997.

[9] J. Lewins and A. Bejan. Vortex tube optimization theory. *Energy*, 24(11):931–943, 1999.

[10] A.J. Reynolds. A note on vortex-tube flow. *J. Fluid Mech.*, 14:18–20, 1962.

[11] A.J. Reynolds. *Studies of Rotating fluids a) Plane Axisymmetric Flow, b) Forced Oscillations in a Rotating fluid, c) The Ranque-Hilsch Vortex Tube.* PhD dissertation, University of London, September 1960.

[12] B. Ahlborn and S. Groves. Secondary flow in a vortex tube. *Fluid Dynamics Research*, 21:73–86, 1997.

[13] Y. Soni and W.J. Thomson. Optimal design of the Ranque-Hilsch vortex tube. *Trans. ASME, J. Heat Transfer*, 94(2):316–317, 1975.

[14] C.D. Fulton. Ranque's tube. *J. ASRE Refrigerating Engng*, 58:473–479, 1950.

[15] A. Gutsol and J.A. Bakken. A new vortex method of plasma insulation and explanation of the Ranque effect. *J. Phys. D: Appl. Phys.*, 39:704–711, 1998.

[16] C.U. Linderstrom-Lang. *Studies on transport of mass and energy in the vortex tube—The significance of the secondary flow and its interaction with the tangential velocity distribution.* Riso report, Denmark, September 1971.

Chapter 5

Design of the RHVT nozzle

In this chapter, the design of the nozzle inside the RHVT system is discussed. In order to design a good RHVT, the inlet nozzle, diameter of the chamber, diameter of the vortex tube, length of the vortex tube, and diameter of the cold exhaust orifice, etc. are all relevant design parameters. In this chapter, the design of the inlet nozzles for the RHVT itself is analyzed. A choice was made for a convergent slot-type nozzle. Optimum RHVT performance is obtained for "choking" condition, i.e. the exit slot Mach number $M_{\mathrm{a,ex}}$ equals unity. Pressure loss and entropy generation are analyzed as a function of the number of slots on the inner-ring, for given total mass flow. The use of 8 slots is possible without adding extra pressure loss. This chapter is mainly based on the discussion "Gas dynamic properties in the slot" [1].

5.1 Design of the inlet nozzle

The inlet nozzle is an important component of the RHVT.

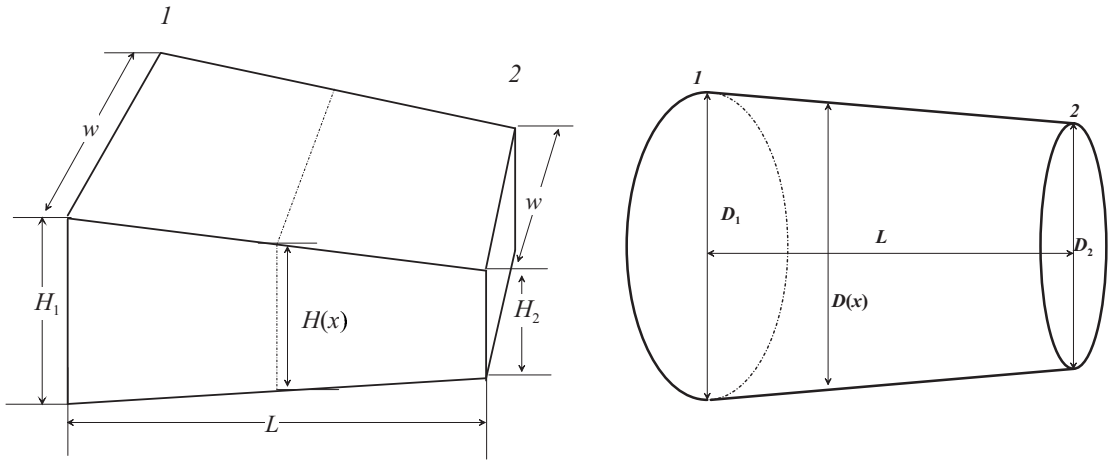

(a) Rectangular slot *(b) Conical nozzle*

Figure 5.1: *Schematic drawing of the inlet nozzles. "1" and "2" are the inlet and exhaust cross sections. w is the width of the inlet rectangular slot, H_1 and H_2 are the heights at the inlet and exhaust of the rectangular slot, D_1 and D_2 are the diameters at the inlet and exhaust of the conical nozzle, L is the length of the inlet nozzle.*

Two typical geometries that will be discussed are a conical nozzle and a convergent (linear) slot nozzle with constant width, as shown in Fig. 5.1. In the analysis, the working medium through the inlet nozzle is chosen nitrogen.

5.1.1 Gas dynamics of nozzle flow

The entrance gas properties are assumed to be known

$$R_\mathrm{e} = \frac{V D_\mathrm{n,e}}{\nu} = \frac{4\dot{m}}{C_\mathrm{n}\mu} \tag{5.1a}$$

$$M_\mathrm{a,1} = \frac{V_1}{a_1} = \frac{\dot{m}}{\rho_1 A_1 \sqrt{\gamma R_\mathrm{m} T_1}} = \frac{\dot{m}\sqrt{R_\mathrm{m} T_1}}{\sqrt{\gamma} p_\mathrm{st,1} A_1}. \tag{5.1b}$$

Here, using indexation 1 A_1 is the cross sectional area at cross section 1, a_1 is the sound speed, C_n is the wetted perimeter of the nozzle, $D_\mathrm{n,e}$ is the equivalent hydraulic diameter of the nozzle with $D_\mathrm{n,e} = 4A/C_\mathrm{n}$, $M_\mathrm{a,1}$ is the Mach number, $\dot{m}$ is the mass flow through the nozzle, which is determined by the flow meter, $p_\mathrm{st,1}$ is the static pressure, R_e is the Reynolds number, which is determined by the mass flow and the geometry, R_m is the specific gas constant for nitrogen, T_1 is the static temperature, V_1 is the gas velocity, $\nu = \mu/\rho$ is the kinematic viscosity, μ is the dynamic viscosity (assumed to be given as function of the temperature), ρ_1 is the gas density and γ is the ratio of the gas specific heats ($\gamma = c_\mathrm{p}/c_\mathrm{v}$). So the Mach number and Reynolds number at cross section 1 are known when the total pressure, stagnation temperature, mass flow and the wetted perimeter at the cross section are given. If $M_\mathrm{a,2} < 1$, it is possible to choose $\dot{m}$, $p_\mathrm{t,1}$, $T_\mathrm{t,1}$ independently in order to obtain a required $M_\mathrm{a,2}$. If $M_\mathrm{a,2} = 1$, then $(\dot{m}\sqrt{R_\mathrm{m} T_\mathrm{t,1}})/p_\mathrm{t,1}$ is approximately constant [2], so in this case, it is not possible to choose the entrance parameters independently.

5.1.1.1 Analysis for a channel

1) In a quasi-one dimensional approximation and for a steady flow, the continuity equation (conservation of mass) reads

$$\frac{1}{\rho}\frac{\mathrm{d}\rho}{\mathrm{d}x} + \frac{1}{V}\frac{\mathrm{d}V}{\mathrm{d}x} + \frac{1}{A}\frac{\mathrm{d}A}{\mathrm{d}x} = 0 \ . \tag{5.2}$$

The geometry information includes the equivalent diameter and the cross sectional area as a function of position x.

For the convergent rectangular channel (slot), shown in Fig. 5.1 (a), with a constant width w, total length L and different heights H_1 and H_2, we obtain

$$h(x) = H_1 - \frac{H_1 - H_2}{L} x \tag{5.3a}$$

$$A(x) = wh(x); C(x) = 2(w + h(x)) \tag{5.3b}$$

$$D_\mathrm{e}(x) = \frac{4A(x)}{C(x)} = \frac{2wh(x)}{w + h(x)} \tag{5.3c}$$

$$\frac{\mathrm{d}x}{D_\mathrm{e}} = -\frac{L}{2w}\frac{w + H_1 - \frac{(H_1 - H_2)x}{L}}{H_1 - H_2}\frac{\mathrm{d}A}{A}. \tag{5.3d}$$

For a conical channel (nozzle), shown in Fig. 5.1 (b), with different diameters D_1 and D_2, and total length L, we obtain

$$D_{\mathrm{e}}(x) = D_1 - \frac{D_1 - D_2}{L}x \tag{5.4a}$$

$$A(x) = \frac{\pi D_{\mathrm{e}}(x)^2}{4}; C(x) = \pi D_{\mathrm{e}}(x) \tag{5.4b}$$

$$\frac{\mathrm{d}x}{D_{\mathrm{e}}} = -\frac{L}{D_1 - D_2}\frac{\mathrm{d}A}{A}\frac{1}{2}. \tag{5.4c}$$

So in the analysis, the above geometry equations should be taken into account.

2) Energy conservation for constant specific heats for an adiabatic flow reads for the total temperature T_{t}

$$T_{\mathrm{t}} = T(1 + \Gamma_2 M_{\mathrm{a}}^2)(= \text{constant throughout}) \ . \tag{5.5}$$

After differentiating this gives

$$\frac{1}{T}\frac{\mathrm{d}T}{\mathrm{d}x} + \frac{(\gamma - 1)M_{\mathrm{a}}}{1 + \Gamma_2 M_{\mathrm{a}}^2}\frac{\mathrm{d}M_{\mathrm{a}}}{\mathrm{d}x} = 0 \ . \tag{5.6}$$

3) Equation of state (ideal gas)

$$p = \rho R_{\mathrm{m}} T \ . \tag{5.7}$$

Differentiation leads to

$$\frac{1}{p}\frac{\mathrm{d}p}{\mathrm{d}x} = \frac{1}{\rho}\frac{\mathrm{d}\rho}{\mathrm{d}x} + \frac{1}{T}\frac{\mathrm{d}T}{\mathrm{d}x} \ . \tag{5.8}$$

4) Mach number definition

$$M_{\mathrm{a}} = \frac{v}{a} = \frac{V}{\sqrt{\gamma R_{\mathrm{m}} T}} \tag{5.9}$$

Differentiation leads to

$$\frac{1}{M_{\mathrm{a}}}\frac{\mathrm{d}M_{\mathrm{a}}}{\mathrm{d}x} = \frac{1}{V}\frac{\mathrm{d}V}{\mathrm{d}x} - \frac{1}{2T}\frac{\mathrm{d}T}{\mathrm{d}x} \tag{5.10}$$

5) Momentum equation [3]

$$\frac{\mathrm{d}p}{p} + \gamma M_{\mathrm{a}}^2\frac{\mathrm{d}V}{V} + \frac{\gamma M_{\mathrm{a}}^2}{2}4f\frac{\mathrm{d}x}{D} = 0 \ , \tag{5.11}$$

where D is the diameter, f is the friction factor that can be determined by the von Karman-Nikuradse equation,

$$R_{\mathrm{e}} = \frac{1}{2\sqrt{f}}10^{0.4+1/4\sqrt{f}}. \tag{5.12}$$

The friction factor f is dependent on the Reynolds number, and therefore on the inlet mass flow and geometry (see Eq. 5.1a). For a given inlet gas flow inside the nozzle, the mass flows at different cross sections are constant, so the Reynolds number only depends on the geometry, and f also depends on the geometry. The friction factor as a function of the Reynolds number is shown in Fig. 5.2. D_{e} depends on the injection geometry. For a convergent channel it is a function of position x, and $\mathrm{d}x/D_{\mathrm{e}}$ can be expressed as a function of $\mathrm{d}A/A$ (see Eqs. 5.3d and 5.4c).

By combining Eqs. 5.8, 5.6, 5.2 and 5.10, the following expression for $\mathrm{d}p/\mathrm{d}x$ is obtained,

$$\frac{1}{p}\frac{\mathrm{d}p}{\mathrm{d}x} = -\frac{1+(\gamma-1)M_\mathrm{a}^2}{1+\Gamma_2 M_\mathrm{a}^2}\frac{1}{M_\mathrm{a}}\frac{\mathrm{d}M_\mathrm{a}}{\mathrm{d}x} - \frac{1}{A}\frac{\mathrm{d}A}{\mathrm{d}x}. \tag{5.13}$$

A second equation for $\mathrm{d}p/\mathrm{d}x$ is obtained by combining Eq. 5.11 with $4f\mathrm{d}x/D_\mathrm{e}(x) = f_\mathrm{s}\mathrm{d}A/A$,which is possible for convergent nozzles[1]. Combining this expression and Eq. 5.13 yields

$$\frac{1}{A}\frac{\mathrm{d}A}{\mathrm{d}x} = -\frac{1}{1+\frac{f_\mathrm{s}\gamma M_\mathrm{a}^2}{2}}\frac{1-M_\mathrm{a}^2}{1+\Gamma_2 M_\mathrm{a}^2}\frac{1}{M_\mathrm{a}}\frac{\mathrm{d}M_\mathrm{a}}{\mathrm{d}x} \tag{5.14}$$

where f_s is the average geometric friction factor and is defined as

① For the convergent rectangular nozzle (slot)

$$\begin{aligned} f_\mathrm{s} &= \tfrac{1}{L}\textstyle\int_0^L 4\overline{f}\frac{L}{2w}\frac{w+H_1-\frac{H_1-H_2}{L}x}{H_1-H_2}dx \\ &= \tfrac{\overline{f}L}{w}(2\tfrac{w+H_1}{H_1-H_2}-1). \end{aligned} \tag{5.15}$$

② For the conical nozzle

$$\begin{aligned} f_\mathrm{s} &= \tfrac{1}{L}\textstyle\int_0^L 4f\frac{L}{D_1-D_2}dx \\ &= \tfrac{4\overline{f}L}{D_1-D_2} \end{aligned} \tag{5.16}$$

where $\overline{f}$ is the mean friction factor.

③ For the channel with constant cross-section, Eq. 5.11 becomes,

$$4f\frac{\mathrm{d}x}{D_\mathrm{e}} = -\frac{2}{\gamma M_\mathrm{a}^2}\left(\frac{\mathrm{d}p}{p}+\gamma M_\mathrm{a}^2\frac{\mathrm{d}v}{v}\right). \tag{5.17}$$

Here the geometric friction factor f_s is taken as,

$$f_\mathrm{s} = \int_0^L 4f\frac{1}{D_\mathrm{e}}dx = \frac{4\overline{fL}}{D_\mathrm{e}}. \tag{5.18}$$

For the three geometries discussed above, f_s refers to integral quantities, which depend on the friction factor and geometry. They are proportional to the friction factor and the length of the channel, and inversely proportional to the diameter of the channel. Fig. 5.2 shows that the friction factor f is not very sensitive to the Reynolds number, so the geometric friction factor is mainly dependent on the geometry. During the calculation, when the inlet mass flow, inlet pressure, inlet temperature and the geometry of the nozzle are known, the Reynolds number distribution along the nozzle is known, then the friction factor is known, furthermore f_s is known. In practice, f_s is determined iteratively.

[1]The assumption is just used as a reference in order to replace the term $\mathrm{d}x/D_\mathrm{e}$ by $\mathrm{d}A/A$ for simplifying these equations, so,

$$f_\mathrm{s} = 4f\frac{A}{D_\mathrm{e}}\frac{\mathrm{d}x}{\mathrm{d}A}\,.$$

For a given convergent channel, the term $\mathrm{d}x/\mathrm{d}A$ is known, while for the constant cross sectional channel $\mathrm{d}A$ is zero, $\mathrm{d}x/\mathrm{d}A$ is infinite so this assumption is not suitable.

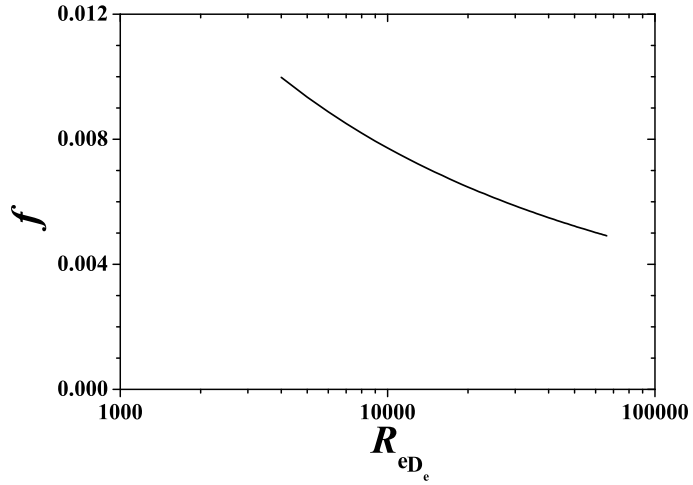

Figure 5.2: *Friction factor as function of Reynolds number $R_{\mathrm{e,D_e}}$ using Von Karman formula.*

6) Furthermore, by definition the following equation holds for the total pressure p_{t}

$$p_{\mathrm{t}} = p(1 + \Gamma_2 M_{\mathrm{a}}^2)^{1/\Gamma}, \tag{5.19}$$

or in differential form

$$\frac{1}{p_{\mathrm{t}}}\frac{\mathrm{d}p_{\mathrm{t}}}{\mathrm{d}x} = \frac{1}{p}\frac{\mathrm{d}p}{\mathrm{d}x} + \frac{\gamma M_{\mathrm{a}}}{1 + \Gamma_2 M_{\mathrm{a}}^2}\frac{\mathrm{d}M_{\mathrm{a}}}{\mathrm{d}x}. \tag{5.20}$$

7) Entropy equation

$$\begin{aligned} T\mathrm{d}s &= \mathrm{d}h - \frac{1}{\rho}\mathrm{d}p = c_p \mathrm{d}T - \frac{1}{\rho}\mathrm{d}p \\ \frac{\mathrm{d}s}{R_{\mathrm{m}}} &= \frac{1}{\Gamma}\frac{\mathrm{d}T}{T} - \frac{\mathrm{d}p}{p} = \frac{1}{\Gamma}\frac{\mathrm{d}T_{\mathrm{t}}}{T_{\mathrm{t}}} - \frac{\mathrm{d}p_{\mathrm{t}}}{p_{\mathrm{t}}} = -\frac{\mathrm{d}p_{\mathrm{t}}}{p_{\mathrm{t}}} \end{aligned} \tag{5.21}$$

with s the entropy.

8) Mass conservation

$$\dot{m} = \rho v A. \tag{5.22}$$

Using the Mach number as the variable and integrating the equations between positions 1 and 2, the further analysis in terms of dependence on Mach number and its derivative $\mathrm{d}M_{\mathrm{a}}/\mathrm{x}$ is straightforward. Finally we obtain the following results:

5.1.1.2 For the channel with constant cross-section

$$\frac{T_2}{T_1} = \frac{1 + \Gamma_2 M_{\mathrm{a},1}^2}{1 + \Gamma_2 M_{\mathrm{a},2}^2}\,, \tag{5.23}$$

$$\frac{V_2}{V_1} = \frac{\rho_1}{\rho_2} = \frac{M_{\mathrm{a},2}}{M_{\mathrm{a},1}}\left(\frac{1 + \Gamma_2 M_{\mathrm{a},1}^2}{1 + \Gamma_2 M_{\mathrm{a},2}^2}\right)^{1/2}, \tag{5.24}$$

$$\frac{p_2}{p_1} = \frac{M_{\mathrm{a},1}}{M_{\mathrm{a},2}}\left(\frac{1 + \Gamma_2 M_{\mathrm{a},1}^2}{1 + \Gamma_2 M_{\mathrm{a},2}^2}\right)^{1/2}, \tag{5.25}$$

$$\frac{p_{\mathrm{t},2}}{p_{\mathrm{t},1}} = e^{\frac{s_1 - s_2}{R_\mathrm{m}}} = \frac{M_{\mathrm{a},1}}{M_{\mathrm{a},2}} \left(\frac{1 + \Gamma_2 M_{\mathrm{a},2}^2}{1 + \Gamma_2 M_{\mathrm{a},1}^2} \right)^{\frac{1+\gamma}{2(\gamma-1)}} , \tag{5.26}$$

$$f_\mathrm{s} = \frac{4\overline{f(x_2 - x_1)}}{D} = \frac{M_{\mathrm{a},2}^2 - M_{\mathrm{a},1}^2}{\gamma M_{\mathrm{a},1}^2 M_{\mathrm{a},2}^2} + \frac{\gamma + 1}{2\gamma} \ln\left(\frac{M_{\mathrm{a},1}^2}{M_{\mathrm{a},2}^2} \frac{1 + \Gamma_2 M_{\mathrm{a},2}^2}{1 + \Gamma_2 M_{\mathrm{a},1}^2}\right) . \tag{5.27}$$

5.1.1.3 For the convergent channel

$$\tau_\mathrm{A} = \frac{A_1}{A_2} = \frac{M_{\mathrm{a},2}}{M_{\mathrm{a},1}} \left(\frac{1 + \Gamma_2 M_{\mathrm{a},1}^2}{1 + \Gamma_2 M_{\mathrm{a},2}^2} \right)^{\frac{\gamma+1}{2(\gamma-1-f_\mathrm{s}\gamma)}} \left(\frac{1 + \frac{f_\mathrm{s}\gamma}{2} M_{\mathrm{a},1}^2}{1 + \frac{f_\mathrm{s}\gamma}{2} M_{\mathrm{a},2}^2} \right)^{\frac{f_\mathrm{s}\gamma+2}{2(f_\mathrm{s}\gamma-\gamma+1)}} , \tag{5.28}$$

$$\tau_\mathrm{T} = \frac{T_2}{T_1} = \frac{1 + \Gamma_2 M_{\mathrm{a},1}^2}{1 + \Gamma_2 M_{\mathrm{a},2}^2} , \tag{5.29}$$

$$\frac{V_2}{V_1} = \frac{M_{\mathrm{a},2}}{M_{\mathrm{a},1}} \left(\frac{1 + \Gamma_2 M_{\mathrm{a},1}^2}{1 + \Gamma_2 M_{\mathrm{a},2}^2} \right)^{\frac{1}{2}} , \tag{5.30}$$

$$\frac{\rho_1}{\rho_2} = \left[\left(\frac{1 + \Gamma_2 M_{\mathrm{a},1}^2}{1 + \frac{f_s\gamma}{2} M_{\mathrm{a},1}^2} \right) \left(\frac{1 + \frac{f_\mathrm{s}\gamma}{2} M_{\mathrm{a},2}^2}{1 + \Gamma_2 M_{\mathrm{a},2}^2} \right) \right]^{\frac{f_\mathrm{s}\gamma+2}{2(f_\mathrm{s}\gamma-\gamma+1)}} , \tag{5.31}$$

$$\tau_\mathrm{p} = \frac{p_2}{p_1} = \left(\frac{1 + \Gamma_2 M_{\mathrm{a},2}^2}{1 + \Gamma_2 M_{\mathrm{a},1}^2} \right)^{\frac{2\gamma - f_\mathrm{s}\gamma}{2(f_\mathrm{s}\gamma-\gamma+1)}} \left(\frac{1 + \frac{f_\mathrm{s}\gamma}{2} M_{\mathrm{a},1}^2}{1 + \frac{f_\mathrm{s}\gamma}{2} M_{\mathrm{a},2}^2} \right)^{\frac{f_\mathrm{s}\gamma+2}{2(f_\mathrm{s}\gamma-\gamma+1)}} , \tag{5.32}$$

$$\tau_{p_\mathrm{t}} = \frac{p_{\mathrm{t},2}}{p_{\mathrm{t},1}} = \left(\frac{1 + \Gamma_2 M_{\mathrm{a},2}^2}{1 + \Gamma_2 M_{\mathrm{a},1}^2} \right)^{\frac{f_\mathrm{s}\gamma(1+\gamma)}{2(f_\mathrm{s}\gamma-\gamma+1)(\gamma-1)}} \left(\frac{1 + \frac{f_\mathrm{s}\gamma}{2} M_{\mathrm{a},1}^2}{1 + \frac{f_\mathrm{s}\gamma}{2} M_{\mathrm{a},2}^2} \right)^{\frac{f_\mathrm{s}\gamma+2}{2(f_\mathrm{s}\gamma-\gamma+1)}} . \tag{5.33}$$

The shear directional component of the momentum flux at the exhaust surface 2 can be calculated as

$$\dot{P} = \dot{m}_2 v_2 = \dot{m} M_{\mathrm{a},2} \sqrt{\gamma R_\mathrm{m} T_2} \tag{5.34}$$

where $\dot{P}$ is the momentum flow. In the operation of the RHVT, the inlet nozzle is given as a convergent channel, so the maximum exhaust velocity corresponds to $M_\mathrm{a} = 1$.

These equations determine the relationship between the channel geometry and the gas properties. Eqs. 5.23$\sim$ 5.27 are used for the constant cross sectional channel and Eqs. 5.28$\sim$ 5.33 are used for the convergent channel. Once the entrance or the exhaust flow properties are known, the relevant properties on another surface can be calculated directly. For instance, if the exhaust Mach number $M_{\mathrm{a},2}$ is 1 and the geometry of the channel is known, the inlet Mach number $M_{\mathrm{a},1}$, the pressure ratio p_2/p_1 can be calculated [3]. Important to note is that friction is taken into account. In the RHVT system the entrance information is known, so the relevant flow properties at the exhaust can be calculated. The flow chart is shown in Fig. 5.3.

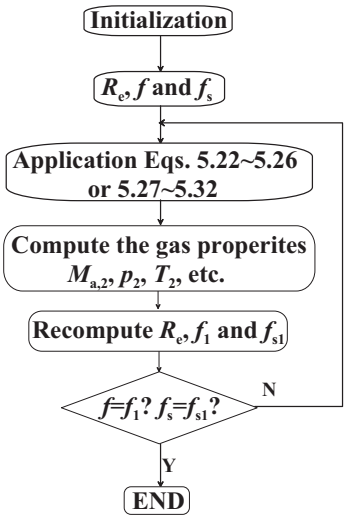

Figure 5.3: *Flow chart of the program for the nozzle analysis calculation. The program stops when the geometric friction factor f_s is convergent.*

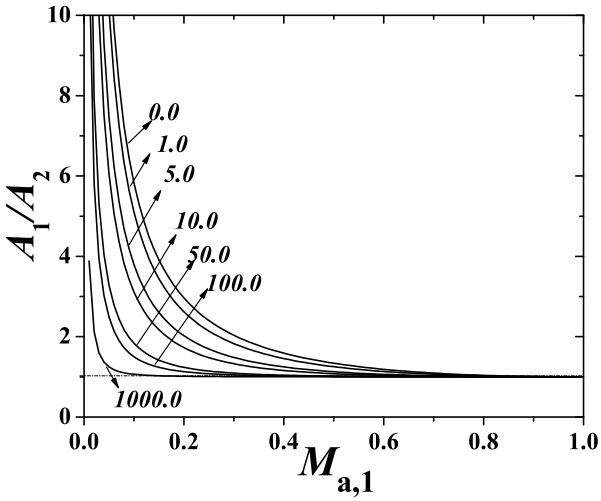

Figure 5.4: *Relationship between $M_{a,1}$ and τ_A (A_1/A_2). The numbers refer to the value of f_s. The exhaust Mach number $M_{a,2} = 1$.*

5.1.1.4 Computation of the thermodynamics parameters in the nozzle

At first, in the initialization step, the parameters (the gas properties at the entrance, the geometry, and the type of the channel) and a known inlet mass flow for the calculation are introduced. In the second step, the Reynolds numbers at the entrance, middle and exhaust of the channel are calculated based on the known inlet mass flow and the geometry using Eq. 5.1a. From these Reynolds numbers the friction factors can be calculated using Eq. 5.12, and the relevant geometric friction factors f_{s1} ($f_{s,in}$, $f_{s,m}$ and $f_{s,ex}$) are found using Eq. 5.16 (5.18 or 5.15) by using the local friction factor replacing the mean friction factors. The Mach number at the entrance is calculated using Eq. 5.1b. In the third step, with these three geometric friction factors, three different gas properties at the exhaust are calculated by using Eqs. 5.28∼5.33 (or Eqs. 5.23∼5.27 depending on the type of channel).

After the third step, with the calculated velocity, the Reynolds numbers at the exhaust are computed for different cases, furthermore the new geometric friction factors f_{s2} at the exhaust are calculated for different f_{s1}. These new geometric friction factors are compared with the ones from the previous iteration. When both values agree within 0.1%, then the iteration is stopped.

5.1.1.5 Example of the above analysis

In Fig. 5.4, the dependency of the ratio A_1/A_2 on inlet Mach number $M_{a,1}$ is shown, in case of $M_{a,2} = 1$. The effect of friction is that the larger f_s is for a fixed entrance Mach number $M_{a,1}$, the smaller the ratio A_1/A_2 has to be in order to obtain "choking" at the exit, i.e. $M_{a,2} = 1$.

Fig. 5.5 shows that, in order to reach $M_{a,2} = 1$ for a fixed entrance speed, the pressure ratio τ_p (p_2/p_1) decreases when f_s increases. This shows that at constant exhaust pressure, the entrance pressure should be increased to overcome the enhanced friction.

Fig. 5.6 shows that at fixed inlet speed, the ratio of the total pressures decreases in order to reach sound speed, if f_s increases. This means that the total pressure loss increases.

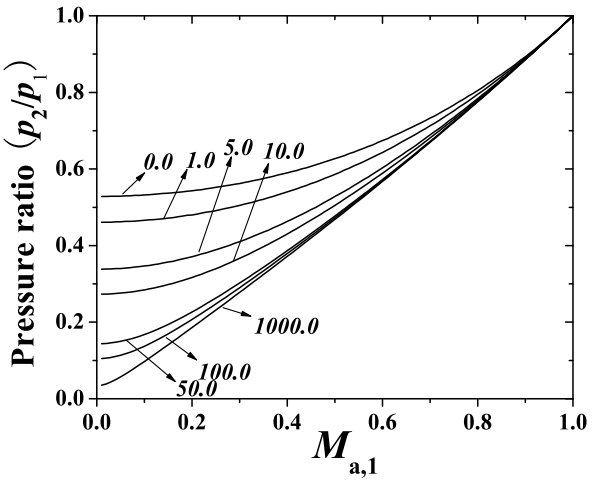

Figure 5.5: *Relationship between τ_p (p_2/p_1) and $M_{a,1}$. The numbers refer to the value of f_s.*

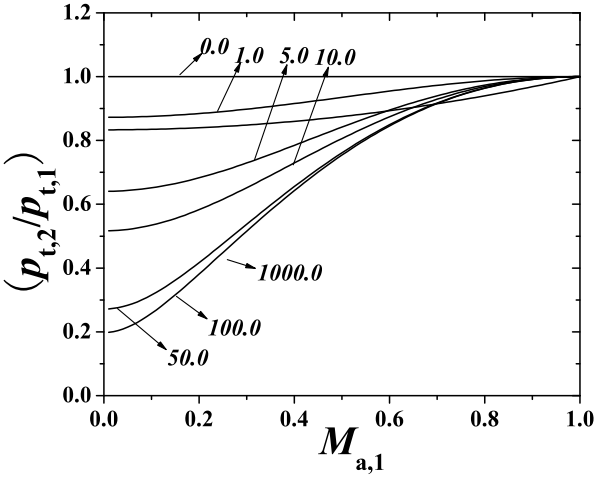

Figure 5.6: *Relationship between τ_{p_t} $(p_{t,2}/p_{t,1})$ and $M_{a,1}$. The numbers refer to the value of f_s.*

Eq. 5.29 shows that the temperature ratio is independent of f_s, and only dependent on the entrance and exhaust Mach numbers.

5.2 Comparison of the constant cross sectional and convergent channels

As mentioned in Chapter 2, the Mach number $M_{a,0}$ (in this Chapter this is denoted as $M_{a,ex}$ or $M_{a,2}$) at the exhaust of the inlet nozzle is important parameter, and should be as high as possible. Due to the chosen geometry of a convergent flow channel and submerged jet inlet in the vortex chamber the maximum M_a equals 1.

The nitrogen supply system has a maximum capacity of about 69.5 g/s. A few cases of the convergent rectangular nozzles (shown in Table 5.1) are analyzed. The gas properties at the entrance are calculated based on Eq. 5.1. For all the cases, the inlet pressure is assumed to be 4.3 bar, and the inlet temperature is 300 K, The number of slots is 8.

Channel type	Case	Height H_1 (mm)	Height H_2 (mm)
Constant	1	1.2	1.2
	2	2.0	2.0
	3	2.5	2.5
	4	3.0	3.0
Convergent	1	2.2	0.2
	2	3.0	1.0
	3	3.5	1.5
	4	4.0	2.0

Table 5.1: *The cases used for the analysis. In all cases $L = 20$ mm, and $w = 14$ mm.*

5.2.1 Calculated results

In Section 5.1.1.3, the influence of the entrance Mach number has been analyzed in order to reach Mach number 1 at the exhaust. In this section, the geometric friction factors f_s, the exhaust Mach numbers $M_{a,2}$, the exhaust pressures p_2 and pressure ratios τ_p, the exhaust temperatures T_2, the entropy generation, and the momentum flux at the exhaust etc. are discussed for the cases (constant, convergent).

5.2.1.1 Geometric friction factor f_s

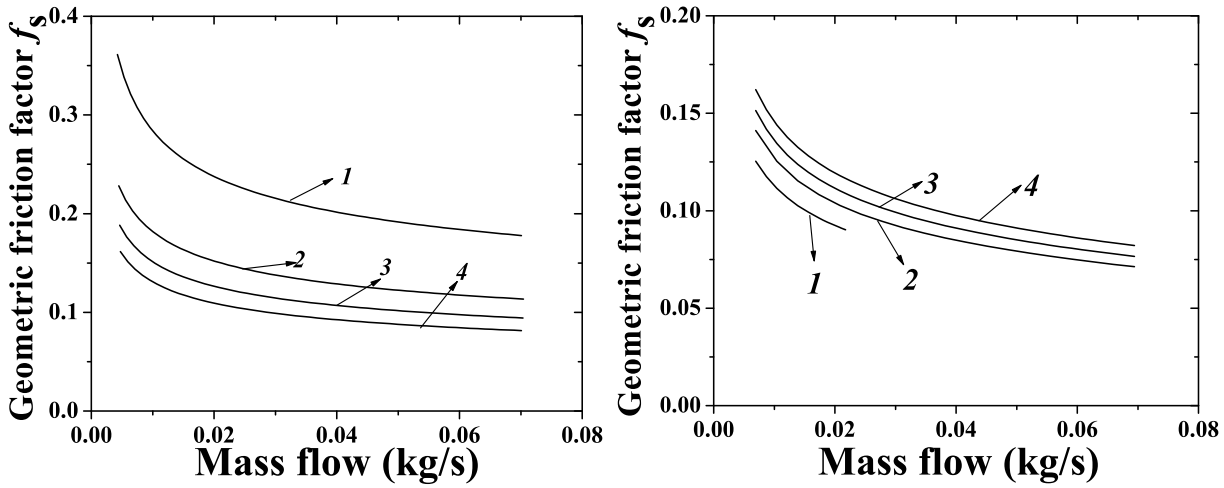

(a) Channel with constant cross-section. *(b) Convergent channel.*

Figure 5.7: *Behavior of the geometric friction factor as a function of the mass flow for different channels. The numbers refer to the cases given in Table 5.1.*

Fig. 5.7 shows the behavior of the average geometric friction factors f_s as function of the mass flow for different channels (1∼4). Fig. 5.7(a) is for the channel with constant cross-section. The geometric friction factor decreases from case (1) to (4) for the same flow. At the same constant cross sectional channel and different flows, the Reynolds number over the whole channel is dependent on the mass flow (see Eq. 5.1a), so the friction factor along the channel is dependent on the mass flow. When the mass flow increases, Reynolds number increases, and the friction factor decreases (Fig. 5.2), so the geometric friction factor f_s ($4\overline{f}L/D$) decreases (see Fig. 5.7 (a)). While from channel 1 to 4, the diameter of the channels increases, the Reynolds number decreases and then the friction factor increases at the same flow and L/D decreases. So at constant flow, the increase of the friction factor term and decrease of the geometry term leads to a decrease of the geometry friction factor, which is shown in Fig. 5.7 (a).

Fig. 5.7(b) is for the convergent channel. For the same channel, f_s decreases when the mass flow increases. For the same flow, f_s increases from case (1) to (4). According to Eq. 5.15, there are two terms that directly influence f_s, one is the mean friction factor $\overline{f}$ and the other is $(L/w)\,(2(w+H_1)/(H_1-H_2)-1)$. According to the geometry shown in Table 5.1, the channel becomes wider and larger from case (1) to (4). This indicates that the wetted perimeters of these channels increase from case (1) to (4), so the Reynolds number increases and the friction factor decreases. This leads to a decrease of the integrated friction factor.

For all cases $H_1 - H_2$ and L/w do not change, while H_1 and H_2 increase from case (1) to (4), so $(w + H_1)/(H_1 - H_2)$ increases. Both terms together cause the geometric friction factors f_s to increase from case (1) to (4) at the same flow. The mass flow for case (1) is lower than 24.3 g/s, because at this value the Mach number at the exhaust becomes 1.

Generally speaking, f_s, for constant cross sectional channels, decreases when the diameter of the channel increases (from case (1) to (4)); f_s, for convergent channels increases from case (1) to (4).

5.2.1.2 Mach numbers

Fig. 5.8 shows the inlet and exhaust Mach numbers as functions of the mass flow for the different channels. The inlet Mach number for the channel with constant cross-section is larger than for the convergent channel at the same conditions. The diameter of the constant cross sectional channel equals the diameter in the middle cross section of the convergent channel that is smaller than the entrance area of the convergent channel, using Eq. 5.1b at the same flow the Mach number with small entrance is larger.

Fig. 5.8 (a) is for the constant cross sectional channel. It is shown that the calculated exhaust Mach number equals the inlet Mach number, and these Mach numbers are all lower than 0.3. For the constant cross sectional channel, the pressure loss is only due to the friction.

Fig. 5.8 (b) is for the convergent channel. With this assumption, the exhaust Mach number increases for all four cases. For case (1), at 24.3g/s, the exhaust Mach number reaches 1. For the other three cases, the mass flow reaches the maximum capacity of the nitrogen supply 69.5 g/s, while the exhaust Mach numbers are still lower than 0.5. In order to yield the best overall performance, the injection slots should be designed in such a way that the exhaust Mach number $M_a = 1$ occurs at the maximum nitrogen supply.

5.2.1.3 Exhaust static pressures and the total pressure ratios

Fig. 5.9 shows the exhaust static pressure as a function of the mass flow for different channels. The relevant frictional pressure losses are given in Table 5.2. It is found that the static pressure losses in the convergent channel are much larger than those for the channel with constant cross-section. The pressure loss for convergent channels is partially due to the friction and partially due to the increase of the velocity.

Channel type	Case	$p_{st,ex}$ at maximum supply (bar)	static pressure loss Δp (bar)
Constant	1	4.25	0.05
	2	4.29	0.01
	3	4.30	< 0.01
	4	4.30	< 0.01
Convergent	1	2.30	2.0
	2	3.80	0.50
	3	4.15	0.15
	4	4.20	0.10

Table 5.2: *The calculated static pressure losses for different cases. The inlet pressure is fixed at 4.30 bar.*

Fig. 5.10 shows the total pressure ratio plots based on Eq. 5.26 and 5.33 for the constant

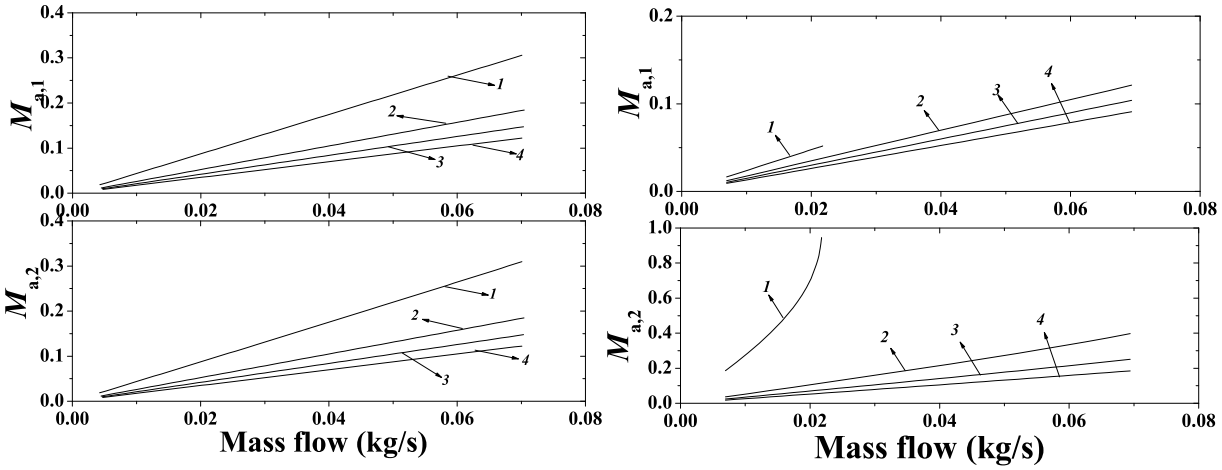

(a) Channel with constant cross-section. *(b) Convergent channel.*

Figure 5.8: *Inlet and outlet Mach numbers as function of mass flow for different channels. The numbers refer to the cases.*

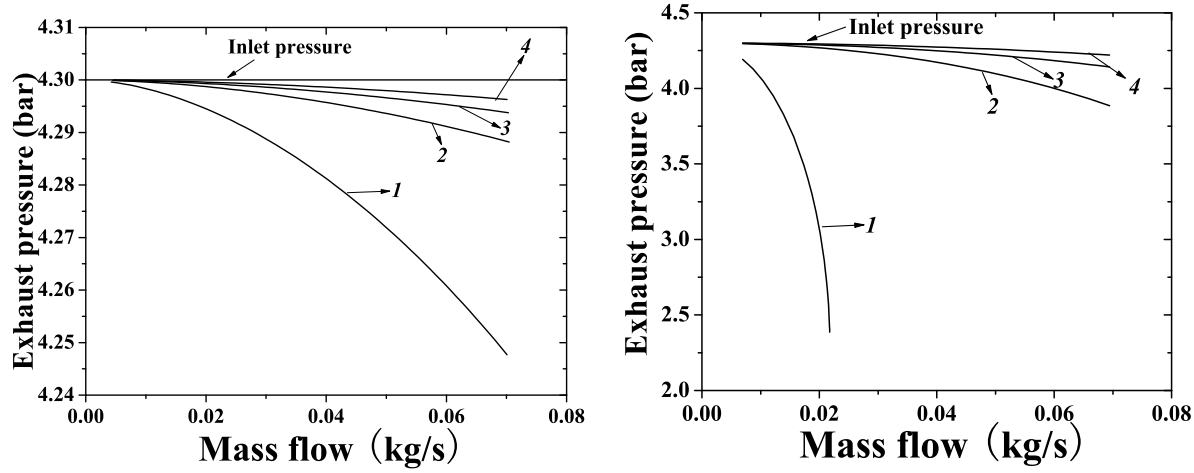

(a) Channel with constant cross section. *(b) Convergent channel.*

Figure 5.9: *Exhaust static pressure behavior as function of the mass flow for different channel conditions. The numbers refer to the cases.*

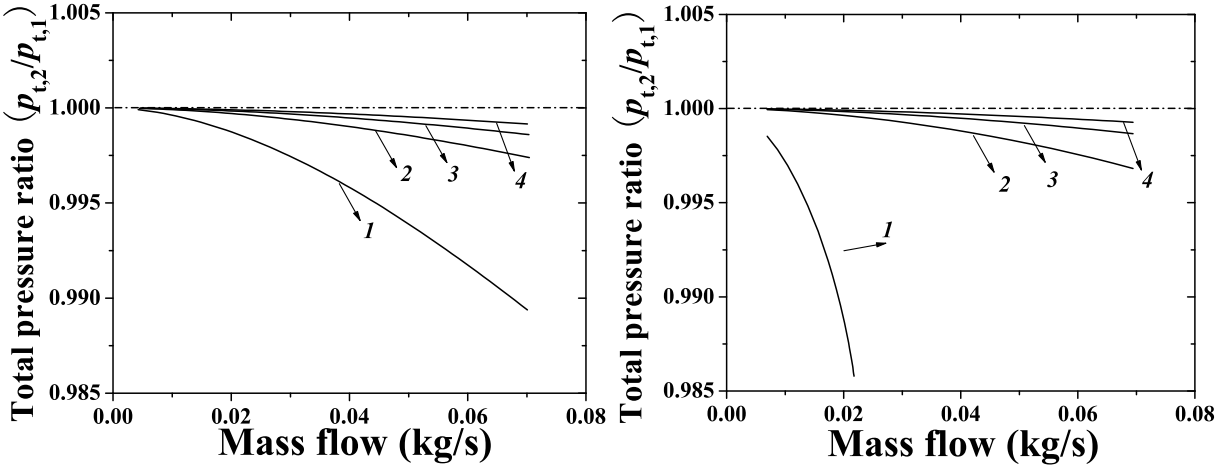

(a) Channel with constant cross-section. *(b) Convergent channel.*

Figure 5.10: *Total pressure ratio as function of the mass flow. The numbers refer to the cases.*

and convergent channels. For the constant cross sectional channel (see (a)), the total pressure loss for case (1) is only around 1%, for the other three cases, even smaller. For the convergent channel (see (b)), the total pressure loss for case (1) is about 1.5 % and for the other cases, all are lower than 1%. The total pressure loss is due to the friction, and it indicates that the total dynamic energy loss in the slot system is very small.

5.2.1.4 The momentum flow $\dot{P}$

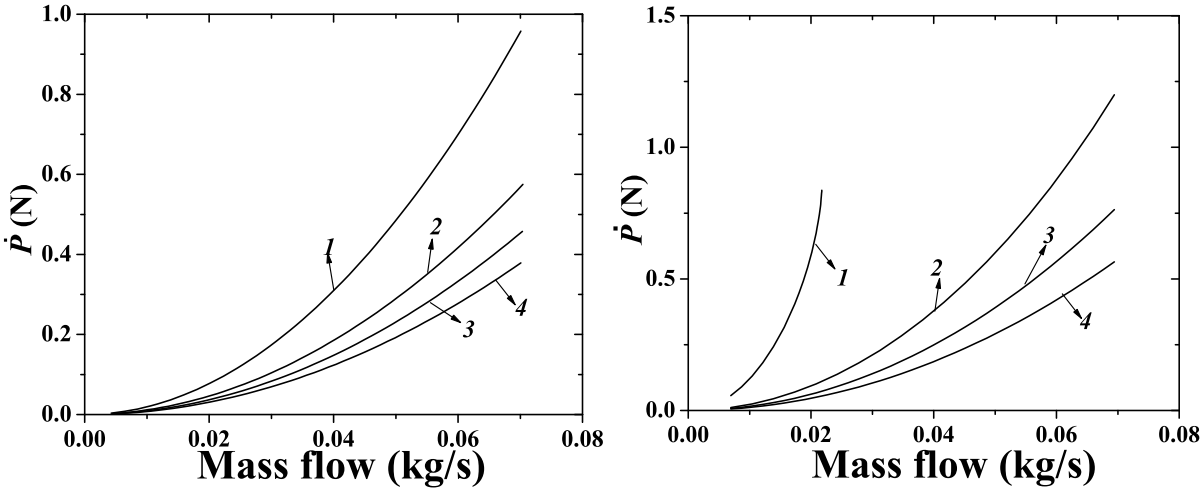

(a) Channel with constant cross section. *(b) Convergent channel.*

Figure 5.11: *Momentum flow $\dot{P}$ (see Eq. 5.34) as function of mass flow. The numbers refer to the cases.*

Fig. 5.11 shows the momentum flow $\dot{P}$ (see Eq. 5.34) as function of the mass flow. Fig. 5.11 (a) shows that $\dot{P}$ increases from case (1) to case (4) for the channels with constant cross section. Fig. 5.11 (b) shows that $\dot{P}$ for case (2) is larger than for the other three cases. The momentum surely is an interesting property to be maximized in vortex tube flow.

5.2.2 Analysis of the results

In Chapter 6, the experimental results will show that the static pressure drop over the inlet nozzle can be 2.0 bar (see Fig. 6.18 (b)) and the total pressure loss can be about 1.10 bar (see Fig. 6.16 (b)) for the case with inlet pressure of 5.10 bar, inlet flow of 69.5 g/s and cold fraction of 0.28 and the geometry of 8 inlet slots (1.0 mm at the exhaust, similar as the case (2) here). So the comparison of both configurations (constant and convergent channels) shows that the convergent channel configuration is best in agreement with the experimental situation, due to the consideration of the geometry information. So in the further analysis, the convergent channel configuration is used.

According to the analysis in Chapter 2, in order to get the best performance of the RHVT, the pressure loss over the inlet nozzle should be small, the Mach number at the exhaust of the inlet nozzle should be 1, and the momentum flow $\dot{P}$ at the exhaust should be large. From the analysis above, it is clear that the geometry of the inlet nozzle can influence the exit gas properties.

In order to reach the best performance, there exists an optimized size with the given shape geometry which matches all three requirements.

5.3 Experimental parameters influence on the nozzle

We take the approach that for the best performance of the RHVT together with the limited capacity of the supply, the Mach number at the exhaust of the nozzle should be as high as possible, the pressure loss should be as small as possible and the momentum at the exhaust should be as large as possible. Taking into account the limited supply, optimization occurs by using a short slot and more number of slots. In order to analyze the influence of these experimental parameters, nozzles with different inlet pressures, and different numbers of slots are investigated with the developed computer codes.

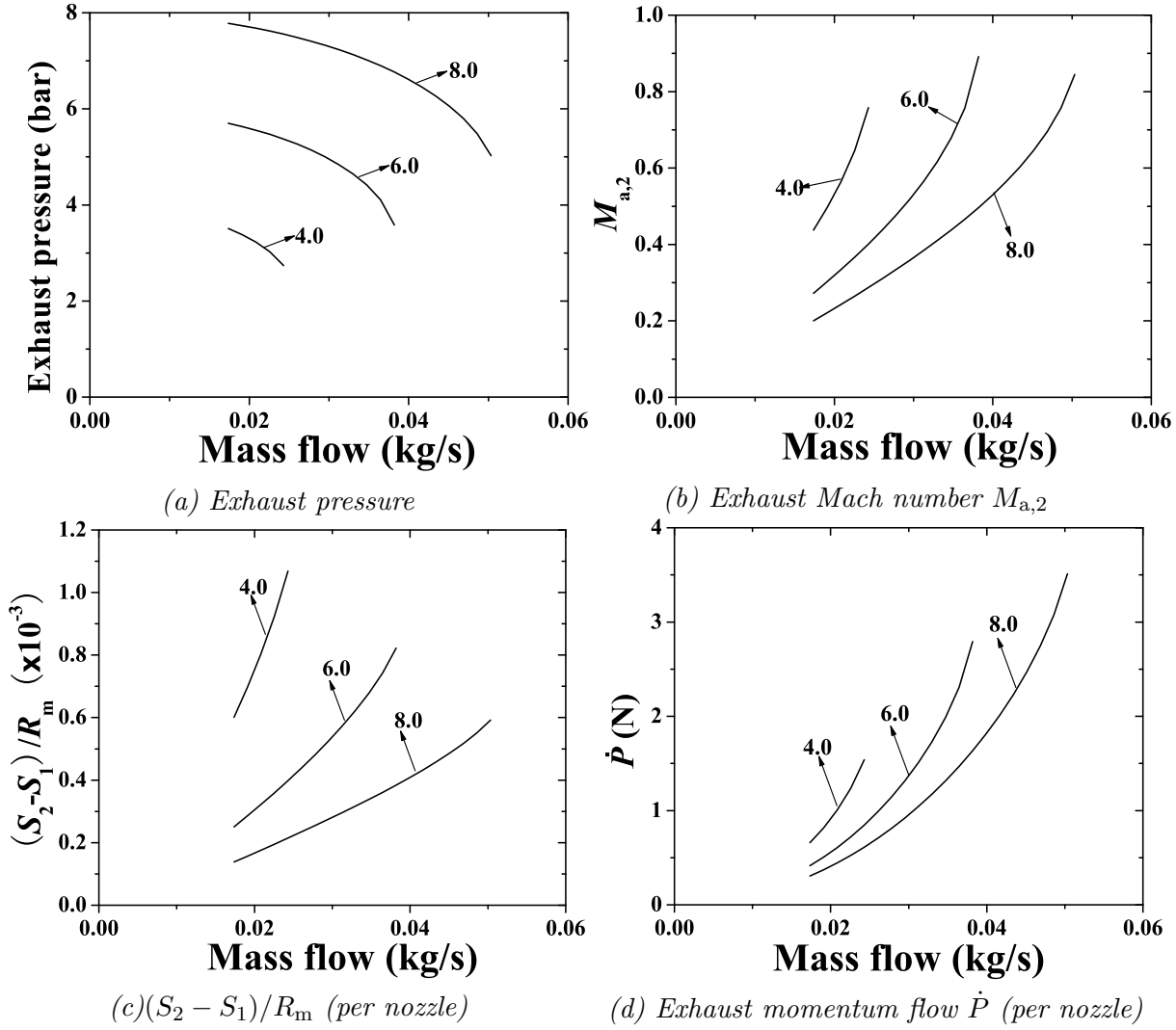

(a) Exhaust pressure

(b) Exhaust Mach number $M_{a,2}$

(c)$(S_2 - S_1)/R_m$ (per nozzle)

(d) Exhaust momentum flow $\dot{P}$ (per nozzle)

Figure 5.12: *Calculated parameters as function of total mass flow for different inlet pressures indicated in bar.*

5.3.1 Input pressure influence

Fig. 5.12 shows the calculated results as function of total mass flow for different inlet pressures with the geometry of the slots as: entrance: 5×14 mm; exit: 0.5×14 mm; length of slot: 10 mm, 4 slots. During the calculation, the maximum flow for three different inlet pressures is different, see Table 5.3. At equal inlet flow, and increasing inlet pressure, the exhaust pressure increases (see figure (a)). The exhaust Mach number shows that the inlet pressure and the value of the mass flow increase until the exhaust Mach number is 1 (see figure (b)). If the inlet pressure increases, the entropy generation is decreased (figure (c)) and the exhaust momentum is increased (figure (d)). So, in short, for the same geometry, increasing the inlet pressure can satisfy the requirement as listed above, the exhaust momentum should be large, the pressure loss should be small.

Term	4 bar	6 bar	8 bar
$F_{\text{in,max}}$ (g/s)	24.31	38.19	50.34
Exhaust static pressure (bar)	2.7	3.5	5.0
$M_{\text{a},2}$	0.8	0.9	0.85
$(S_2 - S_1)/R_{\text{m}}$ ($\times 10^{-3}$)	1.1	0.8	0.6
Exhaust momentum (N)	1.5	2.9	3.5

Table 5.3: *The maximum terms for different inlet pressures at the calculated maximum flows.*

5.3.2 The influence of the number of slots

The geometry of the slots for different numbers of slots are shown in Table 5.4. It can be found that the geometries of the three systems with different slots are scaled,

$$\phi_i n_i = \text{constant}$$

where ϕ is the geometrical parameters, i.e. H_1, H_2 and L, n is the numbers of slots and the subscription i indicates the case for 1, 4 or 8 slots, keeping the width W constant, i.e. 14 mm.

The inlet pressure for different slots stays the same, i.e. 6.0 bar, and the inlet temperature stays at 300 K.

Geometry	$n = 1$	$n = 4$	$n = 8$
H_1 (mm)	40	10	5
H_2 (mm)	4	1	0.5
L (mm)	80	20	10

Table 5.4: *The geometry of the systems with different numbers of slots. The width W for all the cases are 14 mm.*

Figs. 5.13 to 5.15 show the results for the system with a different number of slots with the scaled slot geometry. As we know, in order to realize a strongly and symmetric vortex motion inside the vortex chamber, the placement of these slots should be symmetrical inside the vortex chamber. All the figures show that the exhaust pressures, the exhaust temperatures, and the entropy generation are almost the same if the operating condition is the same (the

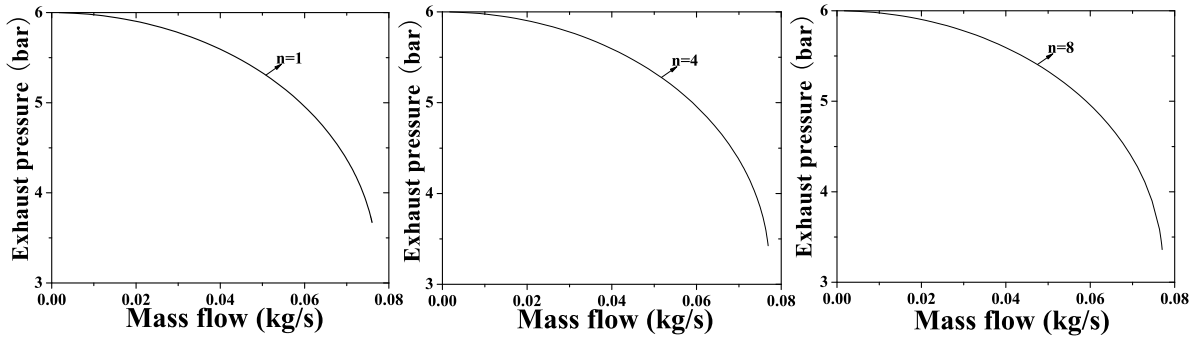

Figure 5.13: *Exhaust pressure vs. total mass flow.*

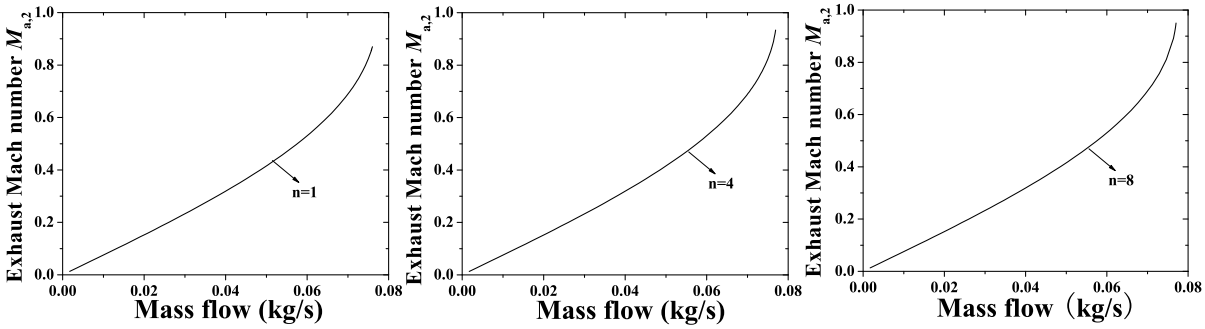

Figure 5.14: *The exhaust Mach number vs. total mass flow.*

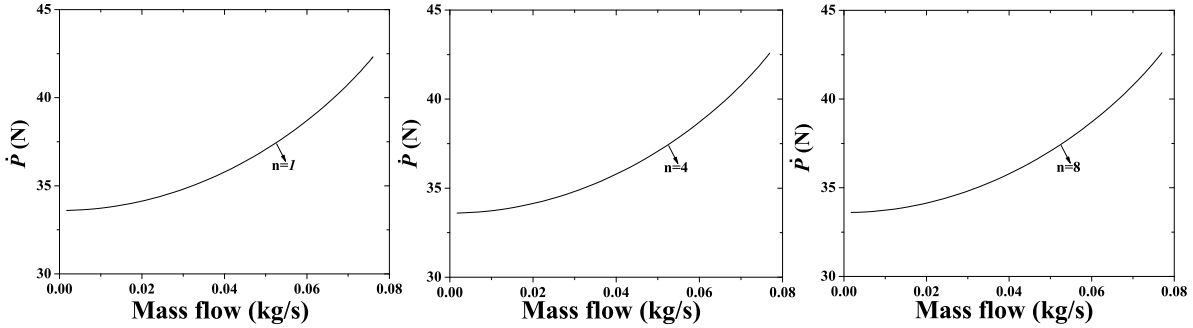

Figure 5.15: *The total exhaust momentum flow vs. total mass flow.*

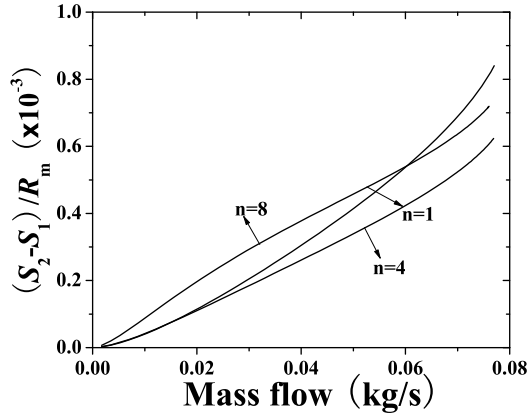

Figure 5.16: *The entropy generation ($s_2 - s_1/R_\mathrm{m}$) over one nozzle vs. total mass flow.*

total inlet mass flow, the inlet pressure are the same). This shows that we can take 8 slots without consequence for pressure loss and entropy generation. In this way the momentum flux is spread along the wall of the inner ring. It is found that the sum of the momentum flows at all exhausts is almost independent of the number of slots, i.e. for the range investigated.

5.4 Summary

Pressure loss and entropy generation due to friction have been analyzed for different geometries and different number of slots, keeping the mass flow constant. As an optimum geometry, the choice has been made for 8 slots. A maximum tangential momentum inflow always corresponds to choked condition.

References

[1] C.Gao, J.C.H. Zeegers, and M.E.H. van Dongen. Gas dynamic properties in the slot—Private communication, July 2004.

[2] H. Schlichting. *Boundary layer theory, Chapter XV.* Mc Graw Hill series in mechanical engineering. Mc Graw Hill Book Co. Inc., 4th edition, 1958.

[3] J.A. Owczarek. *Fundamentals of gas dynamics.* International textbook company, University of Wisconsin, 1964.

Chapter 6

Experimental results

In this chapter, various experiments on the different components of the RHVT have been done in order to investigate their influence. The experimental investigations of the performance of the RHVT with the cylinder type Pitot tube (CPT), single probe hot-wire anemometry (SPHWA) and thermocouple techniques are discussed. The measured velocity, pressure and temperature distributions inside the RHVT are presented and discussed.

6.1 Experimental setup

In this section, the design and optimization of the setup are explained. For the design, the setup is separated into different components, each with its own function. The optimization was carried out based on the experimental research.

6.1.1 Components of experimental setup

The experimental setup is composed out of different segments, as shown in Fig. 6.1. They are listed below. Different vortex tube sections can be mounted, so measurements are possible at various axial positions in the tube.

6.1.1.1 The cold-end exhaust

The cold exhaust ejects the cold gas from the center of the vortex chamber. It consists of the cold-end plate, the cold-end orifice, and the exhaust tube.

The cold-end plate is made of nylon for reducing heat losses. The cold exhaust is shown in more detail in Fig. 6.2. It is a divergent nylon tube with orifice diameter D_c of 15 mm, and an exhaust diameter D_{ex}, the length of the nylon tube is about 90 mm. The size of the cold end exhaust was fixed in this research.

6.1.1.2 The vortex chamber

Fig. 6.2 shows the schematic drawing of the vortex chamber. The vortex chamber is used to generate the vortex flow inside the chamber. The vortex chamber consists of an outer ring and an inner ring. The outer ring directs the nitrogen symmetrically into the outer chamber and applies a uniform pressure distribution to the inner ring. The inner ring generates the

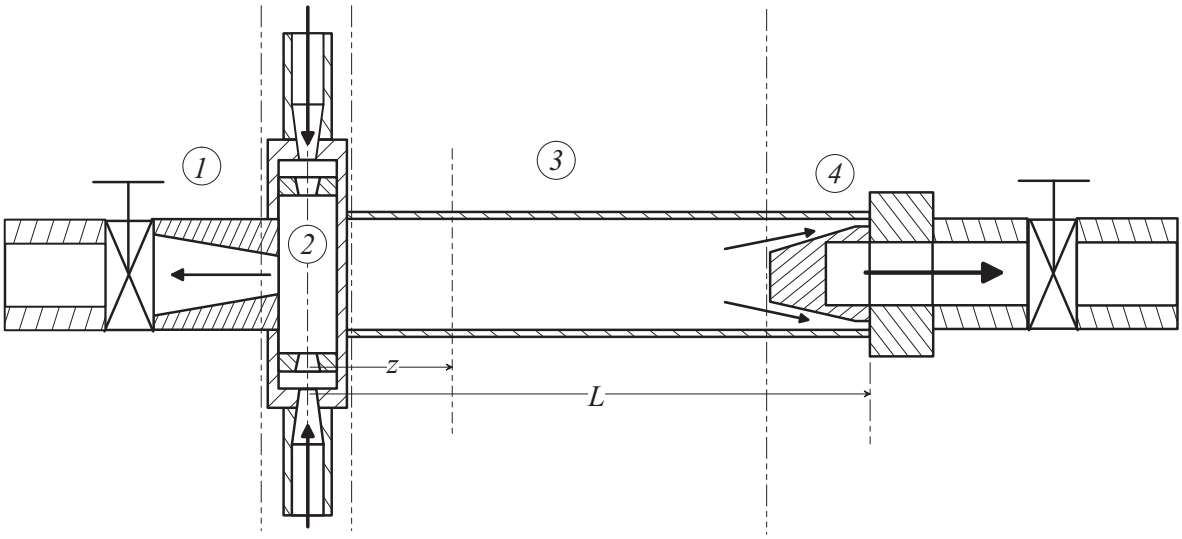

Figure 6.1: *Schematic drawing of the experimental setup: ① cold-end exhaust; ② vortex chamber; ③vortex tube; ④hot-end exhaust. There are two needle valves placed at both exhausts to control the exhausts mass flows as well as the inlet mass flow. The arrows indicate the gas flow direction.*

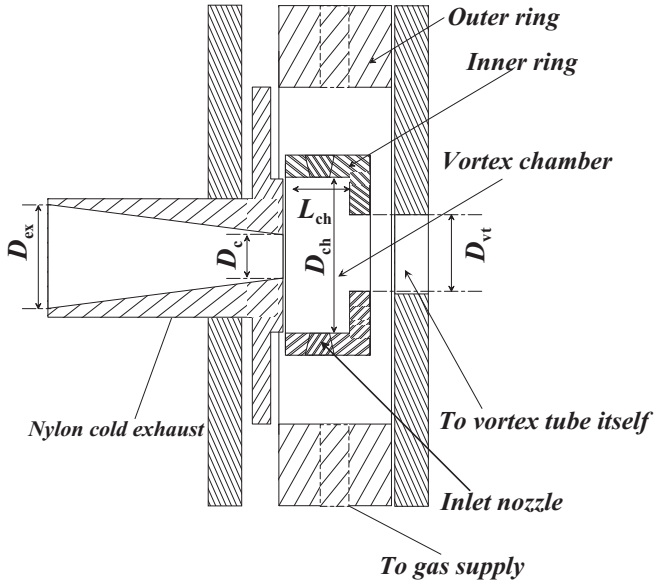

Figure 6.2: *Schematic drawing of the vortex chamber and the cold end exhaust. The figure is not to scale. D is diameter, L is length. Subscriptions:* c *is the cold exhaust orifice,* ex *is the cold exhaust tube,* vc *is vortex chamber,* vt *is the vortex tube.*

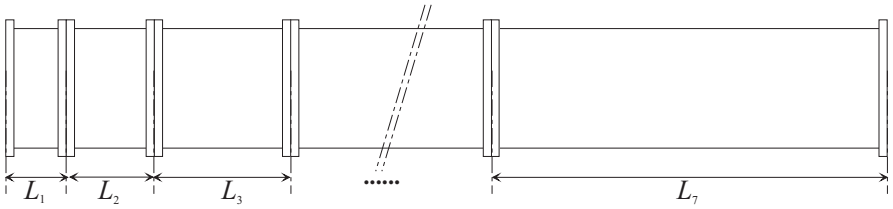

Figure 6.3: *Schematic drawing of the vortex tube indicating the various sections with a length of* L_{i}.

highly swirling flow in the inner chamber via a symmetrically installed series of convergent nozzles or slots. It is an important part of the RHVT set-up.

During all experiments, the size of the vortex chamber was constant. L_{ch} is 14 mm; the inner and outer diameters of the outer ring are 170 mm and 220 mm, respectively and the width of the outer ring is 35 mm; the inner and outer diameters of the inner ring are 80 mm and 100 mm, respectively and its width is 30 mm. The main changes during the experiments are the size and the number of the inlet nozzles and the different entrance conditions to the vortex tube itself.

6.1.1.3 The vortex tube itself

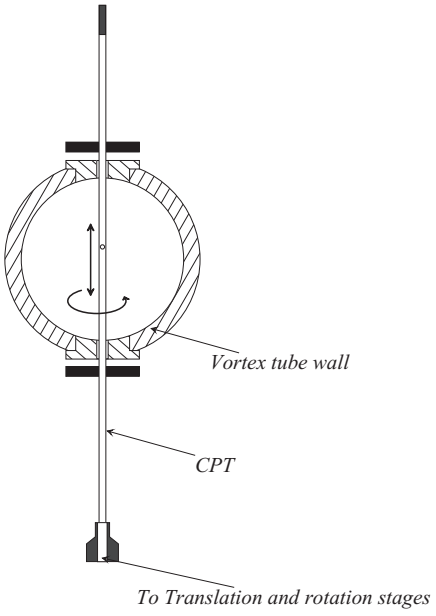

Figure 6.4: *Schematic drawing of the CPT measurement unit. The CPT probe can be rotated and translated along its axis during the measurements. The measurement hole on the wall of the cylinder can be placed at a precise position inside the vortex tube.*

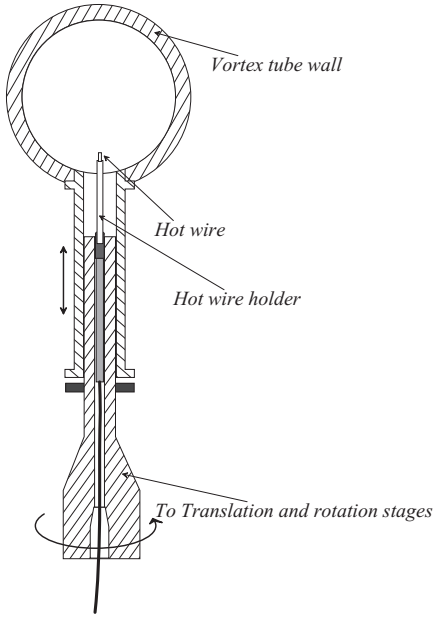

Figure 6.5: *Schematic drawing of the hot-wire measurement unit. The SPHWA probe can be rotated and translated along its axis during the measurements. The hot-wire probe can be placed at a precise position inside the vortex tube.*

The length and diameter of the vortex tube are important parameters [1–3]. So, for flexibility, the vortex tube is composed of a series ($L_1 \sim L_7$) of segments and a few measurement tube units, as shown in Fig. 6.3. With these segments, the influence of the vortex tube length can be investigated. The measurement probes can be mounted in the vortex tube at different positions. The segments include 5 tubes with a length of 37 mm (4 for CPT and THC measurements, one empty[1]). One section has a length of 57 mm and is used for SPHWA measurements. One section has a length of 77 mm and is placed as the connection for the cold end exhaust. The remaining segments include segments with a length of 157 mm, of 317

[1]The empty segment has the same geometry as the measurement units, but this one has no measurement access ports on its wall.

mm, of 637 mm and of 1277 mm. These segmental tubes can be mounted together and so a considerable variation of the total vortex-tube length is possible. The maximum length of the vortex tube is 2586 mm.

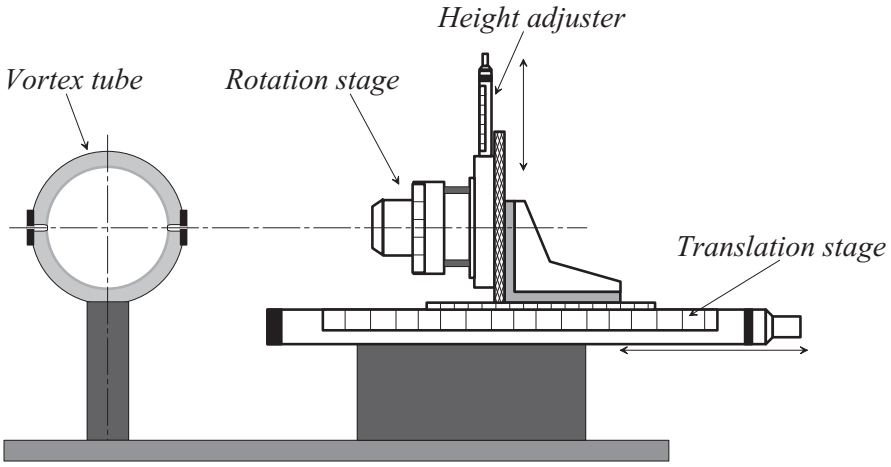

Figure 6.6: *Schematic drawing of the translation and rotation tools.*

There are two types of measurement segments: one is for the CPT measurements and THC measurements with a length of 37 mm, the second is for the SPHWA measurements with a length of 57 mm, as shown in Fig. 6.4 and 6.5. With these two segments, the pressure, temperature and velocity field inside the RHVT can be measured. The feed throughs are free of leaks to the outside. Fig. 6.6 shows the translation and rotation stages. The translation and rotation stages are mounted on a rail, and the RHVT is mounted on another rail. During the measurement, the CPT or SPHWA is clamped by the probe holder and the probe holder is connected to the measurement segment and installed on the translation and rotation stage, the height of the probe can be adjusted.

6.1.1.4 The hot-end plug

In our experiments, three different types of hot end plugs were designed, which are shown in Fig. 6.7. The information on these plugs is presented in Table 6.1, where N_{he} is the number of the exhaust orifices, D_{he} is the diameter of each exhaust orifice, $A_{\mathrm{he}}/A_{\mathrm{vt}}$ is the ratio of the total exhaust area and the vortex tube cross-sectional area.

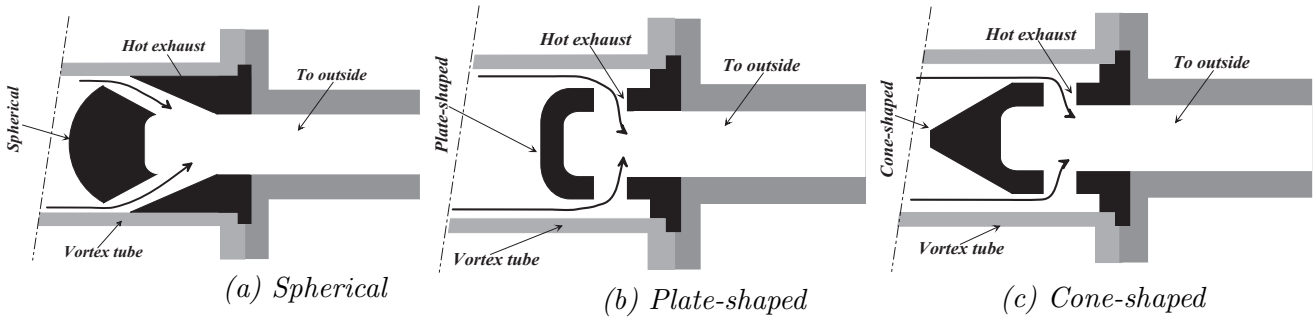

Figure 6.7: *Schematic drawing of the hot-end plugs. The arrows indicate the flow direction.*

Plug type	Plug shape	N_{he}	D_{he} (mm)	A_{he}/A_{vt} (%)
(a)	Spherical shaped plug	8	6	18
(b)	Plate shaped plug	6	10	37.5
(c)	Cone shaped plug	6	10	37.5

Table 6.1: *The geometrical information of the hot-end plugs.*

6.1.1.5 Exhaust tube

The exhaust tubes are made of plastic tube. The hot end exhaust tube has a length of about 5 meters, and the cold exhaust tube has a length of about 3 meters. The diameter of the cold exhaust tube is constant as 17 mm, and the diameter of the hot exhaust tube is investigated with 17 mm and 33 mm. The hot and cold exhaust tubes are vented to outside of the laboratory via a muffler to the open air.

Case	Ring	HEP	N_{in}	L (mm)	p_{in} (bar)	D_{ex} (mm)
1	Nozzle	Type (a)	4	318;1309;2586	5.75	17
2	Slot	Type (a)	1;2;4	2586	5.03	17
3	Nozzle; Slot	Type (a)	4;8	1309	4.85;5.75	17
4	Nozzle	Type (a)	4	2586	3.75;5.75	17
5	Nozzle	Type (a)	4	2586	5.75	17;33
6	Nozzle; Slot	Types (a), (b) and (c)	4;8	2586	4.85;5.75	33

Table 6.2: *The investigated cases for the various operation conditions. HEP means hot-end plug, D_{ex} is the diameter of the exhaust tube, N_{in} is the number of inlet nozzles.*

6.1.2 Optimization experiments

In order to study the performance of the set-up under various conditions, six cases have been defined, in which the influences of the tube length, the shape and size of inlet nozzle, the type of hot-end plug, etc. have been investigated, see Table 6.2. In the investigation, the inlet mass flow $\dot{m}_{in}$ is an important parameter together with the cold fraction ε and the inlet pressure p_{in}, and is controlled by the two needle valves placed at both exhausts. In this section, for the same case, the inlet pressure is constant, the inlet mass flows under different cold fractions are almost constant by adjusting the two control valves. The vortex tube diameter D_{vt} is always equal to 40 mm. For the vortex chamber, the inner diameter of the inner ring D_{vc} is always equal to 80 mm. In all the subsections from this section, for all the figures which are about temperature differences, symbol ■ is for $T_h - T_{in}$ and • for $T_{in} - T_c$. All measurements are made with nitrogen gas.

6.1.2.1 The influence of tube length L

Three different tube lengths (318 mm, 1309 mm and 2586 mm) have been investigated. The geometry of the system is the one of Case 1 in Table 6.2. Fig. 6.8 shows the results for the tube with $L = 318$ mm and 2586 mm under the same operation condition. The result for the tube with $L = 1309$ mm is shown in Fig. 6.10 (a)).

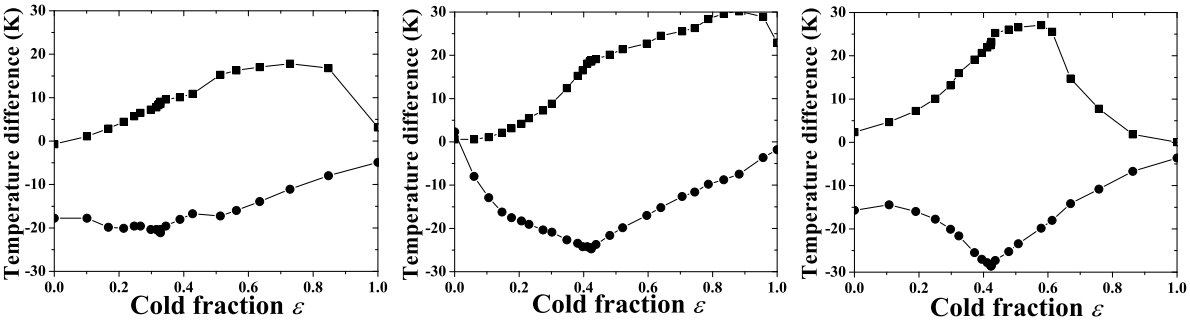

(a) $L = 318$ mm. *(b) $L = 1309$ mm.* *(c) $L = 2586$ mm.*

Figure 6.8: *Case 1: The temperature differences ($T_\mathrm{h} - T_\mathrm{in}$, $T_\mathrm{in} - T_\mathrm{c}$) for two tube lengths as function of the cold fraction ε.*

The influence of the tube length is clear from Fig. 6.8. When the tube length increases from 318 mm up to 2586 mm, the maximum temperature ΔT obtained increases, so the performance improves. Table 6.3 shows the maximum temperature differences obtained for three different lengths, where $\Delta T = T_\mathrm{h} - T_\mathrm{c}$, $\Delta T_\mathrm{h} = T_\mathrm{h} - T_\mathrm{in}$ and $\Delta T_\mathrm{c} = T_\mathrm{c} - T_\mathrm{in}$. So in general, increasing the tube length increases the temperature difference ΔT.

Length (mm)	$\dot{m}_\mathrm{in}$ (g/s)	L/D_vt	ΔT (K)	ΔT_h (K)	ΔT_c (K)
318	52.1	8.0	32.5 at $\varepsilon = 0.5$	18 at $\varepsilon = 0.75$	-21 at $\varepsilon = 0.35$
1309	52.1	32.7	43 at $\varepsilon = 0.45$	30 at $\varepsilon = 0.9$	-25 at $\varepsilon = 0.45$
2586	53.8	64.7	52.5 at $\varepsilon = 0.45$	27 at $\varepsilon = 0.6$	-28 at $\varepsilon = 0.45$

Table 6.3: *Case 1: The maximum temperature differences obtained for different tube lengths. The inlet mass flows are slightly the same.*

6.1.2.2 The influence of the inlet nozzle

In order to investigate the influence of inlet nozzles, a few preliminary tests have been carried out. First the work done with the number of inlet nozzles. Using slot ring. All the slots in the inner ring have the same geometry and are symmetrically placed in the inner ring as shown in Case 2 of Table 6.2. The exhaust of the slot is rectangular 14×1.2 (mm). There are three inner rings with different numbers of slots used, one inner ring with 4 slots, one with 2 slots and one with 1 slot. The tube length for all these tests was the same as 2586 mm; the inlet pressure was 5.03 bar.

Fig. 6.9 shows the influence of the number of slots. The temperature differences at $\varepsilon = 0.30$, for which the differences are maximal, are given in Table 6.4. These experiments show that increasing the number of slots improves the performance. This is also noticed by Takahama [1].

Note that with more slots, the total flow area at the exhaust of the inlet nozzles increases, so at the same inlet pressure, the inlet flow increases, see Table 6.4. This may also be the reason for the improvement.

In our experiments, we investigated slots and circular nozzles for the inlet nozzle to the vortex chamber. The geometry and operation conditions of the two rings are shown in Table 6.5, where N_in is the number of slots or nozzles, $A_\mathrm{in}/A_\mathrm{vt}$ is the ratio of the total injection area over the vortex tube cross-sectional area.

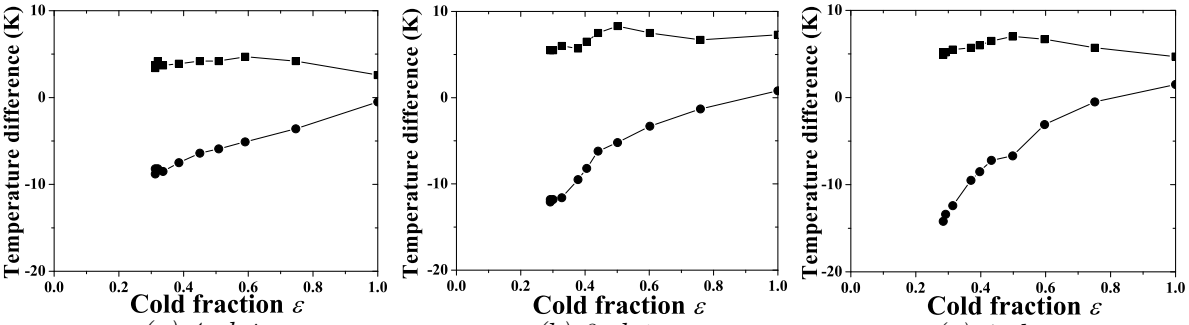

(a) 1 slot *(b) 2 slots* *(c) 4 slots*

Figure 6.9: *Case 2: The temperature differences for different number of slots as function of cold fraction ε.*

Number of slots	$\dot{m}_{\mathrm{in}}$ (g/s)	ΔT (K)	ΔT_{h} (K)	ΔT_{c} (K)
1	18.1	12.5	8.5	-4.5
2	30.2	17.5	12	-8
4	40.3	19.5	14	-7

Table 6.4: *Case 2: The maximum temperature differences for different number of slots. The exhaust of the slot is rectangular* 14×1.2 *mm, and the equivalent diameter* $D_{\mathrm{in,e}}$ *is 2.2 mm.*

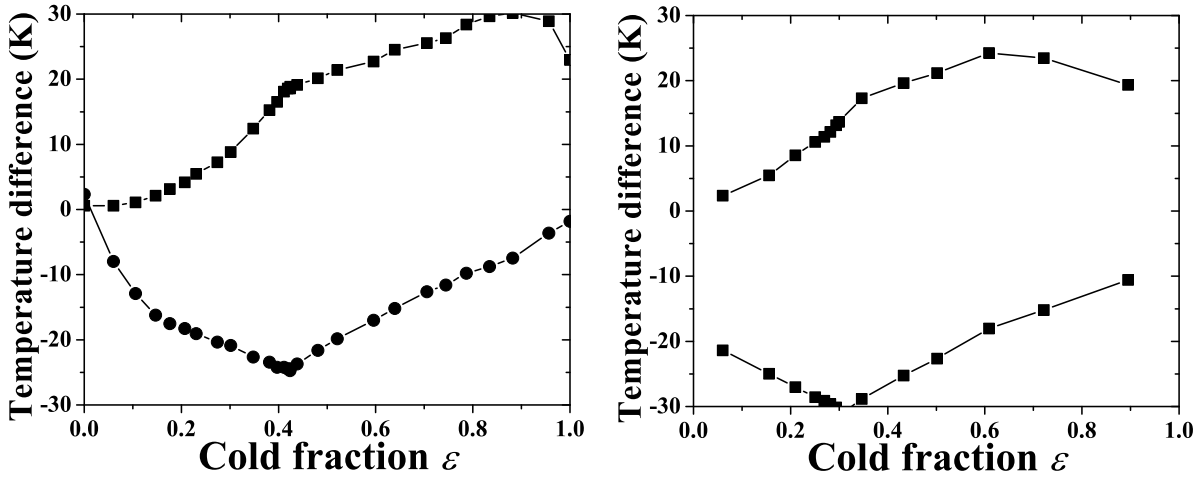

(a) Inner ring with 4 circular nozzles, $p_{\mathrm{in}} = 5.75$ bar.

(b) Inner ring with 8 slots, $p_{\mathrm{in}} = 4.85$ bar.

Figure 6.10: *Case 3: The temperature difference for two different inner rings as function of cold fraction ε.*

Type	N_{in}	$A_{\mathrm{in}}/A_{\mathrm{vt}}$ (%)	p_{in} (bar)	$\dot{m}_{\mathrm{in}}$ (g/s)	ΔT_{hc} (K)	ΔT_{h} (K)	ΔT_{c} (K)
Circular nozzle	4	12	5.75	52.1	43	30	-25
Rectangular slot	8	9	4.75	55.5	48	24	-32

Table 6.5: *Case 3: The geometry, inlet pressure and maximum temperature differences for two different rings. The tube length was 1309 mm, the hot-end plug was type (a).*

Fig. 6.10 shows the temperature difference with different types of inner rings as function of cold fraction ε, (a) is for the ring with 4 circular nozzles and (b) for the ring with 8 slots. The inlet pressure for the measurement with the nozzle ring is 5.75 bar and for the measurement with the slot ring is 4.85 bar. The opening of the injection with nozzle ring is 3% larger than the slot ring, so under the same inlet pressure and same cold fraction, the inlet flow with the nozzle ring is larger than that with the slot ring. Table 6.5 shows the maximum temperature differences achieved in the measurements. It shows that the maximum ΔT of the system with slots is slightly larger than that with nozzles. If the inlet pressures for these two systems would have been equal, then the performance of the system with slots would still be better.

6.1.2.3 The influence of the inlet pressure

The influence of the inlet pressure was already mentioned in Chapters 2 and Chapter 5. The influence of the inlet pressure has also been investigated experimentally in the present study. Fig. 6.11 shows the influence of the inlet pressure, (a) is for an inlet pressure of 5.75 bar and (b) for 3.85 bar. Furthermore, the RHVT has the nozzle ring with 4 circular nozzles, with exit diameter of around 7 mm (for one nozzle), the hot-end plug is type (a), the length of the vortex tube is 2586 mm. The maximum temperature differences are shown in Table 6.6. This shows that when the inlet pressure increases, the maximum temperature differences increase. In Chapters 2 and 5, we found that there exists a critical value for the pressure ratio $p_{\mathrm{in}}/p_{\mathrm{c}}$. The performance of the RHVT can be improved by increasing the inlet pressure to the critical value. It should be noted that when the inlet pressure p_{in} increases, with the same system and same cold fraction ε, the inlet flow $\dot{m}_{\mathrm{in}}$ increases too.

p_{in} (bar)	$\dot{m}_{\mathrm{in}}$(g/s)	ΔT (K)	ΔT_{h} (K)	ΔT_{c} (K)
3.75	34.2	41	20	-24
5.75	53.8	52.5	27	-28

Table 6.6: *Case 4: The maximum temperature differences for two different inlet pressures. The system includes 4 circular nozzles with exit diameter of 7 mm, the hot-end plug is type (a), the tube length is 2586 mm.*

6.1.2.4 The influence of the pressure on the vortex tube exits

As mentioned in Chapters 2 and 5, the exhaust pressure is an important parameter. At best the pressure at the cold end as well as hot end are close to the atmosphere pressure. For the exhaust tubes that have a diameter of 17 mm and 33 mm, length of 10 meters, for the flow of $\dot{m}_{\mathrm{in}}$ 69.5 g/s, the pressure drop for 17 mm tube is about 2.2 bar, while for 33 mm tube, it is less than 0.2 bar. So generally the absolute exhaust pressure is not always 1 bar.

The results of the experiments with the exhaust tubes with inner diameter D_{ex} as 17 mm and 33 mm are shown in Fig. 6.12. The RHVT was mounted with a nozzle ring with 4 nozzles and the exit diameter of the nozzle is 7 mm, the vortex-tube length 2586 mm, the hot-end plug type (a), the inlet pressure as 5.75 bar. Table 6.7 shows that the maximum temperature differences with the 33 mm tube are larger than with the 17 mm tube. This indicates that the pressure at the RHVT exit is important. When the pressure losses over the exhaust tubing are low the performance can be improved because $p_{\mathrm{in}}/p_{\mathrm{ex}}$ is larger.

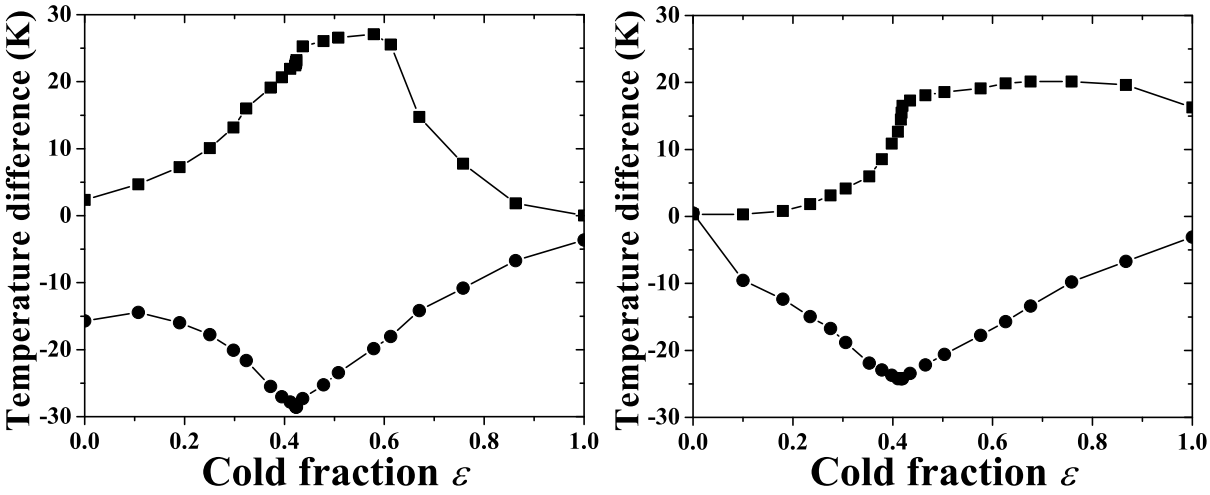

(a) $p_{\text{in}} = 5.75\text{bar}$ *(b)* $p_{\text{in}} = 3.75\text{bar}$

Figure 6.11: *Case 4: The influence of the inlet pressure on the performance of the RHVT with nozzle rings.*

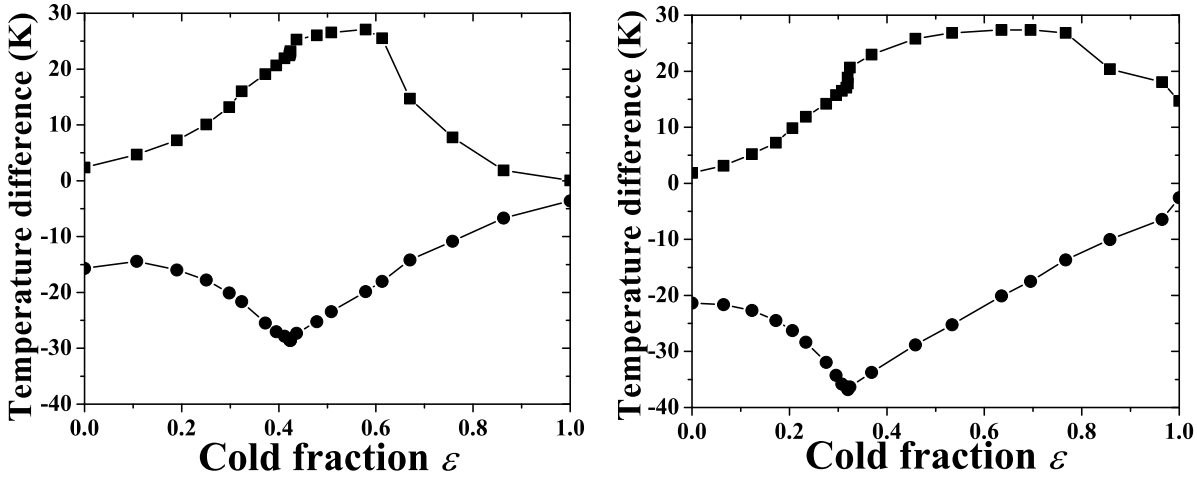

(a) $D_{\text{ex,h}} = 17$ mm, $D_{\text{ex,c}} = 17$ mm *(b)* $D_{\text{ex,h}} = 33$ mm, $D_{\text{ex,c}} = 17$ mm

Figure 6.12: *Case 5: The performance of the RHVT for different exit tubing systems.*

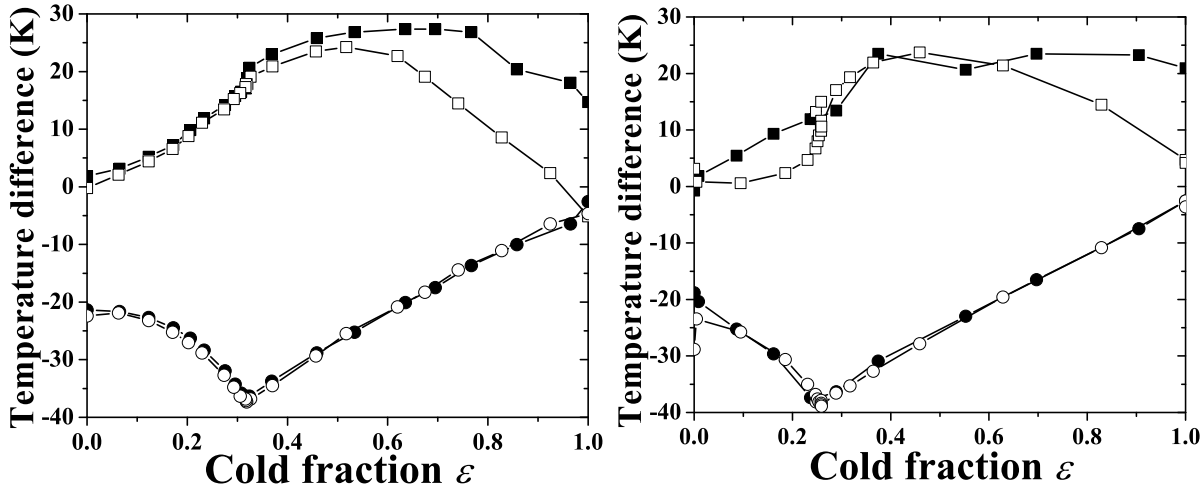

(a) Plug (a) and (b) with the nozzle ring. *(b) Plug (a) and (c) with the slot ring.*

Figure 6.13: *Case 6: The influence of the hot end plugs on the temperature differences.*

D_{ex} (mm)	$\dot{m}_{in}$ (g/s)	ΔT (K)	ΔT_h (K)	ΔT_c (K)
17	53.8	52.5	27	-28
33	66.4	57.5	27.5	-37

Table 6.7: *Case 5: The maximum temperature differences results for different exhaust tubes.*

Some experiments were performed without the exhaust tube during a short time. In that case the gas from the cold end directly escapes into the laboratory. At an inlet pressure of 4.85 bar, flow of 68.1 g/s, the cold fraction ε around 0.4, the vortex tube length 2586 mm and the inner ring with 8 slots (1×14 mm), $\Delta T = 78$ K, $\Delta T_h = 37$ K, and $\Delta T_c = -41$ K. This is the maximum temperature difference ever generated in the system under similar conditions.

Generally, under equal inlet pressures and geometrical conditions, the performance of the RHVT can be improved by decreasing the exhaust pressures to the lowest value.

6.1.2.5 The influence of the hot-end plugs

In section 6.1.1, the different hot-end plugs have been shown. In Fig. 6.13 (a), the comparisons between the results for hot-end plugs (a) and (b) are shown. The maximum temperature differences are shown in Table 6.8. The temperature differences obtained with plug (a) is slightly larger than that with plug (b).

hot end plug	$\dot{m}_{in}$ (g/s)	ΔT (K)	ΔT_h (K)	ΔT_c (K)
(a)	67.0	57.5	27.5	-37
(b)	66.4	55.5	22.5	-35

Table 6.8: *Case 6: The maximum temperature differences for two different hot-end plugs. The inner ring has 4 circular nozzles with exit diameter* $D_{in,e} = 7$ mm*,* $L = 2586$ mm*,* $p_{in} = 5.75$ bar*,* $D_{ex,c} = 17$ mm *and* $D_{ex,h} = 33$ mm*.*

hot end plug	N_{in}	$\dot{m}_{in}$ (g/s)	ΔT (K)	ΔT_h (K)	ΔT_c (K)
(a)	8	55.6	54.5	23.5	-37.5
(c)	4	40.0	55	24	-38.5

Table 6.9: *Case 6: The geometry and maximum temperature differences for two different hot-end plugs. The inner ring consists of numbers* N_{in} *of rectangular slots with exit equivalent diameter* $D_{in,e} = 2.2$ mm*,* $L = 2586$ mm*,* $p_{in} = 4.85$ bar*,* $D_{ex,c} = 17$ mm *and* $D_{ex,h} = 33$ mm*.*

The comparisons between the results for hot-end plugs (a) and (c) are shown in Fig. 6.13 (b). The geometry, operation condition and the maximum temperature differences are shown in Table 6.9. The performances are very close. The temperature differences generated with the hot-end plug (c) are slightly larger than those with the plug (a).

Note that at high ε, there are significant differences for ΔT_h obtained for these plugs. ΔT_h for $\varepsilon = 0.6$ towards 1 for plug (a) is largest.

Experiments without the hot-end plug have also been done, and show that the energy separation effect still exists. using an inner ring with 4 slots with exit equivalent diameter of 2.2 mm, $L = 2586$ mm $p_{in} = 4.85$ bar and $D_{ex,h} = 33$ mm, without hot-end plug, the total

temperature difference obtained is about 30 K. This indicates that the hot-end plug is not a critical component in the RHVT.

6.1.2.6 The influence of the opening in the slot ring

During the experiments, various slot-rings with exhaust geometries 1×14 mm, 0.65×14 mm and 0.4×14 mm have been used. All rings have 8 slots, $L = 2586$ mm, $D_{\mathrm{ex,c}} = 17$ mm and $D_{\mathrm{ex,h}} = 33$ mm. Here only a comparison between the results for the slot ring with 1×14 mm slots and the one with 0.4×14 mm slots is made.

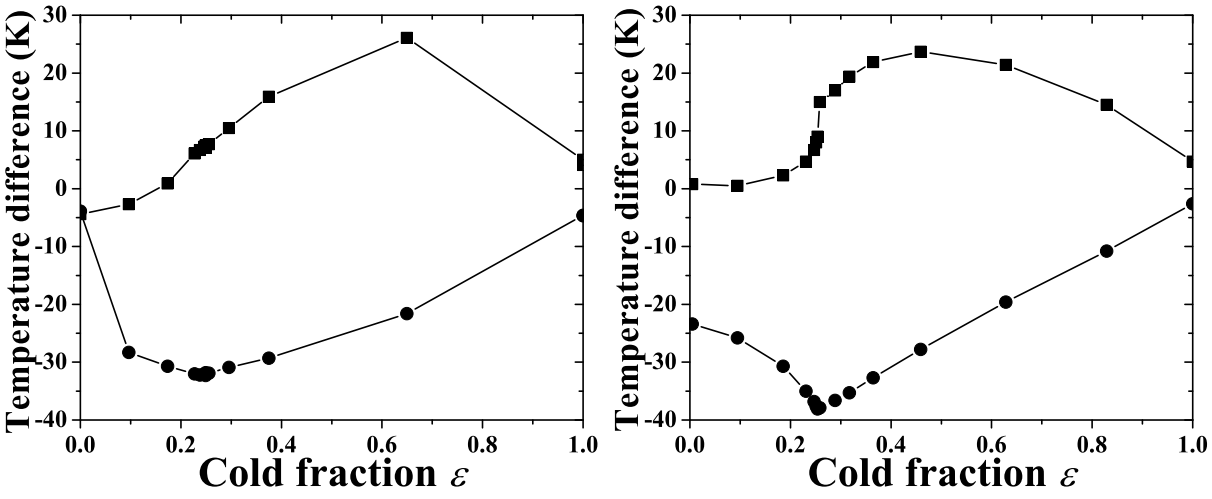

(a) 0.4 × 14 *mm* *(b)* 1 × 14 *mm*

Figure 6.14: *The temperature differences for two openings of the slot ring as function of cold fraction ε.*

Opening	p_{in} (bar)	$\dot{m}_{\mathrm{in}}$ (g/s)	ΔT (K)	ΔT_{h} (K)	ΔT_{c} (K)
0.4×14	4.85	23.3	47	26	-32.5
1.0×14	4.75	55.6	55	24	-38

Table 6.10: *The maximum temperature differences for the different openings of slot-rings. The inner ring has 8 slots,* $L = 2586$ mm, $D_{\mathrm{ex}} = 33$ mm *and the hot end plug is type (c).*

Fig. 6.14 shows the temperature differences for the two different openings of the slots. The maximum temperature differences are shown in Table 6.10. So the temperature differences generated with 1 × 14 mm slots are slightly larger than those with 0.4 × 14 mm slots.

6.1.3 Discussion on the results of the preliminary tests

In [4], Takahama suggested to use a tube length $L \geq 100 D_{\mathrm{vt}}$ in order to obtain a better performance. In [5–7], the tube length was suggested to be longer than $45 D_{\mathrm{vt}}$. In our measurements, the result of the study of the influence of the tube length suggests that a tube length of 2586 mm is optimal, corresponding to L/D_{vt} is about 65 (No larger L/D_{vt} ratios were tested).

In [8], Reynolds suggested to inject the gas in the vortex chamber through a slot. He mentioned that the slot improved the performance of the RHVT. Reynolds suggested to have more slots in the RHVT. He noted that more slots do improve the performance as well. His findings are confirmed by our experiments.

The influence of the inlet pressure and that of the exhaust pressure are very clear, which is because of the increase of the pressure ratio τ_{p} (mentioned in Chapter 2). Increasing the inlet pressure and decreasing the exhaust pressure do improve the performance of the RHVT.

The measured results with the hot-end plug suggest that the hot-end plug is not a critical component. There are small differences between the results for different plugs.

In summary, the tube length L, the inlet pressure p_{in}, the geometry of the nozzle (type, sizes and number) and the exhaust pressure (exhaust tubes) are important parameters. Increasing the vortex tube length, applying a slot-ring instead of the nozzle ring, using a large number of slots and using a larger exhaust tube to decrease the exhaust pressures all can increase the temperature differences and improve the performance.

6.2 Final experimental investigation

After these preliminary investigations in Section 6.1.2, the final experimental set-up is chosen consisting of the following components: the inner ring with 8 slots and rectangular exit 1×14 mm and $D_{\mathrm{vc}} = 80$ mm, the vortex tube with $L = 2586$ mm and $D_{\mathrm{vt}} = 40$ mm ($L/D_{\mathrm{vt}} = 64.65$), the cone-shaped hot-end plug as type (c) in Fig. 6.7.

In Chapter 3, the calibrations of the CPT, SPHWA and THC techniques were discussed, and in Chapter 4 the first impression about application of the CPT and THC techniques on a simple RHVT was given. During the measurements, data were obtained at the following stations:

ⓐ Vortex chamber: Only the CPT was used to measure the pressure and velocity fields inside the vortex chamber;

ⓑ Station $1 \sim 5$: Station 1 is close to the vortex chamber and Station 5 is close to the hot exhaust, z/L (see Fig. 6.1) for these five stations is about 0.033, 0.108, 0.231, 0.477 and 0.985, respectively and z/D_{vt} is about 2.13, 6.98, 14.91, 30.84 and 63.68, respectively.

The inlet mass flow is a function of the cold fraction ε and the inlet pressure p_{in}. The experiments have been done with two inlet flows. One is 69.5 g/s and the other is 34.7 g/s. For the inlet flow of 69.5 g/s, four different cold fractions (0.04, 0.28, 0.39 and 0.90) have been investigated (the inlet mass flow for $\varepsilon = 0.90$ is 55.6 g/s, while the inlet pressure is the same as 5.10 bar). For the inlet flow of 34.7 g/s, only two different cold fractions (0.28 and 0.39) were investigated.

The results for $\varepsilon = 0.28$ at two inlet flows are chosen as examples, and shown here. All examples with the CPT, the SPHWA, and the THC are presented separately. Generally it takes three separate runs to measure with the three different techniques. For the analysis, all experiments made with the same geometry and for equal operation conditions are assumed to be repeatable. Then the measured results with three different techniques are analyzed together in order to calculate the pressure, temperature, and velocity fields.

The static pressure p_{st} is measured by the CPT technique, the stagnation temperature T_{sg} is measured by the THC techniques, and the SPHWA technique is used to determine the mass flow density (ρV). By applying the Bernoulli equation and energy conservation, with the measured terms p_{st}, T_{sg} and ρV, the static temperature T_{st} and the velocity V can be

calculated, see section 6.3.

6.2.1 CPT technique measurements

Here only the results for $\varepsilon = 0.28$ for two different inlet flows will be discussed. The inlet pressure for all the measurements with inlet flow of 69.5 g/s is 5.10 bar; for the measurements with inlet flow of 34.7 g/s the inlet pressure is 2.80 bar. The examples are classified as: Example (a): $\dot{m}_{\text{in}} = 34.7$ g/s and $p_{\text{in}} = 2.80$ bar; Example (b): $\dot{m}_{\text{in}} = 69.5$ g/s and $p_{\text{in}} = 5.10$ bar.

6.2.1.1 Flow directions

There are some common aspects of the flow direction inside the RHVT independent of the parameter settings:

① The angle of the flow[2] in the region $R_{\text{vt}} < r < R_{\text{vc}}$ inside the vortex chamber is 0. The flow in this region has only azimuthal and radial velocity components, the axial velocity component is zero.

② A critical radius, defined as the radius at which the flow reverses its axial direction, exists for both flows, even when the cold fraction is nearly zero. There is even a critical radius at the station that is close to the hot end. This indicates that a secondary circulation occurs in most cases.

③ The critical radius varies along the $Z-$axis, it decreases in Z-direction when the station is closer to the hot end. At Station 5, which is near the hot exhaust, the critical radius cannot be defined due to the small velocity.

④ The angle of the flow near the center is close to -90 deg, which means that the azimuthal velocity near the center is very small and the axial velocity is to the cold end.

⑤ The angle of flow near the vortex tube wall increases for the stations near the hot end. This indicates the decreasing of the azimuthal velocity component towards the hot end.

Fig. 6.15 shows the flow direction as measured with the CPT for inlet flows of 69.5 g/s and 34.7 g/s. The angles of flow, the critical radius, the maximum angle near the wall etc. obtained from the two figures are listed in Table 6.11, where $r_{\text{cr}}|_{\alpha=0}$ is the critical radius, $\alpha_{r=0}$ is the angle of the flow at the center of the tube and $\alpha_{\max}$ is the maximum angle of the flow near the wall. At $r = 0$, the angle of the flow α should be -90 deg, unless the vortex axis oscillates itself, i.e. wobbling of the vortex core.

6.2.1.2 Stagnation and static pressures

The general conclusion of the stagnation and static pressures from all the experiments for different cold fractions and different inlet flows are listed below:

① The drop in the stagnation pressure over the inlet nozzle is dependent on the inlet flow and the cold fraction. At inlet flow of 69.5 g/s, the stagnation pressure drop is about 1.0 bar or larger, while for 34.7 g/s, it is less than 0.5 bar.

② The radial gradient in the stagnation pressure over the vortex chamber is larger than at any other station. For the inlet flow of 69.5 g/s, the radial stagnation pressure gradient over

[2]The angle of flow is defined in Chapter 3 and applied in Chapter 4, which is the angle of the velocity vector with respect to a plane normal to the axis of the tube. An angle zero means that the fluid flows in this plane and the axial component is zero, an angle larger than zero implies a flow towards the hot end. A negative angle implies flow towards the cold end.

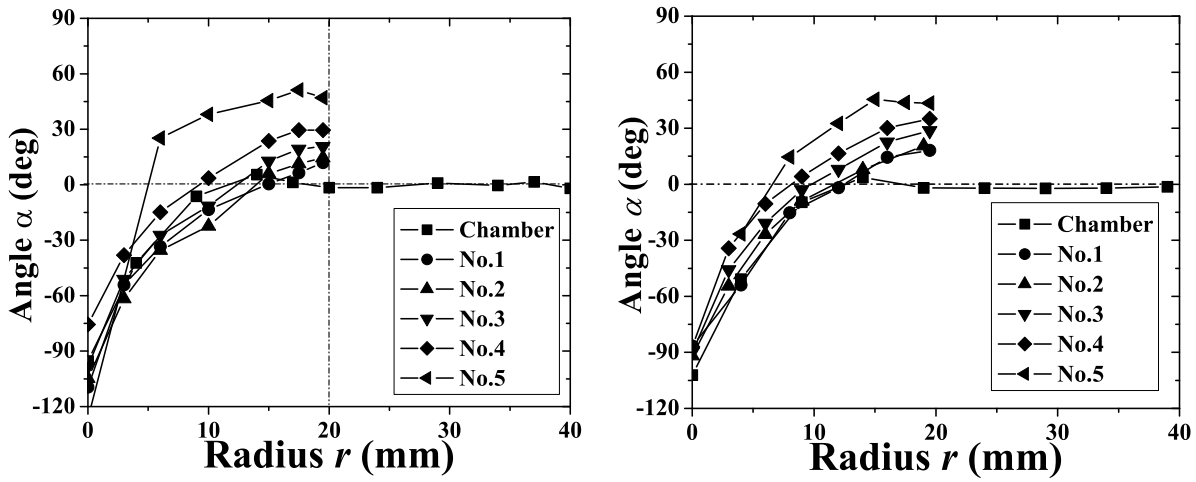

(a) Example (a). *(b) Example (b).*

Figure 6.15: *The angle of the flow for two different inlet flows at* $\varepsilon = 0.28$. *The symbol* ■ *applies to the vortex chamber.*

Situation		**Station**					
Inlet flow (g/s) & p_{in} (bar)	Specified result	Chamber	No.1	No.2	No.3	No.4	No.5
34.7 (g/s), 2.80 bar	$r_{\text{cr}}\|_{\alpha=0}$ (mm)	16	15	13	12	9	5
	$\alpha\|_{r=0}$ (deg)	-95	-109	-105	-98	-76	-126
	$\alpha_{\max}$ (deg)	0	12	15	20	29	51
69.5 (g/s), 5.10 bar	$r_{\text{cr}}\|_{\alpha=0}$ (mm)	16	12.5	11	10	8	6.5
	$\alpha\|_{r=0}$ (deg)	-102	-87	-92	-90	-87	-27
	$\alpha_{\max}$ (deg)	0	18	20	28	35	45

Table 6.11: *The angle of flow at the main positions.*

the vortex chamber is about 60 bar/m for $\varepsilon = 0.04$, 0.28 and 0.39, while the radial pressure distribution at Station 5 is almost flat and the radial gradient is less than 1 bar/m. For 34.7 g/s, the radial stagnation pressure gradient over the vortex chamber is about 25 bar/m for both cold fractions, and the pressure gradient over Station 5 is less than 0.1 bar/m and negligible.

③ The axial gradient in the stagnation pressure over the periphery region is larger than that over the center region. In the periphery region, the stagnation pressure decreases from its value near the chamber towards the hot end, while in the center region, the pressure near the hot end decreases towards the cold exhaust. But in the axial direction the pressure drop for all the measurements is lower than 0.5 bar.

④ All the contour plots of the stagnation pressures show the mapping of the stagnation pressure inside the RHVT.

⑤ With the local stagnation pressure, the local angle-dependent pressure profile and Eqs. 3.10 and 3.11, the local static pressure is calculated.

Figs. 6.16 and 6.18 show the pressure distributions for the two examples. Fig. 6.16 is for the stagnation pressure, and Fig. 6.18 is for the static pressure. Three stagnation pressures and relative static pressures from the two flows are summarized in Table 6.12.

It is found that the loss of the stagnation pressure over the inlet nozzle for example (a) is

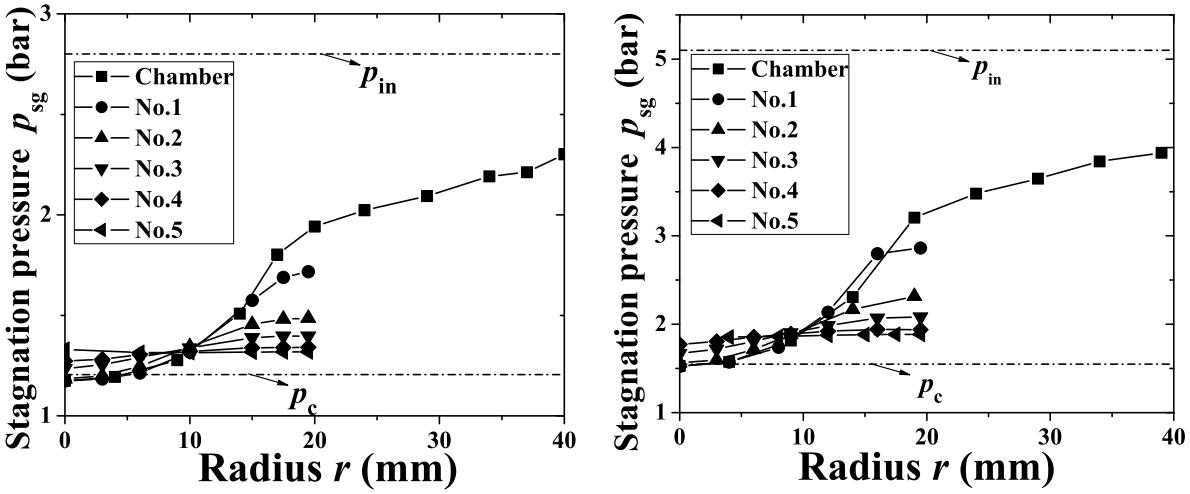

(a) Example (a). (b) Example (b).

Figure 6.16: *The stagnation pressures as function of position at two mass flows.*

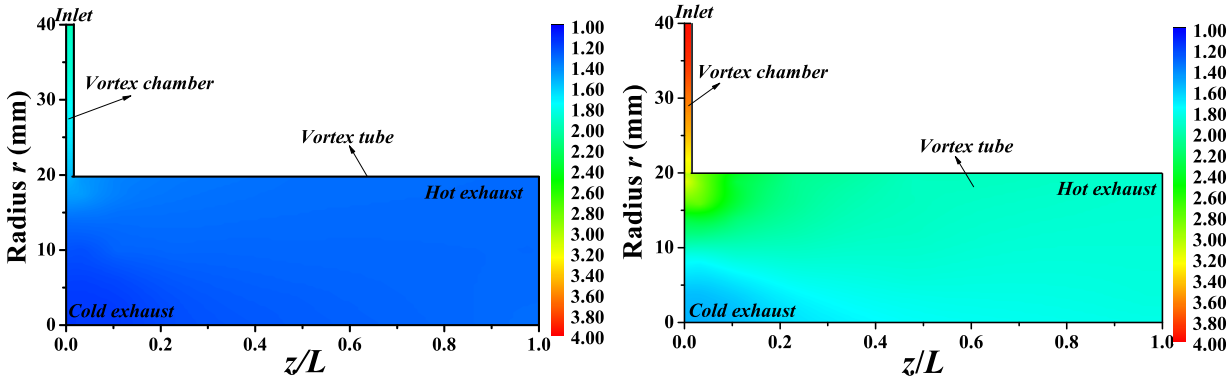

(a) Example (a). (b) Example (b).

Figure 6.17: *The contour plots of the stagnation pressures with the two different examples.*

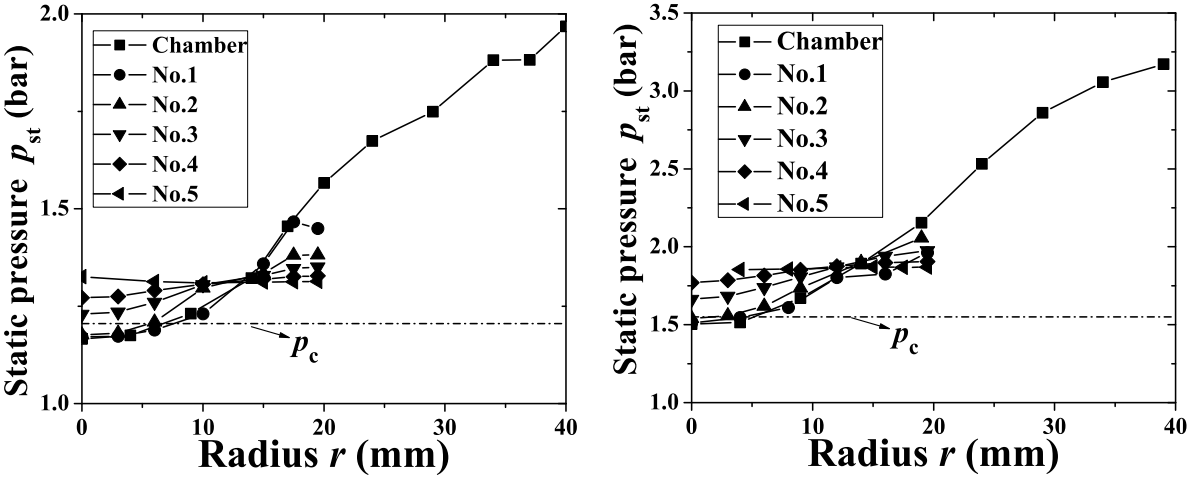

(a) Example (a). (b) Example (b).

Figure 6.18: *The static pressure distributions for the two different examples.*

Situation		Station					
Inlet flow (g/s) & p_{in} (bar)	Specified result	Chamber	No.1	No.2	No.3	No.4	No.5
34.7 (g/s), 2.80 bar	$p_{sg,vc}$	2.30	–	–	–	–	–
	$p_{st,vc}$	1.97	–	–	–	–	–
	$p_{sg,vt}$	1.95	1.72	1.50	1.40	1.34	1.32
	$p_{st,vt}$	1.57	1.45	1.38	1.35	1.33	1.32
	$p_{sg,c}$	1.18	1.17	1.18	1.24	1.27	1.33
	$p_{st,c}$	1.17	1.17	1.18	1.23	1.27	1.33
69.5 (g/s), 5.10 bar	$p_{sg,vc}$	3.94	–	–	–	–	–
	$p_{st,vc}$	3.18	–	–	–	–	–
	$p_{sg,vt}$	3.21	2.87	2.32	2.09	1.94	1.89
	$p_{st,vt}$	2.16	1.97	2.07	1.98	1.91	1.87
	$p_{sg,c}$	1.53	1.53	1.56	1.67	1.77	1.86
	$p_{st,c}$	1.50	1.51	1.54	1.66	1.77	1.85

Table 6.12: *Three stagnation and static pressures for two inlet flows.* $p_{sg,vc}$ *and* $p_{st,vc}$ *are the stagnation and static pressures at the exhaust of the inlet nozzle,* $p_{sg,vt}$ *and* $p_{st,vt}$ *are taken at the radius where* $r = R_{vt}$*,* $p_{sg,c}$ *and* $p_{st,c}$ *are taken at the center. The unit for the pressures is bar.*

about 0.5 bar, while for example (b) is about 1.15 bar. This is similar to computed results in Chapter 5. It shows that, the stagnation and static pressures in the periphery region ($p_{sg,vt}$ and $p_{st,vt}$) decrease from the vortex chamber towards the hot end, while in the center region the stagnation and static pressure ($p_{sg,c}$ and $p_{st,c}$) decrease from the hot end towards the cold exhaust. Fig. 6.17 shows the contour plots of the stagnation pressures for two different examples, which shows that the maximum stagnation pressure inside the RHVT occurs at the exhaust of the inlet nozzle, and the minimum stagnation pressure occurs at the cold exhaust. The radial gradient of the stagnation pressure near the entrance is larger than that near the hot end.

The pressure distribution in the vortex chamber enforces a secondary axial flow in the RHVT. This axial flow is towards the hot end at large radii and towards the cold side on the axis. The typical secondary flow field has similarities with a confined elliptic vortex bubble. These structures have a strong similarity with flow patterns in swirling flow and vortex breakdown work [9].

6.2.1.3 The Mach number

The general properties of the distribution of the Mach number[3] inside the RHVT using the CPT are as follows, see Figs. 6.19, 6.21 and 6.20:

① The maximum Mach number M_a appears at the position where $r = R_{vt}$ inside the vortex chamber. In the center part the cross flow velocity linearly drops to about zero at the center, the nonzero total Mach number is due to the nonzero axial velocity and fluctuation.

[3]With the CPT, three Mach numbers can be predicted. The total M_a and two components: the axial component $M_{a,ax}$ and the azimuthal component $M_{a,az}$. Three Mach numbers are related with the angle of the flow α:

$$\begin{cases} M_{a,ax} &= M_a \sin(\alpha) \\ M_{a,az} &= M_a \cos(\alpha) \end{cases}$$

In the periphery region inside the vortex chamber the velocity drops to the inlet velocity at the wall. At the wall in other stations there is a thin boundary layer of less than 0.5 mm. The maximum value of the total Mach number drops from the vortex chamber towards the hot end.

② The azimuthal Mach number $M_{\mathrm{a,az}}$ shows that in the inner region ($0 \leq r \leq R_{\mathrm{cr}}$), the azimuthal velocity is linearly dependent on the radius (solid-body rotation). In the periphery region ($R_{\mathrm{cr}} \leq r \leq R_{\mathrm{w}}$), it decreases to the wall. It indicates that the azimuthal velocity distribution inside the RHVT tends to a potential vortex motion. R_{cr} is the critical radius where a maximum occurs for the azimuthal speed. In the vortex chamber, $R_{\mathrm{cr}} = R_{\mathrm{vt}}$, while in the vortex tube, R_{cr} gradually decreases towards the hot end.

③ The axial Mach number $M_{\mathrm{a,ax}}$ is directed in the periphery region to the hot end, while in the inner region there is reversed axial flow to the cold end. At position $r = R_{\mathrm{cr}}$, the axial Mach number is zero. The maximum axial Mach number in the periphery region occurs near the wall and drops from the vortex chamber towards the hot end. Inside the vortex chamber the axial Mach number in the region $R_{\mathrm{vt}} \leq r \leq R_{\mathrm{vc}}$ is about zero.

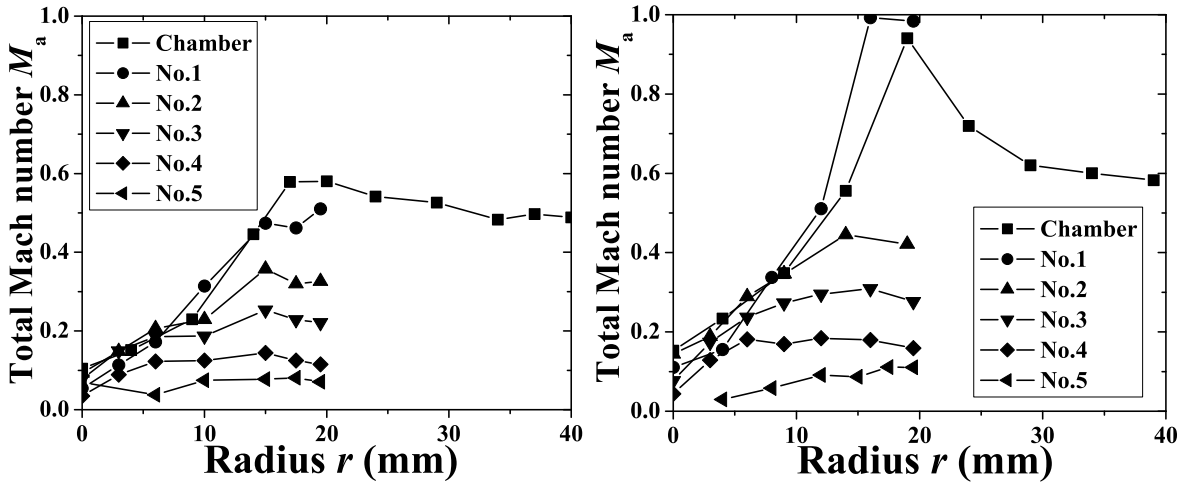

(a) Example (a) *(b) Example (b)*

Figure 6.19: *The total Mach number M_{a} for two different flows.*

Situation		**Station**					
Inlet flow (g/s) & p_{in} bar	Parameters	Chamber	No.1	No.2	No.3	No.4	No.5
34.7 (g/s), 2.80 bar	$M_{\mathrm{a,vc}}$	0.58	–	–	–	–	–
	$M_{\mathrm{a,vt}}$	0.49	0.51	0.33	0.22	0.12	0.07
	$M_{\mathrm{a,c}}$	0.10	0.05	0 09	0.08	0.04	0.07
69.5 (g/s), 5.10 bar	$M_{\mathrm{a,vc}}$	0.58	–	–	–	–	–
	$M_{\mathrm{a,vt}}$	0.95	0.99	0.45	0.31	0.16	0.11
	$M_{\mathrm{a,c}}$	0.15	0.11	0.14	0.08	0.04	0.03

Table 6.13: *Total Mach numbers M_{a} at three positions. $M_{\mathrm{a,vc}}$ is the total Mach number at the injection exit, $M_{\mathrm{a,vt}}$ is near the radius where $r = R_{\mathrm{vt}}$ and $M_{\mathrm{a,c}}$ is at the center.*

Fig. 6.19 shows the total Mach number at $\varepsilon = 0.28$. (a) is for inlet flow 34.7 g/s and (b) for inlet flow 69.5 g/s. The specific results from these two examples are shown in Table 6.13. It is clear that in the vortex chamber speeds occur up to $M_{\mathrm{a}} = 1$.

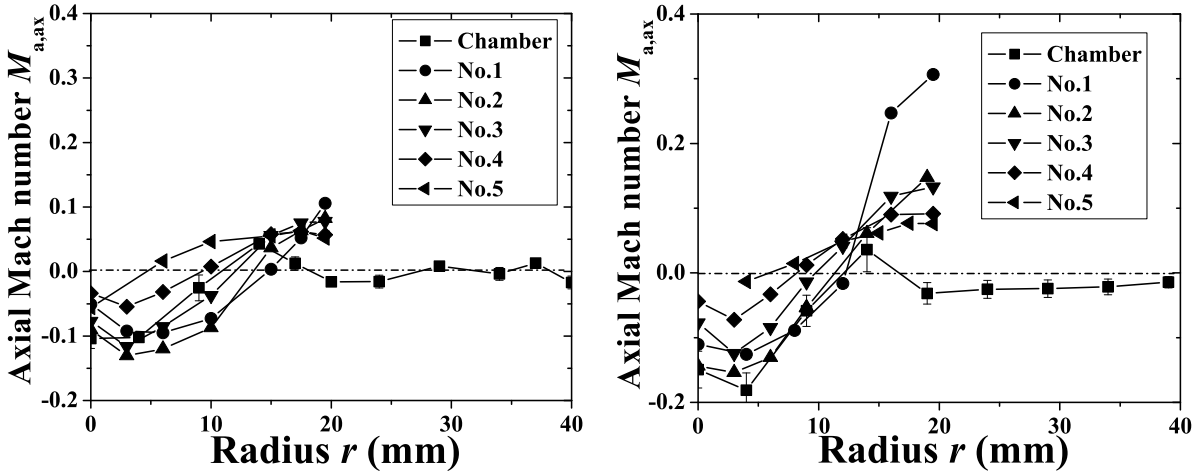

(a) Example (a) *(b) Example (b)*

Figure 6.20: *The axial Mach numbers $M_{\mathrm{a,ax}}$ from two different examples.*

Situation		**Station**					
Inlet flow (g/s) & p_{in} bar	Parameter	Chamber	No.1	No.2	No.3	No.4	No.5
34.7 (g/s), 2.80 bar	R_{cr} (mm)	18.4	15	13.5	12	9	5
	$M_{\mathrm{a,ax,vc}}$	-0.016	–	–	–	–	–
	$M_{\mathrm{a,ax,vt}}$	-0.016	0.11	0.082	0.077	0.06	0.05
	$M_{\mathrm{a,ax,c}}$	-0.11	-0.05	-0.09	-0.08	-0.03	-0.06
69.5 (g/s), 5.10 bar	R_{cr} (mm)	12.0	12.3	11.3	9.7	8.0	5.8
	$M_{\mathrm{a,ax,vc}}$	-0.014	–	–	–	–	–
	$M_{\mathrm{a,ax,vt}}$	-0.03	0.31	0.15	0.13	0.09	0.08
	$M_{\mathrm{a,ax,c}}$	-0.15	-0.11	-0.14	-0.08	-0.04	- 0.013

Table 6.14: *Some experimental parameters at various positions in the tube as obtained from Fig. 6.20. R_{cr} is the critical radius where the axial velocity reverses its direction, $M_{\mathrm{a,ax,vc}}$ is the axial Mach number component near the injection exit, $M_{\mathrm{a,ax,vt}}$ is near the radius where $r = R_{\mathrm{vt}}$ and $M_{\mathrm{a,ax,c}}$ is at the center.*

Fig. 6.20 shows the axial Mach number component distributions for $\varepsilon = 0.28$. Figure (a) is for inlet flow 34.7 g/s. (b) is for inlet flow 69.5 g/s. The axial Mach number component inside the vortex chamber in the periphery region $R_{\mathrm{vt}} \leq r \leq R_{\mathrm{vc}}$ is close to zero as expected. Typical results from these two examples are shown in Table 6.14. It is found that the critical radius R_{cr} decreases towards the hot end.

Fig. 6.21 shows the azimuthal Mach number component $M_{\mathrm{a,az}}$ distributions for $\varepsilon = 0.28$. Figure (a) is for inlet flow 34.7 g/s and (b) is for 69.5 g/s. These results show that in the center region, the azimuthal Mach numbers $M_{\mathrm{a,az}}$ is linearly dependent on the radius r, formatted as solid-body rotation. In the periphery region, the azimuthal Mach number decreases close to the wall. It shows that the azimuthal Mach numbers inside the RHVT have the tendency to form a Rankine vortex motion profile. The azimuthal Mach number decreases from the chamber towards the hot end. Table 6.15 shows the azimuthal Mach numbers at three locations for the two cases.

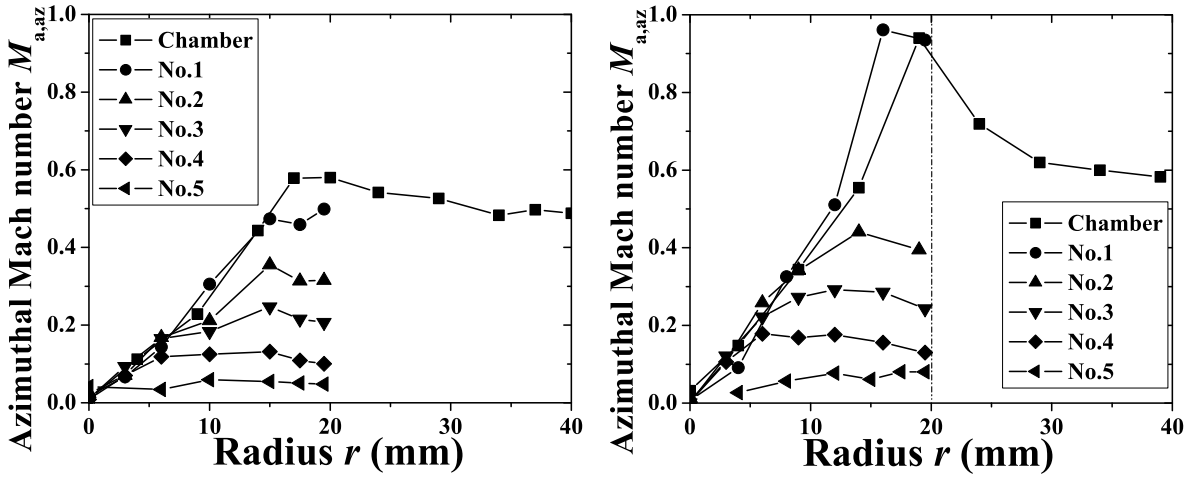

(a) Example (a) *(b) Example (b)*

Figure 6.21: *The azimuthal Mach numbers $M_{\mathrm{a,az}}$ for two different flows.*

Situation		**Station**					
Inlet flow (g/s) & p_{in} (bar)	Parameters	Chamber	No.1	No.2	No.3	No.4	No.5
34.7 (g/s), 2.80 bar	$M_{\mathrm{a,az,vc}}$	0.49	–	–	–	–	–
	$M_{\mathrm{a,az,vt}}$	0.58	0.50	0.32	0.21	0.10	0.05
	$M_{\mathrm{a,az,max}}$	0.58	0.50	0.36	0.25	0.13	0.06
69.5 (g/s), 5.10 bar	$M_{\mathrm{a,az,vc}}$	0.59	–	–	–	–	–
	$M_{\mathrm{a,az,vt}}$	0.94	0.94	0.40	0.24	0.13	0.08
	$M_{\mathrm{a,az,max}}$	0.94	0.96	0.44	0.30	0.18	0.08

Table 6.15: *azimuthal Mach numbers at three locations for two cases. $M_{\mathrm{a,az,vc}}$ is the azimuthal Mach number component near the injection exit, $M_{\mathrm{a,az,vt}}$ is near the radius where $r = R_{\mathrm{vt}}$ and $M_{\mathrm{a,az,max}}$ is the maximum azimuthal Mach number at the local cross section.*

6.2.2 SPHWA measurements

Detailed SPHWA measurements have been carried out for two different inlet flows, i.e. for 69.5 g/s and 34.7 g/s. For the inlet flow of 34.7 g/s, the inlet pressure stays the same for all the measurements as 2.80 bar. Two cold fractions($\varepsilon = 0.28$, 0.39) have been chosen. The measured stations (Station 1 to 5) are the same as for the CPT technique. For the inlet flow of 69.5 g/s (for $\varepsilon = 0.90$ and $p_{\mathrm{in}} = 5.10$ bar, $\dot{m}_{\mathrm{in}} = 55.6$ g/s), the inlet pressure for all the measurements is constant at 5.10 bar which is the same as for the CPT measurements. Four cold fractions ($\varepsilon = 0.04$, 0.28, 0.39 and 0.90) are chosen. The measurements are carried out for four stations (Station 2 to 5). All these measurements were performed under similar operation conditions and at the same stations.

No measurements were made inside the vortex chamber which was because of the geometry. There are no measurements for inlet flow 69.5 g/s at Station 1. This is because of the high flow speed at this station: one hot-wire probe broke.

In this section, like for the CPT technique, only the measurements at $\varepsilon = 0.28$ are reported. The case at inlet flow 34.7 g/s is named as Example (a) and 69.5 g/s named as Example (b).

6.2.2.1 The flow angle

The measured flow direction at different cold fractions and different flows by SPHWA technique have the following general aspects:

① In the periphery region, the sign of the angle is positive, which means the gas flows towards the hot end. In the inner region, the sign is negative. This indicates that the axial flow inside the RHVT reverses.

② There is a critical radius $R_{\rm cr}$ where the sign of the angle changes. The critical radius $R_{\rm cr}$ exists for all cases, i.e. for different cold fractions and different inlet flows.

③ $R_{\rm cr}$ is dependent on ε, the $Z-$position along the vortex tube and the flow. It decreases when the station is closer to the hot end. At the same position and same flow rate, $R_{\rm cr}$ increases with the cold fraction ε.

④ The flow angle varies along the radius at the same station. It increases with the radius. Near the center it is about -90 deg, which means that at the center there is no azimuthal velocity and only an axial velocity towards the cold end. The angle at the same radius increases from the station near the chamber towards the hot end.

⑤ All results are similar to ones found by the CPT technique.

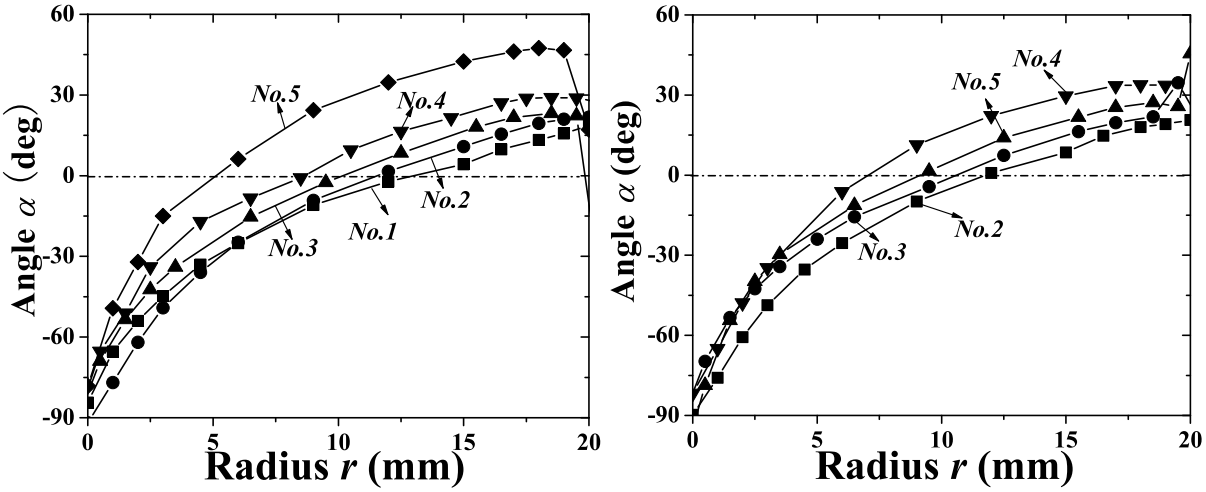

(a) Example (a). *(b) Example (b).*

Figure 6.22: *The flow angle for the two cases at* $\varepsilon = 0.28$.

Situation		**Station**				
Inlet flow (g/s) & $p_{\rm in}$ bar	Specific values	No.1	No.2	No.3	No.4	No.5
34.7 (g/s), 2.80 bar	$R_{\rm cr}\|_{\alpha=0}$ (mm)	13	12	10	9	5
	$\alpha\|_{r=0}$ (deg)	-85	-92	-81	-79	-78
	$\alpha_{\rm max}$ (deg)	16	21	23	29	48
69.5 (g/s), 5.10 bar	$R_{\rm cr}\|_{\alpha=0}$ (mm)	–	10	11	9	7
	$\alpha\|_{r=0}$ (deg)	–	-84	-83	-95	-82
	$\alpha_{\rm max}$ (deg)	–	25	34	45	34

Table 6.16: *Three specific values of angles for two examples.*

Fig. 6.22 shows the flow angles measured by the SPHWA for the two examples. Only the angle at the four stations (from 2 to 5) are shown for example (b). For example (a), there are

five stations (from 1 to 5). Three parameters obtained from Fig. 6.22 are presented in Table 6.16.

6.2.2.2 The quantity $\overline{\rho V}$

According to the description and analysis in Chapter 3 section 3.4, the SPHWA inside the RHVT is used to measure the quantity ρV instead of V. During the measurements, the maximum effective $\overline{\rho V_{\mathrm{e,max}}}$ and the minimum effective $\overline{\rho V_{\mathrm{e,min}}}$ are used, together with attitude of SPHWA, to determine the three components of $\overline{\rho V}$. So here these two effective $\overline{\rho V_{\mathrm{e}}}$ will be discussed first, and then the azimuthal-axial and radial components ($\overline{\rho V}_{\mathrm{azx}}$ and $\overline{\rho V}_{\mathrm{r}}$) are determined for the two examples.

@ The maximum effective $\overline{\rho V_{\mathrm{e,max}}}$

Fig. 6.23 shows the effective $\overline{\rho V_{\mathrm{e,max}}}$ based on the maximum signals for different flows at $\varepsilon = 0.28$. The maximum effective $\overline{\rho V_{\mathrm{e,max}}}$ is not the total $\overline{\rho V}_{\mathrm{to}}$ [4]. The following general properties of the distributions of the maximum effective $\overline{\rho V_{\mathrm{e,max}}}$ can be emphasized:

① the maximum value of $\overline{\rho V_{\mathrm{e,max}}}$ decreases from the vortex chamber towards the hot end, and the maximum value depends on the inlet flow, the cold fraction and the $Z-$position along the tube. If the cold fraction increases, the maximum value of $\overline{\rho V_{\mathrm{e,max}}}$ decreases.

② $\overline{\rho V_{\mathrm{e,max}}}$ near the wall at all stations for different cold fractions and different flows drops to zero.

③ Some distributions of $\overline{\rho V_{\mathrm{e,max}}}$ linearly increase from the center to some radius R_{max} whereas some distributions of $\overline{\rho V_{\mathrm{emax}}}$ are very flat in the periphery region near the wall.

④ Some specific results from Fig. 6.23 are shown in Table 6.17.

Situation		**Station**				
Inlet flow (g/s) & p_{in} (bar)	Specific values	No.1	No.2	No.3	No.4	No.5
34.7 (g/s), 2.80 bar	R_{max} (mm)	17	17	15	12	14
	$\overline{\rho V_{\mathrm{emax}}}\|_{r=0}$ (kg/m^{2}s)	41	86	84	67	7
	$\overline{\rho V_{\mathrm{emax,max}}}$ (kg/m^{2}s)	380	235	172	97	46
69.5 (g/s), 5.10 bar	R_{max} (mm)	–	17	16	13	12
	$\overline{\rho V_{\mathrm{emax}}}\|_{r=0}$ (kg/m^{2}s)	–	164	144	102	23
	$\overline{\rho V_{\mathrm{emax,max}}}$ (kg/m^{2}s)	–	523	316	230	118

Table 6.17: *Specific values from Fig. 6.23.* R_{max} *is the radius of the maximum value of* $\overline{\rho V_{\mathrm{emax}}}$, $\overline{\rho V_{\mathrm{emax}}}|_{r=0}$ *is the value at the center,* $\overline{\rho V_{\mathrm{emax,max}}}$ *is the maximum value.*

[4] In Chapter 3, the effective velocity is defined in Eq. 3.26. With the SPHWA, the maximum and minimum effective ρV are defined in Eqs. 3.35 and 3.36:

$$\begin{cases} \overline{\rho V_{\mathrm{e,max}}} &= \sqrt{(\overline{\rho V_{\mathrm{r}}})^2 + (1.05\overline{\rho V_{\mathrm{azx}}})^2} \\ \overline{\rho V_{\mathrm{e,min}}} &= \sqrt{(\overline{\rho V_{\mathrm{r}}})^2 + (0.02\overline{\rho V_{\mathrm{azx}}})^2} \end{cases},$$

while the total ρV_{to} follows from

$$(\rho V_{\mathrm{to}})^2 = (\rho V_{\mathrm{r}})^2 + (\rho V_{\mathrm{azx}})^2.$$

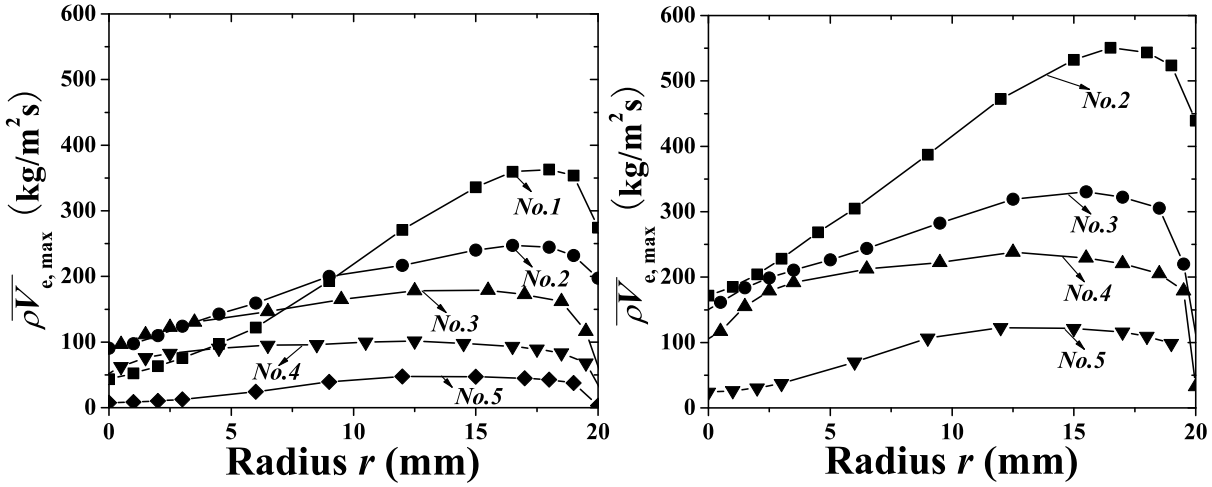

(a) Example (a). *(b) Example (b).*

Figure 6.23: *The maximum effective* $\overline{\rho V}_{\mathrm{emax}}$ *based on the maximum signals of the SPHWA from two flow conditions at* $\varepsilon = 0.28$.

ⓑ The minimum $\overline{\rho V}_{\mathrm{emin}}$

Fig. 6.24 shows the effective $\overline{\rho V}_{\mathrm{emin}}$. The following general results can be made:

① the distributions of $\overline{\rho V}_{\mathrm{emin}}$ at the stations near the hot end are flat;

② $\overline{\rho V}_{\mathrm{emin}}$ is dependent on the mass flow, ε, the $Z-$position along the vortex tube and the flow;

③ along stations near the entrance $\overline{\rho V}_{\mathrm{emin}}$ linearly increases from the center to the wall.

④ The values derived from Fig. 6.24 are shown in Table 6.18.

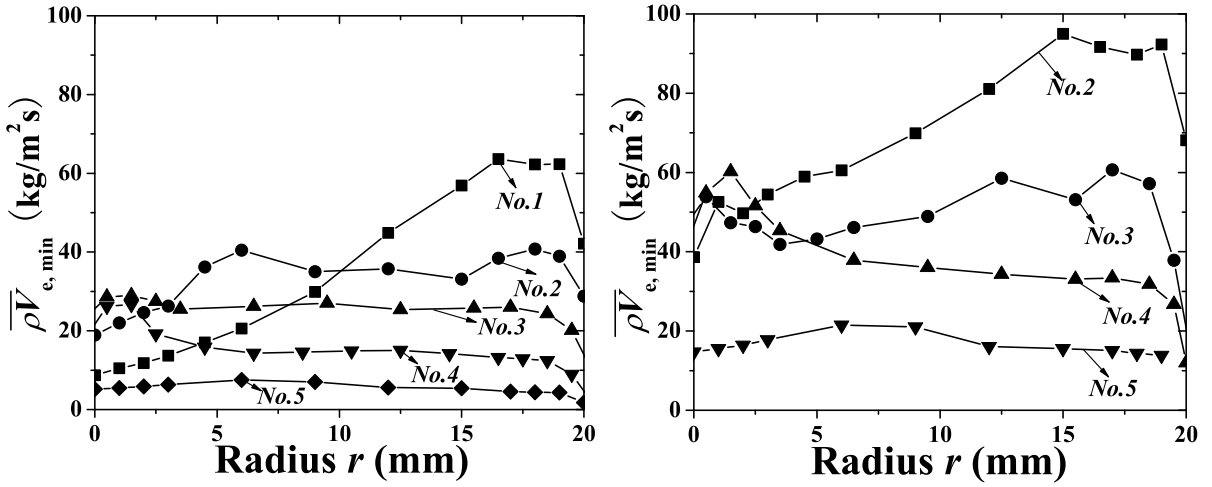

(a) Example (a). *(b) Example (b).*

Figure 6.24: *The minimum effective* $\overline{\rho V}_{\mathrm{emin}}$ *based on the minimum signals of the SPHWA from two examples.*

Situation		Station				
Inlet flow (g/s) & p_{in} (bar)	Parameter	No.1	No.2	No.3	No.4	No.5
34.7 (g/s), 2.80 bar	shape in the center	linear	linear	flat	flat	flat
	R_{cr}	17	6	–	–	–
	$\overline{\rho V_{e}}_{min}\|_{r=0}$ (kg/m^{2}s)	9	19	28	15	5
	$\overline{\rho V_{e}}_{min,max}$ (kg/m^{2}s)	64	41	26	26	5
69.5 (g/s), 5.10 bar	shape	–	linear	flat	flat	flat
	R_{cr}	–	15	13	–	–
	$\overline{\rho V_{e}}_{min}\|_{r=0}$ (kg/m^{2}s)	–	50	42	61	15
	$\overline{\rho V_{e}}_{min,max}$ (kg/m^{2}s)	–	96	60	34	17

Table 6.18: *The values of $\overline{\rho V_{e}}_{min}$ obtained from Fig. 6.24. R_{cr} is the radius where the $\overline{\rho V_{e}}_{min}$ changes its signal, $\overline{\rho V_{e}}_{min}|_{r=0}$ is the value at the center, $\overline{\rho V_{e}}_{min,max}$ is the maximum value.*

ⓒ The radial component: $\overline{\rho V_r}$

With $\overline{\rho V_{e}}_{max}$ and $\overline{\rho V_{e}}_{min}$, the radial component $\overline{\rho V}_r$ is calculated by Eq. 3.37 ($\overline{\rho V}_1$ in the equation). Fig. 6.25 shows the computed $\overline{\rho V}_r$ for the two flows. Their common properties are that:

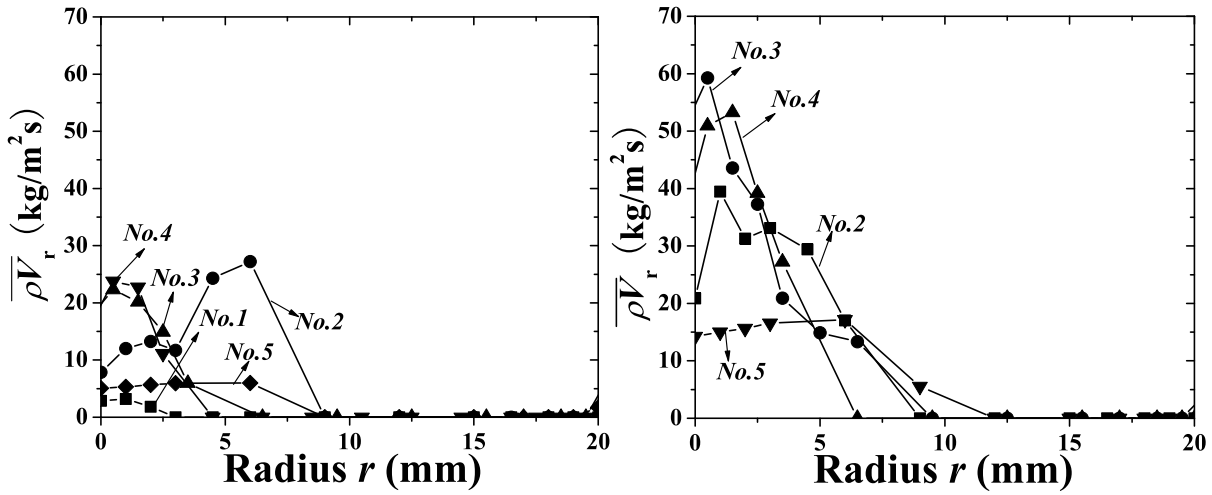

(a) Example (a). *(b) Example (b).*

Figure 6.25: *The radial component of $\overline{\rho V}_r$ as function of r for two flow conditions at $\varepsilon = 0.28$.*

① $\overline{\rho V}_r$ depends on the mass flow, ε and the $Z-$position along the tube;

② for most cold fractions, $\overline{\rho V}_r$ in the periphery region is zero;

③ the maximum value of $\overline{\rho V}_r$ along the radius occurs at the center[5];

④ near the wall, for some cases (for instance $\varepsilon = 0.90$ at $\dot{m}_{in} = 55.6$ g/s and $p_{in} = 5.10$ bar), $\overline{\rho V}_r$ is not zero.

The specific values of $\overline{\rho V}_r$ are shown in Table 6.19.

[5]Because we measured $\rho\sqrt{\overline{V^2}}$ (see Eq. 3.26). The value in the center can be the fluctuation and wobbling of the flow pattern in the vortex tube.

Situation		Station				
Inlet flow (g/s) & p_{in} (bar)	Specific values	No.1	No.2	No.3	No.4	No.5
34.7 (g/s), 2.80 bar	R_0 mm	3	9	7	5	9
	$\overline{\rho V}_{r,max}$ (kg/m^{2}s)	3	27	23	24	6
69.5 (g/s), 5.10 bar	R_0 mm	–	9	10	7	12
	$\overline{\rho V}_{r,max}$ (kg/m^{2}s)	–	40	59	53	17

Table 6.19: *The specific values obtained from Fig. 6.25, R_0 is a radius it requires that $\overline{\rho v}_r < 0$ when $r < R_0$. $\overline{\rho V}_{r,max}$ is the maximum value.*

@ The azimuthal-axial component: $\overline{\rho V}_{azx}$

The azimuthal and axial combined components $\overline{\rho V}_{azx}$ are computed by Eq. 3.37 ($\overline{\rho V}_{2\_3}$ in the equation). Fig. 6.26 shows $\overline{\rho V}_{azx}$. Because the radial component is small, the distributions of the $\overline{\rho V}_{azx}$ are similar to those of the effective $\overline{\rho V}_{emax}$ as shown in Fig. 6.23. From the azimuthal-axial component and the flow angle, the azimuthal and axial components ($\overline{\rho V}_{az}$ and $\overline{\rho V}_{ax}$) can be derived separately using Eq. 3.37. Fig. 6.27 shows $\overline{\rho V}_{az}$ and $\overline{\rho V}_{ax}$ calculated from Fig. 6.26 (b) for example (b).

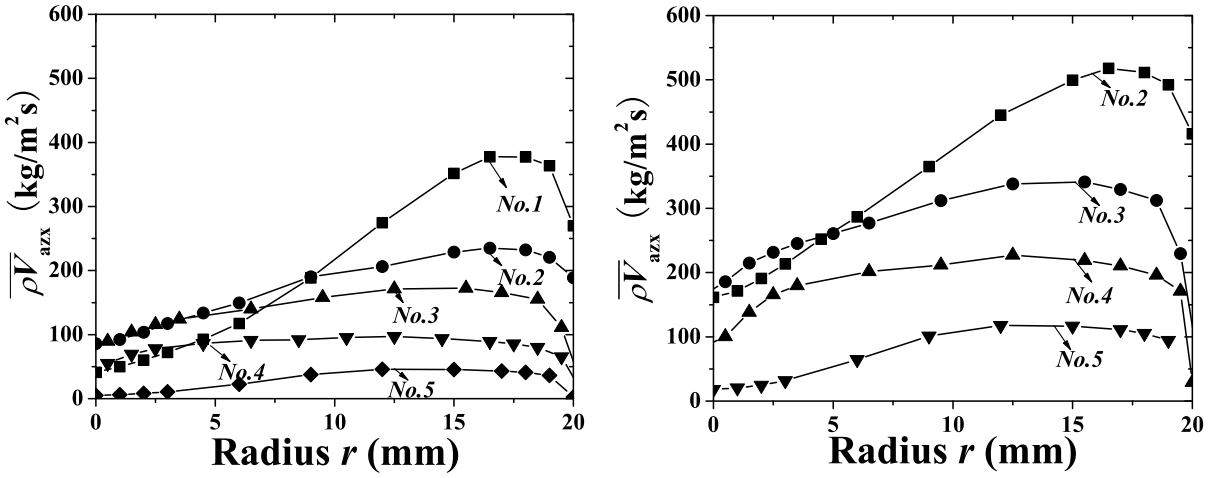

(a) Example (a). *(b) Example (b).*

Figure 6.26: *The distributions of the $\overline{\rho V}_{azx}$ for two examples.*

6.2.2.3 Cumulative mass flows

As mentioned in Chapter 4, the cumulative axial mass flow $\dot{m}_r$ (see Eq. 4.7) can be calculated. In the SPHWA measurement, ρV_{ax} is a measured parameter. The cumulative mass flow up to a radius r is defined as follows

$$\dot{m}_r = \int_0^r 2\pi \overline{\rho V}_{ax,r} r \mathrm{d}r \ . \tag{6.1}$$

Here the cumulative mass flows $\dot{m}_r$ in the axial direction for two examples have been calculated and are shown in Fig. 6.28. The cumulative axial mass flows $\dot{m}_r$ have the following common properties:

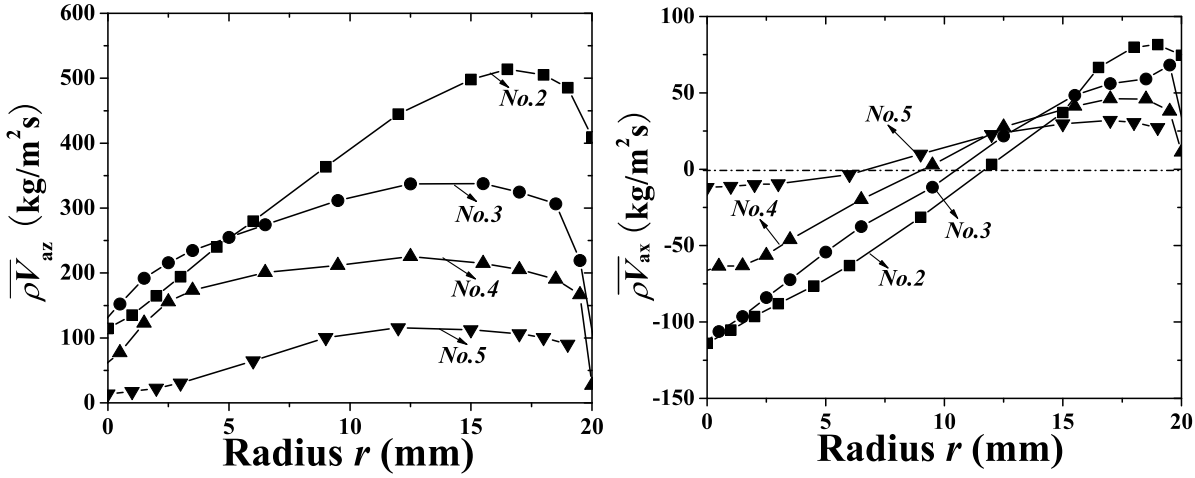

(a) Azimuthal component $\overline{\rho V}_{\mathrm{t}}$. *(b) Axial component $\overline{\rho V}_{\mathrm{a}}$.*

Figure 6.27: *The azimuthal and axial components of $\overline{\rho V}$ calculated from the results of Fig. 6.26 (b).*

① the cumulative axial mass flow $\dot{m}_{R_{\mathrm{vt}}}$ over the whole cross section is equal to the hot end exhaust mass flow, which obeys the mass conservation law;

② the value of the maximum cumulative axial mass flow to the cold end (the maximum negative value) near the entrance is always larger than the cold exhaust mass flow;

③ the start position where the flow reverses to the hot end depends on the flow, cold fraction. The maximum negative cumulative mass flow in Fig. 6.28 (a) for Station 4 is larger than the cold exhaust mass flow, while for Station 5, it is lower, so in between Stations 4 and 5, there should exist one position where the gas reverses to hot end.

④ The distribution of the cumulative axial mass flow is dependent on the inlet mass flow, cold fraction and the $Z-$position along the tube.

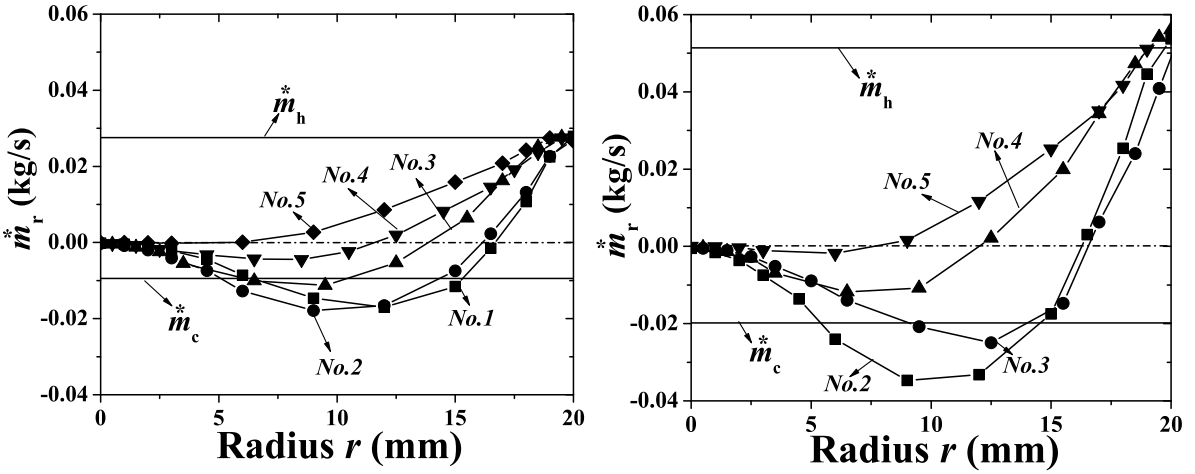

(a) Example (a). *(b) Example (b).*

Figure 6.28: *The cumulative axial mass flows for two examples.*

The specific values from Fig. 6.28 are shown on Table 6.20. For example (a), the maximum

negative cumulative mass flow at Station 3 is 11.3 g/s, whereas at Station 4 it is only 4.5 g/s. The cold exhaust mass flow is 9.5 g/s. Between Stations 3 and 4, there is a position where the gas starts to reverse its direction. For example (b), the position where the gas starts to reverse is in between Station 3 and 4.

Flow (g/s) & $p_{\rm in}$ (bar)	maximum gas mass flow to cold end (g/s)					
	$\dot{m}_{\rm c}$	Station 1	Station 2	Station 3	Station 4	Station 5
34.7 (g/s), 2.80 bar	9.5	17.1	17.9	11.3	4.5	0.2
69.5 (g/s), 5.10 bar	19.8	–	34.7	25.0	11.8	1.8

Table 6.20: *The maximum negative cumulative mass flows on different stations and relevant cold exhaust mass flows for two examples.*

6.2.2.4 Turbulent velocity fluctuations

As mentioned in Chapter 3, with the SPHWA technique, turbulent velocity fluctuations inside the RHVT can be determined. Here, parameters, like average fluctuation $\delta_{\rm av}$, intensity of fluctuation γ_δ, skewness and flatness, and spectral analysis, will be discussed.

@ The root-mean-squared average fluctuations $\delta_{\rm av}$

The root-mean-square fluctuation ($\delta_{\rm rs}$) based on the SPHWA example was defined in Chapter 3. This parameter is independent of time, but dependent on angle and position

$$\delta_{\rm rs}^2(\alpha, r) = \frac{1}{T}\int_0^T \left((\rho v')(\alpha, r, t)\right)^2 dt \simeq \frac{1}{N}\sum_{i=1}^{N}((\rho v')_{(\alpha,r,i)})^2 \ .$$

Here $(\rho v')_{(\alpha,r,i)}$ denotes the example number at position r and rotating angle α. The number of signals is N.

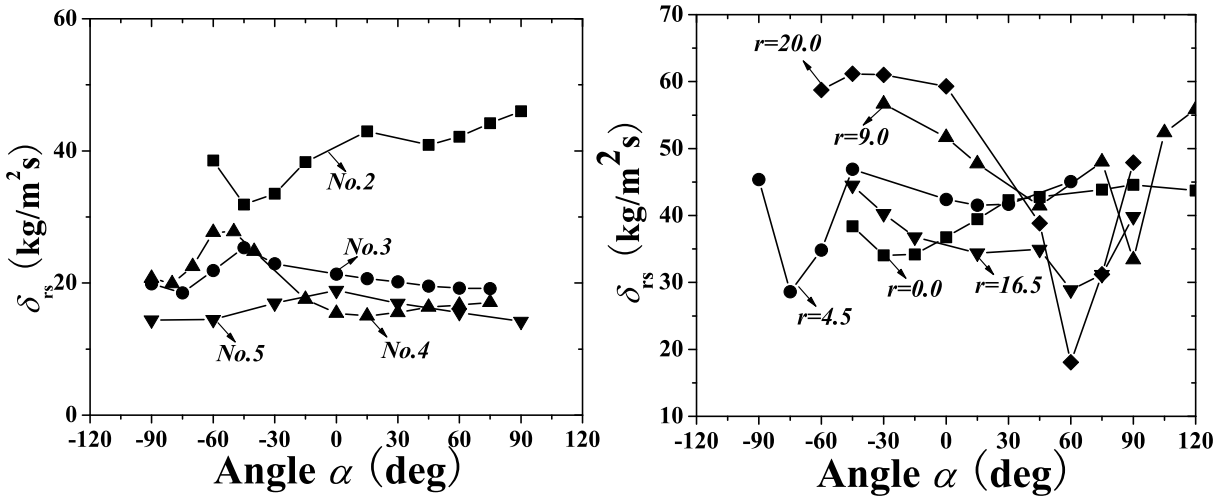

(a) δ_{rs} at $r = 1$ mm for Stations. *(b) δ_{rs} at Station 2 for radii r.*

Figure 6.29: *Examples of the parameter δ_{rs} as functions of α.*

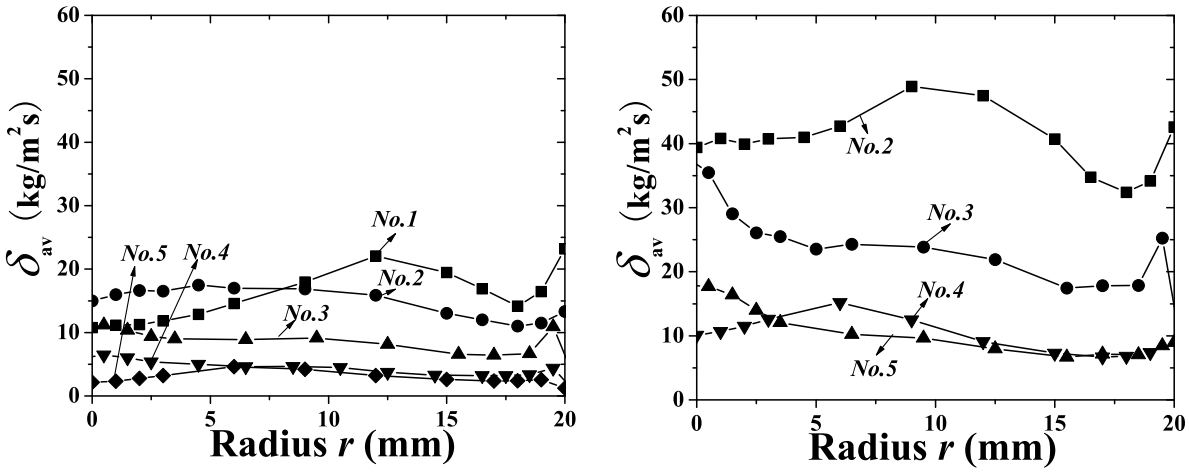

(a) example (a). *(b) example (b).*

Figure 6.30: δ_{av} *as functions of* r *for two examples.*

Fig. 6.29 shows the dependence of δ_{rs} on the probe rotation angle and position at $\varepsilon = 0.04$ and inlet flow 69.5 g/s and inlet pressure 5.10 bar. The influence of the probe angle is very small except for the positions near the wall and at the station near the entrance. This indicates that the turbulence inside is a certain level of isotropy.

In order to simplify the analysis, the average of the δ_{rs} at different angles at a position is chosen as the basis for a velocity fluctuation parameter,

$$\delta_{\mathrm{av}} = \sqrt{\frac{1}{N}\sum_{i=1}^{N}\delta^2_{\mathrm{rs}(\alpha_i)}} \approx O\left((\rho V)'\right) \quad . \tag{6.2}$$

Here α_i means the chosen angles. For one position r, there are up to 18 angles.

Fig. 6.30 shows the average δ_{av} for two examples. The distributions along all the stations are very flat, and the maximum value of δ_{sd} is close to the maximum value of the radial component $\overline{\rho V}_{\mathrm{r}}$. This indicates that the radial velocity is generated by the fluctuations.

ⓑ The intensity

The intensity of the velocity fluctuations is defined as the ratio of δ_{av} to the local total $\overline{\rho V}_{\mathrm{tot}}$

$$\gamma_\delta = \frac{\delta_{\mathrm{av}}}{\overline{\rho V}_{\mathrm{tot}}} \approx \frac{\rho\sqrt{\overline{v'^2}}}{\rho\overline{V}_{\mathrm{tot}}} = \frac{\sqrt{\overline{v'^2}}}{\overline{V}_{\mathrm{tot}}} \quad . \tag{6.3}$$

Fig. 6.31 shows the relative turbulent intensity for two examples. Obviously in the center very irregular flow occurs due to unstable vortex motion. The fluctuations are impeded by the wall when $r > 10$ mm. At Station 5 the fluctuations are larger as here the exhaust system and the low value of the velocity itself will lead to increased relative intensities. Due to the no-slip condition here also boundary-layer generated turbulence occurs leading to fluctuations up to 20%. These fluctuations are larger than common values for a flat-wall boundary layer which are of the order of 10% [10].

The following common aspects from these distributions are found:

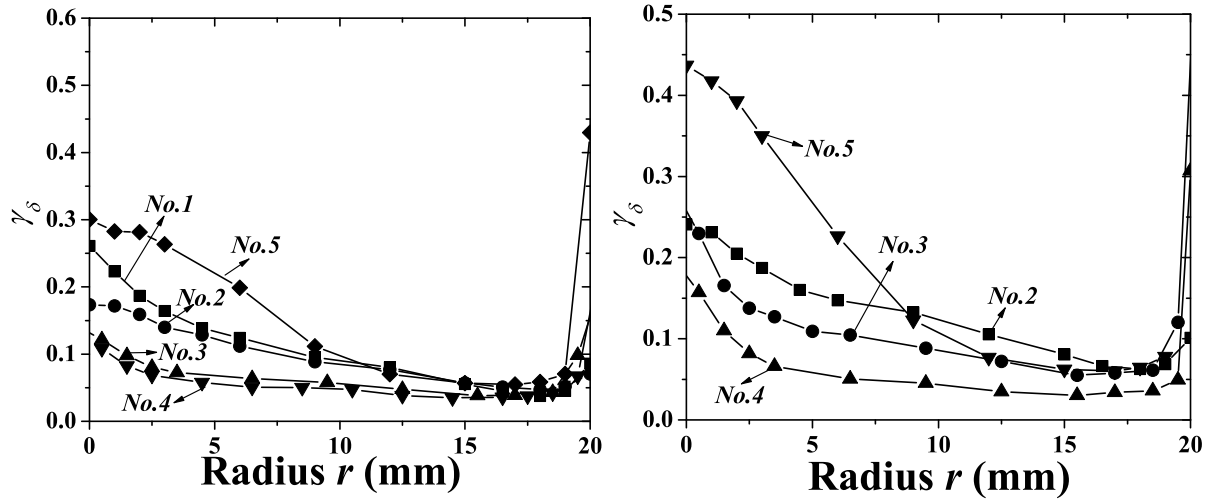

(a) Example (a). *(b) Example (b).*

Figure 6.31: *The relative turbulent intensities of the fluctuations for two examples at* $\varepsilon = 0.28$.

① all these intensities are decreasing from the center to the wall, and near the wall ($r > 18$ mm) they are increasing;

② the maximum intensity for all these cases occurs in the center;

③ the intensity along Station 5 in the center region is larger than the intensity for other cases;

④ comparing with the intensities for Stations 1 to 4, the relative intensity decreases towards Station 4.

ⓒ The skewnesses and flatnesses

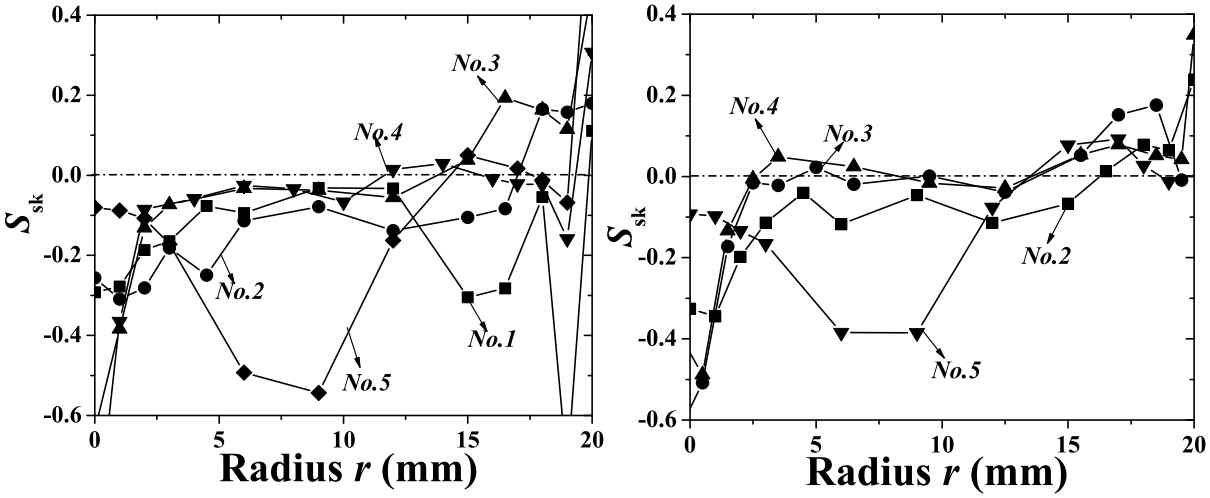

(a) Example (a). *(b) Example (b).*

Figure 6.32: *The skewness as functions of r for the two examples.*

In Chapter 3 the skewness $S_{\rm sk}$ and flatness $F_{\rm fl}$ were introduced. In probability theory and statistics, skewness is a measure of the asymmetry of the probability distribution of a real-

valued random variable [11]. For a Gaussian spectrum, the skewness should be 0. Roughly speaking, a distribution has positive skewness if the distribution is biased to higher value of the argument and negative skewness if the distribution is biased to lower value. Flatness is a measure of the "peakedness" of the probability distribution of a real-valued random variable. For a Gaussian spectrum, the flatness should be 3. Higher flatness means more of the variance is due to infrequent extreme deviations, as opposed to frequent modestly-sized deviations.

The experimental data were used to compute the skewness and flatness and they are plotted as functions of the radius for different stations. The skewness is plotted in Fig. 6.32 for the two examples. It shows as common points that:

ⓐ in the center $r < 2$ mm, there is a trend that the skewness is lower than zero;

ⓑ near the wall $r > 18$ mm, the skewness is larger than zero;

ⓒ in the intermediate region 2 mm $< r <$ 18 mm, it is nearly 0 except at Station 5;

ⓓ Station 5 is a special case as here influences of the exhaust are dominating and will obviously influence the skewness.

Fig. 6.33 shows the flatness distribution for two examples. The flatness is roughly equal to 3 in the intermediate region 5 mm $< r <$ 15 mm. Near the wall as well as in the center the flatness is larger than 3. At Station 5 the flatness deviates from 3 indicating less than statistical turbulent behavior.

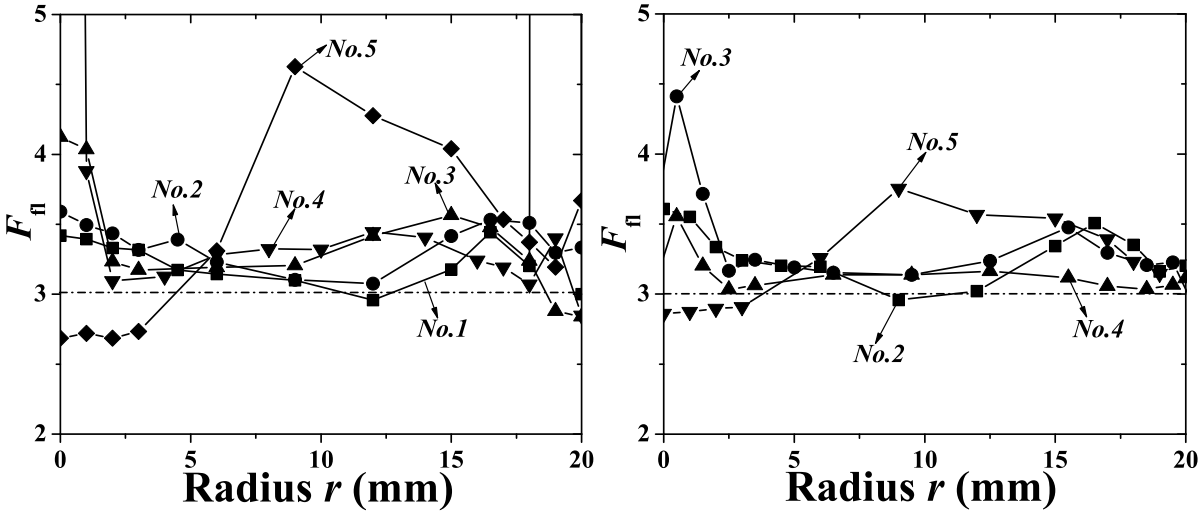

(a) Example (a). *(b) Example (b).*

Figure 6.33: *The flatness as functions of r for the two examples.*

The skewness and flatness in the center region deviate from the values of a Gaussian profile. In the intermediate region, both parameters are roughly equal to the values for a Gaussian profile. In the periphery region, they deviate from the standards again. This indicates that in the center and in the periphery regions the turbulence is less statistical, while in the intermediate region, it is.

ⓓ The PDF profiles

As mentioned in Chapter 3, the distribution of the PDF is related to the skewness and flatness. Here the PDF plots measured at $r = 0$ of Station 2 for example (b) will be shown as example in Fig. 6.34.

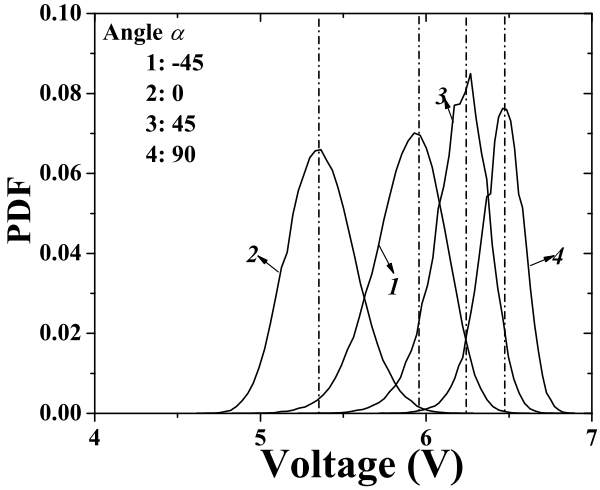

Figure 6.34: *The PDF measured at different angles at* $r = 0$ *of Station 2 for example (b)* ($\dot{m}_{\mathrm{in}} = 69.5$ g/s, $p_{\mathrm{in}} = 5.10$ bar *and* $\varepsilon = 0.28$*).*

The distributions with symmetric tail to the sides indicate a skewness of 0 and a flatness of 3 in the Figs. 6.32 and 6.33. The distributions with a non-Gaussian profile show a skewness of $S_{\mathrm{sk}} \neq 0$ and a flatness of $F_{\mathrm{fl}} \neq 3$ in the above figures.

According to the average fluctuation δ_{av}, the relative intensity, the flatness and skewness, PDF which have been shown above, we can conclude that:

① At the stations near the entrance (Station 1 and 2) and Stations 5, the relative fluctuations are large. The fluctuations in these regions are comparable with the local radial velocity component. The velocity fluctuations have the same magnitude as the radial velocity component. The relative intensities v'/V in these regions are larger than 20%. In these regions, the flatness F_{fl} is unequal to 3 and skewness S_{sk} is not equal to 0 which means that the fluctuations in these regions do not show a gaussian behavior.

② The average fluctuations, the relative intensity, the flatness and skewness are dependent on the inlet flow, the cold fraction ε and the inlet pressure. When the inlet flow, the inlet pressure and the geometry are the same, the maximum value of the relative intensity (v'/V) increases if the cold fraction increases. For the same geometry and same cold fraction, the maximum value of the relative intensity increases if the inlet mass flow increases.

③ Near the wall, the existence of the fluctuation is due to the boundary layer of the wall. In the center, the fluctuation is due to the wobbling of the vortex motion. In order to transfer the energy between the different gas layers inside the RHVT, the strong fluctuations and the turbulence play an important role in the energy transport in the vortex tube.

6.2.2.5 Spectral analysis–acoustic phenomena

In [12–14], Kurosaka et al. have proposed a mechanism to explain the energy transport inside the vortex tube, namely "acoustic steaming". In order to reveal the existence of this acoustic phenomena, spectral analysis is applied to the measurements. The results are presented only for the example of $\varepsilon = 0.28$, $\dot{m}_{\mathrm{in}} = 69.5$ g/s and $p_{\mathrm{in}} = 5.10$ bar for different positions along the radius at two stations.

Fig. 6.35 is the result at Station 2 for different positions for $\varepsilon = 0.28$, $\dot{m}_{\mathrm{in}} = 69.5$ g/s

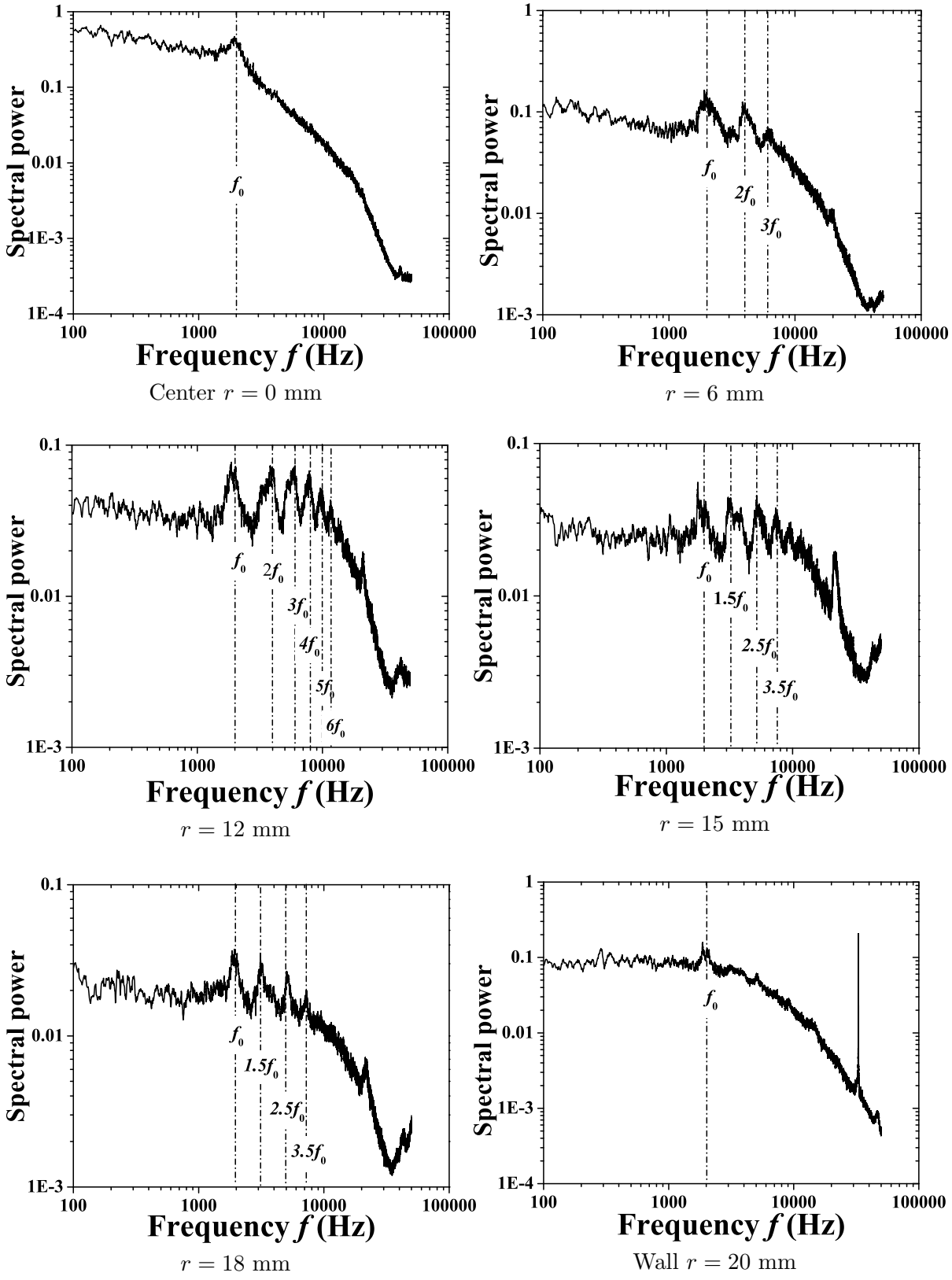

Figure 6.35: *The spectrum for the example of* $\varepsilon = 0.28$, $\dot{m}_{\text{in}} = 69.5$ g/s *and* $p_{\text{in}} = 5.10$ bar *at different positions along Station 2.*

and $p_{\text{in}} = 5.10$ bar. In the center $r = 0$ mm, only one basic frequency occurs which is about 2000 Hz, which is related to the vortex core motion [12–14]. In the region $0 < r \leq 12$ mm multiple frequencies have been found. These frequencies are higher harmonics of the basic frequency, for instance, 2, 3, 4, etc. (or 1.5, 2.5, 3.5). At constant cold fraction and the same inlet flow the power decreases from the center to the wall, the global variation of the power with the frequency is steep in the center and flat near the wall. At $r = 12$ mm, there are 6 peaks, and they multiples of the basic frequency and the orders are 1, 2, 3, 4, 5 and 6. So all these observations indicate the existence of acoustic phenomena [12–14]. Furthermore, the comparisons of the spectrum distributions at $r = 12$ mm for different stations are presented.

Fig. 6.36 shows that along the vortex tube the number of the modes of the frequencies at position $r = 12$ mm are decreasing. At Station 4 and 5, the specific frequencies could not be determined. Near the entrance (Station 2), resonance modes are very strong, while towards the hot end, the resonance modes decrease. At the end, there are no peaks (see Station 4), or the basic frequency decreases (see Station 5).

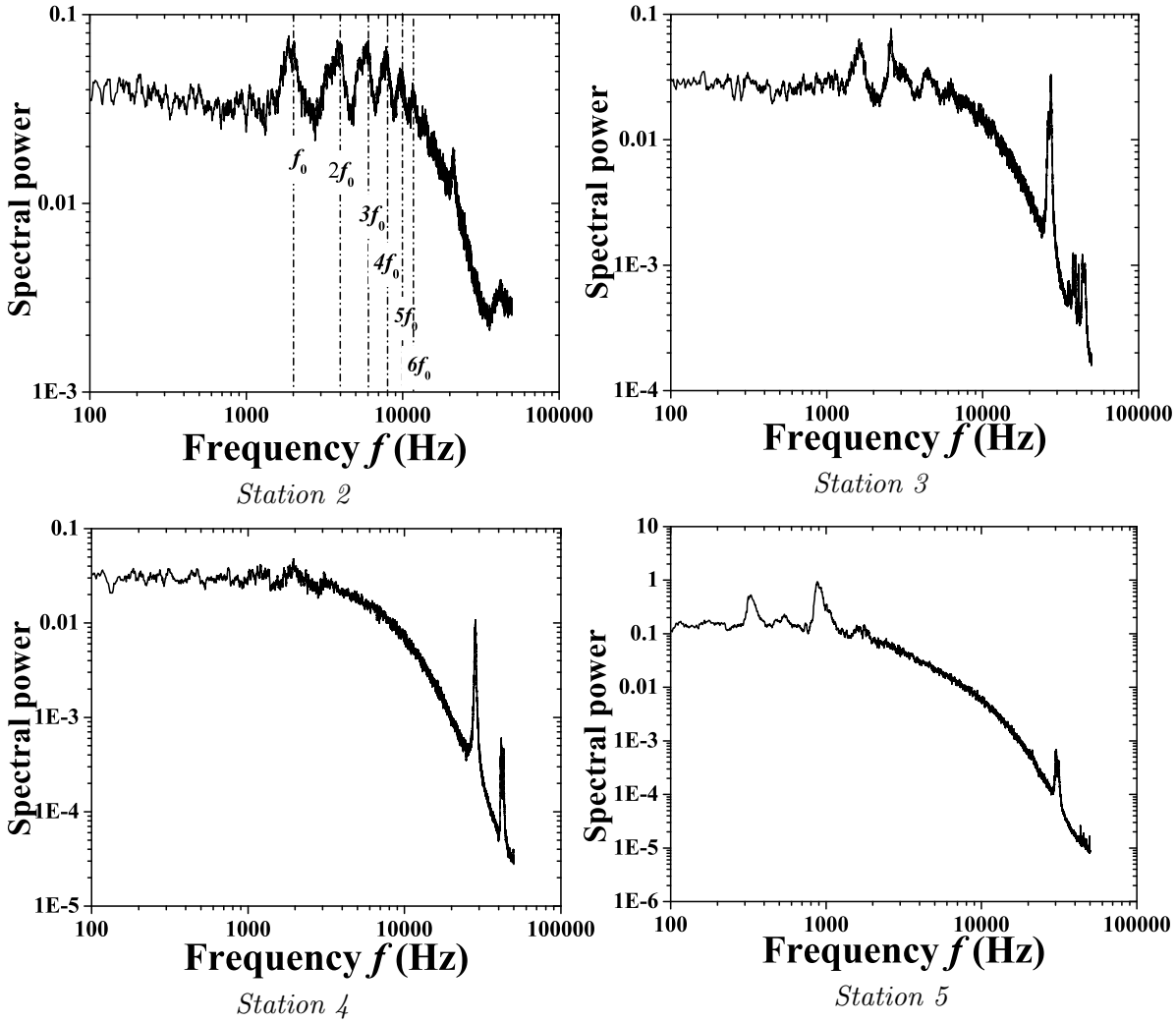

Figure 6.36: *Comparison of the results from the example of* $\varepsilon = 0.28$, $\dot{m}_{\text{in}} = 69.5$ g/s *and* $p_{\text{in}} = 5.10$ bar *at* $r = 12$ mm *for different stations.*

6.2.2.6 Summary of the result with the SPHWA

To summarize the results obtained by the SPHWA, we have found that,

1. The radius R_{cr} at which the signal of the flow angle changes decreases from the chamber towards the hot exhaust.

2. In most cases the radial component $\overline{\rho V_{\mathrm{r}}}$ decreases from the center to the wall. Near the wall it becomes zero. This indicates that the radial component becomes important in the center region. However if the flow is axi-symmetric, at the center the radial velocity must be zero.. So the measured nonzero radial component of $\overline{\rho V_{\mathrm{r}}}$ is due to the fluctuations. This is confirmed by the fact that the calculated average fluctuation δ_{av} has the same order of magnitude as the radial component of $\overline{\rho V}$. So it indicates that the flow patten— vortex core wobbles around the axis. The azimuthal component shows a solid-body rotation in the center region.

3. In the regions near the center, near the wall, close to the vortex chamber, and near the hot exhaust, the relative turbulence intensity γ_δ is more than 20%. These fluctuations are larger than common values for flat wall boundary layers which are of the order of 10% [10]. These parameters of the turbulence are dependent on the cold fraction ε, the inlet flow $\dot{m}_{\mathrm{in}}$ and the geometry. In [8, 15, 16], the authors have pointed out that the turbulence inside the RHVT plays an important role for the energy separation, here we confirmed it with our experiments.

4. The cumulative mass flow distributions show the existence of a secondary circulation. Even at $\varepsilon = 0.90$, the secondary circulation still exists. The shape of the secondary circulation is related to the cold fraction ε and the inlet flow $\dot{m}_{\mathrm{in}}$.

5. Resonance frequencies have been found in the spectral analysis. At the center $r = 0$ mm, only one frequency exists and acts as basic frequency. In the other regions, a sequence of acoustic frequencies occur which are higher order modes of the basic frequency. The maximum value of the number occurs at position $r = 12$ mm near the entrance. At Station 4 and 5, there are no peaks or the peak frequencies damped in the spectral power distribution, so there is no acoustic resonance frequency, while the mean power is larger than near the entrance. This indicates that acoustic damping occurs in the direction of the hot end.

6.2.3 Temperature measurements

The temperature inside the RHVT is measured with the thermocouple mentioned in Chapter 3. Here the results with $\varepsilon = 0.28$ at $\dot{m}_{\mathrm{in}} = 34.7$ g/s and 69.5 g/s are chosen as example (a) and (b), respectively. Fig. 6.37 shows the distribution of the stagnation temperatures for two examples. The stagnation temperature distributions have the following common aspects:

① the stagnation temperature depends on the cold fraction ε, the inlet flow $\dot{m}_{\mathrm{in}}$ and the $Z-$position along the vortex tube;

② along the cross section, the stagnation temperature increases from the center to the wall, it appears to be symmetric to the tube axis;

③ at the same radius, the stagnation temperature increases from the cold end to the hot end except for the case of example (a) at Station 5 (see Fig. 6.37);

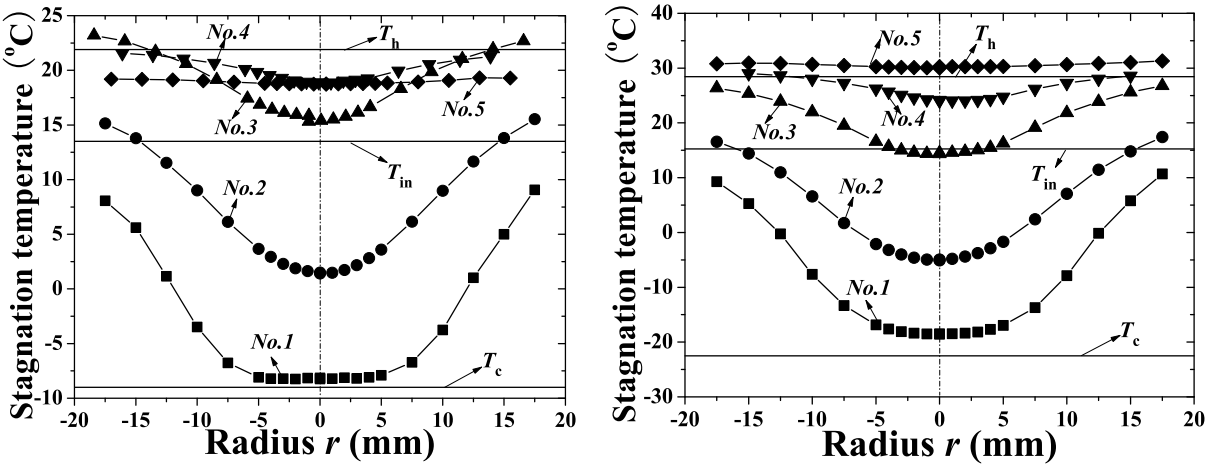

(a) $\dot{m}_{in} = 34.7$ g/s *and* $p_{in} = 2.80$ bar. *(b)* $\dot{m}_{in} = 69.5$ g/s *and* $p_{in} = 5.10$ bar.

Figure 6.37: *Comparison of the distributions of the stagnation temperatures for two examples.*

④ the lowest stagnation temperature occurs in the center region of Station 1, but it is still larger than the cold exhaust temperature T_c;

⑤ the stagnation temperature distribution along Station 5 is very flat and it is close to the hot exhaust temperature T_h.

The specific values from Fig. 6.37 for the two inlet mass flow examples are shown in Table 6.21.

Situation		**Station**				
Inlet flow (g/s) & p_{in} (bar)	Specified result	No.1	No.2	No.3	No.4	No.5
34.7 (g/s), 2.80 bar	T_{min}	-8.2	1.4	15.3	18.9	18.7
	T_{max}	9.1	15.5	23.2	21.5	19.3
69.5 (g/s), 5.10 bar	T_{min}	-18.5	-5.1	14.3	24.0	30.0
	T_{max}	10.7	17.5	26.8	29.0	31.0

Table 6.21: *The maximum and minimum temperatures at different stations for the two examples.* T_{min} *is the lowest temperature from the distribution along the radius of the cross section,* T_{max} *is the maximum temperature from the distribution. The unit of the temperatures is* ^{0}C.

For the cases with $\varepsilon = 0.04$ and 0.90, the stagnation temperature distributions do not always follow the general rules listed above, which is proved by the thermodynamic analysis in Section 2.1.

6.3 Velocity, pressure, and temperature analysis and mapping

The experimental results (p, ρV, T) obtained with different techniques can be used to analyze the gas properties inside the RHVT. With the CPT technique, the stagnation pressure p_{sg}, the static pressure p_{st} and the Mach number were determined. During the THC measurements, the stagnation temperature T_{sg} was measured. In the SPHWA results, the total $\overline{\rho V}$ has been

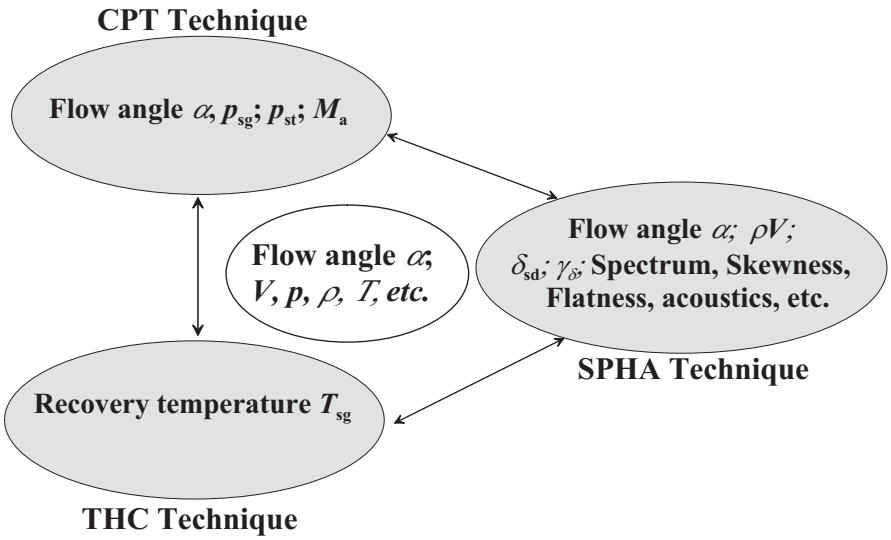

Figure 6.38: *Combining three techniques in the RHVT investigations at constant operating conditions. Based on the experimental results from different techniques (these terms in the gray circles) and the gas dynamic equations, the gas properties in the white circle(flow direction, velocity, density, pressure, and temperature, etc.) can be calculated.*

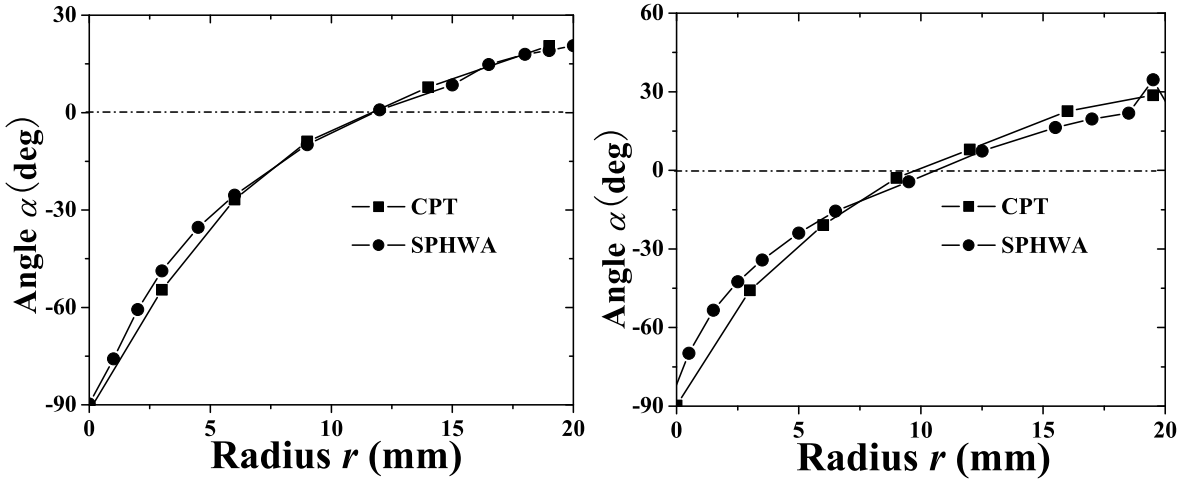

(a) Station 2 *(b) Station 3*

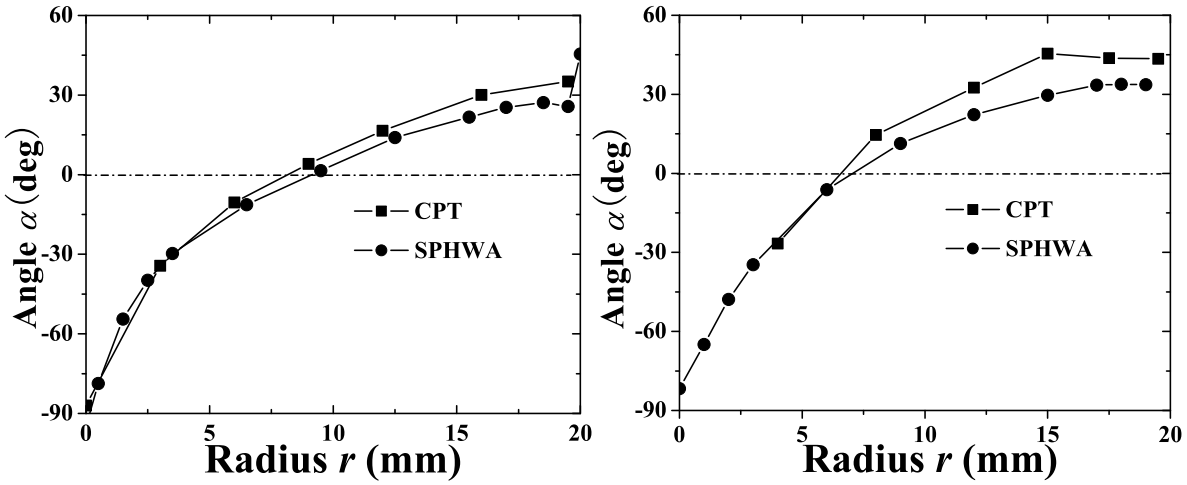

(c) Station 4 *(d) Station 5*

Figure 6.39: *Comparison of the flow directions measured by CPT and SPHWA techniques.*

shown. Now the following equations can be applied

$$\begin{aligned} p_{\mathrm{st}} &= \rho R_{\mathrm{m}} T_{\mathrm{st}} \\ p_{\mathrm{sg}} &= p_{\mathrm{st}} \left[1 + \Gamma_2 M_{\mathrm{a}}^2\right]^{\frac{1}{\Gamma}} \\ M_{\mathrm{a}} &= \frac{V}{a} = \frac{V}{\sqrt{\gamma R_{\mathrm{m}} T_{\mathrm{st}}}} \\ T_{\mathrm{st}} &= \frac{T_{\mathrm{sg}}}{1+\Gamma_2 M_{\mathrm{a}}^2} \end{aligned} \quad . \tag{6.4}$$

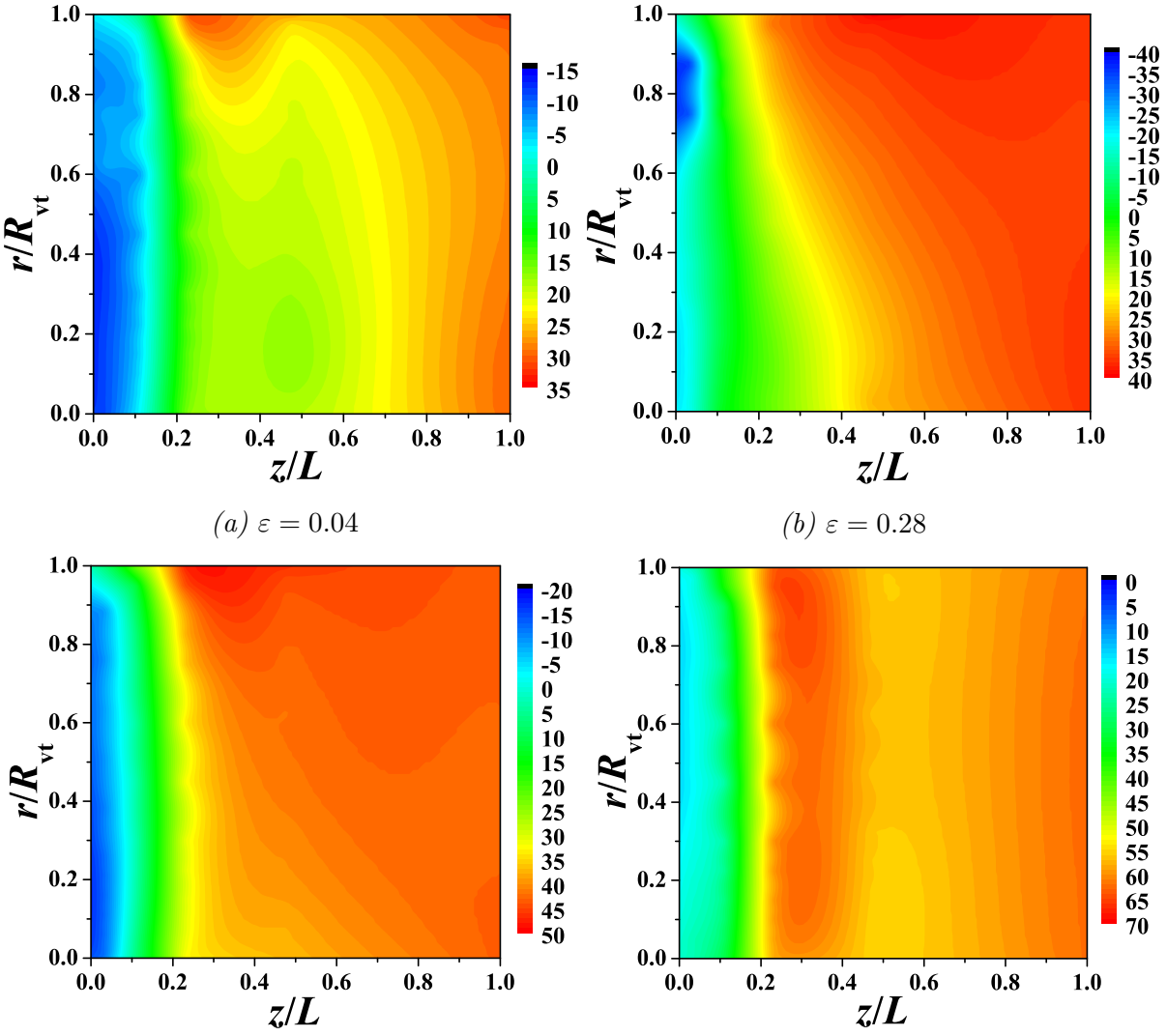

(a) $\varepsilon = 0.04$ *(b)* $\varepsilon = 0.28$

(c) $\varepsilon = 0.39$ *(d)* $\varepsilon = 0.90$

Figure 6.40: *The mapping of the static temperature fields in* ^0C *for different cold fractions at* $\dot{m}_{\mathrm{in}} = 69.5$ g/s *and* $p_{\mathrm{in}} = 5.10$ bar. *Note the difference in the color bar.*

Here, the parameters p_{sg}, T_{sg}, $\overline{\rho V}$ all are known, and from the CPT technique, the azimuthal-axial Mach number $M_{\mathrm{a,azx}}$ is known as well. So, by applying the measured Mach number from the CPT technique as the initial Mach number for calculating T_{st}, p_{st} can be computed by iteration. Then ρ can be calculated, and finally the total velocity $V_{\mathrm{to,1}}$ can be

found and the new total Mach number $M_{a,to}$ is calculated. Using the new total Mach number, T_{sg} and p_{sg}, a second total velocity $V_{to,2}$, by iteration calculation, these two total velocities converges to a value (which is the final total velocity V_{to}) within 0.1%, as indicated in Fig. 6.38.

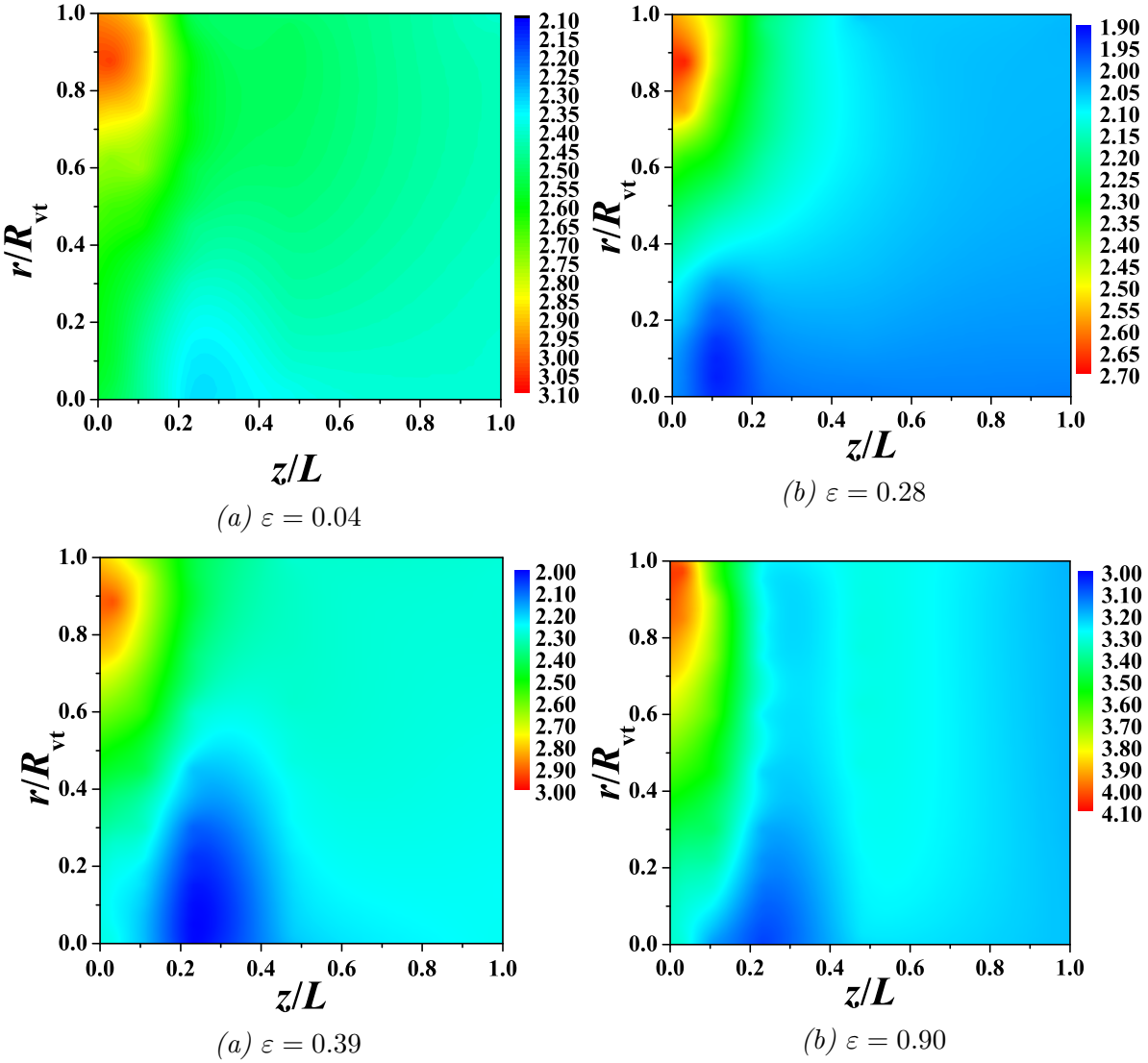

(a) $\varepsilon = 0.04$ (b) $\varepsilon = 0.28$

(a) $\varepsilon = 0.39$ (b) $\varepsilon = 0.90$

Figure 6.41: *The mapping of the density fields in* kg/m^3 *for different cold fractions at* $\dot{m}_{in} =$ 69.5 g/s *and* $p_{in} = 5.10$ bar. *Note the differences in the color bar.*

6.3.1 The possibility of combination

All the experiments with different techniques, at the equal operating conditions, show that the hot and cold exhaust temperatures obtained are in agreement. In addition the flow directions measured by the CPT and the SPHWA are shown for the examples with $\varepsilon = 0.28$ and $\dot{m}_{in} = 34.7$ g/s (example (a)) and 69.5 g/s (example (b)).

Fig. 6.39 shows that the flow directions, measured by the CPT and the SPHWA, are

in agreement. In the center region and near the hot end, the azimuthal and axial velocity components are too small to determine the angle of the flow accurately by the CPT. In Chapter 3, it is mentioned that when the Mach number is lower than 0.25, the CPT becomes an insensitive instrument with about 20% error. At Station 5, the agreement is worse mainly due to such low speeds. For all other settings the agreement is good.

6.3.2 Mapping of the static temperature distribution

With the combined equations, and the measured results by different techniques, the analyzed results for the four different cold fraction cases with $\dot{m}_{\text{in}} = 69.5$ g/s and $p_{\text{in}} = 5.10$ bar are discussed. For the two cases with $\dot{m}_{\text{in}} = 34.7$ g/s and $p_{\text{in}} = 2.80$ bar, the analyzed results are similar to those for the cases with the same cold fraction but $\dot{m}_{\text{in}} = 69.5$ g/s and $p_{\text{in}} = 5.10$ bar.

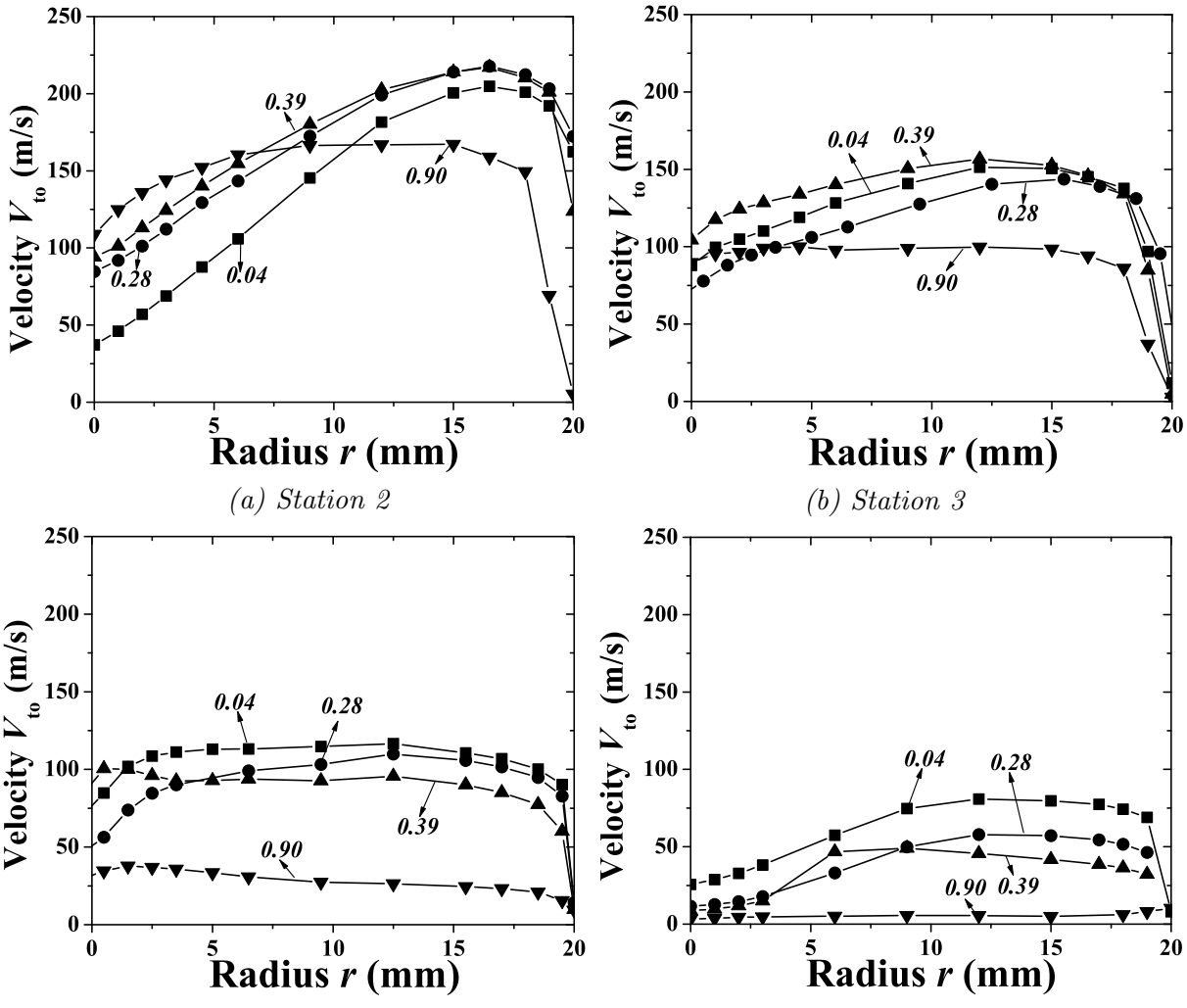

(a) Station 2 (b) Station 3

(c) Station 4 (d) Station 5

Figure 6.42: *The distributions of the velocities for different cold fractions along different stations at* $\dot{m}_{\text{in}} = 69.5$ g/s *and* $p_{\text{in}} = 5.10$ bar.

Fig. 6.40 shows the contour plots of the computed static temperature fields at different

cold fractions. The temperature distribution is layered. In the vortex chamber region, the temperature is the lowest, even lower than the cold exhaust temperature. From the chamber to the hot end, the static temperature inside the system is stratified. At decreasing cold fraction, the position z/L of the contour line where the static temperature is equal to the inlet temperature increases. For $\varepsilon = 0.90$, the contour line where $T = T_{\text{in}}$ is at $z/L = 0.1$, about 0.2 for $\varepsilon = 0.39$, about 0.5 for $\varepsilon = 0.28$, and about 1 for $\varepsilon = 0.04$. Near the wall, the temperature rises, which is partially due to the friction on the wall.

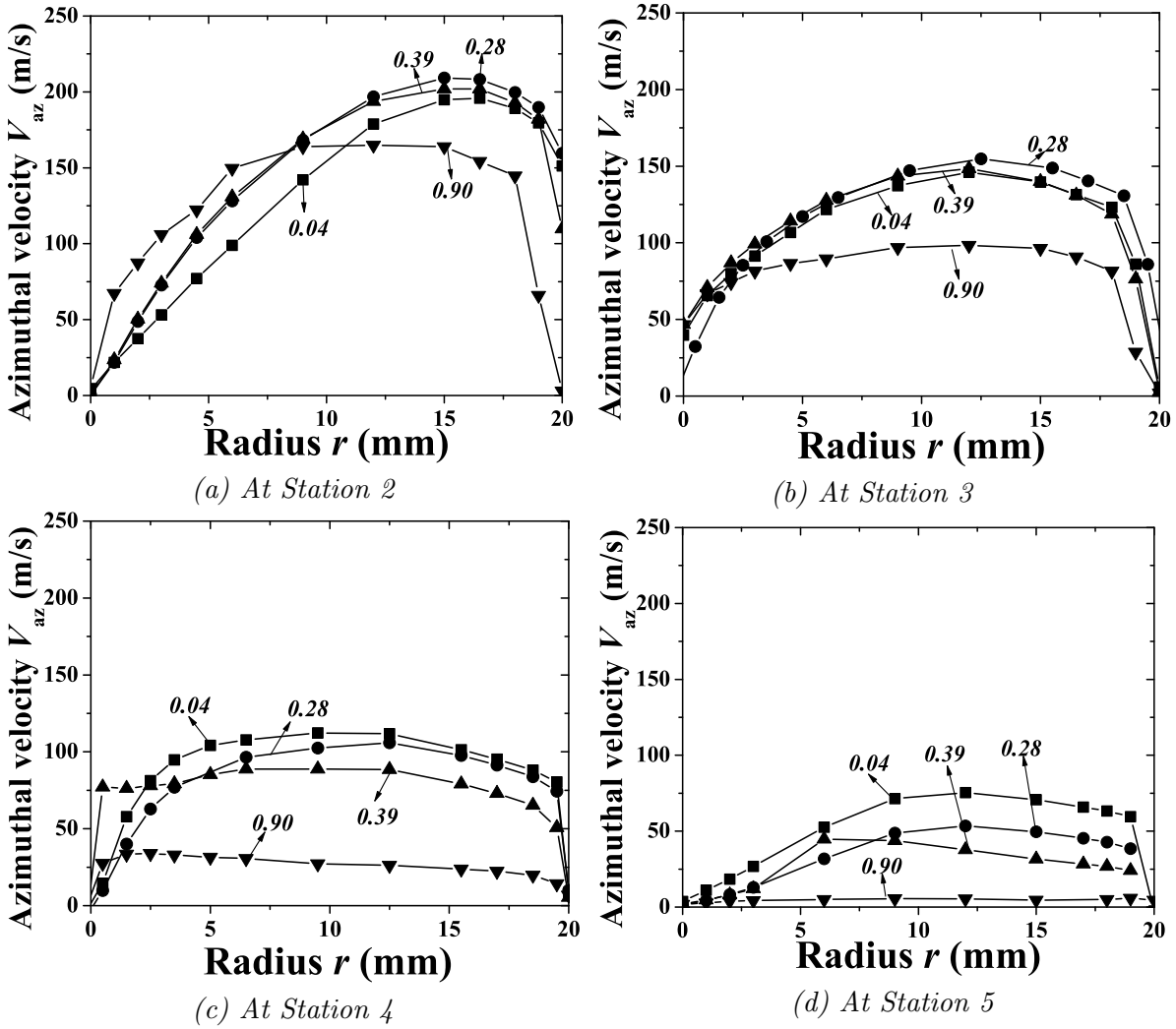

Figure 6.43: *The distribution of the azimuthal velocity component for different cold fractions for the case* $\dot{m}_{\text{in}} = 69.5$ kg/s *and* $p_{\text{in}} = 5.10$ bar.

6.3.3 Mapping of the density

Fig. 6.41 shows the contour plots of the density fields for different cold fractions. A strong density gradient exists at the entrance region, which is due to the local strong variations of the static temperature and pressure. Near the hot exhaust, the density gradients are small. So the density is stratified from the entrance to the hot end as well from the center to the

wall.

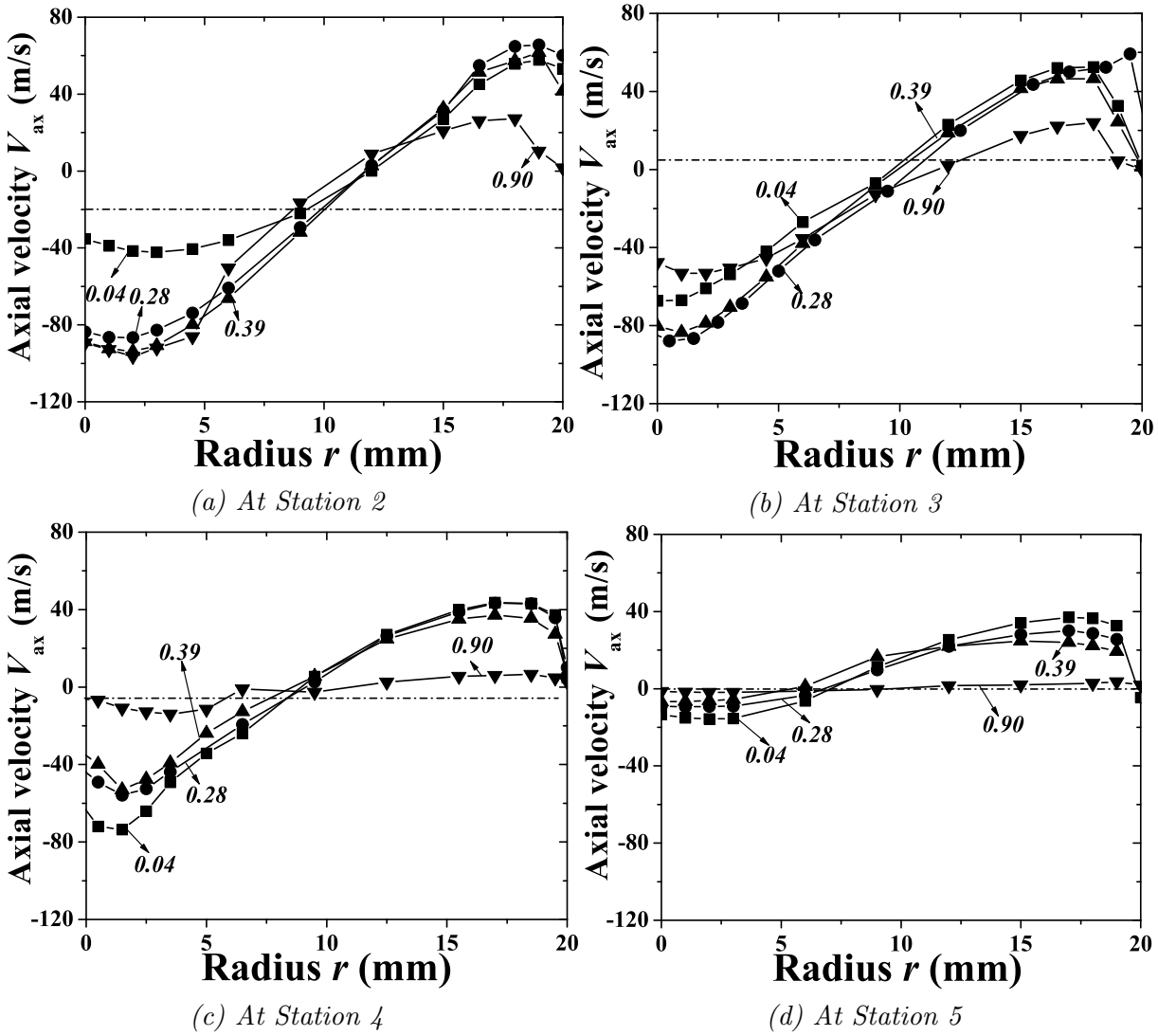

(a) At Station 2 *(b) At Station 3*

(c) At Station 4 *(d) At Station 5*

Figure 6.44: *The distribution of the axial velocity component for different cold fractions for the case* $\dot{m}_{\mathrm{in}} = 69.5$ kg/s *and* $p_{\mathrm{in}} = 5.10$ bar.

6.3.4 Mapping of the velocities

Inside the RHVT, the flow is three dimensional, not axi-symmetric swirling. So the three velocity components (V_{r}, V_{t}, V_{a}) and the total velocity V are presented here. From the azimuthal -axial $\overline{\rho V_{\mathrm{azx}}}$, the radial $\overline{\rho V_{\mathrm{r}}}$, the flow direction α and the local density ρ, the radial, axial and azimuthal velocity components were computed.

Fig. 6.42 shows the total velocity for different cold fractions. The maximum total velocity V is decreasing from the entrance towards the hot end. The velocity in the center is nonzero due to the axial and radial velocity components.

Fig. 6.43 shows the azimuthal velocities at four different cold fractions in the case $\dot{m}_{\mathrm{in}} =$ 69.5 g/s and $p_{\mathrm{in}} = 5.10$ bar. All these components also have been found by CPT technique,

and described before in Fig. 6.21. Here only the results based on the SPHWA are shown. It can be seen that the azimuthal component distribution along Station 2 for $\varepsilon = 0.04$, 0.28 and 0.39 look similar and like a solid-body vortex except for $\varepsilon = 0.90$, along Station 4, only in the center region within a very small radius (about 3 mm) a solid-body vortex is seen. Near the hot end, the azimuthal velocity decreases when ε increases. At the center the azimuthal velocity is zero, the azimuthal velocities measured with the CPT technique in the center (see Fig. 6.21) are zero as well. From this we interpret that the nonzero azimuthal velocity found in the small RHVT in Chapter 4 is due to the asymmetric injection and the wobbling of the flow pattern.

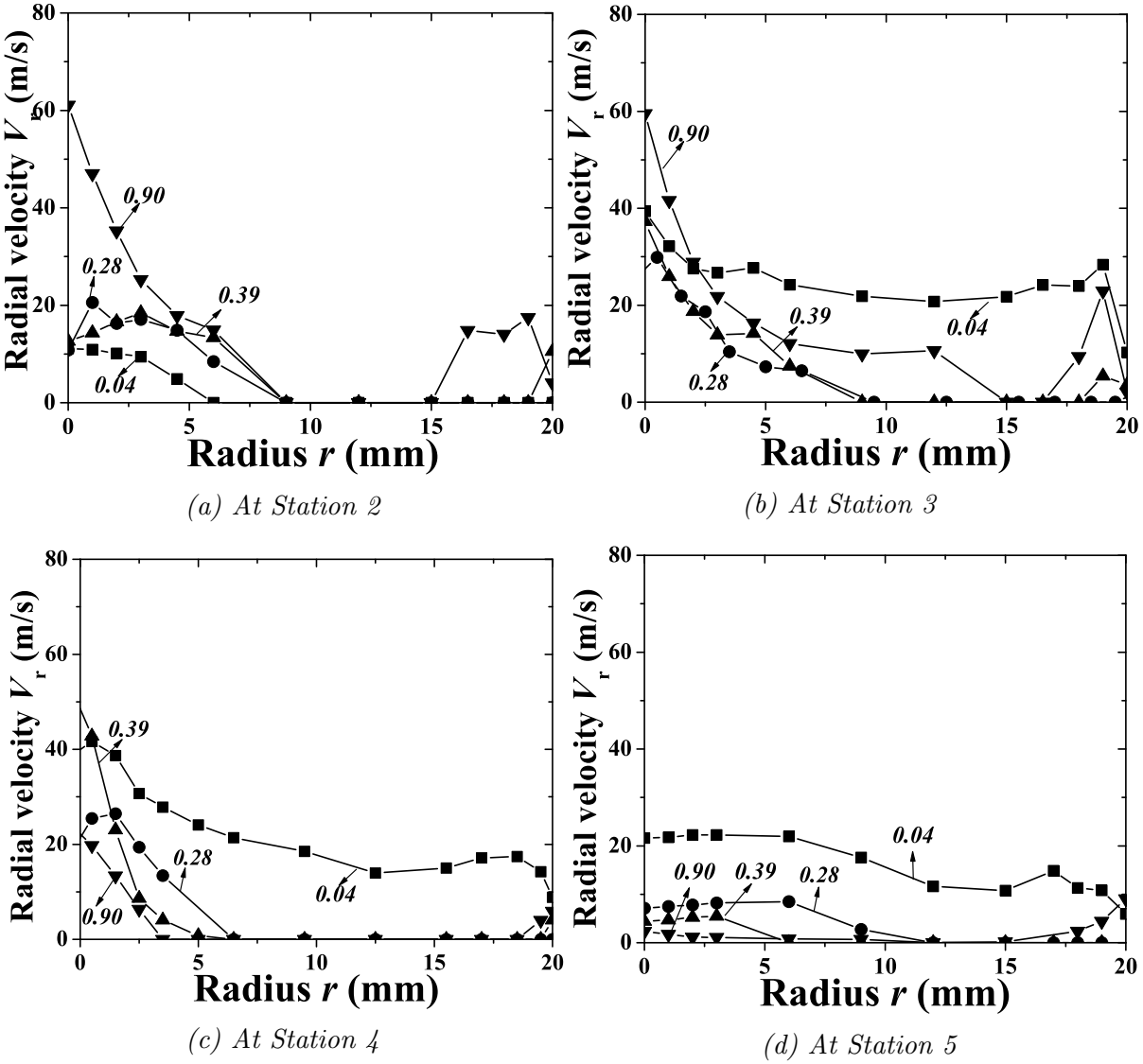

(a) At Station 2 *(b) At Station 3*

(c) At Station 4 *(d) At Station 5*

Figure 6.45: *The distribution of the radial velocity component for different cold fractions for the case* $\dot{m}_{\text{in}} = 69.5$ kg/s *and* $p_{\text{in}} = 5.10$ bar.

Fig. 6.44 shows the axial velocity distributions for four different cold fractions at $\dot{m}_{\text{in}} = 69.5$ g/s and $p_{\text{in}} = 5.10$ bar. It shows that the critical radius where the axial velocity changes

its direction decreases from the entrance towards the hot end. The maximum positive axial velocity decreases from the inlet to the hot end, the maximum negative value as well. The axial velocity measured with the CPT technique (see Fig. 6.20) has also similar characteristics.

Figs. 6.45 shows that, in most cases, the radial velocity component inside the RHVT is much smaller than the azimuthal velocity component. In the center region there is a significant radial velocity. However, also large velocity fluctuations occur in the center region, as shown in Fig. 6.46. So part of the radial velocity is due to the wobbling of the flow pattern.

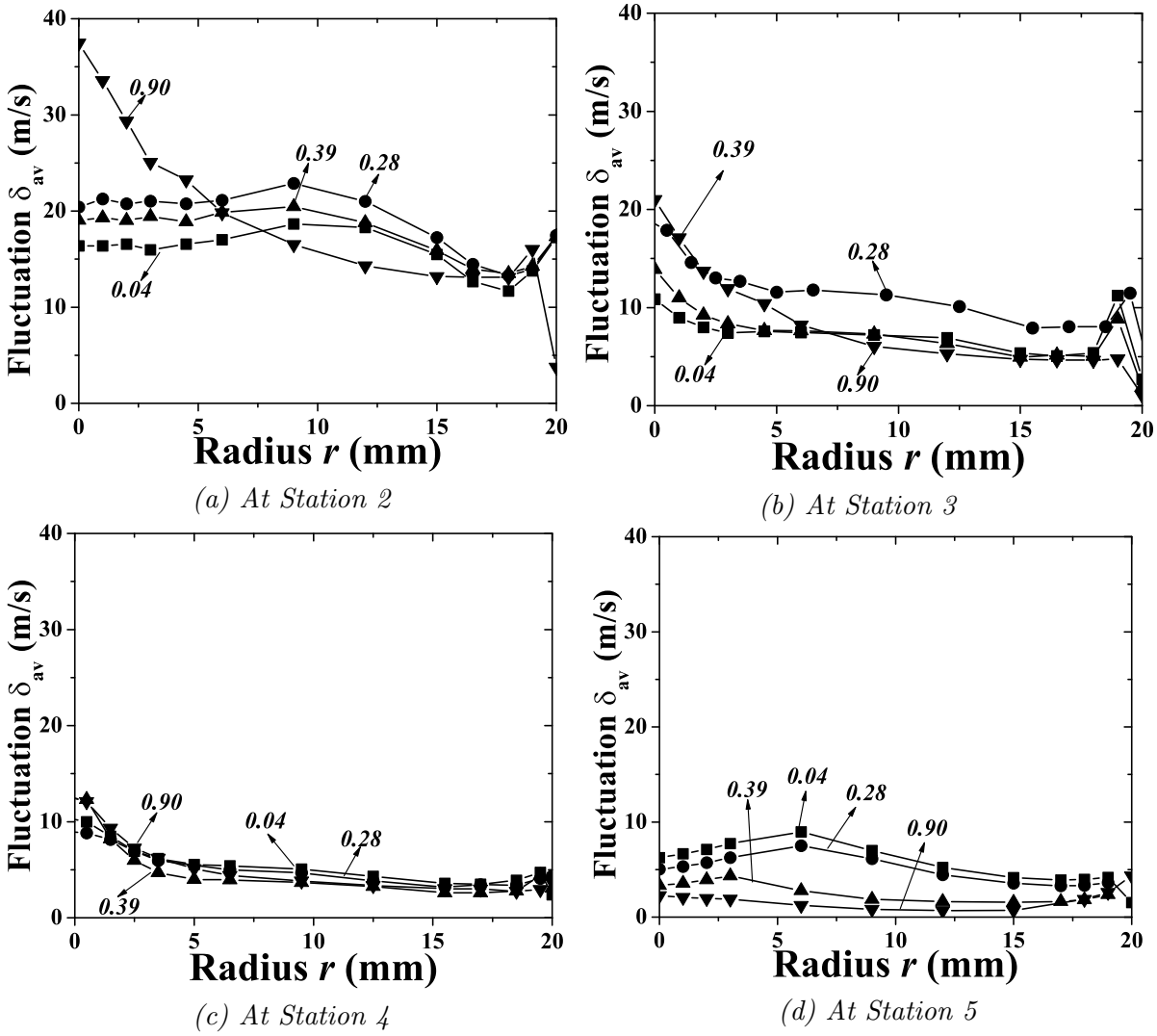

Figure 6.46: *The distribution of the average fluctuations for different cold fractions for* $\dot{m}_{\text{in}} = 69.5$ g/s *and* $p_{\text{in}} = 5.10$ bar.

6.4 Summary

In summary, we can conclude that:

1. With three different techniques, the stagnation and static pressure, the stagnation and

static temperature, the velocity and the density fields inside the RHVT have been determined.

2. The azimuthal velocity shows that near the entrance, the velocity distribution looks like a solid-body vortex. This distribution has the tendency to format towards a Rankine vortex. When the gas flows to the hot end, the solid-body rotation dampens and at the end the profile becomes flat. The azimuthal velocity in the center is zero. Apparently the nonzero azimuthal velocity in the small system in Chapter 4 is due to the asymmetric injection system and the wobbling of the flow pattern.

3. The axial velocity profile shows that the critical radius decreases from the entrance towards the hot end, which further indicates that the flow pattern introduced in Chapter 4 is indeed a good representation of the flow pattern in the vortex tube. The calculated cumulative axial mass flow, based on the axial velocity distribution, shows the existence of a secondary circulation (recirculation) inside the RHVT. This means that the gas that flows to the cold end in the center will partially reverse to the hot end.

4. At the center if the flow is axi-symmetric, the average radial velocity has to be zero. However, in the experiments we measure the root-mean-squared value of the velocities. In this case, the combination of the wobbling and fluctuation lead to the measured profiles which is given a nonzero V_r at $r = 0$.

5. The average fluctuation has the same order of magnitude of the radial velocity which indicates that the turbulence inside the RHVT very strong and plays an important role [8, 15, 16].

6. The spectral analysis shows that the gas flow in the the center region has only one frequency which acts as the basic resonance frequency. In the periphery region, multiple frequencies have been found. These frequencies are higher harmonics of the basic frequency. This indicates acoustic phenomena occurring in the periphery region. The intensity of the acoustic modes decreases towards the hot end.

7. The values of the skewness in the center region and near the wall are far from zero, while in the intermediate region they are approximately equal to zero. The values of the flatness in the center region and near the wall are far from 3, while in the intermediate region they are close to 3. This indicates that the fluctuation profiles are not Gaussian and disordered in the center region and near the wall, while in the intermediate region, the fluctuation profiles are more Gaussian and ordered.

References

[1] H. Takahama. Studies on vortex tubes (1) experiments on efficiency of energy separation (2) on profiles of velocity and temperature. *Bulletin of JSME*, 8(31):433–440, 1965.

[2] J.E. Lay. An experimental and analytical study of vortex-flow temperature separation by superposition of spiral and axial flow, part I. *Trans. ASME J. Heat Transfer*, 81:202–212, Aug. 1959.

[3] J.E. Lay. An experimental and analytical study of vortex-flow temperature separation by superposition of spiral and axial flow, part II. *Trans. ASME J. Heat Transfer*, 81:213–222, Aug. 1959.

[4] H. Takahama and H. Yokosawa. Energy separation in vortex tubes with a divergent chamber. *Trans. ASME, J. Heat Transfer*, 103:196–203, May 1981.

[5] Y.D. Raiskii and L.E. Tunkel. Influence of vortex-tube configuration and length on the process of energetic gas separation. *Journal of Engineering Physics and Thermophysics*, 27(6):1578 – 1581, December 1974.

[6] Y. Soni and W.J. Thomson. Optimal design of the Ranque-Hilsch vortex tube. *Trans. ASME, J. Heat Transfer*, 94(2):316–317, 1975.

[7] P.K. Singh, R.G. Tathgir, D. Gangacharyulu, and G.S. Grewal. An experimental performance evaluation of vortex tube. *Journal of Institution of Engineers (India)*, 84:149–153, Jan. 2004.

[8] A.J. Reynolds. *Studies of Rotating fluids a) Plane Axisymmetric Flow, b) Forced Oscillations in a Rotating fluid, c) The Ranque-Hilsch Vortex Tube.* PhD dissertation, University of London, September 1960.

[9] V. Shtern and F. Hussain. Collapse, symmetry breaking, and hysteresis in swirling flows. *Annual Review of Fluid Mechanics*, 31:537–566, 1999.

[10] J.O. Hinze. *Turbulence.* McGraw-Hill, London, 2nd edition, 1975.

[11] C. Croarkin and P. Tobias, editors. *e-Handbook of Statistical Methods.* Statistical Engineering Division, NIST, http://www.nist.gov/stat.handbook/.

[12] M. Kurosaka. Acoustic streaming in swirling flow and the Ranque-Hilsch (vortex-tube) effect. *J. Fluid Mech.*, 124:139–172, 1982.

[13] J.G. Chu. *Acoustic streaming as a mechanism of the Ranque-Hilsch effect.* PhD dissertation, University of Tennessee, Knoxville, Dec. 1982.

[14] H. Kuroda. *An experimental study of temperature separation in swirling flow.* PhD dissertation, University of Tennessee, Knoxville, Dec. 1983.

[15] A. Gutsol. The Ranque effect. *Physics-Uspekhi*, 40(6):639–658, 1997.

[16] A.J. Reynolds. Energy flow in a vortex tube. *Z. Angew. Math. Phys.*, 12:343–356, 1961.

Chapter 7

Conclusions and Recommendations

In this chapter, the conclusions are presented and some recommendations for future work are given.

7.1 Conclusions

We can conclude that:

1. The irreversible parameters Θ_{ir} for all the measurements in Chapter 4 are about 1.70, which is very close to the critical value of 1.79. This indicates that the process inside the RHVT system is highly irreversible.

2. In this thesis, we have formulated a modification of Ahlborn's model which takes into account that the normalized pressure ratio X depends also on the geometric parameters of the RHVT chamber. It is shown that the modification of Ahlborn's model agrees better with the measurements in Chapter 4 than Ahlborn's original model.

3. With the modified Ahlborn model, it is shown that it is necessary to increase the exhaust velocity at the exhaust of the inlet nozzle, and to keep the pressure drop over the inlet nozzle small for improving the performance of the RHVT. The calculation and simulations for the design of the inlet nozzle agree with measured mass flow rates. The modified Ahlborn model is still considered as an empirical model and can be used to predict the performance of the RHVT system based on the operating conditions.

4. The design aspects of the measurement techniques: cylinder type Pitot tube (CPT), single probe hot-wire anemometry (SPHWA), and the thermocouple (THC) was introduced in detail, including the calibrations of all these instruments. With the CPT it is possible to measure the flow direction, pressure and the velocities, except for the radial component. The SPHWA is used to measure the flow direction, the mean value of ρV, and the fluctuations, the turbulent parameters, and the spectral frequency behavior. With the THC, the stagnation temperature can be measured. It is found that these instruments can be used successfully to investigate the flow quantities inside the RHVT.

5. In all experiments a secondary circulation flow is found. The position where the secondary circulation starts depends on the inlet mass flow, cold fraction and geometry. With a given inlet mass flow and given geometry, for small cold fractions, the secondary

circulation exists even at the station close to the hot exhaust; for large ε, it only occurs close to the entrance section of the RHVT.

6. The turbulence measurements show that in the center and near the wall, the intensity of the turbulence level is very strong ($v'/V > 20\%$), and non-Gaussian. While in the rest of the intermediate region, the turbulence level is smaller, and Gaussian. For very small and very large cold fraction cases, the turbulence is non-Gaussian over the whole cross section.

   The spectral analysis based on the SPHWA shows the existence of acoustic phenomena inside the RHVT. In the center only one frequency exists. In the periphery region multiple frequencies exist. These frequencies are higher harmonics of the basic frequency. The acoustic behavior at the entrance is very strong and near the hot end it is damped. The acoustic frequencies are clear for the two extreme cases $\varepsilon \simeq 0.04$ and 0.90. The spectral results contain a series of frequencies, which has the behavior of the acoustic frequencies mentioned by Kurosaka et al. [1–3].

7.2 Recommendations

1. Experiments with a multi-probe hot-wire anemometry are recommended. Due to the limitation of the single probe hot-wire anemometry, it is not possible to find characteristics of the turbulence based on time, and position together. It is also not possible to get 3D turbulence information.

2. The relationship between the theoretical model, turbulence and acoustics is not yet clear. More theoretical analysis on these aspects is necessary.

3. Numerical simulation of the flow inside the RHVT system is necessary. By numerical work, it is possible to simulate the pressure, velocity, temperature, density, fluctuation simultaneously and overcome the difficulties met in the experiments.

References

[1] M. Kurosaka. Acoustic streaming in swirling flow and the Ranque-Hilsch (vortex-tube) effect. *J. Fluid Mech.*, 124:139–172, 1982.

[2] J.G. Chu. *Acoustic streaming as a mechanism of the Ranque-Hilsch effect.* PhD dissertation, University of Tennessee, Knoxville, Dec. 1982.

[3] H. Kuroda. *An experimental study of temperature separation in swirling flow.* PhD dissertation, University of Tennessee, Knoxville, Dec. 1983.

Summary

The Ranque-Hilsch vortex tube cooler (RHVT) has been investigated in the Low Temperature Group at Eindhoven University of Technology. The research was focussed on a thorough experimental investigation of the flow inside the system at a large variety of experimental conditions.

Three measurement techniques (cylinder type Pitot Tube (CPT), single-probe hot-wire anemometry (SPHWA), thermocouple (THC)) have been designed and calibrated. The CPT is used to measure the pressure and two velocity components. The SPHWA is used to measure the mean-three dimensional ρV, the average fluctuation δ_{av}, the intensity of the fluctuation, the flatness and skewness and the spectral analysis. The THC is used to measure the recovery temperature.

Two set-ups have been designed for the investigation: a small set-up with one inlet nozzle, and a larger set-up with 8 inlet nozzles distributed around the interference. For both set-ups, there are several access ports in the wall of the vortex tube along its length. We proved that the three measurement techniques can be used for the investigation of the flow properties inside the RHVT.

The measured velocity distribution inside the RHVT shows a profile that, in the center region, is a solid-body rotation, and in the periphery region, tends to a potential vortex motion. The root-mean-squared (RMS) value of the radial velocity component has a maximum at the center and decreases with the radius. In the periphery region the RMS of the radial velocity is almost zero. The maximum RMS value of the radial velocity has the same order of magnitude as the average fluctuation, which indicates that it is due to the wobbling of the flow pattern and the fluctuation. The relative intensities of the fluctuation in the center and near the wall are more than 20%. The flatness and skewness of the turbulence indicate that, in the center and near the wall, the turbulence inside the RHVT is random and non-Gaussian, while in the intermediate region, the turbulence is ordered and Gaussian. Near the vortex chamber in the center region, the recovery temperature is constant.

Furthermore, we proved the existence of a recirculating flow inside the RHVT and suggested the existence of acoustic phenomena. The parameters of both these phenomena depend on the inlet flow, the cold fraction, and the geometry. The acoustic phenomena near the entrance are very strong, and damped towards the hot end.

With a thermodynamic analysis, relationships between the three temperatures (T_{in}, T_{h}, T_{c}) and the pressures (p_{in}, p_{h}, p_{c}) are derived using an irreversibility factor Θ_{ir}. It is found that the maximum irreversibility factor depends on the ratio $p_{\mathrm{in}}/p_{\mathrm{c}}$ of the inlet pressure p_{in} and the cold exit pressure p_{c}.

A model, introduced by Ahlborn et al. is analyzed. The assumptions, made by Ahlborn et al., have been discussed. A modification of Ahlborn's model (MAM) has been described. The comparison between the results of the two models shows that the predicted temperature

differences with the modified model are smaller than those predicted with the original Ahlborn model. The results of the modified model agree better with the results of the experiments than the original model. The modified model is still an empirical model. So we expect that turbulence and acoustics play more important roles in the mechanism of the energy separation inside the RHVT.

Samenvatting

In de afgelopen vier jaren is de Ranque-Hilsch wervelbuiskoeler onderzocht in de groep Lage Temperaturen van de Faculteit Technisch Natuurkunde van de Technische Universiteit Eindhoven. Een grondig experimenteel onderzoek is uitgevoerd naar de stromingseigenschappen en temperatuurverdeling in het systeem bij een grote variatie van experimentele condities.

Drie meetmethoden (cilindertype Pitotbuis (CPT), enkelvoudige hete-draad-anemometrie (SPHWA), thermokoppel (THC)) zijn ontwikkeld en gekalibreerd. De CPT wordt gebruikt om de druk en gemiddelde (RMS) snelheid te meten. De SPHWA wordt gebruikt om de drie snelheidscomponenten te bepalen, de snelheidsfluctuaties, de intensiteit van de fluctuaties, de zogeheten flatness en skewness van de signalen en het frequentiespectrum. De THC wordt gebruikt om de stagnatietemperatuur op te meten. Het genereren van een krachtige wervel en een grote impulsstroomdichtheid in de wervelbuis is tot stand gekomen na ontwerp van een sonische inlaatnozzle. Hiervoor is een analyse uitgevoerd met behulp van de gasdynamicavergelijkingen. Er zijn twee meetopstellingen gebouwd voor het onderzoek: een kleine opstelling met slechts één inlaatnozzle en een grote waar de inlaatcondities aangepast konden worden. Voor beide opstellingen zijn meerdere toegangspoorten gemaakt in de wand van de wervelbuis langs de lengte. Hierdoor konden lokaal in de buis metingen worden uitgevoerd. Het onderzoek heeft aangetoond dat de drie technieken consistent zijn.

De gemeten snelheidsdistributie in de Ranque-Hilsch wervelbuis laat een profiel zien dat in het centrum bestaat uit een starre rotatiestroming, terwijl aan de periferie de stroming neigt naar een potentiaalstroming. De RMS-waarde van de radiële snelheid heeft een maximum in het centrum en neemt af met de radius. In de periferie is de radiële snelheid nul. De maximale RMS-waarde van de radiële snelheid is van dezelfde grootte als de gemiddelde fluctuatie, hetgeen aangeeft dat deze radiële snelheid zijn oorzaak vindt in het oscilleren van de wervel ten opzichte van de as van de wervelbuis. De relatieve grootte van de fluctuaties bedraagt in het centrum en nabij de wand 20%. De skewness- en flatnesssignalen van de turbulentie geven aan dat, in het centrum en nabij de wand, de turbulentie niet Gaussisch van karakter is, terwijl dit wel zo is in het tussenliggende gebied. Nabij de wervelkamer in het centrumgebied is de stagnatietemperatuur constant.

In het onderzoek is aangetoond dat er een secundaire stroming in de Ranque-Hilsch wervelbuis heerst en dat akoestische resonantie optreedt. De parameters van beide fenomenen hangen af van het massadebiet, de koude fractie en de geometrie. De akoestische verschijnselen nabij de inlaat zijn zeer intens en dempen uit naar de warme zijde van de wervelbuis. Met de thermodynamische analyse is een relatie tussen de drie temperaturen (T_{in}, T_{h}, T_{c}) en de drukken (p_{in}, p_{h}, p_{c}) afgeleid, waarbij een irreversibiliteitsfactor is gebruikt. Er is gevonden dat de maximale irreversibiliteitsfactor afhankelijk is van de druk verhouding aan de instroom- en de uitstroomkant. Een model, geïntroduceerd door Ahlborn, is geanalyseerd. De aannames gemaakt door Ahlborn zijn kritisch besproken in dit proefschrift. Een aanpass-

ing van het model van Ahlborn is beschreven. Een vergelijking tussen beide modellen laat zien dat de voorspelde temperatuurverschillen met het gemodificeerde model kleiner zijn dan die als voorspeld met het oorspronkelijke model van Ahlborn. Het nieuwe model heeft voor dit onderzoek een betere voorspellende waarde dan het oorspronkelijke model.

Acknowledgement

During the past four years studying the Ranque-Hilsch vortex tube in the Low Temperature group at TU/e, I have received a lot of support from my colleagues, family, and friends. Hereby, I want to thank all of you for your help, discussion, and friendship.

First I want to thank my supervisor Prof. dr. Fons de Waele, who offered me the opportunity to do this PhD project. During the past four years, you gave me inspiration and encouragement, and formulated the research plan of my PhD. This formed the basis of this thesis.

Special thanks goes to Dr. ir. Jos Zeegers who coached me. You motivated me during the research, and the writing of the thesis. I also want to thank you for your efforts to convince the Dutch Embassy in Beijing to issue the VISA for my wife.

I owe many thanks to Dr. Karel Bosschaart, for all analysis and help with work of SPHWA, reading and correcting my thesis with your remarks and suggestions.

I am grateful to all the technicians in the group for their help in designing and building up the set-ups. First to my office-mate, Leo van Hout, thank you for all help on the design and building of the set-up, also for your numerous help for the house moving, fixing, Dutch translating, i.e. to make my stay in the Netherlands comfortable. To Loek Penders, thank you for the help with all the electronic equipment, to Jos van Amelsvoort and Nando Harmsen, for all help with the nitrogen gas supplies and controls.

I like to express my gratitude to Dr. XU Mingyao who introduced me to this group. You were the starting point for my education at TU/e.

I like to thank the committee members Prof. Rini van Dongen, Prof. Harry Hoeijmakers and Prof. Harry van den Akker for reading and correcting my thesis. The remarks and suggestions from all of you improved my thesis significantly.

Furthermore, I like to thank Prof. Willem van de Water for offering me the electronic box for the hot-wire anemometer, and explaining the physics of fluctuations in turbulence.

Then I want to thank the technicians from the workshop of the Physics Department, the computer assistants from the help desk, and Ms. Ina Ruepert and Ms. Liesberth Delissen from the Physics library.

Ms. Jelka Schot, Ms. Jolanda Willems and Ms. Lutgart van Kollenburg kindly helped me to make my stay in the Netherlands comfortable.

I like to thank all other members of the Low Temperature group for bringing the friendly and creative atmosphere, nice X'mas dinners and memorable summer BBQs.

I want to thank all my Chinese friends for generating the homelike staying in Eindhoven, annual BBQs, Chinese New Year's parties, small family parties, tax lectures and sporting.

I want to thank my former supervisor and teachers from Xi'an Jiaotong University: Prof. He Yaling, Prof. Tao Wenquan, Prof. Chen Zhongqi, for your recommendations. With your recommendations, I got the chance to continue my education in TU/e.

Then I owe many thanks to my family. I am grateful to my father Lee Kejing and my mother Gao Cuihua, for giving me their deep love, encouragement and support during my education. I want to thank my sister Lee Yingxia and her family for taking care of our parents, which made my stay in the Netherlands possible.

There are a lot of thanks I want to say to my deeply loved wife XU Hong. Thank you for doing most house work in the past years, especially in the time I was writing the thesis. Thank you for teaching me the LaTeX and MatLab software, for reading the version of this thesis, and giving me the constructive comments. Thank you for always encouraging and supporting me.

At the end, I want to dedicate this thesis to my new-born son Gao Lee Jian; you are so naive, bring me the fresh air of life, give me the hope and good luck; I wish you happiness all days of your life.

CV

29 November 1977	:	Born in Hubei province, China
September 1994 $\sim$ July 1998	:	Bachelor in Thermal Engineering Power and Energy Engineering School Xi'an Jiaotong University, China
September 1998 $\sim$ March 2001	:	Master in Engineering thermal Physicis Power and Energy Engineering School Xi'an Jiaotong University, China
April 2001 $\sim$ April 2005	:	Ph.D research at the Low Temperature Group Department of Applied Physics Eindhoven University of Technology, the Netherlands
October 2005 –	:	Process Engineer Gasification & Hydrogen Manufacturing Shell Global Solutions International B.V. Amsterdam, the Netherlands